GRAVITATIONAL LENSING AS A TOOL TO DETECT DARK MATTER AND TO TEST GRAVITY THEORIES

Dissertation

zur

Erlangung der naturwissenschaftlichen Doktorwürde
(Dr. sc. nat.)

vorgelegt der

Mathematisch-naturwissenschaftlichen Fakultät

der

Universität Zürich

von

Fabiana De Luca

aus

Italien

Promotionskomitee

Prof. Dr. Daniel Wyler (Vorsitz)
Prof. Dr. Philippe Jetzer (Leitung der Dissertation)
Prof. Dr. Gaetano Scarpetta

Zürich 2007

Contents

Einführung

Neue Ergebnisse zeigen an, dass wir in einem ebenen, beschleunigten Universum, das hauptsächlich Energie von unklarem Ursprung enthält, leben. Dennoch besteht ein bedeutender Teil des Universums aus Materie, in allen ihren Formen. Zu diesem Teil gehört die bekannte atomische Materie, aus der ein geringer Teil des Weltalls besteht. Die Aufteilung der dunklen Materie wird noch debattiert und grosser Arbeitsaufwand wurde aufgeführt, um neue Einblicke in diesen Bereich zu gewinnen. Eine der noch unbeantworteten Fragen ist, ob und inwieweit die Galaxien von einem dunklen Halo umgeben sind. In der Tat scheint es, dass die Galaxien nicht nur leuchtende Objekte enthalten, sondern auch dunkle, unsichtbare Materie. Möglicherweise besteht der baryonische Teil dieser unfeststellbaren Materie aus Planeten, Braunen Zwergen, Weissen Zwergen oder Schwarzen Löchern. Diese Kandidaten werden gemeinsam *MACHOs* (*MAssive Compact Halo Objects*) genannt. In dem ersten Teil dieser Dissertation wird die Suche nach MACHOs in der Milchstrasse und in einem ihrer Satelliten, der Grossen Magellanischen Wolke (LMC), angesprochen. Eine solche Suche kann durch die Analyse von *gravitational lensing* Ereignisse durchgeführt werden. Es ist wohlbekannt, dass, wenn ein Stern mit einem massreichen Körper (*Linse*) und einem Beobachter gerichtet ist, wird er viel heller, wobei der Effekt auf die Grösse der Lichtquelle und die Geomtrie des Systems ankommt. Dieser Effekt ist als *gravitational lensing* bekannt und ist ein leistungsfähiges Hilfsmittel um eine unsichtbare Linse zu entdecken. Das heisst, obwohl die Linse dunkel ist, kann ihr Dasein durch die Effekte ihres Gravitationsfeldes verraten werden. Bisher haben viele internationale Kollaborationen gravitational lensing Ereignisse in verschiedene Richtungen (Milchstrassezentrum, LMC, M31) gesucht und viele Daten wurden erhoben. Einige Suchen sind noch im Gange. Ein allgemeines Ergebniss ist, unabhängig von der beobachteten Richtung, dass die Zahl der Ereignisse zu gross ist, im Vergleich mit der von der Theorie erwarteten Zahl im Falle von Sternenlinsen. Das ermutigt die Suche nach dunkler Materie, wie MACHOs. Im 2. Kapitel wird die Theorie des gravitational lensing im Detail beschrieben und Kapitel 3 handelt nützliche Hilfsmittel ab, um Informationen über die Linsenpopulation zu gewinnen. Im 4. Kapitel wird eine vorübergehende Analyse von zahlreichen Ereignissen, die in Richtung des Milchstrassezentrums beobachtet wurden, beschrieben. Im 5. Kapitel wird die Möglichkeit des Daseins eines von MACHOs entstehenden Halos in der Milchestrasse und LMC angesprochen. In Kapitel 6 wird ausserdem die Theorie des gravitational lensing für Schwarzlöcherlinsen angesprochen.

Der zweite Teil dieser Dissertation wurde dem Antrag von gravitational lensing als Test für die Allgemeine Relativitätstheorie in dem *strong deflection regime* gewidmet. Dieses Regime wird geschafft, wenn ein Lichtstrahl nahe an einem massiven, kompakten Objekt, wie einem Schwarzen Loch, vorübergeht. Wenn der minimale Abstand zwischen Lichstrahl und Linse vergleichbar mit dem Schwarzschild Radius der Linse ist, dann wird der Strahl maximal von seiner Trajektorie abgelenkt und schlingt mehrmals um die Linse, bevor er endlich wieder auftaucht. Im diesem Fall, einige einleitende Ergebnisse für kugelsymmetrische Schwarze Löcher werden in Abschnitt 2.3 beschrieben und im 7. und 8. Kapitel werden analytische Rechnungen für axialsymmetrische Kerr Schwarze Löcher entwickelt. Diese Ergebnisse können wahrscheinlich ein Hilfsmittel sein, um die Allgemeine Relativitätstheorie zu testen, da bisher keine Tests in diesem Regime durchgeführt wurden.

Introduction

Recent results suggest that we live in a flat, accelerating universe, mostly composed by an energy of unknown origin, the *dark energy*. Neverthless, a non negligible fraction of the universe is made out of matter, in all its forms. To this fraction belongs the familiar matter made out of atoms that contributes to the universe composition by only a few percent and that can be detected only in small amount.

The location of dark matter and its distribution is still a matter of debate and much effort is peformed to address this issue. One of the open questions is if and to which extent galaxies are surrounded by a dark matter halo. As a matter of fact, next to luminous components, galaxies seem to contain some other, invisible matter. Possible candidates making up the baryonic fraction of this undectable matter are the so called MACHOs (MAssive Compact Halo Objects) that could possibly be stellar remnants, brown dwarfs, planets.
In the first part of this thesis, we will focus on the search for MACHOs in the MW and in one of its satellites, the Large Magellanic Cloud (LMC), exploiting gravitational lensing effects. It is well known that when a star is highly aligned with a massive body and an observer, it can be highly magnified (the effect depending strongly on the source extension and on the geometry of the system). This effect is known as *gravitational lensing* and, if the lens is not directly detectable, as in the case of MACHOs, it allows the observer to indirectly detect the deflector, through the effects of its gravitational field. So far, many international collaborations have looked for gravitational lensing events, collecting huge amounts of data, and others are still working on this search. One of the preliminary results is that the observed number of events, no matter the target monitored, is higher than the one expected from known stellar populations and this encourages the search for non luminous matter, such as MACHOs.

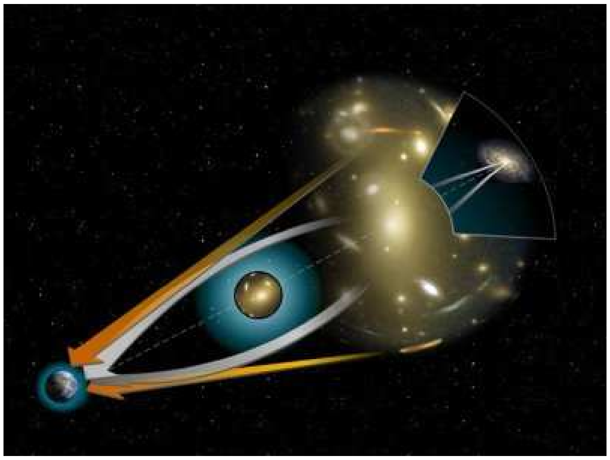

Figure 1: Artistic picture of the effect of gravitational lensing.

In chapter 2 the theory of gravitational lensing in described in some detail, while chapter 3 deals with useful tools to extract information on the lens populations. Then, in chapter 4 a preliminary analysis of microlensing events detected towards the Galactic center is described and in chapter 5 the issue of the existence of a MACHO-composed halo in the MW and in the LMC is addressed.

The second part of this thesis is devoted to the application of gravitational lensing as a test of the General Theory of Relativity (GR) in the so-called *strong deflection regime*. This regime is established when a light ray passes very near to a highly massive, compact object, such as a black hole. If the minimum distance between light ray and deflector is of the order of the lens Schwarzschild radius, then the radiation can be highly deflected from its original, straight trajectory and winds around the lens before eventually reemerging (see fig. 2).

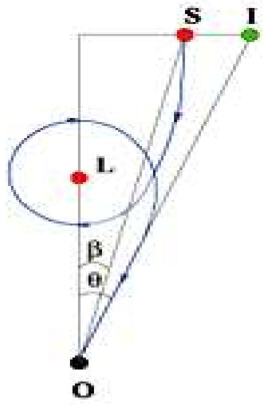

Figure 2: Looping process of a photon around a compact lens. The observer is in O, the lens in L and the source in S. I is the position where the observer detects the source image (see chapter 2 for details).

In this regime, some preliminary results for spherically symmetric black holes are given in section 2.3 while analytical calculations for Kerr black holes are performed in chapters 7-8, the results being a possible tool to test the validity of GR in this regime, since no such tests have been performed yet.

Chapter 1

Dark matter and dark energy

Even though at present we can well reproduce cosmological observations regarding composition and evolution of the Universe by means of the *Standard model*, based on the Big Bang and Inflationary theory, much is yet to be understood. One of the open questions of physical sciences today is the "missing mass problem" arising from the consideration that observed mass, i.e. mass emitting radiation, seems not to be enough to account for all the mass inferred from dynamics of our own and other galaxies, neither does it suffice to provide a unitary cosmological density parameter as inferred from *Cosmic Microwave Background* (CMB) studies [133]. Therefore, it has been established that, beyond luminous matter, some 'dark' matter must exist, too.

1.1 Why dark matter?

An indication for the dark matter existence is the fact that the rotational circular speed, v_c, of the disks of spiral galaxies flattens at large distances from the center (see fig. 1.1 for some examples). If we denote by $M(r)$ the galaxy mass at radius r, then the Newton's law provides the circular speed at distance r,

$$v_c^2 = \frac{GM(r)}{r}. \tag{1.1}$$

A constant velocity implies $M(r) \propto r$, while a constant mass at large radii would give

$$v_c \propto r^{-1/2}, \tag{1.2}$$

as expected by luminous mass estimates. Adding to the model of the galaxy a spherical dark halo component with density mass distribution

$$\rho_h(r) = \rho_0 \frac{a^2 + r_o^2}{a^2 + r^2}, \tag{1.3}$$

where a is a core radius and $\rho_0 = \rho_h(r_o)$, the flatteness of the rotation curve can be explained.
As a matter of fact, as $M(r) = 4\pi \int_0^r \rho_h(r') r'^2 dr'$, for large radii ($r >> a$) one gets $M(r) \propto r$, as $\rho_h(r >> a) \propto r^{-2}$.

The existence of extra matter than observed is suggested by dynamical considerations as well as by studies on the CMB [133]. Best fits of the observed data constrain the average baryonic density, $\rho_b \equiv \rho_c \Omega_b$, in the interval $0.039 < \Omega_b < 0.052$, where $\rho_c = 3H_0^2/(8\pi G) \sim h^2 10^{-29} \frac{g}{cm^3}$ is the critical density of the universe, distinguishing between a closed (positively curved space) and an open (negatively curved space) universe, G is the gravitational constant and $H_0 = h \times 100 Km/Mpc/s$ is the Hubble constant, with the parameter h varying in the range $0.67 < h < 0.77$. Now, luminous

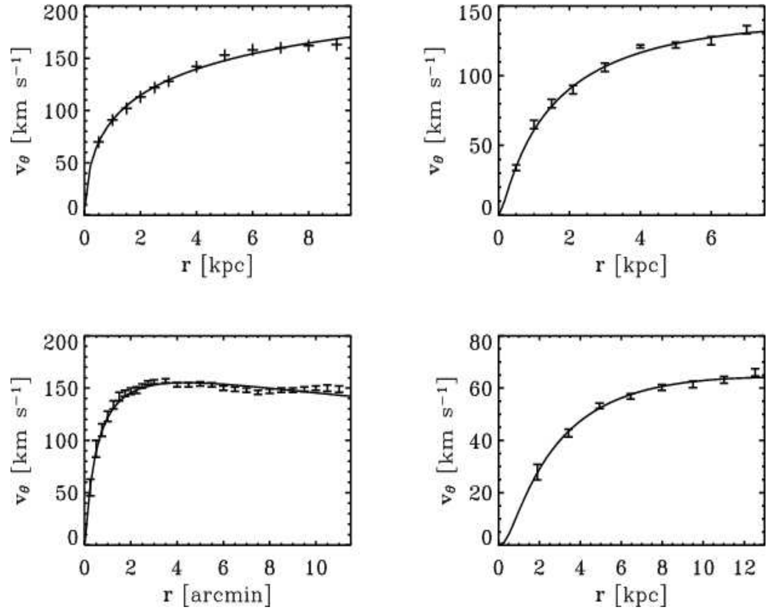

Figure 1.1: Rotation curve fits (from top to bottom, left to right) for NGC 4062, NGC 1035, NGC 3198 (1 arcmin = 2.68 kpc) and DDO 170 ([95] and references therein); The crosses or error bars are the observed data and the solid line is the best fit of the rotation curve.

matter accounts only for $0.007 < \Omega_{lum} < 0.014$ [67] while the average matter density, $\rho_m \equiv \rho_c \Omega_m$, is constrained in the interval $0.20 < \Omega_m < 0.36$. Since $\Omega_{lum} < \Omega_b$ the existence of some non luminous, dark baryonic matter is required. Moreover the discrepancy between Ω_b and Ω_m implies the existence of a dark non baryonic component.

1.1.1 Dark matter components

The open question arising from the conclusion that dark matter exists is: where is it hidden? It seems likely that the distribution of these baryons depends on the scale of the targets that we investigate. In a cosmological context, most of the baryons could be in the form of still collapsing intergalatic medium [145], while it seems likely that in nearby X-ray emitting clusters of galaxies most of the baryonic fraction is in the surrounding hot gas of the intracluster medium [101]. On the scale of individual galaxies a dark matter halo surronding them could explain the flat rotation curves (see section 1.1). Ruling out the possibility that the dark halos are in the form of hot gas (which should produce high amouts of X-rays), the possible candidates for the dark halos baryonic fraction are stellar remnants such as

- massive black holes
- neutron stars
- faint white dwarfs

or

- faint stars
- massive compact dark objects as brown dwarfs or Jupiters, that is, massive objects that are too light ($M < 0.08 M_\odot$) to start efficient nuclear fusion reactions but massive enough ($M > 10^{-7} M_\odot$) not to evaporate within a time comparable to the age of the Galaxy [50].

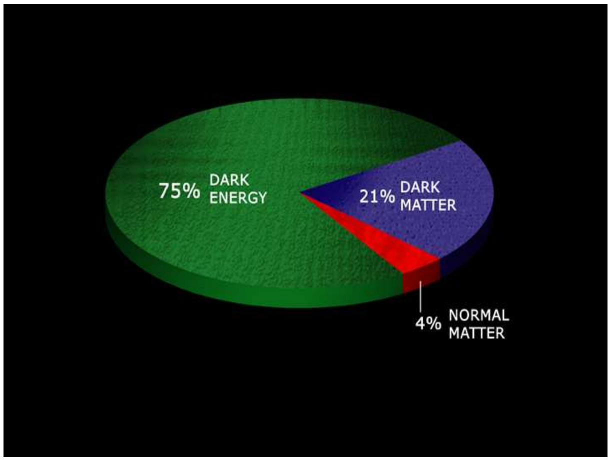

Figure 1.2: Composition of the universe according to most recent results. Taken from the web page http://chandra.harvard.edu/photo/2004/darkenergy/more.html.

As previously stated, a significant fraction of dark matter halos should be non baryonic. The favoured candidates are elementary particles that at the matter-dominated epoch of formation of our universe were non-relativistic and so able to cluster gravitationally. At that epoch, the extension (*Hubble horizon*) of the universe was much smaller than today, but, as the universe expanded, the *primordial*, small clusters could merge to form larger scale structures. This process resulted in a hierarchy of structure, qualitatively in accordance with recent observations. This non-relativistic matter is also known as *cold* dark matter whose most probable candidates are the neutralino and the axion. The former is an example of weakly interacting massive particle ($WIMP$). It is very massive and only interacts through the weak interaction with matter [121]. The latter is a light particle [108] that rarely interacts with photons and that seems to have been produced in great amount in the early universe. To date, none of the performed experiments has had sufficient sensitivity to place strong constraints on the abundances of these particles since the searched interactions are extremely rare and involve very low energies [72].

1.2 Why dark energy?

As already mentioned, the universe seems to be flat with a total energy density equal to the critical value ρ_c [133]. As the estimated Ω_m is much less than unity, this density lack should imply the existence of another component, whose nature is still to be determined and whose existence is also suggested by studies of distant supernovae that reveal an accelerating Universe (see [122] and references therein) as if there were some sort of pressure pushing the expansion faster. To take this fact into account one introduces a new component called *dark energy*, of unknown origin, that makes up almost 2/3 of the universe energy density, does not emit nor does it absorb radiation, is gravitationally self-repulsive and is uniformly spread throughout the universe. From an analytical point of view, *dark energy* translates into the so called *cosmological constant*, λ [87].
For an overview of the universe component fractions see fig. 1.2.

In conclusion, the composition of the Universe is very puzzling and challenging and much is yet to know. In the following we will give our contribution to this challenge and will focus on detection of baryonic dark matter.

1.3 Detection of baryonic dark matter: gravitational lensing

A tool for detecting baryonic dark matter is gravitational lensing, since it produces observable effects due to undetectable sources and/or lenses, whose existence can then be so inferred. Massive objects (lenses) distort space-time. When a light ray passes in the neighborhood of a lens its initial trajectory is deflected. This effect is known as *Gravitational lensing* and has been matter of debate since Newton. At the beginning of the 19^{th} century Soldner [132] computed, by means of the Newtonian gravity, the deflection angle of a light ray suffering gravitational lensing and showed that it depends on how near to the lens the light ray passes. Analogous calculations have been performed, a century later, by Einstein [55] that, using the full equations of General Relativity, found a deflection angle which was twice the Newtonian one. Direct evaluation of this angle through gravitational lensing due to the Sun verified Einstein's prediction within 1% by radio interferometry [60].

Since gravitational lensing has been recognized as an extremely powerful tool for baryonic dark matter detection, several collaborations developped observation projects towards the LMC (MACHO [3, 4, 5, 6], EROS [138]), M31 (AGAPE [38], POINT-AGAPE[40] and references therein) and the Galactic center (MACHO [113, 136], EROS [73], OGLE [135] and references therein), aiming at proving the existence of dark halos and/or of dark components in known populations, such as the Galactic bulge. Many events have been observed since then and crucial insights into the dark matter problem and the non-luminous contribution to the different Galactic components have been provided. In the next chapters we will discuss how observational data can be analysed and the main results arising.

Chapter 2

Gravitational Lensing

According to Einstein's General Theory of Relativity, light rays propagate along null geodesics of space time. The presence of massive objects modifies the structure of space time and, thus, the shape of null geodesics. Therefore, light rays passing near such objects are bent and deviated from their original, straight trajectory. This phenomenon is known as Gravitational Lensing and is nowadays applied to several fields of research, such as cosmological parameters estimates, search of extrasolar planets and baryonic dark matter and probe of theoretical models describing the structure of the Milky Way and other galaxies. In this brief introduction the main properties of gravitational lensing will be introduced (for more details see [83, 105, 106, 107]).

2.1 Simple model: point-like source and lens

2.1.1 Formalism

As a first step, let us consider the system shown in fig. 2.1. A point-like massive object, the lens L, is near the line of sight (l.o.s.) OS of a point-like source, S. Let β be the angle under which the source would be observed in absence of the lens and θ the angle under which the source image, I, is observed in presence of the lens. Due to the deformation of space time, light rays emitted by the source are deflected by a certain angle α. By inspection of fig. 2.1, a relation between the source and image positions and the deflection angle can be derived

$$\tan\beta = \tan\theta - \frac{D_{LS}}{D_{OS}}(\tan\theta + \tan(\alpha - \theta)), \tag{2.1}$$

where D_{LS} and D_{OS} are, respectively, the distance of the lens and of the observer from the source. This is the so called *full lens equation* whose inversion is not an easy task.

Nevertheless, it can be simplied in the *weak field limit* (wfl) which assumes that the light ray passes far enough from the lens to suffer small deviations and is fulfilled when the lens Schwarzschild radius, $R_s \equiv 2\frac{GM}{c^2}$, is much smaller than the impact parameter, r, of the photons on the deflector, defined as the distance between the lens and the final direction of the deflected light ray. In this limit, tangents are expanded to first order in the angles providing $r = \theta D_{OL}$ and the deflection angle, as derived in General Relativity, reduces to

$$\alpha = \frac{2R_s}{r}. \tag{2.2}$$

This relation suggests that in the wfl the deflection angle is $\alpha << 1$.

Notice that the impact parameter does not coincide with the minimum distance between lens and light ray but for vanishing deflection angles. In conclusion, the relation among β, θ and α in

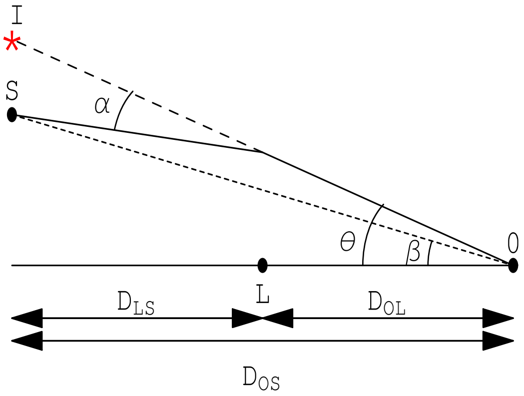

Figure 2.1: Geometry of gravitational lensing

the wfl is

$$\theta = \beta + \alpha \frac{D_{LS}}{D_{OS}}, \tag{2.3}$$

which can be solved exactly. Introducing (2.2) in (2.3), one gets

$$\theta^2 - \beta\theta - \Theta_E^2 = 0, \tag{2.4}$$

with

$$\Theta_E = \sqrt{\frac{4GM}{c^2} \frac{D_{LS}}{D_{OL} D_{OS}}}. \tag{2.5}$$

The two physical solutions of eq. (2.4) are

$$\theta_{\pm} = \frac{\beta}{2} \left(1 \pm \sqrt{1 + \frac{4\Theta_E^2}{\beta^2}} \right), \tag{2.6}$$

thus suggesting that the observer can detect two images of the same source. As shown in fig. 2.2, the two images, I_+ and I_-, are generated on opposite sides with respect to the axis connecting the observer to the lens, no matter the position of the source with respect to the deflector.

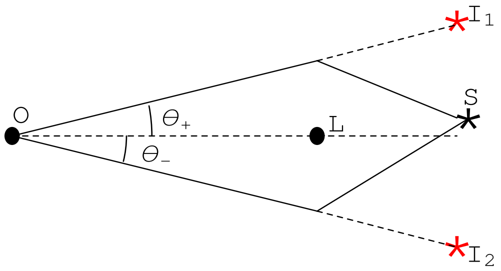

Figure 2.2: Generation of the images in the wfl.

In the special case of vanishing β (i.e. vanishing impact parameter and perfect alignment of observer, lens and source), the solution of eq. (2.4) is $\theta = \pm\Theta_E$. This suggests that an image

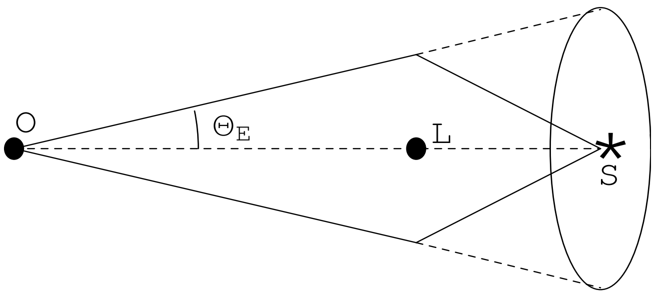

Figure 2.3: Formation of an Einstein ring: source, lens and observer are perfectly aligned.

appears in all the points on a circle of radius $R_E = D_{OL}\Theta_E$ (*Einstein radius*) which is thus the image of the given source and is known as *Einstein ring* (see fig. 2.3). On the deflector plane, R_E and Θ_E are the usual length and angle units.
Coming back to the case of non vanishing β, the angular separation between the two images is

$$\Delta\theta = \theta_+ - \theta_- = 2\Theta_E\sqrt{1 + \frac{\beta^2}{4\Theta_E^2}}. \tag{2.7}$$

Whenever this separation is of the order of the milliarcseconds the two images cannot be distinguished and only their superposition is observed. This is known as *microlensing regime*.

2.1.2 Magnification

When a source is lensed, its luminous flux is split and reaches the observer as if it were emitted by the images I_+ and I_-. The magnification of an image, μ, is defined as the ratio between its flux and the one of the unlensed source. As the emitted flux is the product of the surface brightness and the solid angle under which the source is observed and as gravitational lensing conserves surface brightness, it follows that

$$\mu = \frac{d\Omega}{d\Omega_0}, \tag{2.8}$$

where $d\Omega_0$ and $d\Omega$ are the observed solid angle of the image and the one that would be observed in absence of the deflector, respectively.

As shown in fig. 2.4, the surface element dS of angular position β is seen under the solid angle $d\Omega_0 = \beta d\phi d\beta$, while in presence of the deflector, the surface elements of the images, $dS_\pm$ correspond to $d\Omega_\pm = \theta_\pm d\phi d\theta_\pm$. Thus, from eq. (2.6), one gets

$$\mu_\pm = \frac{1}{2} \pm \frac{\beta^2 + 2\Theta_E^2}{2\beta\sqrt{\beta^2 + 4\Theta_E^2}}, \tag{2.9}$$

suggesting that the image I_+ is magnified ($\mu > 0$) and the other one is demagnified.

In the microlensing regime what can be detected is the total magnification, as images are superimposed and cannot be distinguished. In this case, introducing the reduced impact parameter $u = \frac{\beta}{\Theta_E} \equiv \frac{b}{R_E}$ (here b is the distance between the deflector and the l.o.s. OS),

$$\mu = |\mu_+| + |\mu_-| = \frac{u^2 + 2}{u\sqrt{u^2 + 4}}. \tag{2.10}$$

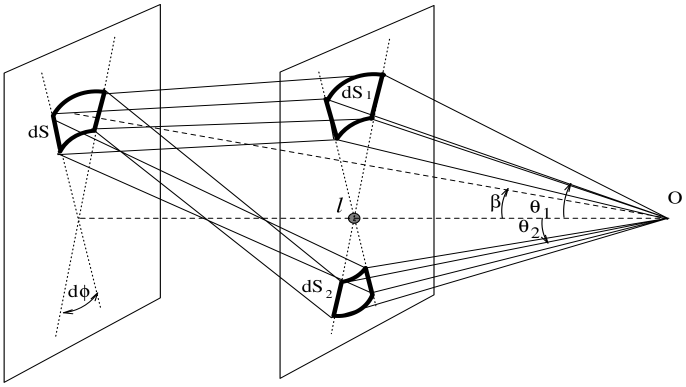

Figure 2.4: Trajectories of light rays emitted by a source dS in presence of a point-like lens, l. $S_{1,2}$ are the image surface elements on the lens plane [120]. In the text $S_{1,2}$ are denoted as $S_{\pm}$.

Note that, for vanishing β, the approximation of point-like source fails since the predicted magnification, as given in the previous equation, diverges. However, at least formally, one can define a locus of points on the source plane, known as *caustics*, such that images of sources lying on a caustic have infinite magnification. The locus of points on the lens plane, in which castics are mapped, is known *critical curve*.

2.1.3 Dynamics

The relative position of source, lens and observer varies in time. The amplification increases as the source gets nearer to the lens and decreases when it moves away. Assuming, as a first approximation, that the lens moves with constant velocity with respect to the l.o.s., the reduced impact parameter, $u(t)$, can be written as

$$u^2(t) = \frac{b_m^2 + [v_t(t-t_0)]^2}{R_E^2} = u_0^2 + \frac{[(t-t_0)]^2}{t_E^2}, \tag{2.11}$$

where b_m is the minimum distance between lens and l.o.s., $u_0 = b_m/R_E$, v_t is the relative transverse velocity of lens and source projected on the lens plane and t_0 is the instant of maximum amplification, i.e. of mimimum impact parameter.

Here $t_E \equiv R_E/v_t$, the Einstein time, is the time the lens needs to cover a distance R_E and is a natural time scale for the microlensing event duration. Thus, from eq. (2.10), the amplification factor of the light curve of a star undergoing gravitational microlensing varies in time as

$$A(t) = \frac{u^2(t) + 2}{u(t)\sqrt{u^2(t) + 4}}. \tag{2.12}$$

As shown in fig. 2.5, the amplification curve (also known as *Paczyński curve* or *light curve*) is symmetric around t_0 and its maximum value depends on the minimum impact parameter, u_0. In particular, when $u_0 = 1$ (the minimum distance between lens and l.o.s. is an Einstein radius), $A_{max} = 1.34$. It is worth highlighting the fact that, as gravitational lensing is a geometric effect, the amplification of the light curve is independent of the wave length.

2.2 Extensions of the model

The gravitational field of a lens is distorted even if the lens is a star, either because of tidal effects due to the galaxy hosting the lens or because of distortion due to galaxies lying near to the l.o.s.

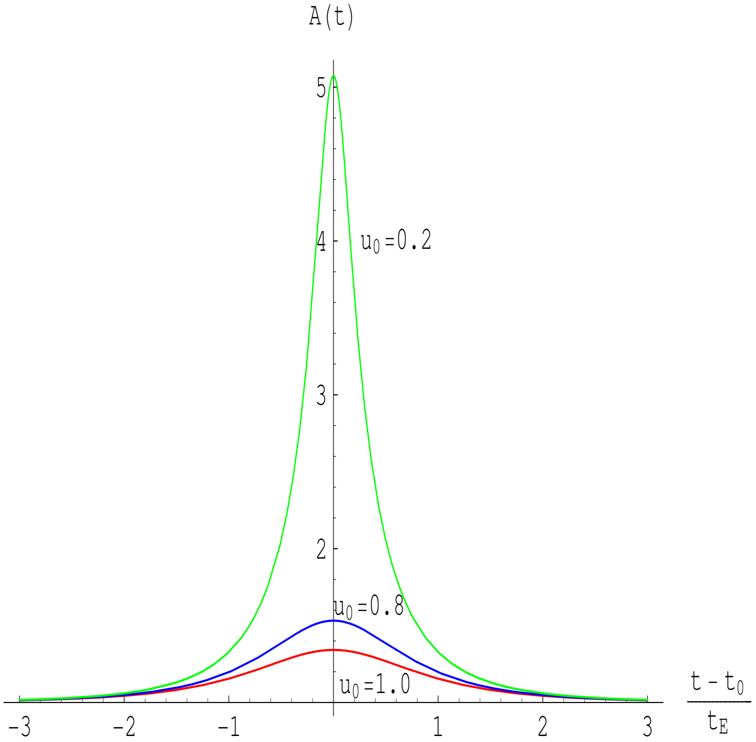

Figure 2.5: Paczyński curves: amplification factor as a function of the distance of the source from the lens, for different values of the minimum impact parameter u_0.

These are the reasons why the point-like lens approximation is an idealization, even though it works whenever a light ray is deflected by a spherical object with an impact parameter much greater than the Schwarzschild radius of the lens. More realistic lensing effects can be studied removing the hypothesis of point-like lens [123] and/or source; the latter is described briefly below.

2.2.1 Extended source

The effect of extended source, i.e. of a source that cannot be considered as point-like, has to be taken into account when the minimum reduced impact parameter, u_0, is of the order of the reduced source radius projected on the lens plane, R (see fig. 2.6). The latter can be written as

$$R \equiv \frac{R_{proj}}{R_E} = \frac{R_\star}{R_E}\frac{D_L}{D_S}, \tag{2.13}$$

where $R_\star$ is the source radius, or, from eq. (2.5),

$$R = 5 \times 10^{-4} \frac{R\star}{R\odot}\sqrt{\frac{D_{OL} \times 10kpc}{D_{OS}(D_{OS} - D_{OL})}} \left(\frac{M}{M\odot}\right)^{-\frac{1}{2}}. \tag{2.14}$$

The higher is the value of R and the easier it is to detect an effect of extended source.
As an example, for a spherical source of uniform surface luminosity [118] one finds

$$A(u_0, R) = \frac{2}{\pi R^2}\int_{|R-u_0|}^{R+u_0} \frac{u^2+2}{\sqrt{u^2+4}} \arccos(\frac{u^2+u_0^2-R^2}{2uu_0})du$$
$$+H(R-u_0)(1-\frac{u_0}{R})^2\sqrt{1+\frac{4}{(R-u_0)^2}}, \tag{2.15}$$

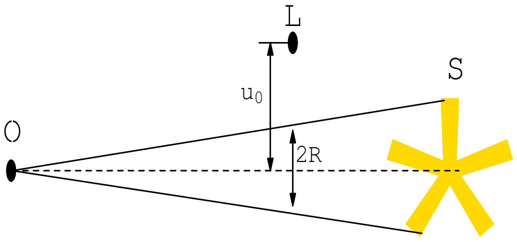

Figure 2.6: Geometry of extended source.

where H is the Heaviside function ($H(x<0)$=0 and $H(x>0)$=1).
The effect of this amplification factor on light curves is shown in fig. 2.7: the higher R is with respect to u_0 and the more the light curves are flattened and widened. Notice that the amplification factor does not diverge any longer for vanishing impact parameter

$$A_{max}(u_0=0)=\sqrt{1+\frac{4}{R}}. \tag{2.16}$$

If one could recognize an extended source effect on a light curve, it could be exploited to measure some parameters that would be otherwise inaccessible. For example, if it were possible to localise the source and, thus, to know D_{OS} and $R\star$, the projected source radius, R, would provide the angular Einstein radius

$$\theta_E=\frac{R_E}{D_{OL}}=R\frac{R\star}{D_{OS}}. \tag{2.17}$$

Moreover, as the Einstein time t_E can be derived from the light curve, then it would be possible to constrain the relative velocity of lens and source and the distance D_L through

$$\eta\equiv\frac{v_t}{D_{OL}}=\frac{\Theta_E}{t_E}. \tag{2.18}$$

So, if the properties of the different populations to which the lens could belong are known, the constraints on v_t and D_{OL} could help localising the deflector.

2.2.2 Multiple lenses

Binary systems in our Galaxy are very common and predictions state that a non negligible fraction of microlensing events observed in the direction of the Galactic center could be due to such systems [94].
In case of multiple lenses the deflection angle of a light ray is the vector sum of the deflections due to each lens.
In the simple case of N point-like multiple deflectors, each with mass M_i ($i=1,..,N$), the lens equation in the weak deflection limit is

$$\vec{\theta}-\vec{\beta}=\sum_{i=1}^{N}\frac{\mu_i}{|\vec{\theta}-\vec{\theta}_i|^2}(\vec{\theta}-\vec{\theta}_i), \tag{2.19}$$

where $\mu_i=\frac{M_i}{M}$, with $M=\sum_{i=1}^{N}M_i$ and $\vec{\theta}_i$ are the angular positions of the deflectors on a reference lens plane.
In the general case, even for binary systems, solutions to equation (2.19) can only be found numerically (for a detailed description see [123] and [124]). A typical light curve generated by binary

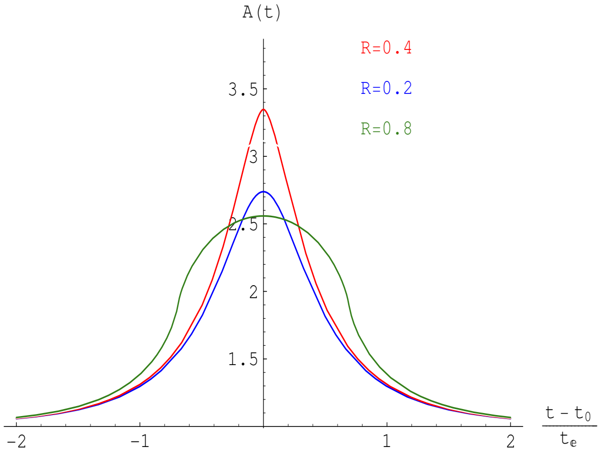

Figure 2.7: Deformation of light curves for extended sources. The minimum reduced impact parameter is $u_o = 0.4$. The values of the source radius projection are shown nearby.

lensing in the Small Magellanic Cloud (SMC) is shown in fig. 2.8: it is a composition of the light curves due to each lens.

Eq. 2.19 can also be applied to extended lenses. Defining the mass element of the lens as $dm = \Sigma(\vec{\theta})d^2\theta$, where $d^2\theta$ is the surface element on the deflector plane and $\Sigma(\vec{\theta})$ is the lens surface mass density at position $\vec{\theta}$, that is the volume mass distribution projected on the lens plane, one gets, in the weak deflection limit,

$$\alpha(\vec{\theta}) = \frac{4G}{c^2}\int_{R^2} d^2\theta' \Sigma(\vec{\theta}') \frac{\vec{\theta} - \vec{\theta}'}{|\vec{\theta} - \vec{\theta}'|^2}. \tag{2.20}$$

This relation is usually applied to face one of the usual problems of GL theory: to find a suitable deflector mass distribution, given the image positions of a resolved source.

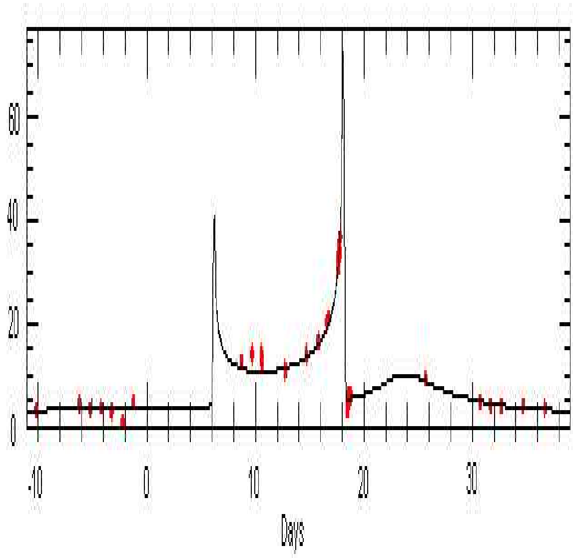

Figure 2.8: Gravitational lensing of a star in the SMC: observed image brightness (red) points are superimposed to the predicted curve. The sharp peaks are due to the caustic crossing. Taken from the web page http://www.astro.ucla.edu/ wright/microlensing.html.

2.3 Gravitational lensing as a tool to test gravity theories

General Relativity predicts that light rays passing sufficiently near to a massive, compact object can be bent so much that their trajectory winds around the lens a given number of times before eventually reemerging and reaching an observer. This effect, known as *gravitational lensing in the strong deflection limit* (SDL), is due to high space curvature that only very massive and compact lenses, such as black holes, can induce. In principle, a photon passing near a black hole can suffer either a weak deflection, if the minimum reached distance from the lens is much higher than the lens Schwarzschild radius, R_s, or a strong deflection in the other case. One can show that in the SDL an infinite set of so called *relativistic images* is produced on both sides of the lens and that each of these images is due to photons looping a given number of times around the deflector. Of course, for main sequence stellar lenses the SDL cannot be established since their R_S is very small and they are more extended than it.

In the SDL regime GR has not been tested yet and much work has been done to investigate this issue.

In particular, for a given geometry, one can deduce position and magnification of the relativistic images and their direct observation could allow us to verify the GR predictions. Lensing by spherically symmetric spacetimes has been widely investigated by means of both numerical and analytical treatments and in the following sections its main properties in the SDL will be described. For a treatment of rotating black holes see chapters 7-8.

2.3.1 Lens equation and deflection angle

The usual, full lens equation,

$$\tan\beta = \tan\theta - \frac{D_{LS}}{D_{OS}}\left[\tan\theta + \tan(\alpha - \theta)\right], \tag{2.21}$$

can be solved in the weak deflection limit that allows series expansions to first order of the tangents, providing two images on both sides of the source (see section 2.1). In the SDL such expansions can be still performed, but with grain of salt. Nevertheless, for Schwarzschild black hole lenses, the deflection angle, evaluated along the geodesic of the light ray, has a well determined, analytical expression as a function of the maximum approach x_0 [26],

$$\alpha(x_0) = \int_{x_0}^{\infty} \frac{2dx}{x\sqrt{\left(\frac{x}{x_0}\right)^2 (1 - 1/x_0) - (1 - 1/x)}}. \tag{2.22}$$

As one can show, the above-defined deflection angle diverges when $x_0 \to \frac{3}{2}$, that is, when light rays pass very near to the so called *lens photon sphere*, which is the locus of points where light rays trajectories are unstable. As we are considering the SDL, one can reasonably assume that α is close to a multiple of 2π, $\alpha = 2n\pi + \Delta\alpha_n$, with n integer, given by the number of loops performed by the light ray around the lens, and $\Delta\alpha_n << 1$. With this assumption, in the limit of small angles, the lens equation turns out to be

$$\beta = \theta - \frac{D_{LS}}{D_{OS}}\Delta\alpha_n. \tag{2.23}$$

Since one is interested in large deflections, one can assume $x_0 = 3/2 + \epsilon$ [26], perform a series expansion in ϵ in eq. (2.22) and substitute $\epsilon = \epsilon(b)$ since [146]

$$x_0^2 = (1 - 1/x_0)\, b^2, \tag{2.24}$$

where b is the impact parameter.

The final expression for α is

$$\alpha \sim -\log\left(b - \frac{3\sqrt{3}}{2}\right) + A, \tag{2.25}$$

with $A = -\log\left(\frac{5+3\sqrt{3}}{1944}\right) - \pi$. suggesting that the deflection angle is a logarithmically diverging function of the "shifted" impact parameter. As shown in [27], the general expression

$$\alpha = -a_1 \log(b - b_m) + a_2 + o(b - b_m), \tag{2.26}$$

with $b_m = 3\sqrt{3}/2$, is preserved for all kinds of spherically symmetric black holes and, since the coeffiecients a_1 and a_2 are functions of the given metric, it is a useful tool either to identify the nature of the lens or to investigate the general theory of relativity in the considered regime. The positions of the relativistic images can doubtlessly help further investigation of these issues and the next section is devoted to their derivation.

2.3.2 Image positions and magnification

If one defines [26] θ_n^0 as the position where an image appears if $\alpha = 2n\pi$ and $\Delta\theta_n$ as the correction to θ_n^0 for deflections $\alpha = 2n\pi + \Delta\alpha_n$, one can show that the image position $\theta_n \equiv \theta_n^0 + \Delta\theta_n$ is

$$\theta_n \sim \theta_n^0 + \frac{e^{A-2n\pi}(\beta - \theta_n^0) D_{OS}}{D_{LS} D_{OL}} \tag{2.27}$$

with

$$\theta_n^0 = \frac{3\sqrt{3} + 2e^{A-2n\pi}}{2D_{OL}}, \tag{2.28}$$

while the magnification of the n_{th} image, that is the image produced by photons looping n times around the lens, is

$$\mu_n \equiv \frac{1}{\frac{\beta}{\theta}\frac{\partial\beta}{\partial\theta}|_{\theta_n^0}} = e^{A-2n\pi}\frac{(3\sqrt{3} + 2e^{A-2n\pi})D_{OS}}{2\beta D_{OL}^2 D_{LS}}, \tag{2.29}$$

where the labels have the usual meaning (see section 2.1). This suggests that the more the photon winds around the lens and the more the corresponding image is demagnified, so putting strong constraints on the possibility of directly detecting relativistic images. At least formally, anyway, the magnification diverges when source, lens and observer are highly aligned ($\beta \to 0$). Moreover, since the relative corrections to the position of the n_{th} image is of the order of 10^{-5} or less (for increasing values of the image order, n), it is likely that the relativistic images cannot be detected individually and that a single image, superposition of the two infinite sets of images, would be revealed with a magnification of

$$\mu_{tot} = 2\sum_{n=1}^{\infty} \mu_n \equiv \frac{e^A(3\sqrt{3}(1 + e^{2\pi}) + 2e^A)}{(e^{4\pi} - 1)\beta D_{OL}^2 D_{LS}}. \tag{2.30}$$

Individual detection of relativistic images would be of course possible for lenses of high mass, since the separation of the two sets of images is of the order of the lens Einstein diameter. Their detection would be nevertheless challenging since the magnification is an exponentially decreasing function of the image order. It seems likely, anyway, that in the near future required sensitivity could be reached (see section 7.6 for some more details).

In the following chapters the issue of SDL in absence of spherical symmetry will be addressed. This analysis is still more relevant since the black hole hosted at the center of our Galaxy seems to be endowed with a non vanishing spin. For this reason we will focus in particular on spinning black holes. We will investigate in detail the structure of critical curves and caustics and will show that, at the least at low orders, some possibility of detecting relativistic images is provided.

Chapter 3

Statistics of microlensing

Direct observations of microlensing events allow the measurement of the magnitude of the star unaffected by the gravitational lens, the Einstein time, t_E, the time of maximum amplification, t_0, and the minimum impact parameter, u_0, the latter following directly from the measurement of the maximum amplification, A_{max}. This information is provided by the approximation of the observed light curve with a theoretical Paczyński curve.

As the number and the duration of microlensing events are affected by the lens mass distribution between a population of sources and the observer, then, in a given direction, long time observations of a relatively big region (so to detect a non negligible number of events and to improve the statistics) can constrain the number and the mass of the deflectors. In the following, two relevant statistical tools are discussed.

3.1 Optical depth

Given a distribution of lenses and sources, one defines the *optical depth*, τ, as the probability that, at a certain time, a source undergoes gravitational microlensing inducing an increase of more than 34% of its original flux, i.e. the minimum impact parameter of the light coming from the source is smaller than an Einstein radius of a given lens ($u_0 < 1$, see eq. 2.12).

In a first approximation τ can be calculated assuming that all the lenses have the same mass M and that their Einstein disk covers the area πR_E^2. Given that the number density of lenses at distance D_{OL} is $n_l = \rho_l / M$, where ρ_l is the lens density in the considered region, then the differential optical depth, $d\tau$, is

$$d\tau = dD_{OL} n_l \pi R_E^2. \tag{3.1}$$

The total contribution to the optical depth must take into account all the lenses between source and observer

$$\tau(D_{OS}) = \int_0^{D_{OS}} dD_{OL} \rho_l / M \pi R_E^2 = \frac{4\pi G D_{OS}^2}{c^2} \int_0^1 \rho_l x(1-x) dx, \tag{3.2}$$

where we have introduced the expression for the Einstein radius (cfr. eq. 2.5) and $x = \frac{D_{OL}}{D_{OS}}$. Notice that in eq. 3.2 the dependence on the lens mass disappeared. It is worth to notice that the aforementioned τ depends only on the density of the deflectors and on the geometry, assuming both populations to be static and not taking into account possible variations of the density of the sources. In realistic observation projects, one monitors large regions where the sources are far from being uniformly distributed. For a given l.o.s. the number of detectable sources at distance D_{OS} is dn_s / dD_{OS}, where n_s is the source number density. Even though it is not always the case that one knows this number, at least formally one can take it into account and give a more general definition of the optical depth as

$$\tau = \frac{1}{N_S} \int dD_{OS} \frac{dn_s}{dD_{OS}} \tau(D_{OS}), \tag{3.3}$$

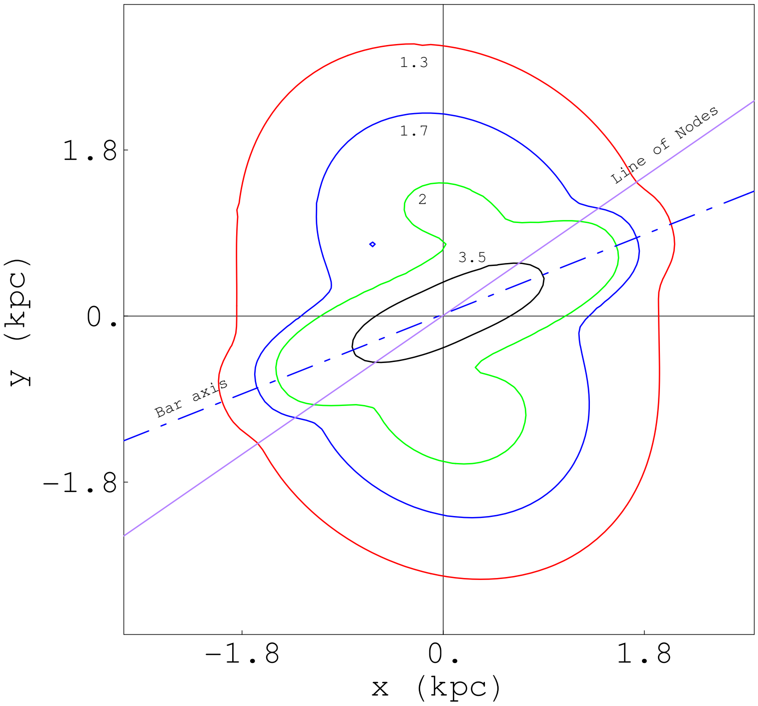

Figure 3.1: Contour lines of the optical depth for self lensing in the direction of the LMC. The values of τ are in units of 10^{-8}. The center of the LMC is in the origin of the reference system. (x, y) are cartesian coordinates on the sky plane, in particular the $y-axis$ is parallel to the declination axis and the $x-axis$ is antiparallel to the right ascension axis.

where $\tau(D_{OS})$ is as given in eq. 3.2 and $N_s = \int dD_{OS} dn_s/dD_{OS}$ is the total number of sources along the l.o.s. and is a normalisation factor.
In any case, eq. 3.2 can be a good estimate for the optical depth if one assumes that all the sources are at the same distance from the observer; this is the case for targets that are much farther from the Earth than a few kpc, which is the usual range of variation of D_{OS} for a population of sources.

As an example, figure 3.1 shows a map of optical depth for Self Lensing (SL), that is sources and lenses both belonging to the disk and bar populations, of the Large Magellanic Cloud (LMC) and fig. 3.2 shows an analogous plot but now considering lenses in the LMC *dark halo*, whose existence is still a matter of debate. Even though in chapter 5 more details are given on this topic, for seek of clarity and completeness, we introduce now the assumed density profiles for the different populations. The mass density of the dark halo is assumed to be that of an isothermal sphere

$$\rho_h = \frac{\rho_{0,h}}{1 + \frac{R^2}{a^2}}, \tag{3.4}$$

where R is the distance from the center of the LMC and a is a core radius (fixed at 2 kpc in the shown figure), while the mass densities for the LMC disk and bar are, respectively,

$$\rho_d = \rho_{0,d} \frac{1}{\cosh(\zeta/\zeta_d)^2} exp \left(-\frac{\sqrt{(\frac{\xi}{q})^2 + \eta^2}}{R_d} \right) \tag{3.5}$$

and

$$\rho_b = \rho_{0,b} exp \left(-\frac{\Xi^2}{\Xi_b^2} \right) exp \left(-\frac{(\gamma^2 + \zeta^2)^2}{R_b^4} \right), \tag{3.6}$$

where the coordinates (ξ, η) and (Ξ, γ) are on the disk plane, coinciding with that of the bar, η being along the disk major axis and Ξ, the bar major axis, being along the disk minor axis ξ (for

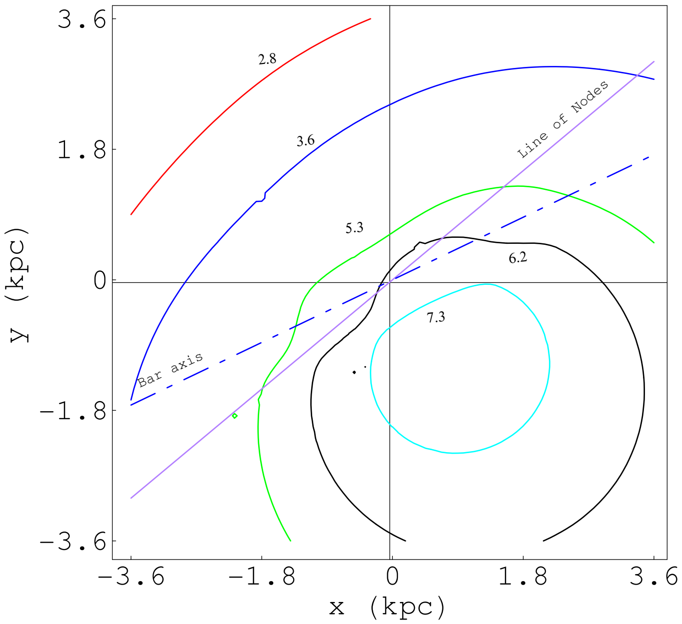

Figure 3.2: As fig. 3.1 but for lenses in the LMC dark halo. The values of τ are in units of 10^{-8}. The shape of the contour lines follow the mass density distributions of sources and lenses. The south-west side of the LMC is farther from the Galaxy: this explains the higher values of τ in that region ([140, 93], see also chapter 5).

more details see [93]). As the plots show, the value of τ in a given direction can be very small (of the order of 10^{-8} or less) and the probability of an event happening and being detected is even smaller, due to observational limits [8]. Let us now briefly discuss the asymmetry shown in fig. 3.2. The optical depth contour lines are very much affected by the mass distribution of the lens and source population. As discussed in [140], the LMC disk and bar are distributed so that the south-west side is farther from us than the north-east side. This means that along a l.o.s. pointing towards the LMC south-west side a higher number of potential lenses is provided due to the higher mean distance between us (observer) and a given source, so increasing the optical depth. Now, since statistical methods are applied to observed microlensing events in order to constrain mass and velocity distributions, a non negligible number of events must be available to make results reliable. Whatever the target, in order to accomplish this task either a large period of observation is needed or a large field must be monitored. The estimation of the number of expected events and their time distribution is the subject of the next section.

3.2 Microlensing event rate

To estimate the number of microlensing events one introduces the differential number of expected events

$$dN_{ev} = N_{obs}T_{obs}d\Gamma \tag{3.7}$$

where $d\Gamma$ is the *differential rate* at which a single star is microlensed by a compact object, N_{obs} is the number of monitored sources and T_{obs} is the whole time of observation. We will refer to the product $N_{obs}T_{obs}$ as to the *total exposition*.

For a single source at position $\vec{x}$, the differential rate is

$$d\Gamma = \frac{n_l(\vec{x}) d^3x f(\vec{v_l}) d^3v_l}{dt}, \tag{3.8}$$

that is, the number of lenses located in a volume element d^3x with velocity d^3v_l per unit time. $n_l(\vec{x})$ and $f(\vec{v_l})$ are, respectively, the number density and velocity distribution of the lenses.
Research of microlensing events is pursued observing a huge number of potential sources. So, one should remove the hypothesis of single monitored star and take into account the density (ρ_s) and velocity ($f(\vec{v_s})$) distributions of the source population. Since the volume element varies with distance as $D_{OS}^2 dD_{OS}$ and since the fraction of monitored stars having a luminosity higher than a minimum detectable luminosity, L_*, scales as $L_*^{-\beta} \sim D_{OS}^{-2\ \beta}$ [83], the previous definition of differential rate can be generalized as follows

$$d\Gamma = \frac{1}{\int \rho_s\ D_{OS}^{2(1-\beta)}\ dD_{OS}} \frac{n_l(\vec{x}) d^3x f(\vec{v_l}) d^3v_l f(\vec{v_s}) d^3v_s \rho_s D_{OS}^{2(1-\beta)}\ dD_{OS}}{dt}, \tag{3.9}$$

where $\int \rho_s D_{OS}^{2(1-\beta)}\ dD_{OS}$ is the total number of detectable stars in a given direction. Main sequence stars have $\beta = 1$ while for bright stars, such as *Red Clump Giants* that can be identified independent of their distance, $\beta = 0$ [75]. The same reasoning can be applied to eq. 3.3 providing

$$\tau = \frac{1}{\int \rho_s D_{OS}^{2(1-\beta)}\ dD_{OS}} \int dD_{OS} \rho_s D_{OS}^{2(1-\beta)} \tau(D_{OS}). \tag{3.10}$$

Let us now find a more detailed expression for $d\Gamma$.
Assuming a source at position $\vec{x}$, the microlensing tube is defined as the region where a deflector must be in order to lens the given source. The microlensing tube volume, d^3x, is as follows (see figs. 3.3, 3.4)

$$d^3x = (\vec{v}_{r,\perp} \cdot \hat{n}) dt dS, \tag{3.11}$$

where $dS = dl dD_{OL}$ is a portion of the tube external surface with $dl = uR_E d\alpha$ and, as usual, u is the reduced impact parameter, $\vec{v}_{r,\perp}$ is the orthogonal-to-the-line-of-sight component of the lens velocity with respect to the tube ($\vec{v}_r$) and $\hat{n}$ is the unit vector normal to the tube inner surface at the point where the microlensing tube is crossed by the lens. In the following $\theta \in (-\frac{\pi}{2}, \frac{\pi}{2})$ will be the angle between $\vec{v}_r$ and $\hat{n}$. Coming back to eq. 3.11, it gives the number of lenses that enter the volume included in the cylindrical surfaces of radius uR_E and $uR_E + (\vec{v}_{r,\perp} \cdot \hat{n})dt$, respectively, angular amplitude $d\alpha$ and length dD_{OL}.
As one requires at least an amplification factor of 1.34 (corresponding to $u = 1$, see section (2.1.3)), then we assume $u = 1$ in our calculations and get

$$d^3x = v_{r,\perp} \cos\theta R_E dt d\alpha dD_{OL}, \tag{3.12}$$

where $v_{r,\perp} =\mid \vec{v}_{r,\perp} \mid$. Due to the introduction of this velocity component, a relation between $\vec{v}_l$ and $\vec{v}_{r,\perp}$ must be searched for.
Given a reference frame, elementary physics states that the lens relative velocity with respect to the microlensing tube is

$$\vec{v}_r = \vec{v}_l - \vec{v}_t, \tag{3.13}$$

where the subscript t refers to tube velocities. Accordingly $\vec{v}_l$ and $\vec{v}_t$ are, respectively, the lens and tube velocity, with $\vec{v}_l = \vec{v}_{ran,l} + \vec{v}_{drift,l}$, having assumed a random ($\vec{v}_{ran,l}$) and a bulk ($\vec{v}_{drift,l}$) motion for the lens population. Moreover, for a tube at distance D_{OL} from the observer, $\vec{v}_t = (1-x)\vec{v}_{obs} + x\vec{v}_s$ where x is defined as in section (3.1) and $\vec{v}_s$ is the source velocity which is the sum of a random ($\vec{v}_{ran,s}$) and a bulk component ($\vec{v}_{drift,s}$). For seek of compacteness, since there is no more possibility of confusion, from now on $\vec{v}_{ran,l} \equiv \vec{v}_l$ and $\vec{v}_{ran,s} \equiv \vec{v}_s$.

In conclusion

$$\vec{v}_r = \vec{v}_l + \vec{v}_{drift,l} - x(\vec{v}_s + \vec{v}_{drift,s}) - (1-x)\vec{v}_{obs}, \tag{3.14}$$

or

$$\vec{v}_l = \vec{v}_r + x\vec{v}_s + \vec{V}, \tag{3.15}$$

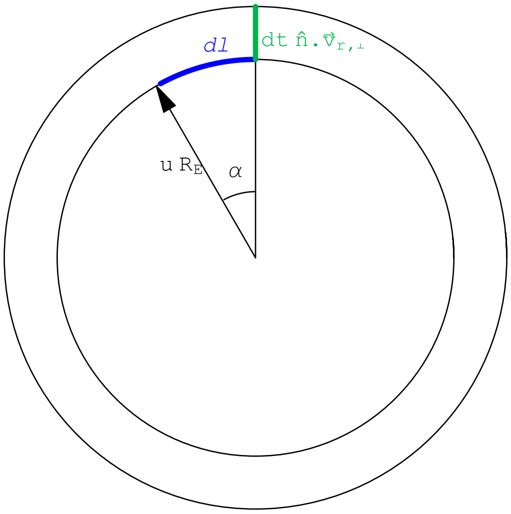

Figure 3.3: Microlensing tube on the lens plane.

where $\vec{V}$ includes all the "ordered" motions:

$$\vec{V} = (\vec{v}_{obs} - \vec{v}_{drift,l}) + x(\vec{v}_{drift,s} - \vec{v}_{obs}). \tag{3.16}$$

As regards the lens (source) random velocity distributions, we assume that both are gaussian in the lens (source) proper reference frame. If $(\sigma_x, \sigma_y, \sigma_z)$ are the velocity dispersions, then the gaussian velocity distribution reads

$$f(\vec{v})d^3v \propto e^{-\frac{v_x^2}{2\sigma_x^2}} e^{-\frac{v_y^2}{2\sigma_y^2}} e^{-\frac{v_z^2}{2\sigma_z^2}} dv_x dv_y dv_z. \tag{3.17}$$

A gaussian distribution remains such if projected on any other reference frame, provided that the corresponding dispersions are properly redefined. Since the lensing time scales are determined by the relative source-lens velocity projected onto the lens plane, one should project the distribution 3.17 on the orthogonal reference frame at the lens position, OL, whose general orientation with respect to the galactic cartesian reference frame is shown in fig. 3.5, and then integrate over the source (and lens) velocity parallel to the l.o.s.

A brief discussion regarding how this projection can be performed follows. Let OS be the orthogonal reference frame at the source position. The intersection of the source (lens) velocity ellipsoid with the lens plane is an ellipse; we call $\{x_{s,1}, x_{s,2}\}$ ($\{x_{l,1}, x_{l,2}\}$) its principal axes and $\{v_{sp,1}, v_{sp,2}\}$ ($\{v_{lp,1}, v_{lp,2}\}$) the source (lens) projected velocities along them. Let then $v_{sp,3}$ ($v_{lp,3}$) be the source (lens) projected velocity component parallel to the l.o.s. If $\vec{v}_s = \{v_{s,1}, v_{s,2}, v_{s,3}\}$ is the source velocity in OS and if the matrix that allows to move from OS to the source proper frame is

$$MAT = \begin{bmatrix} m_0 & m_1 & m_2 \\ m_3 & m_4 & m_5 \\ m_6 & m_7 & m_8 \end{bmatrix} \tag{3.18}$$

then, written in terms of $\vec{v}_s$, expression 3.17 turns into

$$f(\vec{v}_s)d^3v_s \propto e^{-\frac{(m_0\ v_{s,1}+m_1\ v_{s,2}+m_3\ v_{s,3})^2}{2\sigma_x^2}} e^{-\frac{(m_3\ v_{s,1}+m_4\ v_{s,2}+m_5\ v_{s,3})^2}{2\sigma_y^2}} e^{-\frac{(m_6\ v_{s,1}+m_7\ v_{s,2}+m_8\ v_{s,3})^2}{2\sigma_z^2}} dv_{s,1}dv_{s,2}dv_{s,3} \tag{3.19}$$

and integrating over $v_{s,3}$, which is the velocity component parallel to the l.o.s.:

$$f(v_{s,1}, v_{s,2})d^2v_s \propto e^{-c_1\ v_{s,1}^2} e^{-c_2\ v_{s,2}^2} e^{-c_{1,2}\ v_{s,1}v_{s,2}} dv_{s,1}dv_{s,2}, \tag{3.20}$$

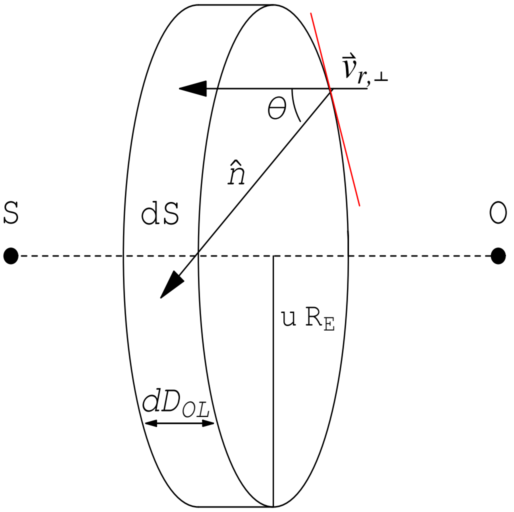

Figure 3.4: Microlensing tube. The vectors $\vec{v}_{r,\perp}$ and $\hat{n}$ as well as θ are on the lens plane. The observer and the source are in O and S, respectively. The red line is the tangent to the tube.

where

$$
\begin{aligned}
c_1 &= -\frac{1}{2}\left[\frac{m_6^2}{\sigma_z^2}+\frac{m_3^2}{\sigma_y^2}+\frac{m_0^2}{\sigma_x^2}-\frac{c_x^2}{c_z^2}\right], \\
c_2 &= -\frac{1}{2}\left[\frac{m_7^2}{\sigma_z^2}+\frac{m_4^2}{\sigma_y^2}+\frac{m_1^2}{\sigma_x^2}-\frac{c_y^2}{c_z^2}\right], \\
c_{1,2} &= -\frac{1}{2}\left[\frac{m_6 m_7}{\sigma_z^2}+\frac{m_3 m_4}{\sigma_y^2}+\frac{m_0 m_1}{\sigma_x^2}-\frac{c_y c_x}{c_z^2}\right], \\
c_x &= \frac{m_6 m_8}{\sigma_z^2}+\frac{m_3 m_5}{\sigma_y^2}+\frac{m_0 m_2}{\sigma_x^2}, \\
c_y &= \frac{m_7 m_8}{\sigma_z^2}+\frac{m_4 m_5}{\sigma_y^2}+\frac{m_1 m_2}{\sigma_x^2}, \\
c_z &= \sqrt{\frac{m_8^2}{\sigma_z^2}+\frac{m_5^2}{\sigma_y^2}+\frac{m_2^2}{\sigma_x^2}}.
\end{aligned}
\tag{3.21}
$$

A further diagonalization of 3.20 provides

$$
f(v_{s,1},v_{s,2})d^2v_s=\frac{1}{2\pi\sigma_{s,1}\sigma_{s,2}}e^{-\frac{v_{s,1}^2}{2\sigma^2_{s,1}}}e^{-\frac{v_{s,2}^2}{2\sigma^2_{s,2}}}dv_{s,1}dv_{s,2}, \tag{3.22}
$$

where $\{\sigma_{s,1},\sigma_{s,2}\}$ are the eigenvalues of the matrix $\begin{bmatrix} c_1 & \frac{c_{1,2}}{2} \\ \frac{c_{1,2}}{2} & c_2 \end{bmatrix}$, and the normalization has been included.

Since the source projected velocity in OL is $\vec{v}_{sp}\equiv\frac{D_{OL}}{D_{OS}}\vec{v}_s\equiv x\vec{v}_s$, then the source velocity distribution in OL reads

$$
f(v_{sp,1},v_{sp,2})d^2v_{sp}=\frac{1}{(2\pi)^{\frac{3}{2}}x^2\sigma_{s,1}\sigma_{s,2}}e^{-\frac{v_{sp,1}^2}{2x^2\sigma^2_{s,1}}}e^{-\frac{v_{sp,2}^2}{2x^2\sigma^2_{s,2}}}dv_{sp,1}dv_{sp,2} \tag{3.23}
$$

So, the source velocity distribution keeps its gaussianity in OL provided that $\sigma_{s,\{1,2,3\}}\rightarrow x\sigma_{s,\{1,2,3\}}$.

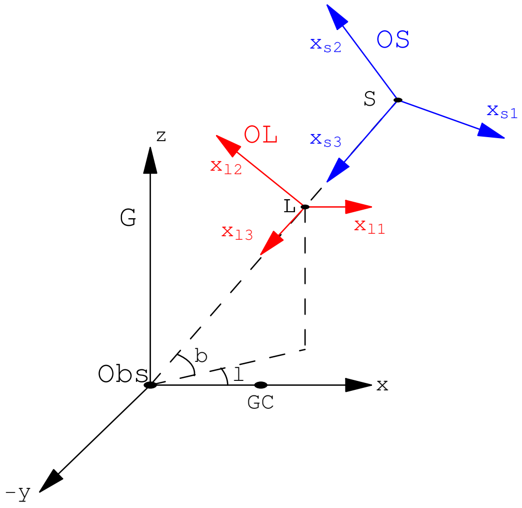

Figure 3.5: Galactic (G, black) and orthogonal (OL, red) reference frames. In the G frame, $\{x, y, z\}$, the origin is in the Sun, the z- and x-axes point towards the North Galactic Pole (NGP) and the Galactic Center (GC), respectively. In the OL system, $\{x_{l,1}, x_{l,2}, x_{l,3}\}$, the origin is in the lens, L, the axis $x_{l,3}$ points towards the observer and $\{x_{l,1}, x_{l,2}\}$ is the lens plane. In the OS frame, $\{x_{s,1}, x_{s,2}\}$ is the plane orthogonal to the line of sight at the source position and $x_{s,3}$ points to the observer.

In a similar way, if $\vec{v}_{lp}$ is the lens velocity in the system OL, then its velocity distribution gets

$$f(v_{lp,1}, v_{lp,2})d^2v_{lp} = \frac{1}{(2\pi)^{\frac{3}{2}}\sigma_{l,1}\sigma_{l,2}} e^{-\frac{v^2_{lp,1}}{2\sigma^2_{l,1}}} e^{-\frac{v^2_{lp,2}}{2\sigma^2_{l,2}}} dv_{lp,1}dv_{lp,2}. \tag{3.24}$$

where $\{\sigma_{l,1}, \sigma_{l,2}\}$ can be calculated from the velocity dispersions in the lens proper reference frame as done for the sources.

Since the frame $\{x_{s,1}, x_{s,2}\}$ does not coincide in general with $\{x_{l,1}, x_{l,2}\}$, we choose the latter as reference frame on the lens plane and call γ the angle between $x_{l,1}$ and $x_{s,1}$. The source velocity components in the new reference frame, $\{v_{spl,1}, v_{spl,2}\}$, are related to $\{v_{sp,1}, v_{sp,2}\}$ through the simple relations

$$\begin{aligned} v_{sp,1} &= v_{spl,1}\cos\gamma + v_{spl,2}\sin\gamma, \\ v_{sp,2} &= v_{spl,2}\cos\gamma - v_{spl,1}\sin\gamma. \end{aligned} \tag{3.25}$$

Moreover, if the "ordered motion" has components $\vec{V} = (V_1, V_2)$ on the lens plane, then using eq. 3.15 we can perform analytic integration of eq. 3.9 over all the source velocity components and get

$$d\Gamma = \frac{1}{\int \rho_s D^{2(1-\beta)}_{OS} dD_{OS}} \frac{n_l(\vec{x})d^3x\rho_s D^{2(1-\beta)}_{OS} dD_{OS}}{dt} \frac{e^{-\left(V_1+v_{r,1}\right)^2 \frac{n_1}{den}} e^{-\left(V_2+v_{r,2}\right)^2 \frac{n_2}{den}} e^{-\left(V_1+v_{r,1}\right)\left(V_2+v_{r,2}\right)\frac{n_{1,2}}{den}}}{2\pi \text{ coeff}} dv_{r,1}dv_{r,2}, \tag{3.26}$$

where $v_{r,1}$ and $v_{r,2}$ are the components on the lens plane of the lens-tube relative velocity. What was previously called $v_{r,\perp}$ will be from now on simply v_r since we moved to the lens plane and the velocities are all orthogonal to the l.o.s.

$$\begin{aligned} \text{coeff} \quad &= \quad \sqrt{(\sigma^2_{l,1} + x^2\sigma^2_{s,1})(\sigma^2_{l,2} + x^2\sigma^2_{s,2}) + x^2(\sigma^2_{l,1} - \sigma^2_{l,2})(\sigma^2_{s,1} - \sigma^2_{s,2})\sin^2\gamma}, \\ &\quad +\sigma^2_{l,1}(\sigma^2_{l,2} + x^2(\sigma^2_{s,2} + \sin^2\gamma(\sigma^2_{s,1} - \sigma^2_{s,2}))), \end{aligned}$$

$$\begin{aligned}
\mathrm{n}_1 &= \sigma_{l,2}^2 + x^2(\sigma_{s,2}^2 + \sin^2\gamma(\sigma_{s,1}^2 - \sigma_{s,2}^2)),\\
\mathrm{n}_2 &= \sigma_{l,1}^2 + x^2((\sigma_{s,1}^2 - \sin^2\gamma(\sigma_{s,1}^2 - \sigma_{s,2}^2)),\\
\mathrm{n}_{1,2} &= 2\sin\gamma\cos\gamma x^2(\sigma_{s,1}^2 - \sigma_{s,2}^2),\\
\mathrm{den} &= 2x^2(x^2\sigma_{s,1}^2\sigma_{s,2}^2 + \sigma_{l,2}^2(\sigma_{s,1}^2 - \sin^2\gamma(\sigma_{s,1}^2 - \sigma_{s,2}^2))).
\end{aligned} \tag{3.27}$$

Eq. 3.26 is a compact expression that can be even more compact if one diagonalizes the matrix $\begin{bmatrix} \frac{n_1}{den} & \frac{n_{1,2}}{2den} \\ \frac{n_{1,2}}{2den} & \frac{n_2}{den} \end{bmatrix}$ in order to let only diagonal terms appear in the exponentials. The diagonalization is a straightforward approach whose final result reads

$$d\Gamma = \frac{1}{\int \rho_s D_{OS}^{2(1-\beta)} dD_{OS}} \frac{n_l(\vec{x}) d^3x \rho_s D_{OS}^{2(1-\beta)} dD_{OS}}{dt} \frac{e^{-\left(V_1+v_{r,1}\right)^2 \frac{m_1+\sqrt{m_2}}{4\mathrm{coeff}^2}} e^{-\left(V_2+v_{r,2}\right)^2 \frac{m_1-\sqrt{m_2}}{4\mathrm{coeff}^2}}}{2\pi\ \mathrm{coeff}} dv_{r,1}dv_{r,2}, \tag{3.28}$$

with

$$\begin{aligned}
m_1 &= \sigma_{l,1}^2 + \sigma_{l,2}^2 + x^2(\sigma_{s,1}^2 + \sigma_{s,2}^2),\\
m_2 &= 4\sin^2\gamma x^2(\sigma_{l,2}^2 - \sigma_{l,1}^2)(\sigma_{s,1}^2 - \sigma_{s,2}^2) + (\sigma_{l,1}^2 - \sigma_{l,2}^2 + x^2(\sigma_{s,1}^2 - \sigma_{s,2}^2))^2,
\end{aligned} \tag{3.29}$$

or, introducing the new vectors

$$\begin{aligned}
\vec{v}_{r,mod} &= \{\sqrt{m_1+\sqrt{m_2}}v_{r,1}, \sqrt{m_1-\sqrt{m_2}}v_{r,2}\},\\
\vec{V}_{mod} &= \{\sqrt{m_1+\sqrt{m_2}}V_1, \sqrt{m_1-\sqrt{m_2}}V_2\},
\end{aligned} \tag{3.30}$$

exploiting eq. 3.12 and moving to cylindrical coordinates on the lens plane:

$$d\Gamma = \frac{dn_l(\vec{x})}{d\mu} \frac{v_r \cos\theta R_E D_{OS}^{2(1-\beta)} \rho_s}{\int \rho_s D_{OS}^{2(1-\beta)} dD_{OS}} \frac{e^{-\frac{|\vec{v}_{r,mod}+\vec{V}_{mod}|^2}{2\ \mathrm{coeff}}}}{2\pi\ \mathrm{coeff}} d\alpha dD_{OL} d\mu dD_{OS} v_r dv_r d\theta, \tag{3.31}$$

where we have introduced the lens number density per unit mass, $\frac{dn_l(\vec{x})}{d\mu}$, that will be described later on in detail. A further integration of expression 3.31 over θ provides

$$d\Gamma = \frac{dn_l(\vec{x})}{d\mu} \frac{2v_r^2 R_E D_{OS}^{2(1-\beta)} \rho_s}{\int \rho_s D_{OS}^{2(1-\beta)} dD_{OS}} \frac{e^{-\frac{|\vec{v}_{r,mod}+\vec{V}_{mod}|^2}{2\ \mathrm{coeff}}}}{2\pi\ \mathrm{coeff}} d\alpha dD_{OL} d\mu dD_{OS} dv_r, \tag{3.32}$$

which is the final expression for $d\Gamma$ whose applications will be described in the next chapters.

Let us now discuss in more detail choices and assumptions regarding the lens number density. We will assume the usual *factorization hypothesis* stating that the lens mass distribution is independent of the spatial distribution:

$$\frac{dn(\vec{x})}{d\mu} d\mu = \frac{dn_0}{d\mu} \frac{\rho_l}{\rho_{0,l}} d\mu, \tag{3.33}$$

where ρ_l and $\rho_{0,l}$ are the lens density and local density, μ is the lens mass in units of the solar mass ($M_\odot$) and $dn_0/d\mu$ is the *mass function* (MF) and is usually assumed to be a power law function

$$\frac{dn_0}{d\mu} \propto \mu^{-\alpha}, \tag{3.34}$$

as supported by star counts [98, 117, 150]. Nevertheless, in some cases, more involved functions fit star counts as well as power laws [42]. If (μ_{min}, μ_{max}) is the lens mass range and if the MF is unique on the whole range, then it is normalized as follows

$$\int_{\mu_{min}}^{\mu_{max}} \frac{dn_0}{d\mu} \mu d\mu = \frac{\rho_{0,l}}{M_\odot}. \tag{3.35}$$

In microlensing studies, if one wants to infer about a dark matter contribution to a known population of lenses, μ_{max} is set by observational constraints and is given by the minimum mass that the observational facilities can directly detect and thus strongly depends on the distance of the observed target: the farther it is and the higher is the minimum detectable mass.
Nevertheless, a more reliable model is a mass function with different slopes. Assuming

$$\frac{dn_0}{d\mu} \propto \begin{cases} \mu^{-\alpha_1} & \text{for } \mu_{\min} < \mu < \mu_{\text{cut}} \\ \mu^{-\alpha_2} & \text{for } \mu_{\text{cut}} < \mu < \mu_{\max} \end{cases} \tag{3.36}$$

then, the normalization is performed as follows

$$C_1 \int_{\mu_{min}}^{\mu_{cut}} \mu\mu^{-\alpha_1} d\mu + C_2 \int_{\mu_{cut}}^{\mu_{max}} \mu\mu^{-\alpha_2} d\mu = \frac{\rho_{0,l}}{M_\odot}, \tag{3.37}$$

and in a similar way for more than two different slopes. By *mass function* the present-day lens number density per unit mass is meant; if, at the formation epoch of the observed target (usually a galaxy), the present-day lenses were sufficiently low-mass stars, then, at the actual epoch, they are still main sequence stars as the time gone by now has been not enough for them to migrate to the red giant branch and the measured present-day mass function coincides with the *Initial Mass Function* (IMF), that is the mass function at the formation epoch of the observed galaxy. Microlensing can thus be a strong tool to cast light on the formation of galaxies. In the next chapters the choice of the mass integration interval and of the IMF will be discussed in more detail.

3.3 Applications of the microlensing event rate

The event rate is a strong investigation tool as it can constrain whatever lens or source parameter involved by means of its shape suggesting a lot about the duration and the number of predicted events, these being directly, even though not in a straightforward way, connected to the above mentioned parameters. In this section we give a brief overview of the possibile applications and postpone more details in the next chapters.
A possible statistical study compares the Einstein time observed distributions with the predicted ones. To get the latter, one calculates $d\Gamma/dT_E$, the probability of observing, in a given direction, a microlensing event with Einstein time T_E:

$$\frac{d\Gamma}{dT_E} = \frac{dn_0(\vec{x})}{d\mu} \frac{R_E^4}{T_E^4} \frac{2D_{OS}^{2(1-\beta)}\rho_s\rho_l}{\rho_{0,l}\int \rho_s D_{OS}^{2(1-\beta)} dD_{OS}} \frac{e^{-\frac{|\vec{v}_{r,mod}+\vec{V}_{mod}|^2}{2\text{ coeff}}}}{2\pi \text{ coeff}} d\alpha dD_{OL} d\mu dD_{OS}, \tag{3.38}$$

since $v_r = R_E/T_E$; this relation follows from the definition of Einstein time as the time spent by the source to cross the lens Einstein circle. Regarding the differential rate, one defines a modal time, $T_{E,mod}$, such that $d\Gamma(T_{E,mod})/dT_E$ is the maximum value assumed by the differential rate and a median Einstein time, $T_{E,med}$, defined as

$$\int_0^{T_{E,med}} \epsilon(T_E) \frac{d\Gamma}{dT_E} dT_E = \frac{1}{2} \int_0^\infty \epsilon(T_E) \frac{d\Gamma}{dT_E} dT_E \equiv \frac{1}{2} \frac{N_{exp}}{N_{obs}T_{obs}}, \tag{3.39}$$

where N_{exp} is the total number of expected events in the given direction, as follows from the definition of differential event rate, and $\epsilon(T_E)$ is the detection efficiency function which weights the detection ability at observing events with a given T_E and is due to observational limits. The ideal detection efficiency is $\epsilon(T_E) = 1$, that is, all events, at any Einstein time, are detected. In realistic hypothesis, the detection efficiency is much smaller than 1 for T_E smaller than a couple of days or larger than some hundreds days and reaches its maximum at $T_E \sim 100$.

An example of detection efficiency is shown in fig. 3.6. Fig. 3.7 shows event rates calculated in the direction of field 1 monitored by the MACHO collaboration [2] towards the LMC for lenses belonging to different populations: LMC or MW halo or SL.
The different height and width of the rates is a most useful tool to discriminate among lens populations. In the example shown, SL appears to favour longer duration events than halo populations

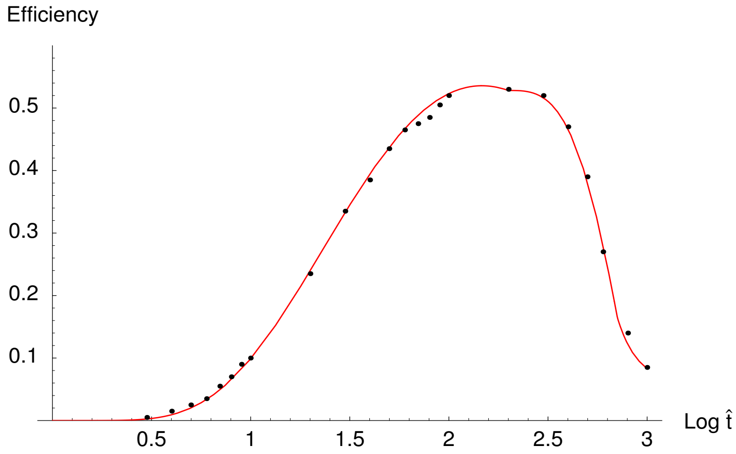

Figure 3.6: Mean Detection efficiency of the MACHO collaboration [8] in the direction of the LMC. Also shown is an interpolation of the points [93].

do. This difference is mostly due to the different geometry and to the different velocity dispersions of the deflectors. Let us discuss it briefly while for more details take a look at chapter 5.
The Einstein time of an event depends on the lens transverse velocity and on its Einstein radius. The faster the lens is, the shorter an event lasts, as the alignment among lens, observer and source is soon lost. Moreover, from eq. 2.5 follows

$$R_E = \sqrt{\frac{4G\mu M_\odot}{c^2}\frac{(D_{OS}-D_{OL})D_{OL}}{D_{OS}}} \equiv \sqrt{\frac{4G\mu M_\odot}{c^2}D_{OS}(1-x)x}, \tag{3.40}$$

where x is defined as in section 3.1; this expression suggests that, for a given source at distance D_{OS} from the observer, the nearer the lens is either to the source or to the observer, the smaller is R_E, thus reducing the Einstein time. The same effect follows decreasing the lens mass as $T_E \propto R_E \propto \sqrt{\mu}$. Of course, eventually, the event rate profile is an involved combination of these two effects.
An heavy dependence on the lens mass is induced by the mass function, too. If it is assumed to be a power law, then the higher the power, the higher the number of low mass lenses to the detriment of high mass ones, thus favouring short duration events and increasing the number of expected events, N_{exp}, as, on average, $T_E \propto <\mu>^{1/2}$ and $N_{exp} \propto <\mu>^{-1/2}$ [49].

The last relation can be immediately recovered if one considers that, for a given lens total mass, the higher the average mass and the smaller the number of lenses, thus reducing the number of expected events. As mentioned at the beginning of this section, some rough conclusions can be derived comparing the observed and predicted Einstein time distributions as fig. 3.8 shows [93], where the set of detected events studied is the one observed by the MACHO collaboration towards the LMC [4, 5, 6, 7]. Out of the 16 detected events, only 14 were analysed, as their nature was not known yet. The observed and predicted median T_E are plotted against the optical depth in the direction of each detected event, thus introducing helpful information provided by the LMC geometry. From the contour plot of the SL optical depth towards the LMC [93], it emerges that the contour line at 2×10^{-8} includes all the LMC disk and bar where a SL event most probably happens. Thus, assuming that an event detected in a direction where the optical depth is higher than this reference value (right side of the graph) is most probably due to SL, one finds that, for the assumed mass and velocity distributions, the four events (except event number 1 [93]) lying in the right side of the plot are the ones whose observed T_E is in best agreement with the predicted one and are the best candidates as SL events.
This conclusion needs, of course, more support.
This can be provided by the study of the modal lens mass, μ_{mod}, defined as

$$\frac{d\Gamma}{dT_E d\mu}(T_{E,obs}, \mu_{mod}) = Max(\frac{d\Gamma}{dT_E d\mu}(T_{E,obs}, \mu)), \tag{3.41}$$

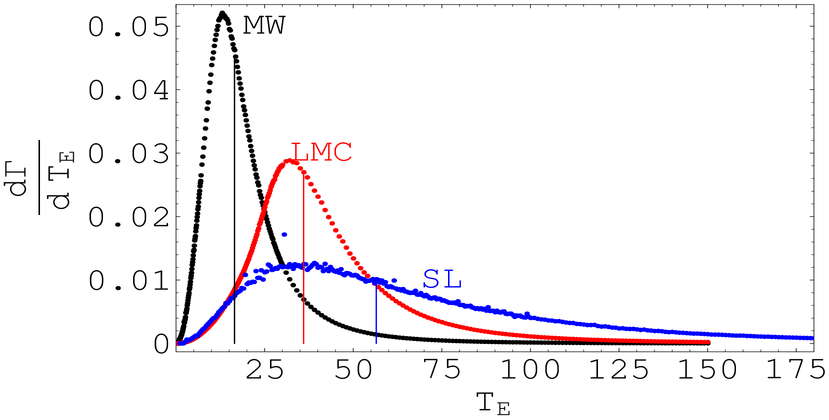

Figure 3.7: Event rate for lenses belonging to the MW or LMC halo or for SL in the direction of the first field monitored by the MACHO collaboration (in their notation) towards the LMC. The IMF is supposed to be a delta function centered at 1 $M_\odot$ for halo lenses and a Chabrier function [42] for the luminous components. Also shown are the median times for each event rate.

where $\frac{d\Gamma}{dT_E d\mu}$ can be derived from eq. 3.38. Fig. 3.9 shows the predicted μ_{mod} plotted, for every event, against the observed T_E. Some events are missing because their μ_{mod} falls below the assumed lower mass limit, $\mu_{min} = 0.08$, for a lens to be a star and this can be assumed as being a strong evidence for those events not to be due to SL. As μ_{mod} does not depend on the amplitude of the chosen interval of allowed lens mass, one plots this value against the observed T_E and, keeping in mind that $T_E \propto \mu^{1/2}$, one expects to find a parabola fitting the points. In fact, this parabola is eventually well approximated by a straight line, due to the small variation range of μ_{mod} (see figure).

Once again, the four events that seem to be due to SL, and for which the expected μ_{mod} is well above the expected one, can be well distinguished from another population whose μ_{mod} fluctuate around the dashed correlation line.
Thus, these results altogether strongly suggest that a non negligible number of events is due to self-lensing, these events being identified from the whole set.
The approach described above is a possible way to analyze data. Others are described in chapter 5.

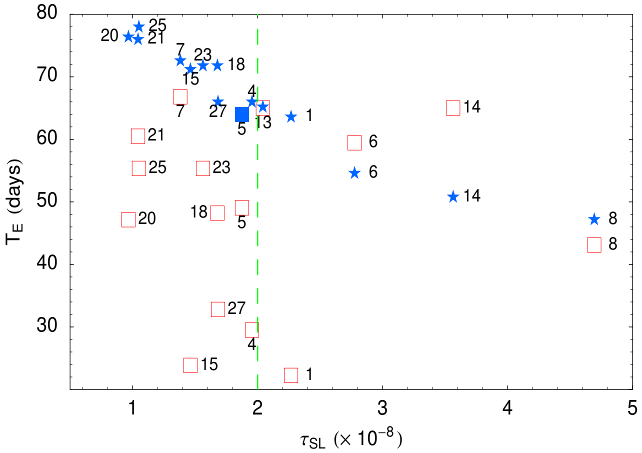

Figure 3.8: Comparison between the expected and observed Einstein time distribution for SL towards the LMC [93] plotted against the optical depth in the direction of the given event. The blue stars are the expected values, the empty boxes are the observed ones. The events are labeled by the MACHO number notation [5].

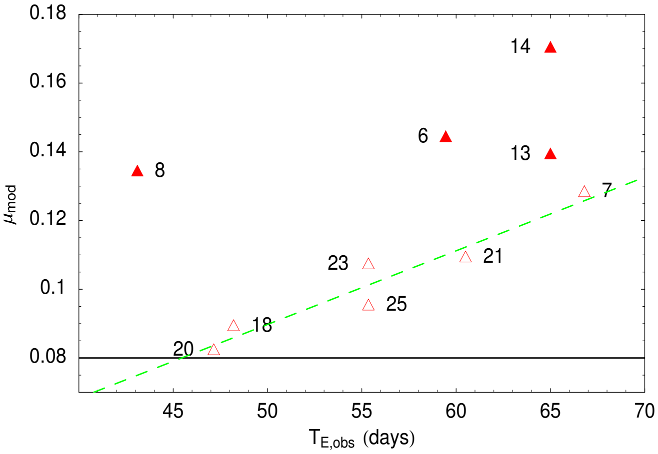

Figure 3.9: Expected μ_{mod} for SL in the LMC [93]. The events are labeled by the MACHO number notation [5]. The full triangles are the events that are most probably due to SL. Some events are missing as their μ_{mod} is below the threshold of 0.08 $M_{\odot}$ (see text). The empty triangles seem to be well correlated and to belong to a distinct population from that of the full ones.

Chapter 4

Microlensing towards the Galactic Bulge: an optical depth analysis

A remarkable number of microlensing events has been recently observed in the direction of the Galactic center [73, 135, 113, 136, 25]. To cast new light on the structure of the Galaxy, we have performed an optical depth analysis of a subset of events [113, 73] which have been sorted out selecting only events whose source is a bulge Red Clump Giant (RCG) [75], that is a red, bright star for which blending effects can be neglected, thus making the optical depth measurement more reliable. An overview of the adopted models for the Galactic components is given in section 4.1, the results for the adopted models are discussed in section 4.2 while section 4.3 describes a similar analysis for an alternative bulge density profile.

4.1 Galactic components: models

4.1.1 Galactic disk

Most of the luminous components of the Galaxy are located in a disk which is assumed to have an exponential distribution on the Galactic plane and a more involved one in the vertical direction, taking into account the thin and thick components. Starting from the Galactic reference frame $\{x, y, z\}$ whose origin is at the Galactic center with the z- and x-axis pointing to the North Galactic Pole and from the Sun to the center, respectively, and the y-axis pointing in the direction of increasing Galactic longitudes, we move to the galactocentric cylindrical coordinates (R, z) where $R = \sqrt{x^2 + y^2}$ is the distance from the Galactic center on the Galactic plane. In these coordinates the disk density profile is [75, 149]

$$\begin{aligned} \rho_D = \rho_{0,D}/\eta(R) exp\left(-\frac{R - R_0}{H}\right) \times \\ \left((1-\beta)\cosh^{-2}\left(\frac{z}{\eta(R)H1}\right) + \beta exp\left(-\frac{|z|}{\eta(R)H2}\right)\right), \end{aligned} \tag{4.1}$$

with $\rho_{0,D} = 0.0493 M_\odot pc^{-3}$, $\beta = 0.565$ and $R_0 = 8.0$ kpc is the distance of the Sun from the Galactic center. The lenght scales are $H = 2.75$ kpc, $H1 = 270$ pc and $H2 = 440$ pc while $\eta(R) = max(\frac{R}{9025pc} + 0.114, 0.670)$. This density profile provides a disk mass of $3.06 \times 10^{10} M_\odot$ inside a radius of 15 kpc.

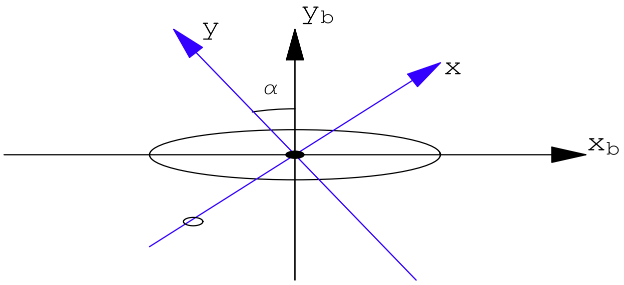

Figure 4.1: Relation between the Galactic coordinates $\{x, y, z\}$ and the bulge proper ones $\{x_b, y_b, z_b\}$ on the Galactic plane. The z_b- and $z-$axes coincide and are orthogonal to the sheet. The Sun is at the empty circle position. The filled circle is the Galactic center.

4.1.2 Galactic bulge

As mentioned above, we have studied a set of events whose sources are bulge RCGs. As density profile for this sample of sources we use one of the best fitting models from Stanek *et al.* [134], the so called model E2 which is a triaxial density profile

$$\rho_B = \rho_{0,B} exp(-r), \tag{4.2}$$

where $r = \sqrt{(\frac{x_b}{x_o})^2 + (\frac{y_b}{y_o})^2 + (\frac{z_b}{z_o})^2}$, with $\{x_b, y_b, z_b\}$ being the bulge proper coordinate system which is described below, and $\{x_o, y_o, z_o\} = \{897, 387, 250\}pc$. As the apparent magnitudes of bulge stars are systematically fainter in fields at lower Galactic longitudes [73], one concludes that the bulge is not edge-on with respect to the Sun but is rotated on the Galactic plane and that its nearest-to-us end lies at positive Galactic longitudes. The relation between the coordinates $\{x_b, y_b, z_b\}$ and the Galactic ones $\{x, y, z\}$ is

$$\{x_b, y_b, z_b\} = R(\alpha)\{x, y, z\}, \tag{4.3}$$

where $R(\alpha)$ is a clockwise rotation matrix on the Galactic plane of an angle α (see fig. 4.1) whose value is still matter of debate. The most reliable values calculated so far vary in a range $(10°, 50°)$ and have been deduced on the basis of analyses of reddening-corrected apparent magnitude distributions of RCG in different directions. We assume $\alpha = 23.8°$ as found in [134] for model E2. Moreover, we assume a bulge corotation radius $R_{CR} = 3.5kpc$ [57].

A reliable value of the bulge central density is still missing. Nevertheless [113] provides a measure of the total optical depth in a given direction, so we have chosen the bulge central density in such a way that the predicted optical depth in the given direction coincides with the measured one, getting $\rho_{0,B} = 7.30 M_\odot pc^{-3}$ and a total bulge mass of $1.2 \times 10^{10} M_\odot$, in good agreement with previous estimations [22, 74].

Fig. 4.2 shows the column density contours of the bulge for model E2 with the chosen central density.

4.2 Results

Given a lens population, the optical depth, τ, for a given star is the probability that at a certain time the star is inside the Einstein radius of any of the foreground lens. This definition implies that the farther away a star is, the more its optical depth increases, since a higher number of lenses can intersect the l.o.s. observer-source, even though the source appears fainter and thus less likely

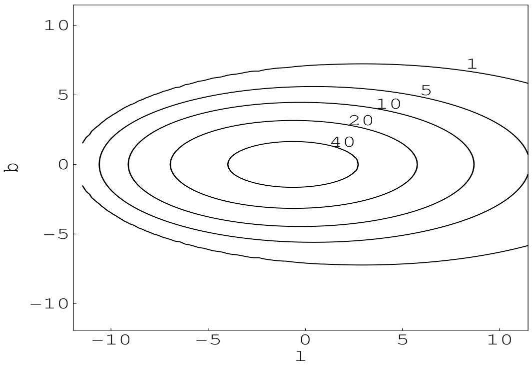

Figure 4.2: Galactic bulge column density. The z-axis points to the North Galactic Pole and the y-axis in the direction of increasing longitudes. The contour lines numbers are in units of $10^{10} M_\odot / kpc^2$.

to be detected. Nevertheless, bright sources, such as RCG, can be detected independently of their distance. In the definition of optical depth this property can be taken into account [75] as follows

$$\tau = \frac{4\pi G}{c^2}\Big(\int_0^\infty dD_{OS} D_{OS}^{2-\gamma}\rho_s)\Big)^{-1} \times \tag{4.4}$$
$$\int_0^\infty D_{OS}^{2-\gamma}\rho_s dD_{OS} \int_0^{D_{OS}} \rho_l D_{OL}\Big(1-\frac{D_{OL}}{D_{OS}}\Big)dD_{OL}$$

where $\rho_{l(s)}$ is the lens (source) density profile and $D_{OL,(OS)}$ is the observer-lens (observer-source) distance. For bright stars $\gamma = 0$.
On the (l, b) plane, with l and b respectively the Galactic longitude and latitude, our model provides the optical depth profile shown in fig. 4.3, where we have assumed RCG bulge sources and lenses belonging to both bulge and disk. As expected, the optical depth falls more rapidly at positive longitudes due to the bulge inclination on the Galactic plane. The red point at $(l, b) = (1.50°, −2.68°)$

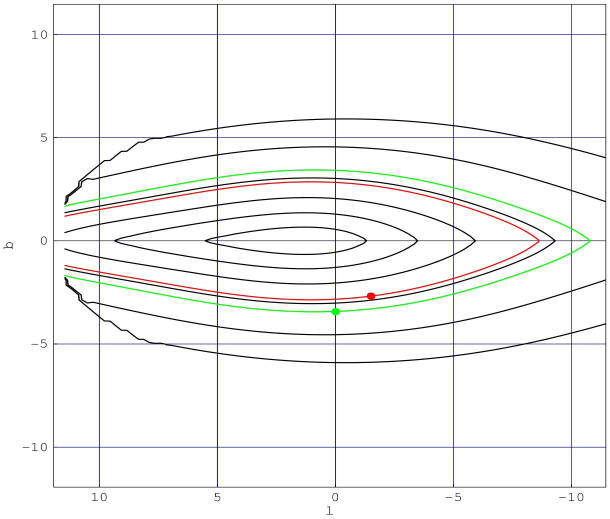

Figure 4.3: Total optical depth contours on the (l, b) plane for bulge model E2. The black lines show the contours at $\{0.5,1,2,3,4,5\}\times 10^{-6}$ (from outside toward the center). The green and red points show the directions where the EROSII and MACHO collaborations, respectively, measured a mean optical depth. The coloured lines show (with corresponding colours) the contours at these measured values.

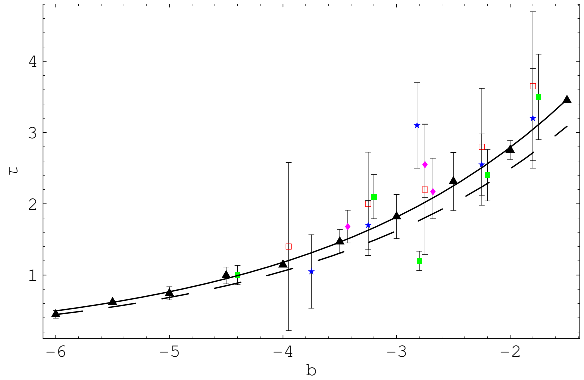

Figure 4.4: Comparison between measured and predicted mean optical depth. Green boxes: EROSII data; blue stars: OGLE data; red empty boxes: MACHO data; fucsia diamonds: average values measured by EROSII, OGLE, MACHO; black triangles: model predictions. For a given value of b, the optical depth average value has been calculated in the interval $-6° < l < 6°$ (see text). The solid line is the model prediction best fit while the dashed line is the EROSII best fit [73].

of fig. 4.3 shows the position where the MACHO survey found $\tau_M = 2.17^{+0.47}_{-0.38} \times 10^{-6}$, this being the value that has been fitted to calculate the bulge central density. The model predicted optical depth contour at τ_M is shown as a red line. Also shown in fig. 4.3 is the green point at $(l, b) = (0, -3.43°)$ where EROSII reports $\tau_E = (1.68 \pm 0.23) \times 10^{-6}$. Remarkably the model predicts a contour at τ_E (green line) that perfectly matches the green point position. Another optical depth measurement has been provided by the OGLE collaboration which reports at $(l, b) = (1.16°, -2.75°)$ a value $\tau_o = 2.55^{+0.57}_{-0.46} \times 10^{-6}$ to be compared to our prediction of $\tau = 2.15 \times 10^{-6}$ that falls well inside the 1σ error bar of the OGLE-measurement.

A direct comparison between the predicted and the calculated mean value of the optical depth as a function of b is shown in fig. 4.4. Here, for a given value of $b = \tilde{b}$, we have selected all the EROSII and MACHO monitored fields whose center is located at (l_f, b_f) such that $|b_f - \tilde{b}| < \Delta_b = 0.5°$ and $|l_f| < 6°$. The solid line of fig. 4.4 shows the model best fit

$$\tau = \tau_0 exp[-a(|b| - 3°)] \tag{4.5}$$

with $\tau_0 = 1.8^{+0.1}_{-0.2} \times 10^{-6}$ and $a = 0.43^{+0.01}_{-0.03}\ deg^{-1}$, whereas the EROSII collaboration finds, fitting its 5 points only [73], $\tau_0 = (1.62 \pm 0.23) \times 10^{-6}$ and $a = (0.43 \pm 0.16)\ deg^{-1}$ (dashed line of fig. 4.4). Our results depend only very slightly on the choice of Δ_b.

Interestingly, a similar analysis performed on the EROSII fields only, with the bulge central density fitted on the EROSII data, provides a best fit function whose slope in $b = -2.7°$ is 0.88 to be compared to their reported value of 0.78 ± 0.27. Similarly, an analysis of the MACHO fields only provides a best fit whose average slope in the interval $b \in (-1.8°, -4.°)$ (where the MACHO survey provides data) is 0.87, whereas [113] reports 1.06 ± 0.71.

4.3 Model comparison

Both the density profile and the inclination of the bulge are still matter of debate [36, 37, 111] and an optical depth analysis could help ruling out inadequate models. Fig. 4.5 shows the optical depth contours on the plane (l, b) for bulge RCG sources and bulge+disk lenses for the bulge model G2 of [134], which is one of the most frequently adopted bulge profiles in literature. This is a gaussian, boxy density profile

$$\rho_B = \rho_{0,B} exp(-r/2), \tag{4.6}$$

with $r = \sqrt{((x/x_o)^2 + (y/y_o)^2)^2 + (z/z_o)^4}$, $\{x_o, y_o, z_o\} = \{1.239, 0.609.0.438\} kpc$ and a bulge inclination $\alpha = 23.8°$. The normalization of the predicted optical depth on the MACHO value provides

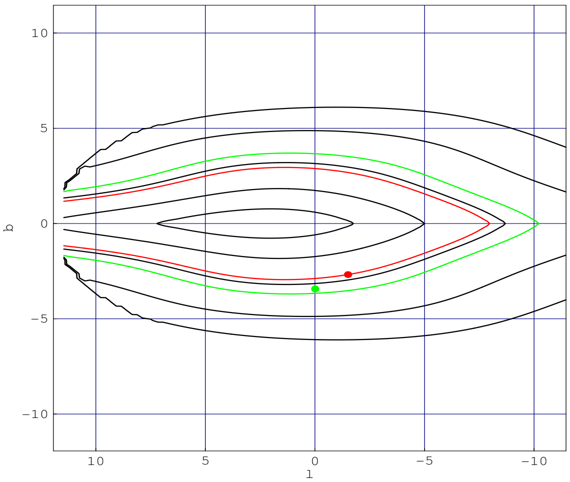

Figure 4.5: Total optical depth contours on the (l, b) plane for bulge model G2. The black lines show the contours at $\{0.5,1,2,3,4\} \times 10^{-6}$ (from outside toward the center). The green and red points show the directions where the EROSII and MACHO collaborations, respectively, measured a mean optical depth. The coloured lines show (with corresponding colours) the contours at these measured values.

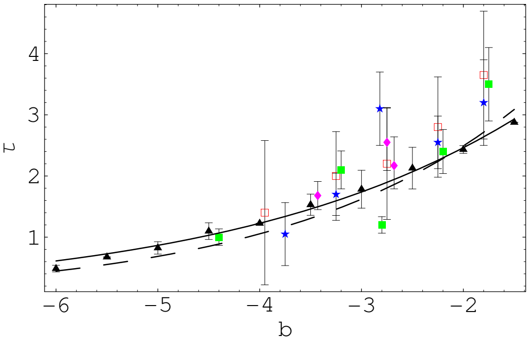

Figure 4.6: Comparison between measured and predicted mean optical depth for bulge model G2. Symbols as in fig. 4.4. The black solid line is the model best fit.

$\rho_{0,B} = 1.85 \times 10^9 M_\odot/kpc^3$ and a total bulge mass of $1.04 \times 10^{10} M_\odot$, being very similar to the one predicted by model E2. Nevertheless, model G2 describes a somewhat broader bulge, this explaining the lower optical depth values reached at the Galactic center with respect to fig. 4.3. Moreover, fig. 4.5 shows that the agreement between the EROS measure and the model prediction is not as good as for model E2, even though the model cannot be ruled out. Similarly, the mean optical depth as a function of the Galactic latitude b does not help further as fig. 4.6 shows.

With respect to the EROS best fit, model G2 predicts higher (lower) average τ at low (high) galactic latitudes. Fitting the model predicted points (black triangles of fig. 4.6) with the function given in eq. (4.5), the best fit parameters turn out to be $\tau_0 = 1.74^{+0.003}_{-0.03}$ and $a = 0.35^{+0.1}_{-0.2}\ deg^{-1}$. The relative freedom of choosing the central bulge density normalizing the predicted τ on the measured one does not enable us to put in evidence a deep difference between models E2 and G2 by means of an optical depth analysis solely, even though more extreme models could be ruled out easily. As a future work, an additional analysis of the spatial and time distribution of the detected events could help constraining the bulge density profile and by means of a maximum likelihood analysis other parameters, such as the slope of the bulge IMF at low masses, could be constrained.

Chapter 5

Microlensing towards LMC: a study of the LMC halo contribution [1]

5.1 Introduction

Since the original proposal of [106], microlensing has been shown to be a powerful tool for investigating the MACHO composition of galactic halos. The microlensing surveys towards the LMC and the SMC probed the existence of compact halo objects along these lines of sight; however, the assessment of these results with respect to the actual fraction of the Milky Way (hereafter "MW") halo in the form of MACHOs is still highly debated.

The MACHO collaboration reported the detection of 13-17 microlensing candidates towards the LMC [4], arguing in favour of a MACHO halo fraction of $\sim 20\%$ of objects of $\sim 0.5\,\mathrm{M}_\odot$ and estimating a microlensing optical depth towards the LMC of $\tau = 1.2^{+0.4}_{-0.3} \times 10^{-7}$. The reported microlensing rate towards the LMC significantly exceeds the expected one from known visible components of our Galaxy. Further analysis mainly confirmed these conclusions [20]. On the other hand, the EROS collaboration, from observations towards both the LMC and the SMC, put more and more lower *upper* limits on the MACHO contribution to galactic halos [89, 1, 137], which are no longer compatible with the MACHO results.

These questions have also been addressed by microlensing surveys towards M31 [11], and a first evidence of a MACHO contribution along this line of sight have been reported [38], although challenged in [47]. Overall, the picture remains unclear, in particular the problem of the nature and location of the observed events. For example, [69] have cast doubts on the interpretation of the microlensing data towards LMC as due to a dominant lens population made by Galactic halo MACHOs. In fact they show, at a high level of confidence, that the distribution of the duration of the observed microlensing events is significantly narrower than what is expected from a standard halo–lens population.

We have already addressed some of these questions in [81] and [93] (hereafter Paper I and Paper II, respectively). A main issue in both works is that the microlensing events towards the LMC, as observed by the MACHO collaboration, do not necessarily all belong to the same lens population. In particular in Paper II, we considered the issue of self lensing in the framework of the [140] picture of the luminous components of the LMC. The main conclusion, based both on the predicted number and characteristics of self–lensing events, was that self lensing alone cannot explain all the observed

---

[1] Published in [39]

events.

In the present work we extend the analysis by fully considering the LMC and MW dark matter halo MACHO lens populations. The main question we want to address is whether and to what extent events due to the lens population residing in the LMC halo can contribute to the observed rates. This issue was first proposed and discussed in [68]. Here we consider again the question taking into account both the results of the MACHO collaboration and the most recent results on the modeling of the LMC.

The paper is organised as follows. In Sect. 5.2 we review the models of the LMC and Galactic components we consider. In Sect. 5.3 we discuss the evaluation of the microlensing rate and present the results for the expected number and duration of the microlensing events. In Sect. 5.4 we carry out our new analysis and present our main conclusions on the LMC MACHO halo contribution, and in Sect. 5.5 we present our conclusions.

5.2 Models

We consider the LMC as composed of a luminous part, the bar, and the disc, plus a stellar and a dark matter halos. We also include the Galactic dark matter halo, but we do not include the Galactic disc and spheroid populations. These components have already been shown to give smaller contributions than the LMC self lensing [4], which we include instead. Accordingly, we exclude from our analysis the single event whose lens, upon a direct search, has been acknowledged to be part of these components.

For the structure and dynamics of the luminous components of the LMC we follow Paper II closely. From the analysis in [140], who derive their results on the assumption that the carbon star population is representative of the bulk of the LMC disc stars, we take up the results on the LMC disc intrinsic ellipticity, vertical thickness, line-of-sight velocity dispersion, rotation curve, and the coincidence of the centre of mass of the disc and the bar components. We assume the following values for the bar and disc components $M_{\rm bar} + M_{\rm disc} = (2.7 \pm 0.6) \times 10^9\,{\rm M}_\odot$ [140], and $M_{\rm bar} = 1/5\, M_{\rm disc}$ [71], which we consider to be both centred at $\alpha, \delta = 5^h 27.6^m \pm 3.9^m, -69.87^\circ \pm 0.41^\circ$ (J2000) at a distance from us of $D_0 = 50.1 \pm 2.5\,{\rm kpc}$ [140]. We use the same density star distribution as in Paper II, characterised by a vertical distribution for the exponential disc described by a sech^2 function and a boxy bar, with a Gaussian profile along the major axis and the section described by a $\exp(-r^4)$ function (see also section 3.1). The vertical structure of the LMC has been recently the object of an intensive debate (for a discussion see [141]). We considered this issue with respect to the expected self lensing signal in Paper II. In the present analysis, where we focus on the contribution of the two halos, we do not enter into this discussion but consider only the configuration with coplanar disc and bar.

The presence of a significant LMC stellar halo population is a matter of debate [100, 9, 63]. In the present analysis we include the contribution of such a possible component following [9], who proposes a spherically symmetric spheroid with density profile

$$\rho = \rho_0 \left(1 + \frac{R^2}{a_{\rm C}^2}\right)^{-k}, \tag{5.1}$$

with $k = 3/2$, central density $\rho_0 = 6.3 \times 10^6\,{\rm M}_\odot\,{\rm kpc}^{-3}$, and core radius $a_{\rm C} = 1.42\,{\rm kpc}$ for a total mass, within 8.9 kpc, of $0.35 \times 10^9 {\rm M}_\odot$ somewhat smaller than that of the bar. The optical depth profile of this component shows a near-far asymmetry due to the LMC disc inclination, whose overall shape recalls that of the optical depth profile of the LMC MACHO halo component (Paper II, Figure 4), with a maximum value around 0.9×10^{-8} reached in correspondence of the field MACHO 6.

Following [140], who present observational evidence based on the rotation curves, we include a significant LMC dark matter halo component. We assume a total LMC mass of $8.7 \times 10^9 {\rm M}_\odot$ within 8.9 kpc with a truncation radius of 15 kpc [140], which we consider to also include the contribution from the stellar halo. We assume a spherical isothermal model ($k = 1$ in Eq. 5.1) with a core radius of $a_{\mathrm{C}} = 2\,\mathrm{kpc}$ [4].

This spherical symmetric configuration might not be a realistic description of this component given that the dynamical environment of the LMC can induce tidal distortions and disruptions, especially in the outer parts. To take this issue into account, in Paper II we compared the LMC halo optical depth profiles for both a spherical and an elliptical configuration (Figs. 4 and 5 respectively): the overall shape is similar even if in the latter case the maximum value rises by about 20% and the near-far asymmetry is enhanced. However, as we lack any strong constraint, we prefer not to introduce a further parameter in the present analysis; therefore, we only consider the spherical configuration, in view also of the possibility of carrying out a more direct comparison with previous works.

In this same perspective, we consider the "standard" isothermal profile for the Galactic dark matter halo with a core radius of 5 kpc, local density $7.9 \times 10^6\,\mathrm{M}_\odot\,\mathrm{kpc}^{-3}$, and a distance from the Galactic centre of 8.5 kpc [4].

5.3 The microlensing rate

The main tool of investigation we use is $\frac{\mathrm{d}\Gamma}{\mathrm{d\,T_E}}$, the differential rate of microlensing events with respect to the Einstein time T_{E} [49, 70, 120]. This allows us to make predictions on the timescale, the number, and the spatial distribution of the expected events, which we can compare with the corresponding observed quantities. With respect to the self–lensing configuration that we analysed in Paper II (Sect. 4.2), we can no longer adopt the useful approximation $\frac{D_{ol}}{Dos} \equiv x \approx 1$. Moreover we now have to take the bulk velocity of the LMC components and the relative motion between the LMC and the Galaxy [140] fully into account.

The source stars belong to the luminous components, disc or bar, of the LMC, whereas the lenses can belong either to the LMC or the MW halo. We assume an isotropic Maxwellian profile[1] for the velocity distribution for both lenses and sources. For the flattened LMC luminous components, this is a rough approximation; still, it gives a fair description of the average properties of these populations that we consider to be sufficient in the present framework.

For the LMC disc component we consider the rotational velocity as in [140] with $\sigma = 20.2\,\mathrm{km/s}$. For the LMC bar stars we use a higher value of the velocity dispersion than for the disc, $\sigma = 24.7\,\mathrm{km/s}$ [44]. For both the LMC halo components, stellar and MACHO, we use $\sigma = 46\,\mathrm{km/s}$ [140, 9] (we tested that our results remain qualitatively unaltered by changing this value up to 20%); for the Galactic halo, $\sigma = 155\,\mathrm{km/s}$.

The expression for the random motion velocity for the lenses reads[2]

$$\vec{v}_{l\perp} = \hat{\vec{v}}_{l\perp} + x\,\vec{v}_{\mathrm{s}\perp} \; + \vec{A}_{\perp}\,, \tag{5.2}$$

where $\hat{\vec{v}}_{l\perp}$ is the velocity relative to the microlensing tube at position x, whose modulus is the ratio between the Einstein radius and the Einstein time ($\hat{v}_{l\perp} = R_E/T_E$), and $\vec{v}_{\mathrm{s}\perp}$ the random component of the velocity of the sources. All the bulk motions are included in $\vec{A}_{\perp}$, defined as

$$\begin{aligned} \vec{A}_{\perp} \;\; = \;\; & \tilde{\vec{v}}_{\odot\perp} + x\left(\tilde{\vec{v}}_{\mathrm{LMC}\perp} - \tilde{\vec{v}}_{\odot\perp} + \vec{v}_{\mathrm{s,drift}\perp}\right) - \\ & \eta\left(\tilde{\vec{v}}_{\mathrm{LMC}\perp} + \vec{v}_{l,\mathrm{drift}\perp}\right) \end{aligned} \tag{5.3}$$

where $\eta = 0,\,1$ for lenses in the Galaxy and in the LMC, respectively; $\vec{v}_{l,\mathrm{drift}\perp}$ is the drift velocity of the lens star belonging to the LMC disc (for the bar sources as well as for the halo lenses we only

---

[1] The Maxwellian profile of the velocity distribution is the first term of a series expansion in terms of Gauss–Hermite moments [139, 64]. See Sect. 3.2 of Paper I.

[2] The velocity components parallel to the line of sight are integrated out, and the subscript $\perp$ indicates the vectorial component in the plane orthogonal to the line of sight.

consider a random motion component), and a tilde over a vector indicates a quantity measured by an observer comoving with the Galactic centre. In the self–lensing configuration, $\vec{A}_\perp \approx 0$, and Eq. (5.2) reduces to Eq. (13) of Paper II.

We call α the angle between the inner normal to the tube, $\hat{\vec{n}}$, and the source velocity $\vec{v}_{\mathrm{s}\perp}$; θ the angle between $\hat{\vec{n}}$ and $\hat{\vec{v}}_{l\perp}$, $\theta \in (-\pi/2, \pi/2)$; φ the angle between $\vec{v}_{\mathrm{s}\perp}$ and $\vec{A}_\perp$; so that the angle between $\vec{v}_{l\perp}$ and $\vec{v}_{\mathrm{s}\perp}$ is $\alpha - \theta$, and that between $\vec{v}_{l\perp}$ and $\vec{A}_\perp$ is $\gamma = \alpha + \varphi - \theta$. Both α and φ vary in the range $(0,\, 2\pi)$ (Fig. 5.1).

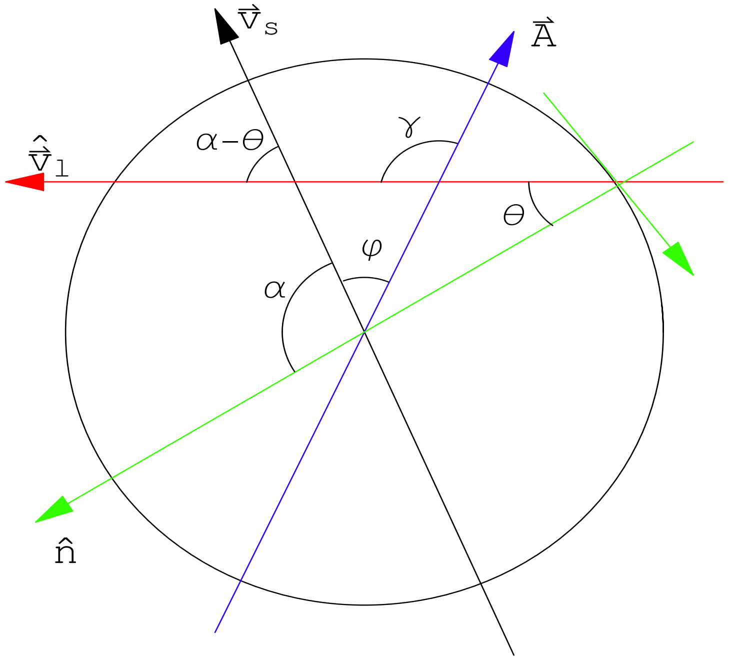

Figure 5.1: Scheme of a section of the microlensing tube with indicated the positions of the vectors and the angles involved.

In the case of $\vec{A}_\perp = 0$, all the integrations over the angular variables can be carried out analytically. This is now only possible for the θ variable. Altogether, after an analytical integration on the modulus of the source velocity, we are left with the following expression of the differential rate with respect to the Einstein time T_{E}:

$$\begin{aligned}
\frac{\mathrm{d}\Gamma}{\mathrm{dT_E}} = & \int_0^{2\pi} \mathrm{d}\alpha \int_0^{2\pi} \mathrm{d}\varphi \int_{d_{\min}}^{d_{\max}} \mathrm{dD_{os}} \int_{\mathrm{x_{min}}}^{1} \mathrm{dx} \int_{\mu_{\min}}^{\mu_{\max}} \mathrm{d}\mu \\
& \frac{\mathrm{dn_l}}{\mathrm{d}\mu} \, \frac{D_{os}\, \rho_l\, \rho_s\, \hat{v}_{l\perp}^4}{2\,\pi^2 (\sigma_l^2 + x^2 \sigma_s^2)\, \mathcal{N}} \times \\
& \Bigg\{ \exp\left[-\frac{A^2 + \hat{v}_{l\perp}^2 + 2A\, \hat{v}_{l\perp} \cos(\alpha+\varphi)}{2\,\sigma_l^2} \right] - \\
& \frac{\sqrt{\pi}\, x\, \sigma_s \left(\hat{v}_{l\perp} \cos(\alpha) + A \cos(\varphi) \right)}{\sigma_l \sqrt{2\,(\sigma_l^2 + x^2 \sigma_s^2)}} \times \\
& \exp\Bigg[-\frac{A^2 + \hat{v}_{l\perp}^2 + 2A\, \hat{v}_{l\perp} \cos(\alpha+\varphi)}{2\,(\sigma_l^2 + x^2 \sigma_s^2)} - \\
& \frac{x^2\, \sigma_s^2\, (\hat{v}_{l\perp} \sin(\alpha) - A \sin(\varphi))^2}{\sigma_l^2\, 2\,(\sigma_l^2 + x^2 \sigma_s^2)} \Bigg] \times
\end{aligned}$$

$$\left(1-\mathrm{Erf}\left(\frac{\mathrm{x}\sigma_{\mathrm{s}}\left(\hat{\mathrm{v}}_{\mathrm{l}\perp}\cos(\alpha)+\mathrm{A}\cos(\varphi)\right)}{\sigma_{\mathrm{l}}\sqrt{2(\sigma_{\mathrm{l}}^2+\mathrm{x}^2\sigma_{\mathrm{s}}^2)}}\right)\right)\Bigg\}\,, \tag{5.4}$$

where the normalization factor $\mathcal{N}$ is the integral over the line of sight of the sources

$$\mathcal{N}=\int_{d_{\min}}^{d_{\max}}\mathrm{dD}_{\mathrm{os}}\,\rho_{\mathrm{s}}(\mathrm{D}_{\mathrm{os}})\,,$$

having assumed that the number of detectable stars varies with the distance as D_{os}^{-2}. We define $x_{\min}=d_{\min}/D_{\mathrm{os}}$, $A=|\vec{A}|$; the integration limits along the line of sight, $d_{\min}$ and $d_{\max}$, represent the distances from the observer to the intersection with the LMC tidal surface, for lenses in the LMC, whereas $d_{\min}=0$ for lenses in the Galactic halo. We use solar mass units, defining $\mu=\frac{M}{\mathrm{M}_{\odot}}$, where M is the lens mass. For lenses belonging either to the disc or the bar of the LMC, as well as for the stellar LMC halo contribution, we use the exponential function as in [42] for the mass function $\frac{\mathrm{dn_l}}{\mathrm{d}\mu}$, with integration limits $\mu_{\min}=0.08$ and $\mu_{\max}=1.5$. If the lenses belong to the MW halo or to the LMC halo, the would be MACHOs, we use a set of delta functions with values going from 10^{-5} up to 10 $\mathrm{M}_{\odot}$.

Finally, to compare with the results of the observations, we have to take the expression for the detection efficiency into account, so that we obtain

$$\left(\frac{\mathrm{d}\Gamma}{\mathrm{dT_E}}\right)_{\varepsilon}=\frac{\mathrm{d}\Gamma}{\mathrm{dT_E}}\cdot\mathcal{E}(T_{\mathrm{E}})\,. \tag{5.5}$$

To discuss the results of the MACHO collaboration we use the efficiency as a function of as in [4] for which an analytical approximation is given in Paper II. We take the correction reported in [19] into account.

5.3.1 Expected number and duration

Following the prescription outlined in the previous section, we evaluate the differential microlensing rate, for each different lens population we consider, along the lines of sight towards the MACHO fields. In particular for each lens population, we calculate the expected number of events per field as

$$N_{\mathrm{field}}=E_{\mathrm{field}}\int_0^{\infty}\frac{\mathrm{d}\Gamma}{\mathrm{dT_E}}\,\mathcal{E}(T_{\mathrm{E}})\,\mathrm{d\,T_E}\,, \tag{5.6}$$

where the "field exposure" E_{field} is defined in [4], as the product of the number of distinct light curves per field and the relevant time span. Furthermore, we take care to eliminate the field overlaps.

To characterise the expected timescale, we report the *median* value of the asymmetric distribution $(d\Gamma/dT_E)_{\varepsilon}$, together with the values $T_{E,\,16\,\%}$ and $T_{E,\,84\,\%}$ that single out the extremes of the 68% probability range around the median.

In Table 5.1 we report, for both MW and LMC MACHO lens populations, the total number of the expected events in all the MACHO fields, in the case of a full MACHO halo, together with the expected timescales. We recall that the expected timescale varies with the square root of the mass of the MACHO, and that very short timescales are strongly suppressed by the detection efficiency function.

The predicted durations turn out to be almost independent of the position for both the halo populations we consider, whereas the issue of the variation of the expected timescales with the position across the fields for the self–lensing population was discussed thoroughly in Paper II. Indeed, for lenses in the Galactic halo, we find a dispersion of the median timescales towards the different fields smaller than 1%. In the case of the LMC lenses, the dispersion is only slightly larger, at most

Table 5.1: Expected duration, median values with 68% CL errors, and expected number of events for a full dark matter halo, respectively averaged and summed over the MACHO fields, as a function of the MACHO mass.

lens mass	MW		LMC	
$M_\odot$	T_E (days)	N_{exp}	T_E (days)	N_{exp}
10^{-5}	$3.3^{+3.0}_{-1.3}$	0.9	$3.3^{+3.0}_{-1.3}$	0.4
10^{-4}	$3.5^{+3.0}_{-1.5}$	8.3	$3.5^{+3.1}_{-1.3}$	3.2
10^{-3}	$4.3^{+3.6}_{-1.6}$	52	$5.4^{+4.4}_{-1.9}$	13.5
10^{-2}	$8.0^{+6.5}_{-3.1}$	115	$13^{+8.7}_{-4.4}$	17.3
0.1	$20^{+15}_{-8.0}$	97	36^{+21}_{-13}	9.9
0.2	26^{+20}_{-10}	82	48^{+27}_{-17}	7.6
0.5	41^{+29}_{-16}	59	75^{+46}_{-27}	5.0
1	55^{+38}_{-21}	44	103^{+57}_{-37}	3.4
10	149^{+79}_{-57}	12	245^{+94}_{-87}	0.5

$\sim 5\%$. The expected total number of events due to the LMC stellar halo turns out to be ~ 0.6, about half of those due to the LMC disc-bar self–lensing contribution (Paper II). The expected median timescale, averaged on the 30 fields, is $T_E = 45^{+43}_{-23}$ days.

Overall, we recover the result [4] that stellar lensing alone cannot explain the signal, so that most of the detected events must belong either to the MW or to the LMC dark matter halo.

5.4 The LMC MACHO contribution to microlensing events

A straightforward conclusion to be drawn from the results on the expected number of events due to the dark matter MW and LMC halos is that, with the implicit hypothesis that the halo fractions in both the MW and the LMC halos are the same, most of the lenses should indeed belong to the Galactic halo. Our aim is to challenge this point of view.

First, we recall the current status about the microlensing events observed by the MACHO collaboration. Next, we carry out a statistical analysis of the observed characteristics of the events (timescale and spatial distribution). The purpose here is to determine to what extent the available data allow the two halo populations to be distinguished. Eventually, using a likelihood analysis based on the microlensing rate, we study whether a viable solution to the MACHO puzzle can come from a significant contribution of a lens population belonging to the LMC halo.

5.4.1 The microlensing MACHO candidates

In the final analysis of 5.7 years of data in 30 fields towards the LMC, the MACHO group presented two sets of microlensing candidates, sets A and B, with 13 and 17 candidates, respectively, the former being a subsample of the latter [4].

Further works allowed more information to be gathered on some of these candidates. The lens for the event LMC-5 is located in the Galactic disc [7]. LMC-22 has been identified as a very likely supernova [2]. LMC-23 has been acknowledged as a probable variable star [20]. LMC-9 is a double–lens system with caustic crossing [4]. The microlensing candidates LMC-9, LMC-20, LMC-22, and LMC-27 only belong to set B. For most of the remaining events, a further photometric follow-up allowed confirmation of the microlensing origin of the flux variation [20].

We restrict the present analysis to a homogeneous set of Paczyński-like events, so we exclude

LMC-9. Furthermore, we do not include the Galactic disc lens population, so that we exclude LMC-5, as well as all those candidates whose microlensing origin has been put in doubt. Accordingly, in the following we consider a subset of 13 events taken from the original larger set B, from which we exclude the candidates LMC-5, LMC-9, LMC-22, and LMC-23. Furthermore, we have verified that our main conclusions would not change had we started from the smaller set of 11 events, a subsample of the original set A, just excluding the candidates LMC-5 and LMC-23.

5.4.2 Duration and position: a statistical analysis

As previously noted, the expected timescale distributions for microlensing events due to lenses either in the LMC or in the MW halo are almost independent of the position. This property allows us to carry on an analysis in which we compare the observed timescales to the predicted one for each population. In particular, we investigate whether it is possible to draw from such an analysis any conclusion on the relative fraction of the Galactic over the LMC dark matter halo events. Here we neglect the stellar lensing contributions.

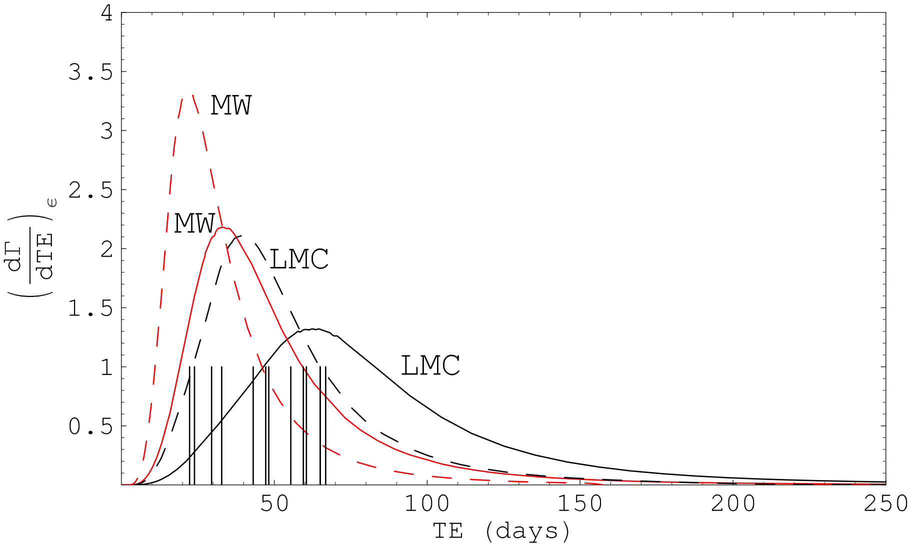

Figure 5.2: Normalised differential rate $(d\Gamma/dT_{\rm E})_\varepsilon$ for both MW and LMC halos for 0.2 and 0.5 $M_\odot$, dashed and solid lines, respectively. Superimposed is the value of the observed durations. The y-axis values are in 10^{-2} units.

For a given value of the MACHO mass, the expected LMC median timescales are larger than the MW ones [68]. We show in the same plot (Fig. 5.2) the normalised differential rate distribution for lenses in the LMC and the MW halo, corresponding to two values of the MACHO mass (0.2 and $0.5\,M_\odot$). Superimposed, the vertical lines indicate the Einstein time of the observed events. To investigate this issue further, we make use of the Kolmogorov-Smirnov test (hereafter KS). This allows us to test the null hypothesis that the events are drawn from a given population. The resulting KS coefficient gives the significance level of the test. In the first place, we apply the KS hypothesis test separately to the two populations of lenses in the MW and the LMC halo. Then we introduce a parameter α, defined as the ratio of the MW events over the total (MW plus LMC events), in order to explore the possibility that an intermediate solution, with the two populations mixed, has to be preferred. To this purpose we look for the value of α that minimises the corresponding KS coefficient.

To take the variations of the microlensing rate across the fields into account, mainly in the case of lenses in the LMC halo, we carry out the test on each of the MACHO fields separately. We

Table 5.2: Kolmogorov-Smirnov test results

lens mass ($M_\odot$)	ks_{MW}	ks_{LMC}	ks_α	α
0.01	1.000	1.000	1.000	0.000
0.10	0.999	0.683	0.683	0.000
0.15	0.994	0.159	0.085	0.095
0.20	0.984	0.450	0.118	0.347
0.22	0.969	0.655	0.144	0.471
0.30	0.877	0.957	0.240	0.703
0.40	0.579	0.997	0.228	0.871
0.50	0.176	1.000	0.176	1.000
0.60	0.398	1.000	0.398	1.000
0.80	0.743	1.000	0.743	1.000
1.00	0.911	1.000	0.911	1.000

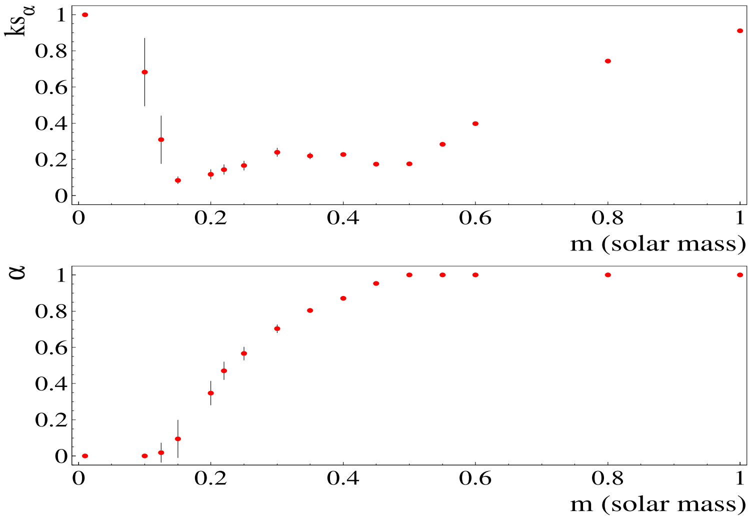

Figure 5.3: Kolmogorov-Smirnov and α coefficients as a function of the MACHO mass, with α the ratio of the MW over the total number of dark matter halo events.

then evaluate and report the value averaged on the 30 MACHO fields. The associated dispersion gives the error bars drawn in Fig. 5.3. In Table 5.2 and Fig. 5.3 we present the results of this analysis. We report the value of the parameter α and the KS coefficient in the three cases considered, ks_{MW}, ks_{LMC}, and ks_α, respectively, as a function of the MACHO mass. We report the results only in the range 0.01-1 $M_\odot$ where the preferred solution are found (see below).

When we consider the MW and the LMC halos separately, the solutions with the highest level of confidence are found for a MACHO mass of $\approx 0.5\ M_\odot$ and $\approx 0.15\ M_\odot$, respectively. This result is confirmed by the microlensing–rate–normalised distributions in Fig. 5.2, where the profile corresponding to the case of $0.5\,M_\odot$ MW lenses is almost coincident with that of $0.2\,M_\odot$ LMC lenses.

For the case of the combined populations, we find that the coefficient ks_α presents two minima near the two values of mass found in the previous case. The absolute minimum, which we note is lower than the values obtained in the case of the separate test analysis, is found at $m = 0.15\,M_\odot$ with $\alpha \sim 0.1$, and it gives us the parameters with the highest confidence level. Moreover we observe that the α parameter grows monotonically as a function of the mass from 0 up to 1 (Fig. 5.3).

We conclude that the statistical analysis made on the duration of the events gives a first suggestion that a significant fraction of the observed events could belong to the LMC MACHO halo population.

Next we consider the issue of the spatial distribution of the observed events [68]. The optical depth profiles clearly show that the LMC halo events are characterised, with respect to LMC self–lensing and to MW halo ones, by a strong asymmetry with respect to the line of nodes (Paper II). Looking at the expected number of events per field, this asymmetry is somewhat weakened but still present, because of the different source density as a function of the position. In order to get insight into the more complex two–dimensional situation we have to deal with, we show the normalised number of the expected events ($\tilde{N}_{\rm ev}$) in Fig. 5.4, for the different lens populations we consider, evaluated along the axis orthogonal to the line of nodes passing through the LMC centre (the ξ axis in the plot). $\tilde{N}_{\rm ev}$ has been calculated in the LMC centre and in six more positions, specularly symmetric two by two with respect to the centre. This plot shows clearly that the distribution in the case of self–lensing events is symmetric and, moreover, that outside the bar region it declines sharply. The profile for MW events presents a slight asymmetry with respect to the line of nodes, whereas that corresponding to LMC MACHO lenses have a pronounced asymmetric distribution.

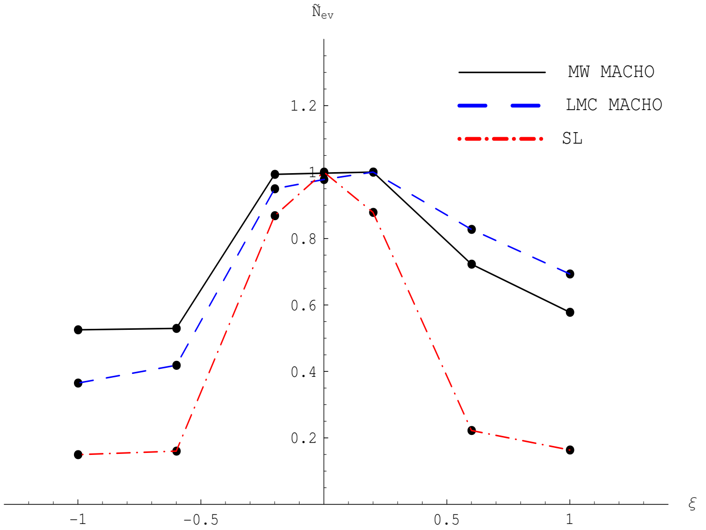

Figure 5.4: Normalised expected number profiles along the axis, pointing south–west, orthogonal to the line of nodes and passing through the LMC centre, for different lens populations: self lensing, dot dashed line; MW MACHO, solid line; LMC MACHO, dashed line. Values on the ξ axis are in kpc.

In Paper II we addressed the question of whether the observed asymmetrical distribution of the detected events, which goes indeed in the same sense predicted by a halo LMC population, really does reflect the observational strategy, mainly to argue against the self–lensing origin of the events. Here we take advantage of knowing the expected number of events for all the populations of interest to study this issue in more detail.

We take the line of nodes as the symmetry axis, and as in Paper II we bin the observed space in two regions, the north–east "near" and the south–west "far" ones (Fig. 5.5). We delimit them by two straight lines parallel to the line of nodes, each at a distance from the latter of $\approx 0.35\,$kpc, the 1 σ error in position as calculated by [140]. Note that this way the innermost LMC regions are excluded from the asymmetry analysis. Our purpose is to test the asymmetry with respect to the prediction of the different lens populations, assigning the probability p_i that a microlensing event would fall in the first or second region to be proportional to the expected number of events of the given population. As in Paper II we make use of the non-parametric Pearson test, which allows us to evaluate the probability to accept the null hypothesis that the p_i match the measured distribution, for which we get 1 and 7 observed events in the near and far regions, respectively. This analysis is carried out by normalising the number of expected events of each population to that of the observed

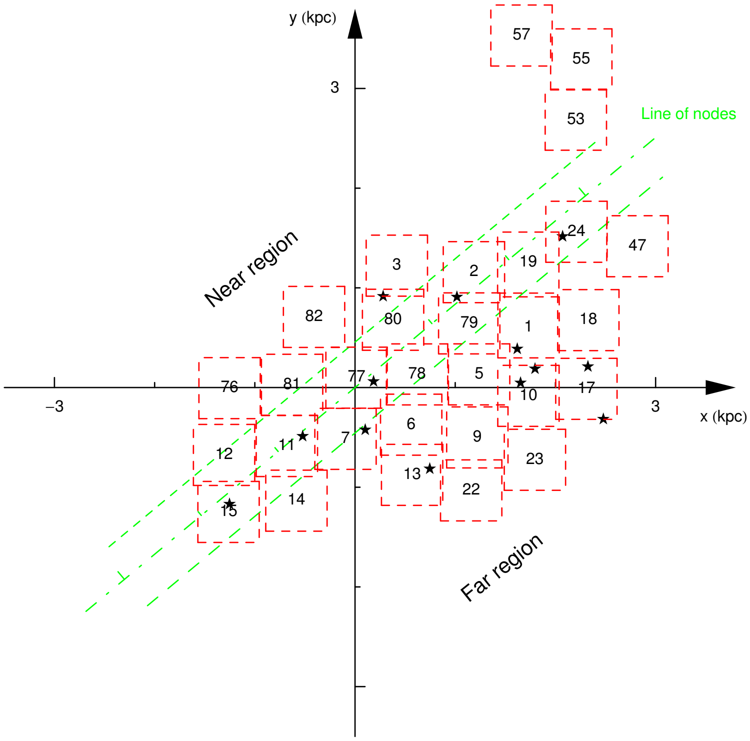

Figure 5.5: Location of the 30 MACHO fields in a reference frame centred in the LMC centre with the x-axis antiparallel to the right ascension, the y-axis parallel to the declination, and the z-axis (not shown) pointing towards the observer. The location of the 13 microlensing candidates, a subset of the original set B of MACHO candidates that we use in the present analysis (Sect. 5.4.1), is shown. Also shown is the position of the line of nodes and the central band around it, which we exclude in the asymmetry analysis.

events.

The result of this analysis gives us a probability of 46% and 26% for a MACHO LMC and MW halo lens population, respectively. This outcome makes the lack of a predominant lens population very clear. Indeed, the expected smoother spatial distribution of MW halo lenses is barely coherent with the observed distribution, thus challenging the explanation that attributes most of the events to this population. Rather, we find much better agreement with the expected asymmetric distribution of LMC halo events. Finally, we note that, contrary to the previous analysis based on the timescale distribution, this result turns out to be independent of the value of the MACHO mass. As a byproduct of the present analysis (confirming that carried out in Paper II), we note that the probability of accepting the hypothesis of a self–lensing origin on the basis of the observed spatial distribution turns out to be only 19%.

Both these analyses, carried out working on *normalised* distributions (i.e. independent of the actual halo fraction) indicate that a large fraction of the lenses could indeed belong to the LMC dark matter halo.

5.4.3 The Galaxy and the LMC: two different halo fractions?

The previous analysis has provided us with two important clues, both showing that a significant fraction of the events detected by the MACHO collaboration could be part of the LMC dark matter

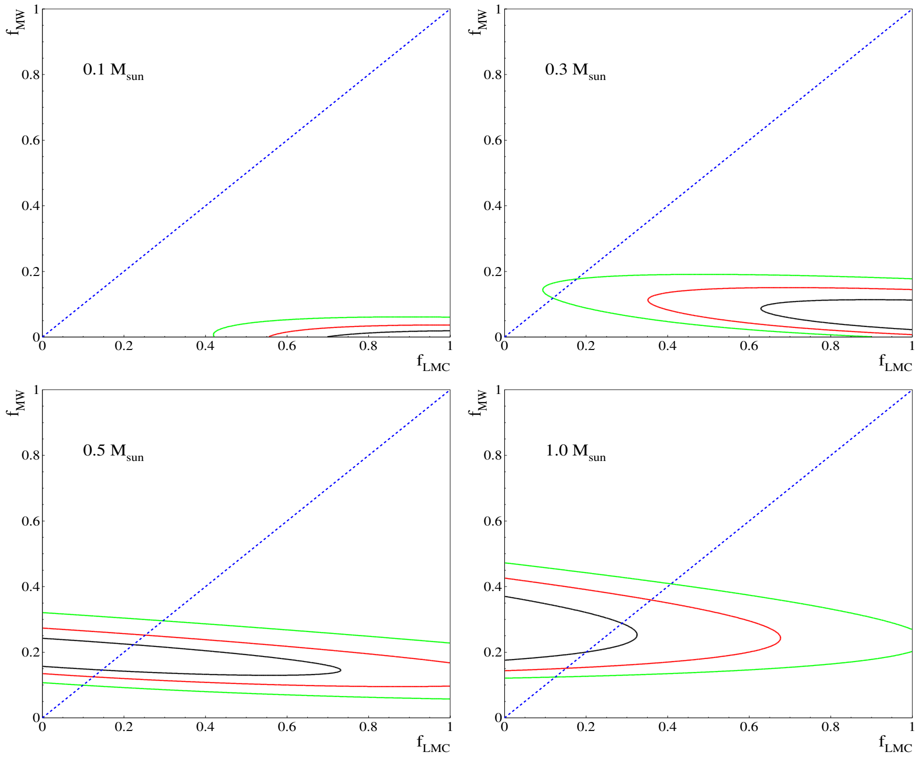

Figure 5.6: Probability isocontours with 34%, 68% and 90% regions for the LMC and MW dark matter halo fraction for four values of the MACHO mass.

halo. To reconcile this result with the predicted number of events (Table 5.1), we now drop the hypothesis of equal halo MACHO fractions in the Galactic and the LMC halo.

We start by evaluating the likelihood function

$$L\left(f_{\rm MW}, f_{\rm LMC}\right) = \\ \exp\left(-N_{exp}\right) \prod_{i=1}^{N_{obs}} \left[E\,\mathcal{E}(T_{E_i})\,\frac{d\Gamma}{dT_E}\;(T_{E_i})\right] , \qquad (5.7)$$

where $f_{\rm MW}$ and $f_{\rm LMC}$ are the halo fractions for the MW and the LMC, respectively. For both N_{exp}, the expected number of events, and the differential rate $\frac{d\Gamma}{dT_E}$, we sum over all the lens populations (including the stellar ones), multiplying the MACHO contributions for the appropriate halo fraction. The product runs over the N_{obs} observed events. By Bayesian inversion, using a flat prior probability, it is then possible to compute the probability distribution for the halo fractions given the observed events, $P\left(f_{\rm MW}, f_{\rm LMC}\right)$. Note that we are now taking the MACHO mass as a parameter, equal for both halo populations.

In Fig. 5.6 we show the 2-dimensional probability isocontour for the two halo fractions for four values of the MACHO mass. Eventually, after marginalisation over one variable with respect to the other, we get the results for the two halo fractions as a function of the MACHO mass shown in Fig. 5.7.

The main outcome of this analysis is that in a significant range of the MACHO mass, the LMC and MW dark matter halo fractions are *not* expected to be equal. In particular, from 0.1 up to 0.3 M$_\odot$, both a high value for $f_{\rm LMC}$ and a low one for $f_{\rm MW}$ are expected.

This behaviour is mainly due to the observed timescales. It is therefore not surprising that this

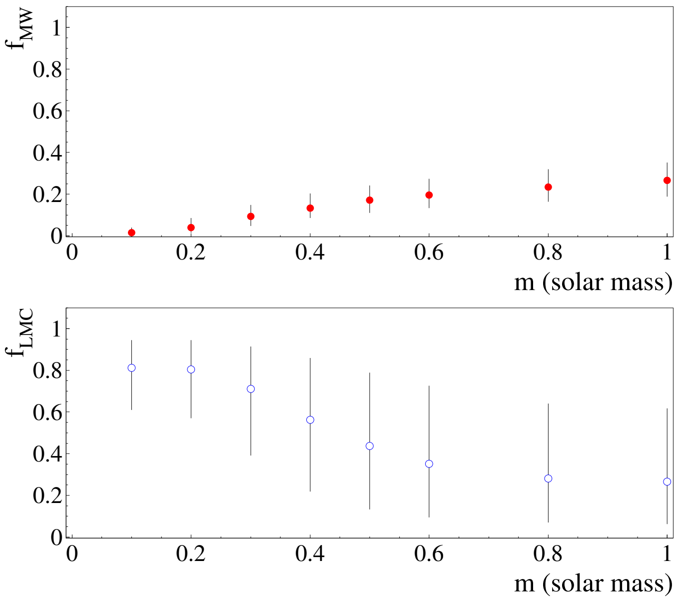

Figure 5.7: MW and LMC dark matter halo fraction, median value with 68% CL errors, as a function of the MACHO mass.

result is coherent with the one obtained with the KS test, where we found a preferred value of the mass of about $0.2\,\mathrm{M}_\odot$, with a significant expected contribution from LMC MACHO halo lenses. The likelihood analysis gives, for $m = 0.2\,\mathrm{M}_\odot$, $f_{\mathrm{MW}} \sim 4\%$ and $f_{\mathrm{LMC}} \sim 80\%$. At face value, given the number of expected events, we get to the overall prediction of about 6-7 events to be attributed to the LMC dark matter halo lens population, 2-3 to the MW halo one, to be looked for among those with the shorter durations, still allowing for a contribution of about 2-3 events, distributed among self–lensing and LMC stellar halo lenses.

For higher values of the mass, the LMC MACHO halo fraction turns out to be almost degenerate though compatible with zero, and, for 0.5 $\mathrm{M}_\odot$, we recover the result of a Galactic MACHO halo fraction of about 20% [4]. This is again coherent with the issue of the KS test.

We stress that the outcome of this analysis has to be looked at together with the outcomes of the previous analysis on the timescale and the spatial distributions of the observed events. Overall, they indicate that *i*) a sizeable fraction of the observed events show characteristics in accord with those expected for a MACHO LMC halo population; *ii*) such a contribution may be expected by dropping the hypothesis that the halo fractions in the form of MACHOs in the Galactic and the LMC dark matter halo are equal.

As a last point, we discuss the dependence of our results on the choice of the LMC dark matter halo parameters, the central density, and the truncation radius (Sect. 5.2). We find that any variation in the parameters in a reasonable range around their fiducial values does not change, at least qualitatively, our results. As for the central density, any variation downward (upward) is linearly related to a corresponding change in the total number of expected events. This implies a scaling upward (downward) for the halo fraction without affecting the main conclusion on the contribution of the LMC halo. As for the truncation radius (R_t), as a first approximation the situation is similar, as a lower (higher) value of R_t roughly give rises to a lower (higher) total LMC mass. However, the issue is slightly subtler. First, the problem is not symmetric with respect to the choice of our fiducial value, $R_t = 15$ kpc. Second, different choices for R_t enhance different spatial distributions for the number of expected events. In particular, *i*) the decrease in the number of expected events, for lower values of R_t than the fiducial value, is relatively larger than the increase obtained by choosing higher values; *ii*) the spatial asymmetry of MACHO LMC halo events is enhanced for a lower value of R_t. (Both effects are easily explained, as most of the lenses are expected to be located in the innermost LMC region.) We tested our results with 4 values of R_t, respectively lower (higher) of our fiducial value by 20% and 40%. The relative average decrease in the number of expected events for $R_t = 9$ and 12 kpc with respect to the $R_t = 15$ kpc case is $\sim$ 20% and 8.7%, whereas the relative increase for $R_t = 18$ and 21 kpc is $\sim$ 7.4% and 14%, respectively. As for the spatial distribution, we characterise the asymmetry by the relative difference between the number of expected events evaluated at the extremes of the ξ axis (as defined in Fig. 5.4) $\xi = 1$ kpc and $\xi = -1$ kpc. Where the fiducial case turns out to be of 47%, for $R_t = 9$ and 12 kpc we find a relative increase of 11% and 4%, and for $R_t = 18$ and 21 kpc a relative decrease of 2% and 6%, respectively. Overall, lower values of R_t strengthen our conclusions.

5.5 Conclusions

In this paper we have addressed the issue of the interpretation of the microlensing results towards the LMC. In particular, starting from the sample of microlensing candidates reported by the MACHO collaboration, we discussed the contingent contribution of a lens component belonging to the LMC dark matter halo besides that of the Galactic one. As a main result of the present analysis, we show that a sizeable fraction of the observed events, up to about half of the total, could indeed be part of the first component.

We summarise our analysis as follows. First, we compared the observed timescales with those expected for the two different MACHO populations, the MW and the LMC. As a result, we have shown that the preferred values for the MACHO mass are about 0.5 and 0.2 $\mathrm{M}_\odot$, respectively and, through a KS test, that the latter solution is preferred. Second, we studied the spatial distribution of the observed events, recalling that, because of the inclination of the LMC disc with respect to our line of sight, an asymmetry is expected for LMC halo events. As a result we have shown that, independent of the value of the MACHO mass, the observed distribution better matches that expected for a LMC halo population than for a MW halo population. Overall, these are clues suggesting the presence of a significant MACHO LMC halo population among the observed events.

The extremely high value of the overall Galactic halo mass compared to the LMC one implies that generally one can safely ignore the LMC halo component. To explain such a large contribution of the latter, one way out is to consider that the halo fractions in the form of MACHOs of the two components, the MW, and the LMC halos may be different. Coherently with the timescale analysis, this issue turns out to be strongly dependent on the value of the MACHO mass.

In order to get to more quantitative results, we tested this hypothesis through a likelihood analysis. Eventually we have shown that for a wide range of mass values a different (and larger) fraction for the LMC halo compared to the MW one is indeed expected. In particular, for a MACHO mass of $\sim 0.2\,\mathrm{M}_\odot$, we evaluated a high halo fraction for the LMC, $\sim$ 80%, together with a small one for the MW, $\leq 5\%$, thus implying that about half of the observed events should belong to the LMC dark matter halo. On the other hand, for MACHOs of $\sim 0.5\,\mathrm{M}_\odot$, we recovered the well–known result of a MW halo fraction $\sim$ 20% with a (possibly) negligible contribution from the LMC dark matter halo.

A possible explanation of the origin of different halo fractions could come from the different formation histories of the two galaxies, or more simply, could be related to the fact that one observes all the LMC halo but, practically, only a line of sight through the Galactic halo.

These conclusions should be taken *cum grano salis.* The overall implicit assumption is the validity of the MACHO results, whereas they are actually challenged by the EROS collaboration. Furthermore, an intrinsic limit for all the analyses carried out up to now is the result of the lack of available statistics. The SuperMACHO collaboration [16] is expected to provide a larger sample of candidates spread over a much larger field of view, and this should allow the problem to be constrained further. Eventually we stress that the model issue, in particular for the LMC components, is still a matter of

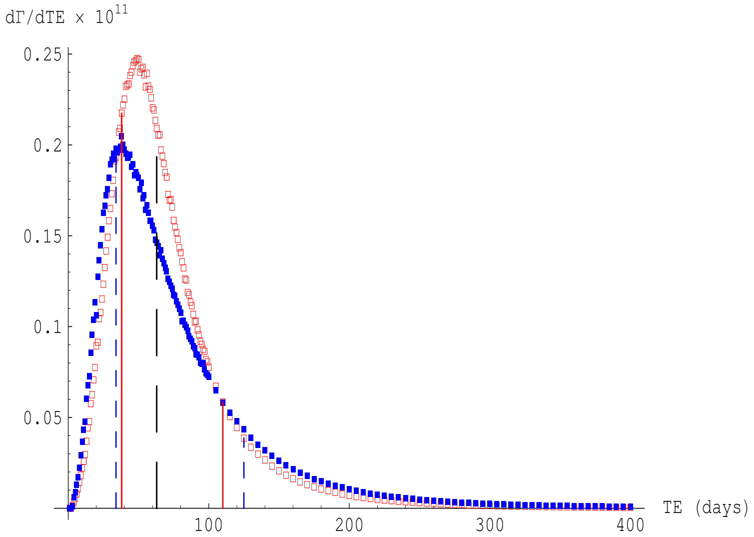

Figure 5.8: Self lensing event rate comparison. Empty red boxes: Dirac delta IMF, full blue boxes: Chabrier IMF. The model parameters are in both cases the ones given in sections 5.2-5.3. The blue short dashed (red solid) vertical lines show $T_{E,16\%} = 34(38)$ days and $T_{E,84\%} = 125(110)$ days for the Chabrier (Dirac delta) IMF. The long dashed line shows the median Einstein time, $T_{E,50\%}$, which is the same in both curves.

debate. Our analysis shows, however, that it is in principle possible to characterise and distinguish the two halo lens populations and, moreover, challenge the usual implicit assumption of equal halo fractions in the form of MACHO for both the Galactic and the LMC dark matter halos.

5.6 Further considerations

The shape of the microlensing event rate depends on the average mass $<\mu>$ of the lens population. In particular the average predicted Einstein time $< T_E > \propto < \mu >^{1/2}$ and the predicted number of events $N_{ev} \propto < \mu >^{-1/2}$ [49]. This relations are corroborated by the following results.
We have compared the self lensing microlensing event rate in a given direction as predicted for a *Chabrier* IMF [42]

$$\frac{dn}{d\mu} \propto \mu^{-3.3} e^{-(\frac{716.4}{\mu})^{\frac{1}{4}}}, \tag{5.8}$$

with a given average mass μ_{av} and a Dirac delta IMF centered on μ_{av}. Fig. 5.8 shows the results. The event rates have been calculated in the direction of the MACHO event 13 detected toward the LMC [5]. The model parameters are as given in this chapter. In order to perform a comparison, we have normalized the rate for the Chabrier IMF in the whole present day mass interval providing non detectable lenses, namely (0.08,1.5) $M_\odot$ as stated in section 5.3. In this mass interval $\mu_{av} = 0.327$. Even though the amplitudes and the peak position of the curves do not superimpose, the median Einstein times $T_{E,50\%}$ (shown as a vertical long dashed line in fig. 5.8) perfectly coincide and the ratio of the numbers of expected events in this direction is $N_{ev,delta}/N_{ev,Ch} = 1.1$. The average Einstein time, $< T_E >$, is 72 (76) days for the delta (Chabrier) IMF. With a Dirac delta IMF the event rate is somewhat narrower than for the Chabrier one (see the solid and short dashed lines of fig. 5.8) since the 68% of the total subtended area is spanned in the first case in the interval (38,110) days and in (34,125) days in the second case.

Chapter 6

Analytical Kerr black hole lensing in the weak deflection limit [1]

We present an analytical treatment of gravitational lensing by a Kerr black hole in the weak deflection limit. Lightlike geodesics are expanded as a Taylor series up to and including third-order terms in m/b and a/b, where m is the black hole mass, a the angular momentum and b the impact parameter of the light ray. Positions and magnifications of individual images are computed with a perturbative analysis. At this order, the degeneracy with the translated Schwarzschild lens is broken. The critical curve is still a circle displaced from the black hole position in the equatorial direction and the corresponding caustic is point-like. The degeneracy between the black hole spin and its inclination relative to the observer is broken through the angular coordinates of the perturbed images.

6.1 Introduction

The gravitational deviation suffered by photons passing near massive compact bodies provided one of the first observational tests of general relativity and is still considered as an excellent probe for gravity theories. Black hole lensing has been emerging as a pretty promising tool for gravitational investigations in both weak and strong fields. On the observational side, interest in this topic is mainly motivated by the super-massive black hole supposed to be hosted in the radio source Sgr A* in the Galactic center. Planned high-resolution observations at the astrometric resolution of the microarcosecond (μas) should allow in the next future a clean detection of higher order effects in gravitational lensing. It is now well understood that a photon passing near a black hole can suffer either a strong or a weak deflection. The latter occurs when the minimum distance is much larger than the gravitational radius. The former occurs when photons wind around the black hole making one or more loops and producing images very near to the shadow.

Analytical treatments have been worked out for generic spherically symmetric spacetimes, just assuming that the light ray follows the geodesic equations. The deflection angle always diverges logarithmically when the minimum impact parameter is in the very neighborhood of complete capture [27], whereas for larger distances and in the weak deflection limit a Taylor series expansion works pretty well [82]. Some investigations interpolating between the two limits have been also performed [10].

Whereas lensing by either Schwarzschild or generic spherically symmetric black holes has been extensively investigated, a full analytical description of lensing by a Kerr Black hole is still missing. An intrinsic angular momentum breaks the spherical symmetry heavily affecting the gravitational

---

[1] Published in [131]

field. The modern era in the study of Kerr geodesics came when Carter [41] was able to fully separate the Hamilton-Jacobi equation. Based on this technique of separation of variables, many later investigations addressed the light propagation near a rotating body [43] and numerical studies flourished. [45] considered the optical appearance of a point source in a circular orbit in the equatorial plane of an extreme Kerr black hole. [144] investigated the image positions through a code based on the quasi-analytic solution of the geodesic problem by elliptical integrals. [115] provided a detailed analysis of the optical structure of the primary caustic surface. The analytical extension of the strong deflection limit methodology to the Kerr black hole has been performed as well in the limit of small values of the angular momentum and for sources in the asymptotically flat region of the space-time [28, 31, 32]. A full description of caustics and the inversion of lens mapping for sources near them has been performed up to the second order in a.

Several analytical investigations in the weak deflection limit, considering the first correction due to the angular momentum, were performed in the past. The null tetrad formalism of geometrical optics was used to study the optical properties of images into the field of an axisymmetric system [112]. [58] performed a calculation based on the post-Newtonian expansion. The motion equations for two spinning point-like particles, when the spin and the mass of one of the particles were zero, were resolved in [79, 78] by expanding the Kerr metric in a power series of the gravitational constant G. [35] evaluated the equations of motion for a light ray in the weak deflection limit up to and including second order corrections in m/b e a/b, where m is the black hole mass, a the angular momentum and b is the impact parameter. [52] discussed the additional time-delay due to rotation by integrating the light geodesics. [66] considered light rays passing outside a spinning star in the framework of the Lense-Thirring metric. Kopeikin and collaborators [84, 85, 86] investigated the gravito-magnetic effects in the propagation of light in the field of self-gravitating spinning bodies. [12] considered the light deflection angle caused by an extended, slowly rotating lens. These analyses where then extended to generic spinning mass distributions, in the usual framework of gravitational lensing theory [125, 128, 126, 127, 129, 130], i.e. *i)* weak field and slow motion approximation for the lens and *ii)* thin lens hypothesis. Expressions for bending and time delay of electromagnetic waves were found for stationary rotating deflectors with general mass distributions.

At second order in m/b and a/b, the Kerr lens is observationally equivalent to the Schwarzschild one because of the invariance under the global translation of the center of the lens mass [12]. In this paper we take a step forward and study the lensing up to the next order. Following [35], we start from the lightlike null geodesics and then move to the gravitational lensing for a configuration in which both source and observer lie in the asymptotically flat region of the spacetime. We take care of expressing the results in terms of the invariants of the light ray, avoiding ambiguities connected to coordinate-dependent quantities [82, 23].

The paper is organized as follows. In Section 6.2, we introduce our notation and recall some properties of the Kerr spacetime. In Section 6.3, the lens equations in the weak deflection limit are derived starting from the geodesics. Section 6.4 is devoted to the solution of the lens equations with a perturbative method. Sections 6.5 and 6.6 discuss the magnification of the images and the singularity of the lens mapping, respectively. Section 6.7 is devoted to some considerations. Finally, sections 6.8 and 6.9 report some details on the evaluation of the integrals appearing in the geodesic equations. In this paper, we will use units $G = c = 1$, with c the light speed in the vacuum.

6.2 Basics

The Kerr black hole metric in the Boyer-Lindquist coordinates, $\{t, r, \vartheta, \phi\}$, is given by

$$ds^2 = \left(1 - \frac{r_{Sch} r}{\rho^2}\right) dt^2 - \frac{\rho^2}{\Delta} dr^2 - \rho^2 d\vartheta^2 - \left(r^2 + a^2 + \frac{a^2 r_{Sch} r \sin^2\vartheta}{\rho^2}\right) \sin^2\vartheta d\phi^2 + \frac{a r_{Sch} r \sin^2\vartheta}{\rho^2} dt d\phi, \tag{6.1}$$

where

$$\rho^2 \equiv r^2 + a^2 \cos^2\vartheta, \tag{6.2}$$

$$\Delta \equiv r^2 + r_{Sch} r + a^2. \tag{6.3}$$

The constant $r_{Sch} = 2m$ is the gravitational radius. We consider a static observer and a static emitter in the asymptotically flat region of the spacetime, $r \gg r_{Sch}$. The observer coordinates are denoted $\{r_o, \vartheta_o, \phi_o = 0\}$, where ϕ_o has been fixed without loss of generality. The source coordinates are denoted as $\{r_s, \vartheta_s, \phi_s\}$. In what follows, we will also use the modified polar coordinate $\mu \equiv \cos\vartheta$. The null geodesics for a light ray can be expressed in terms of the first integrals of motion J and Q [41, 43]. The photon trajectory from the source to the observer can then be written as

$$\pm \int \frac{dr}{\sqrt{R}} = \pm \int \frac{d\vartheta}{\sqrt{\Theta}}, \tag{6.4}$$

$$-\phi_s = \int \frac{a\,(r_{Sch} r - aJ)}{\pm \Delta \sqrt{R}} dr + \int \frac{J d\vartheta}{\pm \sin^2\vartheta \sqrt{\Theta}}, \tag{6.5}$$

where

$$R(r) \equiv r^4 + \left(a^2 - J^2 - Q\right) r^2 + \left[(J-a)^2 + Q\right] r_{Sch} r - a^2 Q, \tag{6.6}$$

$$\Theta(\vartheta) \equiv \left(a^2 - J^2 \csc^2\vartheta\right) \cos^2\vartheta + Q. \tag{6.7}$$

The signs of $\sqrt{R}$ and $\sqrt{\Theta}$ are adhered to the signs of dr and $d\vartheta$, respectively. The signs change at the inversion points in the r or ϑ-motion. We consider the standard framework of gravitational lensing, where the source of radiation and the observer are remote from the lens. In such a configuration the equatorial plane is crossed at least once, so that the range $Q < 0$ is excluded in our analysis.

Along his path from the source to the observer, the photon passes by the black hole at a minimum distance r_{min} which, in the weak deflection limit, is much larger than the gravitational radius. This distance of closest approach is the only turning point in the r-motion. Differently from the strong deflection limit, when the photon may perform several oscillations around the equatorial plane, in the weak deflection limit there is just one inversion point also in the angular polar motion. ϑ can attain either a maximum or a minimum depending on the direction taken by the photon starting from ϑ_s. If ϑ is initially growing (μ decreasing), the polar motion will attain a maximum ϑ_{max} (a minimum μ) and then it will decrease to get to the observer at ϑ_o (μ increases to get to μ_o), otherwise for an initially decreasing ϑ.

The light ray minimum radial distance r_{min} to the lens is determined by $R(r) = 0$, whose roots represent inversion points in the radial motion. In general, there can be up to four real roots with r_{min} being the largest one. In the weak deflection limit, there is just one inversion point at a distance of order of the impact parameter [35]. The impact parameter is an invariant of motion defined geometrically by the perpendicular distance from the center of the lens to the asymptotic tangent line to the light ray at the observer. For the spherically symmetric case it reduces to $\sqrt{J^2 + Q}$. A fundamental assumption in the weak deflection limit is that the point of closest approach lies well outside the gravitational radius, i.e. $r_{Sch} \ll \sqrt{J^2 + Q}$. Let us now introduce two independent expansion parameters in terms of the invariants of motion

$$\epsilon_m = \frac{m}{\sqrt{J^2 + Q}}, \tag{6.8}$$

$$\epsilon_a = \frac{a}{\sqrt{J^2 + Q}}. \tag{6.9}$$

In what follows, we will expand quantities of interest in both ϵ_m and ϵ_a. For the sake of brevity, we will refer to terms of order $\mathcal{O}(\epsilon_m^i \epsilon_a^j)$ as terms of order $\mathcal{O}(\epsilon^n)$ with $n = i + j$. We will produce our results up to a given formal order in ϵ, collecting terms of a given order in ϵ coming from any combination of the two quantities ϵ_a and ϵ_m. We recall how terms like $\mathcal{O}(a\ m)$ or $\mathcal{O}(m^2)$, which according to our notation are both of formal order $\sim \epsilon^2$, are not necessarily of the same physical order. This is the case only for a maximal (or nearly maximal) Kerr black hole, when $|a| \sim m$.

Let us find the minimum radial distance in the weak deflection limit. We can solve the equation $R(r_{min}) = 0$ expressing r_{min} as a power series in ϵ. We then find

$$r_{min} \simeq (J^2 + Q)^{1/2} \left\{ 1 - \frac{r_{Sch}}{2\sqrt{J^2 + Q}} - \frac{a^2 J^2}{2\,(J^2 + Q)^2} + \frac{a r_{Sch} J}{(J^2 + Q)^{3/2}} - \frac{3 r_{Sch}^2}{8\,(J^2 + Q)} \right. \tag{6.10}$$

$$
\begin{aligned}
- & \frac{r_{Sch}^3}{2\left(J^2+Q\right)^{3/2}} + \frac{3aJr_{Sch}^2}{2\left(J^2+Q\right)^2} - \frac{J^2a^2r_{Sch}}{\left(J^2+Q\right)^{5/2}} - \frac{J^2(J^2-4Q)a^4}{8\left(J^2+Q\right)^4} \\
+ & \left. \frac{J\left(J^2-Q\right)r_{Sch}a^3}{\left(J^2+Q\right)^{7/2}} + \frac{\left(8Q-51J^2\right)r_{Sch}^2a^2}{16\left(J^2+Q\right)^3} + \frac{3Jr_{Sch}^3a}{\left(J^2+Q\right)^{5/2}} - \frac{105r_{Sch}^4}{128\left(J^2+Q\right)^2} + \mathcal{O}(\epsilon^5) \right\} .
\end{aligned}
$$

An expression for the minimum approach including terms $\mathcal{O}(\epsilon^3)$ can be found in [35]. Eq. (6.10) for the spherical symmetric case ($a=0$) agrees with the result in [82]. The observer and the source lie very far from the lens in the asymptotically flat region of the spacetime. It can be shown that $b/r_o \sim b/r_s \sim \epsilon_m$ [82]. This scaling relation will be useful when collecting terms r_{min}/r_o and r_{min}/r_s in the integrals. In what follows, without loss of generality, we will consider non negative values of the spin a.

6.3 Lens equations

The geodesic equations, Eqs. (6.4, 6.5) will provide the lens equations. They can be viewed as a map between the angular position of the source, $\{\mu_s, \phi_s\}$, and the image position, which is a function of the couple of invariants $\{J, Q\}$. Details on the resolution of the radial and angular integrals in the weak deflection limit are given in sections 6.8 and 6.9, respectively. Following [35], we can recast the geodesic equation in a quite compact form. The first equation, Eq. (6.4), provides a description of the polar motion. It can be written as

$$
\mu_s = -\mu_o \cos\delta + (-1)^k \sin\delta \left(\frac{Q}{J^2+Q} - \mu_o^2 \right)^{1/2} , \tag{6.11}
$$

where

$$
\begin{aligned}
\delta \ = \ & \frac{2r_{Sch}}{\sqrt{J^2+Q}} + \frac{15\pi r_{Sch}^2}{16\left(J^2+Q\right)} - \frac{4Jr_{Sch}a}{\left(J^2+Q\right)^{3/2}} \\
+ \ & \frac{16r_{Sch}^3}{3\left(J^2+Q\right)^{3/2}} - \frac{15\pi Jar_{Sch}^2}{4\left(J^2+Q\right)^2} + \left(\mu_o^2 + \frac{5J^2-3Q}{J^2+Q} + \frac{Q}{\frac{J^2\mu_o^2}{\mu_o^2-1}+Q} \right) \frac{r_{Sch}a^2}{(J^2+Q)^{3/2}} \\
- \ & (J^2+Q)^{1/2}\frac{r_o+r_s}{r_or_s} - \frac{(J^2+Q)^{3/2}}{6}\frac{r_o^3+r_s^3}{r_o^3r_s^3} + \frac{\sqrt{J^2+Q}\mu_o^2\left(1-\mu_o^2\right)}{2\left(J^2\mu_o^2-Q\left(1-\mu_o^2\right)\right)}\frac{r_o+r_s}{r_or_s}a^2 + \mathcal{O}(\epsilon^4).
\end{aligned} \tag{6.12}
$$

Up to terms $\sim \epsilon^2$, δ was already evaluated in [35]. For a null angular momentum ($a=0$) and for very distant source and observer, $r_o, r_s \to \infty$, the parameter δ reduces to the deflection angle induced by the Schwarzschild black hole [82]. The parameter k in Eq. (6.11) accounts for the direction in the polar motion of the photon at the observer. k is even (odd) if ϑ attains ϑ_{max} (ϑ_{min}), i.e for photons coming from below (above) the black hole.

The second geodesic equation, Eq. (6.5), accounts for the azimuthal motion. Using Eq. (6.11), we can write

$$
-\phi_s = \frac{J}{|J|}\pi + \frac{J\delta}{\sqrt{J^2+Q}}\frac{1}{1-\mu_o^2}\left[1-(-1)^k\delta\frac{\mu_o}{\sqrt{1-\mu_o^2}}\sqrt{\frac{Q}{J^2+Q}-\mu_o^2}\right] + \frac{2ar_{Sch}}{J^2+Q} + \delta\phi_s, \tag{6.13}
$$

where $\delta\phi_s$ is a contribution of order $\sim \epsilon^3$,

$$
\begin{aligned}
\delta\phi_s \ \equiv \ & -\frac{8Jr_{Sch}^3\left(2\left(J^2+Q\right)\mu_o^4+\left(2J^2-Q\right)\mu_o^2-Q\right)}{3\left(J^2+Q\right)^3\left(1-\mu_o^2\right)^3} - \left(\frac{Q}{Q-\left(J^2+Q\right)\mu_o^2}+3\right)\frac{Jr_{Sch}a^2}{(J^2+Q)^2} \\
- \ & \frac{a^2J\mu_o^2}{2\left(J^2\mu_o^2-Q\left(1-\mu_o^2\right)\right)}\frac{r_o+r_s}{r_or_s} + \frac{5\pi r_{Sch}^2a}{4\left(J^2+Q\right)^{3/2}} \qquad (6.14) \\
+ \ & \frac{J\left(2J^2\mu_o^2\left(\mu_o^2+1\right)-Q\left(-2\mu_o^4+\mu_o^2+1\right)\right)}{\left(J^2+Q\right)\left(1-\mu_o^2\right)^3}\left[\frac{1}{3}\left(J^2+Q\right)\frac{\left(r_o+r_s\right)^2}{r_o^2r_s^2}\right.
\end{aligned}
$$

$$- \quad \frac{2\left(r_o+r_s\right) r_{Sch}}{r_o r_s}+\frac{4 r_{Sch}^2}{J^2+Q}\Bigg] \frac{r_o+r_s}{r_o r_s}.$$

Up to including terms of order of $\mathcal{O}(\epsilon^2)$, Eqs. (6.13, 6.14) have been already evaluated in [35].

The lens equation are usually given in terms of the apparent angular position of the image onto the plane of the sky (POS), i.e. the coordinate angles $\{\theta_1, \theta_2\}$, and of the angular position of the source in absence of the lens, $\{B_1, B_2\}$. In the asymptotic flat region, the Boyer-Lindquist coordinates can be thought as spherical coordinates. We can introduce a Cartesian observer coordinate system centered on the black hole, with the x_3-axis running along the line of sight (LOS), i.e. the line from the observer to the lens, and the x_2-axis tracing the projection of the spin axis onto the POS. Then, θ_1 and θ_2 are measured along the x_1- and the x_2-axis, respectively. In other words, $r_o \tan\theta_1$ and $r_o \tan\theta_2$ are the apparent (length-)displacement of the image perpendicular to the projected axis of symmetry of the black hole and the apparent (length-)displacement perpendicular to the equatorial plane in the sense of the angular momentum of the black hole, respectively. The angles $\{\theta_1, \theta_2\}$ are strictly linked to the invariants of motion and to the impact parameter through the relations

$$r_o \frac{\tan\theta_1}{\sqrt{1+\tan^2\theta}} = -\frac{J}{\sqrt{1-\mu_o^2}} \tag{6.15}$$

$$r_o \frac{\tan\theta_2}{\sqrt{1+\tan^2\theta}} = -(-1)^k \sqrt{Q+a^2\mu_o^2-J^2\frac{\mu_o^2}{1-\mu_o^2}}, \tag{6.16}$$

with θ being the angular separation of the image from the black hole, $\tan^2\theta = \tan^2\theta_1 + \tan^2\theta_2$. The parameter k can be expressed in terms of θ_2 as

$$(-1)^k = -\frac{\theta_2}{|\theta_2|}. \tag{6.17}$$

Equations (6.15, 6.16) can be obtained by defining the tangent to the ray at the observer through the equations of motion of the photon. Photons are named prograde (retrograde) if they turn on the equatorial plane in the same (opposite) sense of the black hole. Prograde photons ($J > 0, Q = 0$) are seen by the observer on the left side of the black hole ($\theta_1 < 0$). The relation between the angular position of the image and the impact parameter for a spherically symmetric lens, $b = \sqrt{J^2+Q} = r_o \sin\theta$, can be easily recovered from Eqs. (6.15, 6.16)

The angular position of the source $\{B_1, B_2\}$ can be expressed in terms of the Boyer-Lindquist coordinates. Considering the intercept of the line through the source and the observer with the POS, we find

$$D_s \tan B_1 = \sin\phi_s r_s \sqrt{1-\mu_s^2}, \tag{6.18}$$

$$D_s \tan B_2 = r_s \left(\mu_s\sqrt{1-\mu_o^2} - \mu_o\sqrt{1-\mu_s^2}\cos\phi_s\right), \tag{6.19}$$

where D_s is the distance along the LOS from the observer to the plane of the source, i.e. the plane through the source and perpendicular to the LOS. The relations between the radial coordinates and the distances measured along the LOS are

$$D_d = r_o, \tag{6.20}$$

$$D_{ds} = -r_s\left(\mu_o\mu_s + \cos\phi_s\sqrt{(1-\mu_o^2)(1-\mu_s^2)}\right), \tag{6.21}$$

$$D_s = D_d + D_{ds}. \tag{6.22}$$

D_{ds} is the distance along the LOS between the lens plane and the source plane. The D_i distances must be properly intended as angular diameter distances. The relations in Eqs. (6.15, 6.16) and Eqs. (6.18, 6.19) allows us to put the geodesics, Eqs. (6.11, 6.13), in the classical form of the lens mapping

$$B_1 = B_1(\theta_1, \theta_2), \tag{6.23}$$

$$B_2 = B_2(\theta_1, \theta_2). \tag{6.24}$$

Once we use angular coordinates for the image positions instead on the invariants of motion, it can be appropriate to introduce a series expansion parameter in the weak deflection limit based on the angular Einstein ring,

$$\theta_E \equiv \sqrt{2 r_{Sch} \frac{r_s}{r_o (r_o + r_s)}}. \tag{6.25}$$

Following [82], we define

$$\varepsilon \equiv \frac{\theta_E}{4D}, \tag{6.26}$$

where $D \equiv r_s/(r_o + r_s)$. We remark as differently from usual analyses in the weak deflection limit, we are adopting radial distances in the definition of the Einstein radius instead of the distances measured along the LOS. Differences are of order of ε^3. Angles can be rescaled in terms of θ_E. We then assume that the solution of the lens equations can be written as a series in ε,

$$\begin{aligned}
\theta_1 &= \theta_E \left\{ \theta_{1(0)} + \theta_{1(1)} \varepsilon + \theta_{1(2)} \varepsilon^2 + \mathcal{O}(\varepsilon^3) \right\}, && (6.27)\\
\theta_2 &= \theta_E \left\{ \theta_{2(0)} + \theta_{2(1)} \varepsilon + \theta_{2(2)} \varepsilon^2 + \mathcal{O}(\varepsilon^3) \right\}, && (6.28)\\
\theta &= \theta_E \left\{ \theta_{(0)} + \theta_{(1)} \varepsilon + \theta_{(2)} \varepsilon^2 + \mathcal{O}(\varepsilon^3) \right\}. && (6.29)
\end{aligned}$$

The above expressions must be read with the same caveats we discussed about the parameter ϵ after introducing the proper expansion parameters ϵ_m and ϵ_a in Eqs. (6.8, 6.9). As a matter of fact, a coefficient of the form $\theta_{(i)}$ will be written as a polynomial of i-th order in a/m, collecting terms which are not necessarily of the same order.

The source position can be rescaled defining

$$\beta_i \equiv \frac{\tan B_i}{\theta_E}. \tag{6.30}$$

Including terms up to $\sim \varepsilon^2$, the lens equations take the very simple form

$$\begin{aligned}
B_1 &= \theta_1 - D \hat{\alpha}_1(\theta_1, \theta_2), && (6.31)\\
B_2 &= \theta_2 - D \hat{\alpha}_2(\theta_1, \theta_2), && (6.32)
\end{aligned}$$

where $\hat{\alpha}$ is the bending angle, defined as the angle between the asymptotic direction of the light ray at the observer and the asymptotic direction at the emitter. At order $\sim \varepsilon^3$, equations become more complicated. The deflection angle is an invariant of motion and can be expressed in terms of the constants J and Q together with the mass and the spin of the black hole. On the other hand, by its own definition, it does not depend on the source and observer positions once they lie in the very asymptotic region of spacetime. The source position can then be directly related to the deflection angle considering source and observer at an infinite distance. This allows us to neglect higher order contributions to the path of the light ray near the black hole. The two components of the deflection angle can then be evaluated considering the geodesics for source and observer Eqs. (6.11, 6.12) at $r_o, r_s \to \infty$, through the equation

$$\tan B_i(\mu_s(r_o, r_s \to \infty), \phi_s(r_o, r_s \to \infty)) = -\frac{D_{ds}}{D_s} \tan \hat{\alpha}_i. \tag{6.33}$$

It is simple to verify that for an equatorial motion, $\mu_s = \mu_o = 0$, Eq. (6.33) reduces to the well known $\hat{\alpha} = \Delta\phi - \pi$. For the Kerr black hole, we get

$$\begin{aligned}
\hat{\alpha}_1 &= 2 \frac{r_{Sch}}{b} \frac{b_1}{b} + \frac{15\pi}{16} \left(\frac{r_{Sch}}{b} \right)^2 \frac{b_1}{b} - \frac{2 \left(b_2^2 - b_1^2 \right) r_{Sch} a \sqrt{1 - \mu_o^2}}{b^4} && (6.34)\\
&+ 8 \left[1 - \frac{1}{3} \left(\frac{b_1}{b} \right)^2 \right] \left(\frac{r_{Sch}}{b} \right)^3 \frac{b_1}{b} - \left[\frac{2 \left(b_2^2 - b_1^2 \right) \left(1 - \mu_o^2 \right)}{b^2} + 1 \right] \frac{a^2 r_{Sch}}{b^3} \frac{b_1}{b} \\
&- \left[\frac{5\pi \sqrt{1 - \mu_o^2} \left(b_2^2 - 2 b_1^2 \right)}{4 b^2} - \frac{4 b_2 \mu_o}{b} \right] \frac{a r_{Sch}^2}{b^3} + \mathcal{O}(\epsilon^4), \\
\hat{\alpha}_2 &= 2 \frac{r_{Sch}}{b} \frac{b_2}{b} + \frac{15\pi}{16} \left(\frac{r_{Sch}}{b} \right)^2 \frac{b_2}{b} + \frac{4 b_1 b_2 a r_{Sch} \sqrt{1 - \mu_o^2}}{b^4} + && (6.35)
\end{aligned}$$

$$
\begin{aligned}
&+ \quad 8\left[1-\frac{b_2^2}{3b^2}\right]\left(\frac{r_{Sch}}{b}\right)^3\frac{b_2}{b},+\left(\frac{15\pi b_1 b_2\sqrt{1-\mu_o^2}}{4b^2}-\frac{4b_1\mu_o}{b}\right)\frac{a r_{Sch}^2}{b^3} \\
&+ \quad \left[\left(\frac{b_2}{b}\right)^2\left(\left(\frac{b_1}{b_2}\right)^2-1\right)^2\mu_o^2-2\frac{b_1^2(3-2\mu_o^2)-2b_2^2}{b^2}\right]\frac{a^2 r_{Sch}}{b^3}\frac{b_2}{b}+\mathcal{O}(\epsilon^4),
\end{aligned}
$$

where inspired by Eqs. (6.15, 6.16) we have introduced the parameters

$$
\begin{aligned}
b_1 &\equiv -\frac{J}{\sqrt{1-\mu_o^2}} && (6.36)\\
b_2 &\equiv -(-1)^k\sqrt{Q-J^2\frac{\mu_o^2}{1-\mu_o^2}}, && (6.37)
\end{aligned}
$$

and $b=\sqrt{b1^2+b_2^2}=\sqrt{J^2+Q}$. For the spherically symmetric Schwarzschild black hole, Eqs. (6.35,6.36) agree with the result in [82]. The spin enters in the deflection angle only if coupled with the mass. A first attempt to evaluate the term proportional to m^2a in the deflection angle was already performed in [13]. We remark as in the derivation in [13], some higher order geometrical terms are neglected or, in other words, angles are identified with their tangents. This can affect the relation between the impact parameter and the distance of closest approach. The discussion of the equatorial motion, $b_2=0, \mu_o=0$ is enough to understand some features of how the spin affects the deflection angle. We have

$$
\hat{\alpha}_1=2\frac{r_{Sch}}{b}\frac{b_1}{b}+\frac{15\pi}{16}\left(\frac{r_{Sch}}{b}\right)^2\frac{b_1}{b}+2\frac{a r_{Sch}}{b^2}+\frac{16}{3}\left(\frac{r_{Sch}}{b}\right)^3\frac{b_1}{b}+\frac{a^2 r_{Sch}}{b^3}\frac{b_1}{b}+\frac{5\pi}{2}\frac{a r_{Sch}^2}{b^3}+\mathcal{O}(\epsilon^4). \quad (6.38)
$$

Whereas the gravito-electric field is always attractive, the gravito-magnetic field attracts towards the black hole only photons which move in the equatorial plane in the opposite sense of the spinning lens ($b_1>0$) . Terms directly proportional to the angular momentum a are strictly related to the dragging of inertial frames and then act differentially on opposite sides of the hole. The deflection angle is enhanced for retrograde photons ($b_1>0$) and reduced for prograde photons ($b_1<0$). The term proportional to a^2 is instead related to the quadrupolar distortion caused by the black hole spin [115]. It just perturbs the spherical symmetry of the system but it does not act differentially.

To give some numerical estimates, let us consider Sgr A* in the Galactic center, at nearly 8 Kpc from the Sun, which should host a supermassive black hole with mass $\sim 3.6\times10^6 M_\odot$ [17]. The minimum distance of orbiting stars from the central black hole is 100 AU, nearly 1500 times greater than the Schwarzschild radius, so that such sources can be considered in the asymptotic region of the spacetime. The Einstein radius corresponding to such a configuration is ~ 0.5 $m$as, i.e nearly 4 AU ($\sim 50\ r_{Sch}$) at the distance of Sgr A*. Let us consider a light ray in the equatorial plane with an impact parameter of $\sim 50\ r_{Sch}$. The total deflection angle is $\sim 4\times10^{-2}$ radians, so that the weak deflection limit still holds. The size of the contribution to the deflection due to the dragging term $\propto a\ m$ ($\propto a\ m^2$) is $\sim 80(a/m)$ as ($6(a/m)$ as). The contribution of the term $\propto a^2 m$ is $\sim 0.8(a/m)^2$ as. We see that corrections are sizeable even for low values of the angular momentum.

6.4 Image positions

Lens equations can be solved term by term. At the first order in the deflection angle, Kerr lensing is pure Schwarzschild lensing. The lens equations take the standard form

$$
\begin{aligned}
\beta_1 &= \theta_{1(0)}\left(1-\frac{1}{\theta_{(0)}^2}\right), && (6.39)\\
\beta_2 &= \theta_{2(0)}\left(1-\frac{1}{\theta_{(0)}^2}\right), && (6.40)
\end{aligned}
$$

where $\theta_{(0)} = \sqrt{\theta_{1(0)}^2 + \theta_{2(0)}^2}$, with the usual solutions

$$\begin{aligned} \theta_{1(0)}^{\pm} &= \frac{1}{2}\left(1 \pm \sqrt{1 + \frac{4}{\beta^2}}\right)\beta_1, && (6.41) \\ \theta_{2(0)}^{\pm} &= \frac{1}{2}\left(1 \pm \sqrt{1 + \frac{4}{\beta^2}}\right)\beta_2, && (6.42) \end{aligned}$$

with $\beta^2 \equiv \beta_1^2 + \beta_2^2$. The first contribution of the angular momentum appears at the next order in ε.

The second order terms of the solution read

$$\begin{aligned} \theta_{1(1)} &= \theta_{(1)}^{Sch}\frac{\theta_{1(0)}}{\theta_{(0)}} + \frac{(1 - \theta_{1(0)}^2 + \theta_{2(0)}^2)a_m\sqrt{1 - \mu_o^2}}{1 - \theta_{(0)}^4}, && (6.43) \\ \theta_{2(1)} &= \theta_{(1)}^{Sch}\frac{\theta_{2(0)}}{\theta_{(0)}} - \frac{2\theta_{1(0)}\theta_{2(0)}a_m\sqrt{1 - \mu_o^2}}{1 - \theta_{(0)}^4}, && (6.44) \end{aligned}$$

where $a_m \equiv a/m$ and with

$$\theta_{(1)}^{Sch} = \frac{15\pi}{16(1 + \theta_{(0)}^2)}. \tag{6.45}$$

At this order there is a full degeneracy between a Kerr black hole and a Schwarzschild black hole displaced from the center along the equatorial plane in $\{\theta_1, \theta_2\} \simeq \theta_E\{a\sqrt{1 - \mu_o^2}\varepsilon, 0\}$. The lens equations are degenerate as well with those of a binary point-like lens with very short separation. Then, at this order, the line joining the perturbed images always goes through the 'shifted' Schwarzschild lens. What happens in the POS is that, due to a positive angular momentum, the two images are apparently counterclockwisely rotated about the line of sight through the centre with respect to the line passing through the near unperturbed image produced in the Schwarzschild case [126].

Suppose a source at a distance $r_s \sim 10$ pc beyond the supermassive black hole in the Galactic center and an Earth-based observer. Then $\theta_E \sim 0.07(r_s/10\,pc)^{1/2}$ as and $\varepsilon \sim 0.76 \times 10^{-4}(r_s/10\,pc)^{-1/2}$. The shift to the image positions due to the dragging of inertial frames turns out to be of order of $\sim 4(a/m)\mu$as, at the reach of future astrometric missions.

Equations at the third order become quite long, but solutions can be still put in a compact form. We have

$$\begin{aligned} \theta_{1(2)} &= \theta_{(2)}^{Sch}\frac{\theta_{1(0)}}{\theta_{(0)}} + \frac{16D^2}{3}\theta_{1(0)}\theta_{2(0)}^2 + a_m\left\{-\frac{4\theta_{2(0)}\mu_o}{\theta_{(0)}^2}\right\} && (6.46) \\ &+ a_m\left\{\frac{5\sqrt{1 - \mu_o^2}\pi}{16\theta_{(0)}^3(1 - \theta_{(0)}^2)(1 + \theta_{(0)}^2)^3}\left[\theta_{(0)}^2(1 + \theta_{(0)}^2)^2(1 + 4\theta_{(0)}^2) - (12\theta_{(0)}^6 + 5\theta_{(0)}^4 + 4\theta_{(0)}^2 - 1)\theta_{1(0)}^2\right]\right\}, \\ &+ a_m^2\left\{-\theta_{1(0)}\left(1 - \mu_o^2\right)\left[\frac{4\left(\theta_{(0)}^4 + \theta_{(0)}^2 + 1\right)\theta_{2(0)}^2}{\left(1 - \theta_{(0)}^2\right)^2\left(\theta_{(0)}^2 + 1\right)^3} - \frac{\theta_{(0)}^2}{\left(\theta_{(0)}^2 + 1\right)^3}\right]\right\}, \\ \theta_{2(2)} &= \theta_{(2)}^{Sch}\frac{\theta_{2(0)}}{\theta_{(0)}} + \frac{16D^2}{3}\theta_{1(0)}^2\theta_{2(0)} && (6.47) \\ &+ a_m\left\{\frac{4\theta_{1(0)}\mu_o}{\theta_{(0)}^2} + \frac{5\left(-12\theta_{(0)}^6 - 5\theta_{(0)}^4 - 4\theta_{(0)}^2 + 1\right)\theta_{1(0)}\theta_{2(0)}\sqrt{1 - \mu_o^2}\pi}{16\theta_{(0)}^3\left(1 - \theta_{(0)}^2\right)\left(\theta_{(0)}^2 + 1\right)^3}\right\} \\ &+ a_m^2\left\{\frac{\theta_{2(0)}\left(\theta_{(0)}^2\left(3\theta_{(0)}^4 + 2\theta_{(0)}^2 + 3\right) - 4\left(\theta_{(0)}^4 + \theta_{(0)}^2 + 1\right)\theta_{2(0)}^2\right)\left(1 - \mu_o^2\right)}{\left(1 - \theta_{(0)}^2\right)^2\left(\theta_{(0)}^2 + 1\right)^3}\right\}, \end{aligned}$$

where

$$\begin{aligned}\theta^{Sch}_{(2)} &= -\frac{225\pi^2\left(2\theta^2_{(0)}+1\right)}{256\theta_{(0)}\left(\theta^2_{(0)}+1\right)^3} \qquad (6.48)\\ &- \frac{8\left[3\left(\theta^4_{(0)}-\theta^2_{(0)}-1\right)r_o^2-3r_s\left(\theta^4_{(0)}-\theta^2_{(0)}+3\right)r_o+r_s^2\left(2\theta^6_{(0)}-7\theta^4_{(0)}+6\theta^2_{(0)}-6\right)\right]}{3(r_o+r_s)^2\theta_{(0)}(1+\theta^2_{(0)})} \qquad (6.49)\end{aligned}$$

At this order, images are no longer lined up on a line passing for a fixed position. The intercept with the axis of abscissae depends on the source position. This proves that the degeneracy between a Kerr lens and a displaced Schwartzscild lens gets lost. For a source at r_s beyond Sgr A*, the shift at this order to the image position due to the spin is $\sim (a/m)^i \mathcal{O}(\theta_E \varepsilon^2) \sim 0.3(a/m)^i(10pc/r_s)^{1/2}p$as, with $i = 1$ when considering the higher order correction due to the dragging and $i = 2$ when considering quadrupolar distortion. For $r_s \sim 100$ AU and $a < m$, we get a shift of $\sim 4 \times 10^{-2}\mu$as, near the accuracy requirement for the space mission project MAXIM [2].

The angular distance of an image from the black hole has coefficients

$$\theta_{(1)} = \theta^{Sch}_{(1)} + \frac{a_m\theta_{1(0)}\sqrt{1-\mu_o^2}}{\theta_{(0)}\left(\theta^2_{(0)}+1\right)}, \qquad (6.50)$$

$$\begin{aligned}\theta_{(2)} &= \theta^{Sch}_{(2)} + \frac{5a_m\left(4\theta^4_{(0)}+2\theta^2_{(0)}+1\right)\theta_{1(0)}\sqrt{1-\mu_o^2}\pi}{8\theta^2_{(0)}\left(\theta^2_{(0)}+1\right)^3} \qquad (6.51)\\ &+ \frac{2(1-\theta^2_{(0)})\theta^6_{(0)}+\left(4\theta^6_{(0)}+3\theta^4_{(0)}+4\theta^2_{(0)}+1\right)\theta^2_{2(0)}}{2\theta_{(0)}\left(1-\theta^2_{(0)}\right)\left(\theta^2_{(0)}+1\right)^3}a_m^2\left(1-\mu_o^2\right).\end{aligned}$$

The degeneracy in the image positions between the absolute value of the spin and its inclination breaks down with the second order corrections if we consider the angular distances measured along the coordinate axes in the POS, since terms proportional to $a\mu_o$ appear together with those proportional to $a\sqrt{1-\mu_o^2}$. On the other hand, when we consider the angular distance from the center, the spin appears only in the form $a\sqrt{1-\mu_o^2}$.

An image position in $\theta = \theta_E\left\{\theta^{\pm}_{(0)} + \theta^{Sch}_{(1)}\varepsilon + \theta^{Sch}_{(2)}\varepsilon^2 + \mathcal{O}(\varepsilon^3)\right\}$ solves the general form of the lens equation for a spherically symmetric deflector [34]

$$r_{os}\sin B = r_o\sin\theta\cos(\hat{\alpha}_{Sch}-\theta) - \sqrt{r_s^2 - r_o^2\sin^2\theta}\sin(\hat{\alpha}_{Sch}-\theta). \qquad (6.52)$$

with $\hat{\alpha}_{Sch}$ being the deflection angle for the Schwarzschild black hole and $r_{os} = r_o\cos B\sqrt{r_s^2 - r_o^2\sin B^2}$ the linear path from the source to the observer. The left hand side can be rewritten in terms of $\tan B$ as $\left\{\sqrt{r_s^2-\sin^2(\theta)r_o^2}\cos\left(\theta-\hat{\alpha}_{Sch}\right)+\left[1-\sin\theta\sin\left(\theta-\hat{\alpha}_{Sch}\right)\right]r_o\right\}\tan B$. The angles describing image positions and deflection in Eq. (6.52) are assumed to be positive. The source position β should be taken to be positive when studying an image on the same side of the black hole as the source, and negative when studying an image on the opposite side.

6.5 Magnification

The ratio between the angular area of the image in the observer sky, $d\theta_1 d\theta_2$, and the angular area of the source in absence of lensing, $dB_1 dB_2$, gives the (signed) luminous amplification of the image,

---

[2] http://maxim.gsfc.nasa.gov.

A. It can be calculated as the inverse of the Jacobian determinant of the lensing mapping, J,

$$\begin{aligned} A &= J^{-1} \qquad (6.53) \\ &= \left[\frac{\partial B_1 \partial B_2}{\partial \theta_1 \partial \theta_2}\right]^{-1}. \qquad (6.54) \end{aligned}$$

For a source emitting isotropically, the unlensed source as seen by the observer is $(r_s/r_{os})^2$ smaller than as seen by an observer in the black hole position [31]. Then,

$$J = \left(\frac{r_s}{r_{os}}\right)^2 \left[\frac{\partial \mu_s \partial \phi_s}{\partial \theta_1 \partial \theta_2}\right]. \qquad (6.55)$$

The Jacobian can be written as a Taylor expansion in ε. We first write the angular position of the source $\{\mu_s, \phi_s\}$ in terms of the angular variable in the POS and then derive with respect to θ_1 and θ_2. Finally, we introduce the scaled angular variables and rearrange the result as a series expansion in ε. We get

$$\begin{aligned} J \;=\;& 1 - \frac{1}{\theta_{(0)}^4} + \left\{\frac{15(1-\theta_{(0)}^2)^2\pi}{16\theta_{(0)}^5(1+\theta_{(0)}^2)} - \frac{4\theta_{1(0)} a_m \sqrt{1-\mu_o^2}}{\theta_{(0)}^4(1+\theta_{(0)}^2)}\right\}\varepsilon \qquad (6.56) \\ -\;& \Bigg\{\frac{8(1-\theta_{(0)}^2)}{(r_o+r_s)^2\theta_{(0)}^6(1+\theta_{(0)}^2)}\Big[(\theta_{(0)}^8 + 2\theta_{(0)}^6 + 2\theta_{(0)}^4 + 1)r_o^2 - r_s^2(\theta_{(0)}^8 + 2\theta_{(0)}^6 + 4\theta_{(0)}^4 - 8\theta_{(0)}^2 + 3 \\ -\;& 2r_s r_o \theta_{(0)}^2(\theta_{(0)}^4 + 2\theta_{(0)}^2 - 4)\Big] + \frac{225\pi^2}{256}\frac{(1-\theta_{(0)}^2)(1-5\theta_{(0)}^4 - 2\theta_{(0)}^2)}{\theta_{(0)}^6(1+\theta_{(0)}^2)^3} \\ -\;& \frac{5a_m\left(-12\theta_{(0)}^8 + 27\theta_{(0)}^6 + 7\theta_{(0)}^4 - 7\theta_{(0)}^2 + 1\right)\theta_{1(0)}\sqrt{1-\mu_o^2}\pi}{16\theta_{(0)}^7\left(\theta_{(0)}^2+1\right)^3} \\ -\;& \frac{2a_m^2\left(\theta_{(0)}^2\left(\theta_{(0)}^2+1\right)^2 + 2\left(1-3\theta_{(0)}^4\right)\theta_{1(0)}^2\right)(1-\mu_o^2)}{\theta_{(0)}^4\left(1-\theta_{(0)}^2\right)\left(\theta_{(0)}^2+1\right)^3}\Bigg\}\varepsilon^2 + \mathcal{O}(\varepsilon^3). \end{aligned}$$

The corresponding magnification is

$$\begin{aligned} A \;=\;& \frac{\theta_{(0)}^4}{\theta_{(0)}^4 - 1} - \left\{\frac{15\theta_{(0)}^3\pi}{16(1+\theta_{(0)}^2)^3} + \frac{4a_m\theta_{(0)}^4\theta_{1(0)}\sqrt{1-\mu_o^2}}{(1-\theta_{(0)}^2)^2(1+\theta_{(0)}^2)^3}\right\}\varepsilon \qquad (6.57) \\ -\;& \Bigg\{\frac{\theta_{(0)}^2}{(1-\theta_{(0)}^2)(1+\theta_{(0)}^2)^5}\Bigg[\frac{675\theta_{(0)}^4\pi^2}{128} - \frac{8(1+\theta_{(0)}^2)^2}{(r_o+r_s)^2}(\theta_{(0)}^8 + 2\theta_{(0)}^6 + 2\theta_{(0)}^4 + 1)r_o^2 \\ -\;& 2r_s r_o\theta_{(0)}^2(\theta_{(0)}^4 + 2\theta_{(0)}^2 - 4) - r_s^2(\theta_{(0)}^8 + 2\theta_{(0)}^6 + 4\theta_{(0)}^4 - 8\theta_{(0)}^2 + 3)\Bigg] \\ +\;& \frac{5\theta_{(0)}(1 - 12\theta_{(0)}^8 + 27\theta_{(0)}^6 - 17\theta_{(0)}^4 + 17\theta_{(0)}^2)\theta_{1(0)}\pi}{16(1-\theta_{(0)}^2)^2(\theta_{(0)}^2+1)^5} a_m\sqrt{1-\mu_o^2} \\ +\;& \left[\theta_{(0)}^2 - \frac{6(1+\theta_{(0)}^4)\theta_{1(0)}^2}{(1+\theta_{(0)}^2)^2}\right]\frac{2\theta_{(0)}^4}{(1-\theta_{(0)}^2)^3(\theta_{(0)}^2+1)^3} a_m^2(1-\mu_o^2)\Bigg\}\varepsilon^2 + \mathcal{O}(\varepsilon^3). \end{aligned}$$

The luminous amplification depends on the angular momentum only through terms proportional to $a\sqrt{1-\mu_o^2}$.

6.6 Critical curves and caustics

Critical curves are the locus of all images with formally infinite magnification. Points in the lens plane are critical when the Jacobian is singular, $J = 0$. We look for a parametric solution in the form

$$\theta_1 = \theta_E \cos\varphi \left\{1 + \delta\theta_{E,(1)}(\varphi)\varepsilon + \delta\theta_{E,(2)}(\varphi)\varepsilon^2\right\}, \tag{6.58}$$

$$\theta_2 = \theta_E \sin\varphi \left\{1 + \delta\theta_{E,(1)}(\varphi)\varepsilon + \delta\theta_{E,(2)}(\varphi)\varepsilon^2\right\}, \tag{6.59}$$

where φ is the polar angle in the POS, i.e. $\tan\varphi = \tan\theta_2/\tan\theta_1$. In Eqs. (6.58, 6.59), we have already considered that the critical curve for the Schwarzschild black hole is a circle of radius equal to the Einstein radius θ_E. The condition $J = 0$ is fulfilled order by order when

$$\delta\theta_{E,(1)}(\varphi) = \frac{15\pi}{32} + a_m\sqrt{1-\mu_o^2}\cos\varphi, \tag{6.60}$$

$$\begin{aligned}\delta\theta_{E,(2)}(\varphi) = & -\frac{675\pi^2}{2048} + 4(1+D) - \frac{4}{3}D^2\cos(4\varphi) + \frac{15}{32}\pi a_m\sqrt{1-\mu_o^2}\cos\varphi \\ & -\frac{1}{2}a_m^2\left(1-\mu_o^2\right)\sin^2\varphi.\end{aligned} \tag{6.61}$$

The critical curve corresponding to the above equations is a circle in the plane $\{\tan\theta_1, \tan\theta_2\}$. With respect the static black hole, the circle centre is displaced along the equatorial direction by

$$\frac{ma\sqrt{1-\mu_o^2}}{r_o}\left(1 + \frac{15\pi}{32}\varepsilon + \mathcal{O}(\varepsilon^2)\right); \tag{6.62}$$

the angular momentum does not contribute to the radius, which can be written as

$$\theta_E\left\{1 + \frac{15\pi}{32}\varepsilon + \left[4\left(1+D+D^2\right) - \frac{675\pi^2}{2048}\right]\varepsilon^2 + \mathcal{O}(\varepsilon^3)\right\} \tag{6.63}$$

Note that $4D\varepsilon^2 = m/r_o$.

The corresponding locations in the source plane are the caustics. Given the circular symmetry of the critical curve, the caustics will be point-like and centered in

$$\{B_1, B_2\} \simeq \left\{4Da_m\sqrt{1-\mu_o^2}\varepsilon^2\left(1 + \frac{5\pi}{16}\varepsilon + \mathcal{O}(\varepsilon^2)\right), 0\right\}. \tag{6.64}$$

At this leading order in B, the tangent can be approximated by the angle.

At the first order correction in a, a circle whose radius is equal to the critical radius in the spherically symmetric case and displaced from the black hole along the equatorial direction by a distance $(\delta - a\sqrt{1-\mu_o}) \sim \varepsilon^2$ maps onto a circle in the source plane displaced by the same amount $(\delta - a\sqrt{1-\mu_o})$ and of radius δ [115]. At the next order in a, circles map in circles only for displacements of higher order, $(\delta - a\sqrt{1-\mu_o}) \sim \varepsilon^3$.

6.7 Conclusions

In this paper we have addressed the study of gravitational lensing by a Kerr black hole in the weak deflection limit. Lensing by rotating objects has been considered a number of times in the past and with very different approaches. Here, we built up the lens equations starting from the geodesics for light rays and then solved for the lensing quantities with a standard perturbative technique. This method allowed us to consider corrections proportional to $a^2 r_{Sch}$ and $a r_{Sch}^2$. We showed as pure spin terms $\propto a^2$, a^3 do not contribute to the observable lensing quantities, in particular to the deflection angle.

Up to the first order correction in the spin, the Kerr lens is equivalent to a displaced Schwarzschild deflector. This is a very general property of spinning lenses [125]. To the next order, this degeneracy is broken and some particular features show up. The two perturbed images are no more aligned with a fixed position. The degeneracy between the absolute value of the spin and its inclination on the line of sight is also broken. All observable quantities at the first order correction in the spin are functions of $a \sin\vartheta_o$ but terms proportional to $a \cos\vartheta_o$ appear at the next order in the angular coordinates of the images in the plane of the sky. However, the angular displacement of the images from the center is still a function of $a \sin\vartheta_o$. The shape of the critical curve is still a circle displaced along the equatorial direction and the caustic is still point-like. The finite size of the caustic should show up at the next order due to terms $\propto a^2 r_{Sch}^2$ as suggested by numerical results [115].

It could be of interest to draw some comparison with the case of the strong deflection limit [28, 31, 32]. Such a limit has been treated considering small values of the angular momentum and including corrections proportional to a^2. That is two orders beyond the Schwarzschild lens. This was enough to obtain finite shaped caustics. In the present study of the weak deflection limit, we made no assumptions on the absolute value of the spin and still considered two orders beyond the spherically symmetric lens but we did non get the caustic structure. This is only an apparent discrepancy, as we have to remind that the minimum distance in the strong deflection limit is of order of the gravitational radius. In fact the finite size of the caustic springs from terms proportional to $(a^2 r_{Sch}^2)/r_{min}^4$. Since in the strong deflection limit $r_{min} \sim r_{Sch}$, we see as these terms are included in an analysis at the second order in a.

If the supermassive black hole at the Galactic center has a significant angular momentum, some features of Kerr lensing could be detected by future space astrometric mission with a planned resolution of the microarcsecond.

In a forthcoming paper we will present an analytical treatment of Kerr lensing in the weak deflection limit accounting for the caustic structure.

6.8 Radial integrals

These appendices are devoted to the resolution of the integrals in the geodesic equations. Let us start with some considerations on the radial integrals. The sign convention in the geodesic equations remind us that integrations must be performed summing up with the same sign all contributions from paths bounded by consecutive inversion points. For a standard gravitational lensing configuration, the r-motion, $r_s \to r_{min} \to r_o$, has only one inversion point so that we have to add the contributions due to the approach and the departure of the photon. Integrals can be easily evaluated expanding the integrand as a Taylor series in ϵ and then performing the integration term by term. When evaluating the expanded primitive function in the extrema r_s and r_o, we remind that $\sqrt{J^2+Q}/r_s$ and $\sqrt{J^2+Q}/r_o$ are of order of ϵ. Let us first consider the left-hand side of Eq. (6.4). The integral reads

$$\begin{aligned}\int_{r_{min}}^{r_s} \frac{dr}{\sqrt{R}} + \int_{r_{min}}^{r_o} \frac{dr}{\sqrt{R}} \simeq\; & \frac{\pi}{\sqrt{J^2+Q}} + \frac{2}{J^2+Q} r_{Sch} \\ & + \frac{15\pi r_{Sch}^2}{16\left(J^2+Q\right)^{3/2}} - \frac{4Jar_{Sch}}{\left(J^2+Q\right)^2} + \frac{a^2\pi\left(2J^2-Q\right)}{4\left(J^2+Q\right)^{5/2}} \\ & + \frac{16 r_{Sch}^3}{3\left(J^2+Q\right)^2} - \frac{15aJ\pi r_{Sch}^2}{4\left(J^2+Q\right)^{5/2}} + \frac{a^4\left(6J^2-2Q\right) r_{Sch}}{\left(J^2+Q\right)^3} \\ & - \frac{J^2+Q}{6r_o^3} - \frac{J^2+Q}{6r_s^3} - \frac{1}{r_0} - \frac{1}{r_s}.\end{aligned} \tag{6.65}$$

Let us now consider the radial integral in the right hand side of Eq. (6.5). We have

$$\begin{aligned}\int_{r_{min}}^{r_s} \frac{a\left(r_{Sch} r - aJ\right)}{\pm\Delta\sqrt{R}} dr + \int_{r_{min}}^{r_o} \frac{a\left(r_{Sch} r - aJ\right)}{\pm\Delta\sqrt{R}} dr \simeq\; & \frac{2r_{Sch}a}{J^2+Q} - \frac{\pi a^2}{2\left(J^2+Q\right)^{3/2}} \\ & - \frac{4Jr_{Sch}a^2}{\left(J^2+Q\right)^2} + \frac{5\pi r_{Sch}^2 a}{4\left(J^2+Q\right)^{3/2}}.\end{aligned} \tag{6.66}$$

Corrections due to the finiteness of r_o and r_s in Eq. (6.66) of order $\sim \epsilon^4$. We remark as radial integrals can be more easily solved changing to the variable $u = r_{min}/r$.

6.9 Angular integrals

The angular integrals follow the photon polar trajectory from the source, ϑ_s, to the turning point, which is either the minimum ϑ_{min} or the maximum ϑ_{max}, to the observer at ϑ_o. As for the radial motion, the integration is a path integral over the whole trajectory of the photon with all contributions to be summed with the same sign. The two branches, i.e $\vartheta_s \rightarrow (\vartheta_{min}, \vartheta_{max}) \rightarrow \vartheta_o$ sum up positively if we take the sign of $\sqrt{\Theta}$ to be positive (negative) if integrating from ϑ_s to ϑ_{max} (ϑ_{min}) and negative (positive) from ϑ_{max} (ϑ_{min}) to ϑ_o. It is useful to change to $\mu \equiv \cos\vartheta$. The right hand side of Eq. (6.4) can be then rewritten as

$$I_\mu = \int \frac{1}{\pm\sqrt{\Theta_\mu}} d\mu, \tag{6.67}$$

where

$$\begin{aligned} \Theta_\mu &\equiv a^2(\mu_-^2 + \mu^2)(\mu_+^2 - \mu^2), && (6.68)\\ \mu_\pm^2 &\equiv \frac{\sqrt{b_{JQ}^2 + 4a^2 Q_m} \pm b_{JQ}}{2a^2}, && (6.69)\\ b_{JQ} &= a^2 - J^2 - Q. && (6.70) \end{aligned}$$

The turning point in the polar motion is a zero of Θ_μ, i.e. $\pm\mu_+$, with μ_+ corresponding to ϑ_{min}. To the lowest orders

$$\mu_+ \simeq \sqrt{\frac{Q}{J^2+Q}} \left[\frac{a^2 J^2}{2\left(J^2+Q\right)^2} + \frac{a^4 J^2 (3J^2 - 4Q)}{8\left(J^2+Q\right)^4} + \mathcal{O}(\varepsilon^6) \right]. \tag{6.71}$$

The primitive function of the integral in Eq. (6.67) is

$$PI(\mu) = \frac{1}{a\mu_-} F\left(\sin^{-1}\left(\mu/\mu_+\right), -(\mu_+/\mu_-)^2\right) + \mathcal{O}(\varepsilon^6), \tag{6.72}$$

where F is the elliptic integral of the first kind. We remark as the integral in Eq. (6.67) can be more easily solved in terms of the integration variable μ/μ_+ [43, 35, 32]. The function in Eq. (6.72) can be expanded as

$$PI(\mu) \simeq \frac{1}{\sqrt{J^2+Q}} \left\{ \sin^{-1}\mu_\sigma - \left[\frac{2J^2 - Q(1-\mu_\sigma^2)}{4(J^2+Q)} \frac{\mu_\sigma}{\sqrt{1-\mu_\sigma^2}} + \frac{Q - 2J^2}{4(J^2+Q)} \sin^{-1}\mu_\sigma \right] \frac{a^2}{J^2+Q} \right\}, \tag{6.73}$$

with $\mu_\sigma \equiv \mu/\sqrt{Q/(J^2+Q)}$. In $\mu = \mu_+$, the primitive function reduces to

$$PI(\mu_+) \simeq \frac{\pi}{2\sqrt{J^2+Q}} + \frac{a^2 \pi \left(2J^2 - Q\right)}{8\left(J^2+Q\right)^{5/2}}. \tag{6.74}$$

The turning point is attained in either μ_+ or $-\mu_+$, according to that photon gets a minimum or a maximum polar angle, respectively. We remind that μ is a decreasing function of ϑ so that the considerations on the signs must be accordingly updated. Using the property that $PI(-\mu_+) = -PI(\mu_+)$ and following the sign convention sum, we sum up the paths as

$$I_\mu = 2PI(\mu_+) + (-1)^k [PI(\mu_s) + PI(\mu_o)], \tag{6.75}$$

with k an integer number defined to be even (odd) if the photon gets to the observer from below (from the top), i.e. after having reached ϑ_{max} (ϑ_{min}).

Let us now consider the angular integral in the right hand side of Eq. (6.5),

$$J_\vartheta = \int \frac{csc^2\vartheta}{\pm\sqrt{\Theta}} d\vartheta. \tag{6.76}$$

In terms of μ, the above integral can be written as

$$J_\mu = \int \frac{1}{\pm(1-\mu^2)\sqrt{\Theta_\mu}} d\mu; \tag{6.77}$$

the primitive function can be expressed in terms of the incomplete elliptic integral of the third kind,

$$PJ(\mu) = -\frac{J\Pi\left(\mu_+^2; -\sin^{-1}\left(\frac{\mu}{\mu_+}\right) | -\frac{\mu_+^2}{\mu_-^2}\right)}{a\mu_-}. \tag{6.78}$$

To the lowest orders, Eq. (6.78) reduces to

$$PJ(\mu) \simeq \tan^{-1}\left(\frac{J\mu_\sigma}{\sqrt{J^2+Q}\sqrt{1-\mu_\sigma^2}}\right) - \frac{a^2 J}{2\left(J^2+Q\right)^{3/2}}\left(\frac{\mu_\sigma}{\sqrt{1-\mu_\sigma^2}} - \sin^{-1}\mu_\sigma\right). \tag{6.79}$$

In $\mu = \mu_+$,

$$PJ(\mu_+) \simeq \frac{J\pi a^2}{4\left(J^2+Q\right)^{3/2}} + \frac{J\pi}{2|J|}. \tag{6.80}$$

The sum convention works as in Eq. (6.75).

Chapter 7

Analytic Kerr black hole lensing for equatorial observers in the strong deflection limit [1]

In this paper we present an analytical treatment of gravitational lensing by Kerr black holes in the limit of very large deflection angles, restricting to observers in the equatorial plane. We accomplish our objective starting from the Schwarzschild black hole and adding corrections up to second order in the black hole spin. This is sufficient to provide a full description of all caustics and the inversion of lens mapping for sources near them. On the basis of these formulae we argue that relativistic images of Low Mass X-ray Binaries around Sgr A* are very likely to be seen by future X-ray interferometry missions.

7.1 Introduction

General relativity predicts that light rays passing close to a black hole suffer gravitational lensing, so that an observer almost aligned with the line connecting a source and a black hole sees two images of the original source. These images are due to small deviations of photons that pass far enough from the black hole to allow a weak field approximation of the metric tensor. However, already Darwin in 1959 noticed that photons passing very close to a black hole may suffer much larger deflections without falling into the event horizon [46]. In principle, an observer situated on the line connecting the source and the black hole, besides the two classical weak field images, would detect two infinite series of images very close the black hole. These images are produced by photons making one or more complete loops around the black hole before re-emerging in the observer direction. Of course, these relativistic images are largely demagnified w.r.t the original source and for some time they just remained a mathematical curiosity of General Relativity.

Nevertheless, things changed after the great progress of interferometric techniques and the widely-accepted opinion that the radio-source Sgr A* in the Galactic center actually hosts a supermassive black hole of 3.61×10^5 solar masses [56] (for a review see [97]). These facts motivated Virbhadra & Ellis to propose that this black hole may be an ideal candidate for the generation of relativistic images of sources eventually passing behind it [143]. In fact, the angular radius of the shadow of Sgr A* is predicted to be 23 μas, which is comparable to the best resolution achieved in the millimeter band (18 μas [88]). A complete imaging in the sub-mm band was suggested in Ref. [59]. Future space missions in the infrared and in the X-rays may reach even higher resolutions (for a complete discussion, see Ref. [33]).

---

[1] Published in [31]

A new field of Gravitational lensing was definitively opened and several authors proposed alternative methods to overcome the evident difficulties of full general relativity calculations of geodesics which typically result in cumbersome equations and heavy numerical integrations [62, 109]. However, Darwin himself proposed a surprisingly easy formula for the positions of the relativistic images generated by a Schwarzschild black hole [46]. This formula and its consequences were later discussed or re-discovered several times [14, 92, 104, 103] before Virbhadra & Ellis proposal. After that work, it was revived in Ref. [26], where it was called the strong field limit of the deflection angle. It was then extended to Reissner-Nordstrom black holes in Ref. [54] and applied to microlensing by Sgr A* by Petters [110]. In this paper, as suggested by Perlick [109], we shall revise this terminology, referring to a Strong Deflection Limit (SDL), since an infinite deflection angle is not necessarily related to a large curvature. This can be realized by considering a very large black hole. The minimum distance reachable by a photon without being captured is of the same order of the horizon radius. The Riemann invariant $R_{\alpha\beta\gamma\delta}R^{\alpha\beta\gamma\delta}$, evaluated in the inner region probed by the photon, scales as the curvature at the horizon, i.e. $1/M^4$. Increasing the mass of the black hole, the curvature felt by the photon becomes arbitrarily low, even if its deflection may be large. So, it is more correct to speak of a strong deflection limit without referring to the curvature.

The power of the SDL expansion of the deflection angle became evident when its universality was demonstrated in Ref. [27]. Any class of spherically symmetric black holes leads to the same SDL expansion; the coefficients of this expansion depend on the specific class of the black hole, representing a sort of identity card, from which all the parameters of the black hole can be extracted. By observing the relativistic images of a gravitational lensing event induced by a black hole, it is possible, in principle, to deduce all its parameters and properties. Since this could also provide the key to discriminate between General Relativity and some extended theories of gravitation, this method has been applied to several interesting classes of black holes coming from string theory, braneworlds and wormholes [18]. Some limitations were removed in Refs. [53, 29], while time delay analysis was performed in Ref. [30].

As regards spinning black holes, the story is more complicated. Almost forty years have passed since Carter reduced the geodesics equations in Kerr spacetime to first order equations depending on four constants of motion [41]. This fundamental achievement allowed a complete study and classification of all possible trajectories of massive particles and photons moving around spinning black holes [43]. In order to visualize and study these geodesics, a very large amount of numerical methods has been developed through years. In the context of gravitational lensing, these methods have been used to describe the light curve of a star orbiting a black hole [45] and the apparent shape of the accretion disk [92, 144]. Rauch & Blandford have proved the formation of extended 4-cusped caustics numerically [115].

Extending the SDL methodology to axially symmetric black holes is not immediate and the simplicity of the approach may be easily lost. In Ref. [28] the SDL formula was recovered for light rays lying close to the equatorial plane of a Kerr black hole, but the coefficients of the formula had to be calculated numerically as functions of the black hole spin. Vazquez & Esteban solved the lens equation far from the equatorial plane for some particular cases [142], but a complete analytical treatment of Kerr lensing is still missing.

In this paper we make a considerable step towards this objective, focusing on observers lying on the equatorial plane and solving the general lens equation for small values of the black hole spin. Perturbative methods allow us to use the Schwarzschild SDL formula as starting point to describe the deflection of light rays looping around a Kerr black hole in a completely analytical way. Our treatment leads to an amazingly simple description of all relativistic caustics and to the immediate inversion of lens mapping for sources near caustics. The limitation to the equatorial observer is motivated by the fact that the most important candidate black hole, Sgr A*, is likely to have a spin axis perpendicular to the galactic plane, where the solar system lies, in a first approximation. It is natural, then, to take advantage of this configuration and deal with considerably simplified equations.

Our paper is structured as follows. Sect. 2 recalls the main results of Kerr geodesics. Sect. 3

explains how the SDL is introduced in Kerr gravitational lensing and illustrates the strategy we use to solve the geodesics equations. Sect. 4 contains the derivation of the caustics order by order. In Sect. 5 we analyze the lens map close to the relativistic caustics, finding the additional images and their magnification. Sect. 6 considers the perspectives for observations in the light of what we have found, focusing on the study of relativistic images around Sgr A*. Sect. 7 summarizes the main results of the paper. Appendix A complements the calculations explained in Sect. 3 with more details.

7.2 Kerr geodesics

In Boyer-Lindquist coordinates [24] $x^\mu \equiv (t, x, \vartheta, \phi)$, the Kerr metric reads

$$\begin{aligned} ds^2 = & \frac{\Delta - a^2 \sin^2\vartheta}{\rho^2} dt^2 - \frac{\rho^2}{\Delta} dx^2 - \rho^2 d\vartheta^2 \\ & - \frac{\left(x^2+a^2\right)^2 - a^2 \Delta \sin^2\vartheta}{\rho^2} \sin^2\vartheta d\phi^2 \\ & + \frac{2ax\sin^2\vartheta}{\rho^2} dt d\phi \qquad (7.1) \\ \Delta = & \, x^2 - x + a^2 \qquad (7.2) \\ \rho^2 = & \, x^2 + a^2\cos^2\vartheta \qquad (7.3) \end{aligned}$$

where a is the specific angular momentum of the black hole. All distances are measured in Schwarzschild radii ($2MG/c^2 = 1$). ϑ and ϕ represent the polar and azimuthal angles respectively, while x is the radial coordinate. The event horizon is a spherical surface of radius $x_H = (1 + \sqrt{1-4a^2})/2$. In our notations, a runs from 0 (Schwarzschild black hole) to 1/2 (extremal Kerr black hole).

Carter showed that the Kerr geodesics can be resolved in terms of first integrals of motion [41]. The final expressions for lightlike geodesics take the following form (following Ref. [43])

$$\pm \int \frac{dx}{\sqrt{R}} = \pm \int \frac{d\vartheta}{\sqrt{\Theta}} \qquad (7.4)$$

$$\begin{aligned} \phi_f - \phi_0 = & \, a \int \frac{x^2 + a^2 - aJ}{\Delta\sqrt{R}} dx - a \int \frac{dx}{\sqrt{R}} \\ & + J \int \frac{\csc^2\vartheta}{\sqrt{\Theta}} d\vartheta, \qquad (7.5) \end{aligned}$$

where

$$\begin{aligned} \Theta = & \, Q + a^2\cos^2\vartheta - J^2 \cot^2\vartheta \qquad (7.6) \\ R = & \, x^4 + (a^2 - J^2 - Q)x^2 + (Q + (J-a)^2)x \\ & - a^2 Q. \qquad (7.7) \end{aligned}$$

In these expressions, J and Q are two constants of motion that, along with the initial condition ϕ_0, completely identify the geodesic. The double signs in front of the integrals in Eq. (7.4) remind that the integrals must be performed piecewise, between two consecutive values of x and ϑ that annihilate the denominators R and Θ (inversion points). Then the sign of each piece between two inversion points is chosen in such a way that all of them sum up with the same sign, giving a final positive contribution.

In the context of gravitational lensing, we are interested to those photons that come from an infinite distance, approach the black hole reaching a minimum distance x_0 and then escape back to infinity. This selects trajectories characterized by $Q \geq 0$. Moreover, since the roots of R represent inversion points in the radial motion, we have to impose that R has one non-degenerate positive root. This amounts to require that $R(x_0) = 0$, $R'(x_0) \neq 0$. The limiting situation, when x_0 becomes a degenerate root, is obtained when the equations $R(x_m) = 0$, $R'(x_m) = 0$ are simultaneously fulfilled at some point x_m. Solving these equations w.r.t. J and Q we get

$$J_m = \frac{x_m^2(-3+2x_m)+a^2(1+2x_m)}{a(1-2x_m)} \tag{7.8}$$

$$Q_m = \frac{x_m^3\left[2a^2 - x_m(x_m-3/2)^2\right]}{a^2(x_m-1/2)^2}. \tag{7.9}$$

Given a value of x_m, the quantities J_m and Q_m represent the values of J and Q that characterize those trajectories that bring a photon down to the distance x_m in an infinite time. Asymptotically the photon keeps orbiting forever at a fixed distance x_m from the black hole. However, this orbit is unstable and small perturbations make the photon fall into the black hole or deviate it back to infinity. In Schwarzschild black hole, the radius x_m of the unstable photon orbit is fixed to 3/2 in Schwarzschild units (the sphere of radius x_m is then called photon sphere). In the case of Kerr black holes, the radius of the orbit depends on the initial orientation of the photon trajectory. In practice, x_m may vary between two limiting values x_{m+}, x_{m-}, which respectively represent the radius of the orbit described by a photon co-rotating with the black hole and the radius of the orbit of a counter-rotating photon in the equatorial plane. All intermediate values correspond to photons whose orbits are not equatorial and do not lie on a single plane. In order to find these limiting values, we have to impose $Q_m = 0$. So, x_{m+} and x_{m-} are found as the two largest roots of this equation. This is a third degree equation whose solution can be found exactly. However, since the successive calculations would soon become too cumbersome, we will already consider their expansions in powers of a. To describe second order effects in the lens equation, it is necessary to take terms up to the third order:

$$x_{m\pm} = \frac{3}{2} \mp \frac{2}{\sqrt{3}}a - \frac{4}{9}a^2 \mp \frac{20}{27\sqrt{3}}a^3 + O(a^4). \tag{7.10}$$

We see that in the limit $a \to 0$, the two limiting values converge to the Schwarzschild photon sphere $x_m = 3/2$. When a is different from zero, x_{m+} and x_{m-} are distinct. The specific value of x_m in the interval $[x_{m+}, x_{m-}]$ uniquely fixes the amplitude of the oscillations on the equatorial plane performed by the photon along its orbit. In consideration of this fact we introduce a more convenient parametrization, replacing a by $a\xi$:

$$x_m(\xi) = \frac{3}{2} - \frac{2}{\sqrt{3}}a\xi - \frac{4}{9}a^2\xi^2 - \frac{20}{27\sqrt{3}}a^3\xi^3. \tag{7.11}$$

Varying the parameter ξ in the range $[-1, 1]$ we obtain all possible values of x_m in the range $[x_{m+}, x_{m-}]$, corresponding to orbits with different amplitude of the oscillations on the equatorial plane (a different parameterization with similar properties was used in Ref. [148]). We shall see that all quantities assume very simple expressions in terms of this parameter ξ. Now, using this parametrization in Eqs. (7.8)-(7.9), we can expand J_m and Q_m to second order in a and read them as functions of ξ:

$$J_m(\xi) = \frac{3\sqrt{3}}{2}\xi - 2a - \frac{a^2\xi(2-\xi^2)}{\sqrt{3}} + O(a^3), \tag{7.12}$$

$$Q_m(\xi) = \frac{27}{4}(1-\xi^2) + 3a^2\xi^2(1-\xi^2) + O(a^3). \tag{7.13}$$

Notice that the presence of a in the denominators of Eqs. (7.8)-(7.9) allows ξ to appear at zero order already. That is why we needed a third order expansion for x_m. So, even in the Schwarzschild limit, ξ can be used to parametrize the photon sphere in the (J, Q) plane.

In Fig. 7.1 we plot the locus of points (J_m, Q_m) when we vary ξ in the range $[-1, 1]$, for different values of a. We recall that purely prograde photons travelling on the equatorial plane are characterized by $Q = 0$ and positive J, while retrograde photons have negative J. Photons with

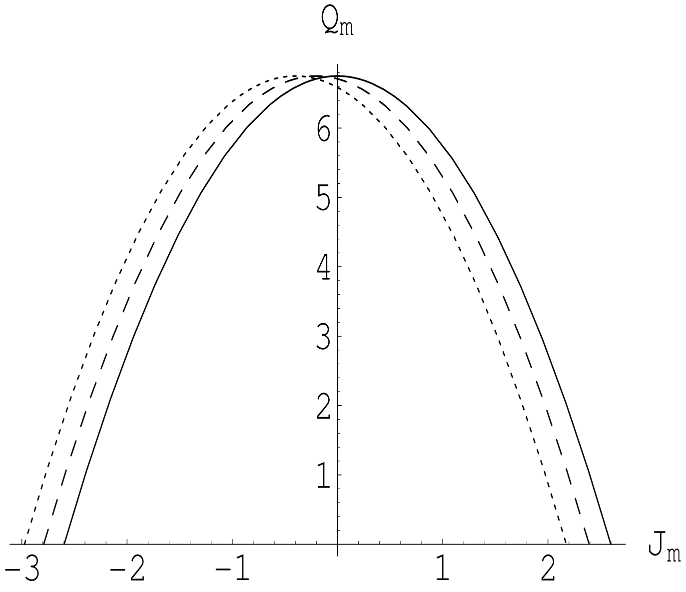

Figure 7.1: The limiting values J_m and Q_m for the constants of motion J and Q corresponding to trajectories reaching the unstable orbit around the black hole asymptotically. The solid line is for $a = 0$, the dashed line is for $a = 0.1$ and the dotted line is for $a = 0.2$.

$J = 0$ and $Q > 0$ run on polar trajectories. Any geodesics characterized by J and Q outside this locus (with $Q \geq 0$), correspond to acceptable gravitational lensing trajectories. All photons with J and Q inside this locus are destined to fall inside the black hole.

There is an immediate connection between these constants and the point in the sky where the observer detects the photon. Throughout the paper, we consider a static observer at a radial Boyer-Lindquist coordinate D_{OL}, lying on the equatorial plane. This restriction will keep all equations simple enough to be solved, while ensuring an exhaustive description of the expected phenomenology for Sgr A*. This definition has no ambiguity from a mathematical point of view, but needs to be linked to the astrophysical notion of distance from the solar system to Sgr A*. The current measurements of the distance to the Galactic center are typically based on the dynamical investigation of the stars orbiting around Sgr A*. The orbital fits are done in the context of Newtonian gravity. As a consequence, the current estimate of the distance to the Galactic center, which amounts to about 8 kpc [116, 56], assumes a flat background geometry. This flat distance makes sense as long as all scales are much larger than the Schwarzschild radius of the central black hole, which is

$$R_{Sch} = \frac{2GM}{c^2} = 1.1{\times}10^{10}\ \mathrm{m} \tag{7.14}$$

for $M = 3.61 \times 10^6\ \mathrm{M}_\odot$ [56]. Now it is evident that in the limit of large distances, one can simply translate any flat distance from the black hole, as calculated by Newtonian physics, into Boyer-Lindquist coordinates in the Kerr geometry. In fact, far from the black hole, in the asymptotic region, the Boyer-Lindquist coordinate coincide with the euclidean spherical coordinates centered on the black hole. The ambiguity in this identification is of the order of R_{Sch}/x (x being the distance from the black hole) and becomes relevant only close to the event horizon, where Newtonian physics loses any meaning. So, we can safely assume $D_{OL} = 8$ kpc, when speaking about Sgr A* in any calculations.

Then, considering only observers in the asymptotic region ($D_{OL} \gg 1$), where the geometry is close to be Minkowskian, it is possible to define angular coordinates (θ_1, θ_2) in the observer sky. We will put the black hole in $(0, 0)$, and let θ_1 run parallel to the equatorial plane of the black hole while θ_2 will run on the perpendicular axis (see Fig. 7.2). As $D_{OL} \gg 1$, θ_1 and θ_2 will always be

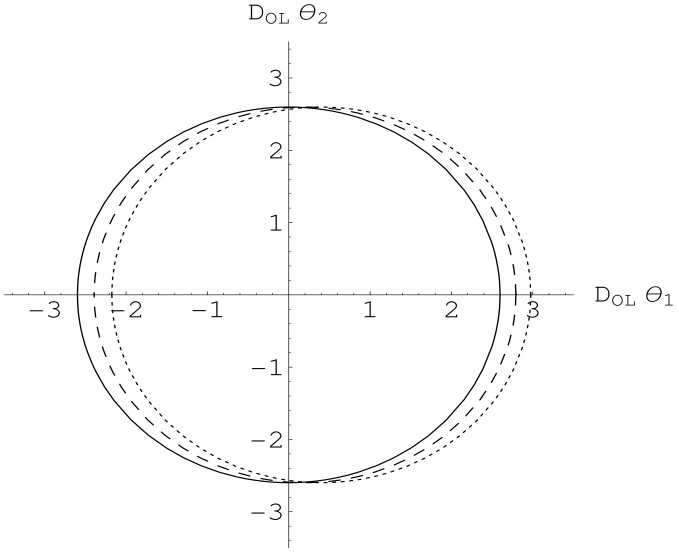

Figure 7.2: The shadow shape in the observer sky. The solid line is for $a = 0$, the dashed line is for $a = 0.1$ and the dotted line is for $a = 0.2$.

assumed to be very small. As shown in Ref. [43], photons reaching the observer from the generic point (θ_1, θ_2) are characterized by the constants

$$J = -\theta_1 D_{OL} \tag{7.15}$$

$$Q = \theta_2^2 D_{OL}^2 \tag{7.16}$$

w.r.t. to the black hole. We have taken the spin axis of the black hole parallel to the θ_2 direction and we have considered a photon moving towards the observer. Then, it is immediate to pass from (J, Q) to the corresponding coordinates in the observer sky (θ_1, θ_2) and viceversa, apart from an ambiguity of sign in θ_2.

We can use these formulae to translate the locus (J_m, Q_m) into a new one $(\theta_{1,m}, \theta_{2,m})$ in the plane (θ_1, θ_2). This is given by

$$D_{OL}\theta_{1,m}(\xi) = -\frac{3\sqrt{3}\,\xi}{2} + 2a + \frac{a^2\xi(2-\xi^2)}{\sqrt{3}} + O(a^3) \tag{7.17}$$

$$D_{OL}\theta_{2,m}(\xi) = \pm\left(\frac{3\sqrt{3}}{2} + \frac{a^2\xi^2}{\sqrt{3}}\right)\sqrt{1-\xi^2} + O(a^3). \tag{7.18}$$

and is called the shadow of the black hole.

Fig. 7.2 shows the shape of the shadow in the observer sky for different values of a. From what we have said before, all photons deflected by the black hole must reach the observer from directions (θ_1, θ_2) outside the shadow. Photons reaching the observer from the inside of the shadow cannot come from gravitational deflection but must have been generated by sources in front of the black hole. So, if we had enough resolution to fully image a black hole, we would see a black shadow with the shape described by Eqs. (7.17) and(7.18), bordered by a luminous ring due to gravitational lensing of all sources around the black hole [59].

In Fig. 7.2 we see that the Schwarzschild shadow is circular. Increasing the black hole spin a, the shadow is slightly distorted and gets displaced to the right, meaning that prograde photons (coming from the left side as seen from the observer) are allowed to get closer to the black hole, while retrograde photons (coming from the right side) must keep farther.

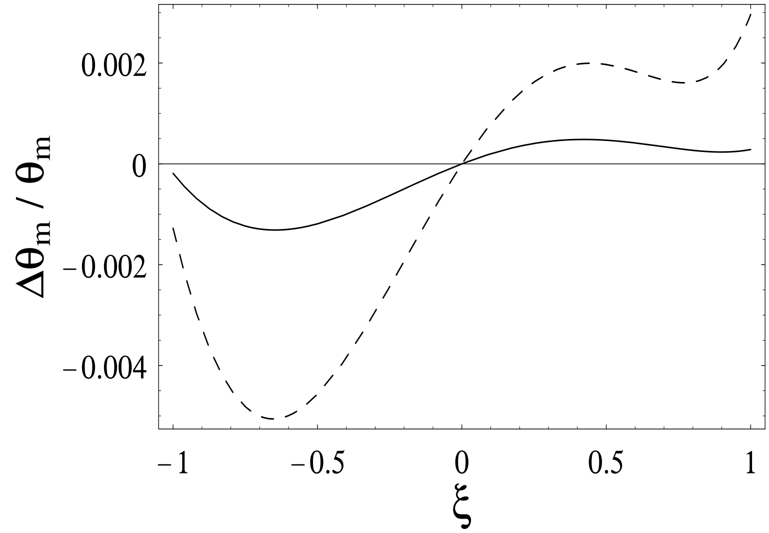

Figure 7.3: The relative variation in the radial distance of the black hole shadow shape between the exact solution and the second order approximation as a function of the azimuthal variable ξ. The solid line is for $a = 0.1$, the dashed line is for $a = 0.2$.

Here, for later convenience, we are introducing and making use of expressions expanded to the second order in a. However, the exact expression for the shadow can be easily derived, combining Eqs. (7.8)-(7.9) with Eqs. (7.15)-(7.16). Comparing the exact shadow to its second order approximation, we find that the latter works surprisingly well up to very high values of the black hole spin. In Fig. 7.3, we plot the relative error in the radial angular distance of the apparent shadow θ_m in the approximate solution w.r.t the exact one as a function of the variable ξ, which follows the azimuthal angle in the observer's sky. Up to $a \leq 0.28$, relative variations are well under 1%, at $a = 0.4$ we find an error of 2%, while in the extremal case $a = 0.5$ the error only reaches 5%. Such errors must be compared to the displacement of the relativistic rings from the shadow, see Sect. IV, and turn out to be negligible for the higher order critical curves up to large values of the spin.

7.3 Kerr lensing in the Strong Deflection Limit

It is useful to introduce the following parametrization:

$$\left\{ \begin{array}{l} \theta_1(\epsilon,\xi) = \theta_{1,m}(\xi)(1+\epsilon) \\ \theta_2(\epsilon,\xi) = \theta_{2,m}(\xi)(1+\epsilon) \end{array} \right. . \tag{7.19}$$

Varying ξ in the range $[-1,1]$ and ϵ in the range $[-1,\infty]$, we can obviously cover the whole upper half of the observer sky, since ξ establishes the anomaly of the light ray w.r.t. a reference axis in the sky (through Eqs. (7.17)-(7.18)) and ϵ fixes the angular distance from the center of the black hole.

In this paper, we are interested into light rays experiencing very large deflections by a Kerr black hole. These light rays reach the observer from directions (θ_1, θ_2) very close to the shadow. In the parametrization (7.19), they are thus described by light rays with very small positive ϵ, while keeping ξ in the whole range $[-1,1]$. The SDL amounts to performing the integrals in the geodesics equations (7.4)-(7.5), to the lowest orders in ϵ.

Now, we can easily derive the values of J and Q for these strongly deflected photons using Eqs. (7.15)-(7.16):

$$J(\xi,\epsilon) = \quad J_m(\xi)(1+\epsilon) \tag{7.20}$$

$$Q(\xi,\epsilon) = \quad Q_m(\xi)(1+2\epsilon). \tag{7.21}$$

Substituting these expressions in Eq. (7.7) and solving the equation $R=0$ for x_0, we get the closest approach distance as

$$x_0(\xi,\delta) = x_m(\xi)(1+\delta) \tag{7.22}$$

$$\delta = \sqrt{\frac{2\epsilon}{3}}\left[1-\frac{2}{3\sqrt{3}}a\,\xi - \frac{8}{27}a^2(4\xi^2-3)\right] \tag{7.23}$$

In general, we see that the relation between δ and ϵ depends on ξ, contrarily to what happens in the Schwarzschild case, which, by the way, is correctly recovered when a is set to zero (compare with Ref. [27]). In the resolution of the geodesics equation we will mostly use δ rather than ϵ. However, they can be immediately interchanged by Eq. (7.23) and its inverse.

7.3.1 Resolution strategy

Let us introduce our gravitational lensing configuration. As said before, we restrict to observers on the equatorial plane of the black hole at radial coordinate D_{OL}. We choose the zero of the azimuthal Boyer-Lindquist coordinate ϕ on the observer position. The source is assumed to be static at Boyer-Lindquist coordinates $(D_{LS},\vartheta_s,\phi_s)$. To make contact with previous works, we call $\gamma=\phi_s-\pi$.

Our lens equations are provided by Eqs. (7.4)-(7.5), where we identify $\phi_f=0$, $\phi_0=\phi_s$. In these equations there are four different integrals to solve:

$$I_1 = 2\int_{x_0}^{\infty}\frac{dx}{\sqrt{R}} \tag{7.24}$$

$$I_2 = 2\int_{x_0}^{\infty}\frac{x^2+a^2-aJ}{\Delta\sqrt{R}}dx \tag{7.25}$$

$$J_1 = \pm\int\frac{1}{\sqrt{\Theta}}d\vartheta \tag{7.26}$$

$$J_2 = \pm\int\frac{csc^2\vartheta}{\sqrt{\Theta}}d\vartheta. \tag{7.27}$$

In the radial integrals I_1 and I_2 we have taken the higher extrema to be infinite, because we assume $D_{OL}, D_{LS} \gg 1$. As the two integrands go to zero as x^{-2} for $x\to\infty$, the relative errors committed in this approximation are of order D_{OL}^{-1} and D_{LS}^{-1} respectively. Moreover, since the only inversion point in the radial motion is x_0, the infalling pieces and the outgoing pieces of the integral are equal and we can solve the sign ambiguity considering only the outgoing pieces and putting a factor 2 in front of the integrals. The radial integrals I_1 and I_2 can then be solved using the SDL technique explained in Ref. [27]. In practice, considering photons with minimum distance very close to some x_m, and introducing the parametrizations (7.20), (7.21), (7.22), we can expand the integrals in terms of the parameter δ, introduced before. The leading terms diverge logarithmically as δ goes to zero, while the next-to-leading order terms are constants in δ. The details of this procedure are reported in Appendix A. Here we just rewrite the final results

$$I_1 = \quad -a_1\log\delta + b_1 \tag{7.28}$$

$$I_2 = \quad -a_2\log\delta + b_2, \tag{7.29}$$

where the coefficients a_i and b_i are functions of a and ξ. Their expansions to second order in a are reported in Appendix A.

As regards the angular integrals (7.26)-(7.27), it is convenient to introduce the new variable $\mu = \cos\vartheta$. The final results, expanded to second order in a are functions of ξ and the source position $\mu_s = \cos\vartheta_s$. They are reported with a full derivation in Appendix A. We will just recall them in the following sections when we need them.

Once all integrals are calculated, we have to solve Eqs. (7.4)-(7.5) in terms of the source coordinates (γ, μ_s), so that they are in the lens map form

$$\left\{ \begin{array}{l} \mu_s = \mu_s(\delta, \xi) \\ \gamma = \gamma(\delta, \xi) \end{array} \right. . \tag{7.30}$$

Since all transformations from (γ, ϑ_s) to (γ, μ_s) and from (θ_1, θ_2) to (δ, ξ) are non-singular (except for the points $\xi = \pm 1$), the singularities of the Jacobian of the map (7.30) represent gravitational lensing critical points.

In the following sections, we will calculate the critical curves and the caustics of the Kerr gravitational lens order by order. Then we will describe the lens mapping in a neighborhood of a generic caustic, deriving the images position and magnification.

7.4 Derivation of the relativistic caustics

7.4.1 Zero order caustics

Sending a to zero, we must recover the Schwarzschild results, i.e. that critical curves are concentric rings corresponding to point-like caustics aligned on the optical axis, alternatively located behind and in front of the black hole. Of course, as $a \to 0$, all expressions are considerably simplified, and it is possible to follow calculations without too much effort.

Reading all the zero-order results for the integrals in Appendix A, Eq. (7.4) becomes

$$\begin{aligned} -2\log\delta \quad & +2\log[12(2-\sqrt{3})] = \\ & = \pm\arcsin\frac{\mu_s}{\sqrt{1-\xi^2}} + m\pi. \end{aligned} \tag{7.31}$$

Defining the new variable

$$\psi = -2\log\delta + 2\log[12(2-\sqrt{3})], \tag{7.32}$$

Eq. (7.31) can be easily solved as

$$\mu_s = \pm\sqrt{1-\xi^2}\sin\psi. \tag{7.33}$$

The second lens equation (7.5) now reads

$$\gamma = -(m-1)\pi \mp \arctan\frac{\mu_s\xi}{\sqrt{1-\mu_s^2-\xi^2}}. \tag{7.34}$$

Using Eq. (7.33) to eliminate μ_s, we find

$$\gamma = -(m-1)\pi - \arctan\left[\xi\tan\psi\right]. \tag{7.35}$$

The number m appearing in this equation is the integer part of $(\psi/\pi + 1/2)$ and must be interpreted as the number of inversions in the polar motion of the photon.

Eqs. (7.33) and (7.35) represent the lens equations for a Schwarzschild black hole without the classical identification of the equatorial plane with the source-lens-observer plane. We can recover the results of Ref. [27] imposing that the motion takes place on the equatorial plane, i.e. setting $\xi = 1$. Then we have $\mu_s = 0$ (the source must coherently lie on the equatorial plane) and $\gamma = -\psi + \pi$. The quantity $\psi - \pi$ represents the deflection angle of a photon approaching the Schwarzschild black hole at a distance $x_0 = x_m(1 + \delta)$. Eqs. (7.33) and (7.35) can also be obtained from the traditional planar treatment by a trivial rotation by an angle $\arccos \xi$ of the reference plane around the optical axis using some spherical trigonometry.

Now we can easily calculate the Jacobian of our lens map. We find

$$\frac{\partial \mu_s}{\partial \xi} = \mp \frac{\xi}{\sqrt{1-\xi^2}} \sin\psi \tag{7.36}$$

$$\frac{\partial \mu_s}{\partial \psi} = \pm \sqrt{1-\xi^2} \cos\psi \tag{7.37}$$

$$\frac{\partial \gamma}{\partial \xi} = -\frac{\tan\psi}{1+\xi^2 \tan^2\psi} \tag{7.38}$$

$$\frac{\partial \gamma}{\partial \psi} = -\frac{\xi \sec^2\psi}{1+\xi^2 \tan^2\psi} \tag{7.39}$$

and

$$D = \frac{\partial \mu_s}{\partial \xi}\frac{\partial \gamma}{\partial \psi} - \frac{\partial \mu_s}{\partial \psi}\frac{\partial \gamma}{\partial \xi} = \pm \frac{\sin\psi}{\sqrt{1-\xi^2}}. \tag{7.40}$$

The critical curves are the solutions of the equation $D = 0$, which, in our case, simply gives

$$\psi_{cr} = k\pi. \tag{7.41}$$

The critical ψ does not depend on ξ. Recalling that ψ is just a function of δ expressed by Eq. (7.32), we have

$$\delta_{cr} = 12(2-\sqrt{3})e^{-k\pi/2}. \tag{7.42}$$

Switching to ϵ by Eq. (7.23), we have

$$\epsilon_{cr} = 216(2-\sqrt{3})^2 e^{-k\pi}. \tag{7.43}$$

Then, recalling the meaning of ϵ by Eq. (7.19) and taking $\theta_{1,m}$ and $\theta_{2,m}$ from Eqs. (7.17)-(7.18), we finally find

$$\begin{array}{l} D_{OL}\theta_{1,cr}(\xi) = -\frac{3\sqrt{3}\xi}{2}\left[1+\epsilon_{cr}(k)\right] \\ D_{OL}\theta_{2,cr}(\xi) = \pm\frac{3\sqrt{3}}{2}\sqrt{1-\xi^2}\left[1+\epsilon_{cr}(k)\right] \end{array}, \tag{7.44}$$

that is a series of rings parameterized by ξ, slightly larger than the shadow of the black hole, in full agreement with Refs. [46, 103, 26, 27]. The critical curves are labelled by the number k. We shall refer to k as the critical curve order or the caustic order, when we consider the corresponding caustic.

Coming to the caustics, inserting Eq. (7.41) in the lens equations Eqs. (7.33)-(7.35) and noting that the number of inversions in polar motion is $m = k$, we find

$$\mu_s = 0, \quad \gamma = -(k-1)\pi. \tag{7.45}$$

The caustics are points aligned on the optical axis. For odd k they are behind the black hole, while for even k they are in front of the black hole (retro-lensing caustics). In the Schwarzschild limit, the number of loops performed by photons forming critical images of order k is just $(k-1)/2$. However, this is not exactly true for spinning black holes, as we shall see in the next section. So, it is better to think of the order of the critical curve k as the number of inversions in the polar motion done by photons associated to it.

Of course, the first caustic for $k = 1$ is the classical weak field limit one, which is outside the range of the SDL approximation, so we cannot expect to recover the Einstein ring radius putting $k = 1$ into Eq. (7.44) (the first caustic is no longer described even by the weak field approximation if the source is close to the black hole). However, as shown in Refs. [27, 33], the SDL approximation works better and better for higher k, starting from the first retro-lensing caustic in $k = 2$. It is these caustics that we are going to study in the following sections. In particular, we will find out how they are displaced and deformed by the black hole spin, obtaining a full analytic description of their shape.

7.4.2 First order caustics

Up to now we have just re-obtained all the Schwarzschild black hole results in a more complicated form, starting from Kerr geodesics equations and sending a back to zero. Now, we shall introduce first order corrections to our lens equations, re-deriving the critical curves and the caustics. We anticipate that the caustics get displaced from the optical axis in the azimuthal direction, though remaining point-like.

Using the first order terms of the radial and angular integrals from the Appendix A, we can add the terms proportional to a in the equations (7.33), (7.35). The inversion of the μ_s equation can be easily performed order by order in a. Then, repeating the same steps of the previous section, we find

$$\mu_s = \pm\sqrt{1-\xi^2}\sin\psi \pm \frac{4a\xi}{3\sqrt{3}}\sqrt{1-\xi^2}\sin\psi \tag{7.46}$$

$$\begin{aligned}\gamma = \; & -(m-1)\pi - \arctan\left[\xi\tan\psi\right] \\ & -\frac{4a}{3\sqrt{3}}\left[\psi + \frac{\xi^2\tan\psi}{1-(1-\xi^2)\sin^2\psi}\right. \\ & \left. -\tan\psi + 3\sqrt{3}\log(2\sqrt{3}-3)\right].\end{aligned} \tag{7.47}$$

Note that for ψ close to $m\pi + \pi/2$ and ξ close to zero, the first order correction to μ_s may bring it to absolute values larger than 1. As μ_s is the cosine of the polar angle, these values are unphysical. This inconsistency comes out because, when we solve for μ_s order by order, we expand the arcsin function in points very close to the extrema of its definition range, where the arcsin is not analytic. Then, the linear approximation obviously takes us out of the interval $[-1, 1]$. The dangerous values of ψ and ξ correspond to nearly polar trajectories where the final direction is very close to one of the two poles. However, as we shall see, the highest magnification for the relativistic images is obtained when the source is close to a caustic. Luckily, the caustics lie at $\mu \simeq 0$ for an equatorial observer, so that we will always work very far from these dangerous regions. This danger will become effective for very high order caustics, which may become very large, as we shall see in the next subsection.

Now we can calculate the derivatives of the lens equation as before. The Jacobian reads

$$D = \pm\frac{\sin\psi}{\sqrt{1-\xi^2}}\left(1 + \frac{8a\xi}{3\sqrt{3}}\right), \tag{7.48}$$

which tells us that the critical curves are still described by Eq. (7.41) even at first order. This means that there is no correction to the critical δ (7.42) of the previous section. The fact that we do not get any corrections to δ does not mean that the shape of the critical curves is not altered by the black hole spin at first order. Indeed going back from δ to ϵ we get a first order correction, according to Eq. (7.23). Moreover, the shadow shape is modified according to Eqs. (7.17)-(7.18).

Then, to first order, the critical curves are

$$\begin{array}{rl} D_{OL}\theta_{1,cr}(\xi) = & -\frac{3\sqrt{3}\xi}{2}\left(1+\epsilon_{cr}\right) \\ & +2a\left[1+\epsilon_{cr}(1-\xi^2)\right] \\ D_{OL}\theta_{2,cr}(\xi) = & \pm\frac{3\sqrt{3}}{2}\sqrt{1-\xi^2}\left[1+\epsilon_{cr}\right] \\ & \pm 2a\epsilon_{cr}\xi\sqrt{1-\xi^2} \end{array}, \tag{7.49}$$

with ϵ_{cr} still given by Eq. (7.43).

Also the caustics are modified. In fact, plugging $\psi_{cr} = k\pi$ into Eqs. (7.46)-(7.47), we find

$$\mu_s = 0 \tag{7.50}$$

$$\gamma = -(k-1)\pi - 4a\left[\frac{k\pi}{3\sqrt{3}} + \log(2\sqrt{3}-3)\right] \tag{7.51}$$

The caustics are still fully confined to the equatorial plane, they are still point-like, but they are displaced from the optical axis. The displacement is negative, which means that the caustics drift clockwise if we look at the Kerr black hole from the northern pole. So, we can say that if a source lies on a caustic point of order k, prograde light rays perform more than $(k-1)/2$ loops while retrograde light rays perform less than $(k-1)/2$ loops. The number of inversions in the polar motion is still k. Higher order caustics are more displaced, because of the k dependence in Eq. (7.51). Of course, as said before, this formula correctly describes all caustics except for the weak field one, corresponding to $k = 1$. Going to second order in a we will describe the full shape of the caustics.

7.4.3 Second Order Caustics

At first order in a the caustics still remain point-like, while it is known that they get a finite extension when a is different from zero [115, 28]. So, it is necessary to proceed to second order. To the right hand side of Eqs. (7.46)-(7.47) we have to add the following quantities respectively:

$$\begin{aligned} \delta\mu_s^{(2)} &= \pm\frac{\sqrt{1-\xi^2}}{108\sqrt{3}}a^2 \times \\ &\left[12\sqrt{3}(1-\xi^2)\psi_n\cos\psi - \sqrt{3}(1+31\xi^2)\sin\psi \right. \\ &\left. -\sqrt{3}(1-\xi^2)\sin 3\psi\right] \end{aligned} \tag{7.52}$$

$$\begin{aligned} \delta\gamma^{(2)} &= \frac{2a^2}{27\xi^2}(1-\xi^2)(23\xi^2-4)\arctan(\xi t) \\ &+\frac{2}{9}a^2\xi(16-\psi_n) - \frac{1-\xi^2}{9(1+\xi^2t^2)}a^2\xi\left[(1+t^2)\psi_n\right. \\ &\left.+\frac{t}{3}\left(23-\frac{8}{\xi^2}-16\frac{1+t^2}{1+\xi^2t^2}\right)\right] \end{aligned} \tag{7.53}$$

where $t = \tan\psi$ and $\psi_n = 5\psi + 8\sqrt{3} - 20$.

Note that a term directly proportional to ψ appears in Eq. (7.52) through ψ_n. This is another danger for the approximation, since for very large ψ, i.e. photons performing several loops around the black hole, $\delta\mu_s^{(2)}$ may become even larger than 1. This break-down sets the true limit to the applicability range of the perturbative expansion in a, which gets smaller and smaller for photons making many loops. However, the brightest images are formed by photons associated to critical images of low order. For these images, as we shall see, the range of applicability of the perturbative expansion is considerably large.

Now let us find out the corrections to the critical curves. Once we have calculated all derivatives of the lens equations and written the Jacobian to the second order in a, we set

$$\psi = k\pi + a^2 \delta\psi, \tag{7.54}$$

as we already know the zero order critical curve and we know that there is no correction at the first order. Then we easily get rid of all the trigonometric functions and the final Jacobian reads

$$D = \pm \frac{(-1)^k a^2}{9\sqrt{1-\xi^2}} \left[9\,\delta\psi - (92 - 24\sqrt{3} - 15k\pi)(1-\xi^2) \right]. \tag{7.55}$$

The $(-1)^k$ is a consequence of the expansions of the trigonometric functions, while the double sign inherited by the Jacobian at all orders depends on the fact that the (ϵ, ξ) parametrization only covers half of the observer sky and we are forced to introduce a double sign in the equation for μ_s.

The equation $D = 0$ gives the second order correction to the critical ψ in a very simple form

$$\delta\psi = \frac{92 - 24\sqrt{3} - 15k\pi}{9}(1-\xi^2). \tag{7.56}$$

Now we can remount the complete second order expansion of the critical curves, which reads

$$\begin{array}{rl} D_{OL}\theta_{1,cr}(\xi) = & -\frac{3\sqrt{3}\xi}{2}\left(1+\epsilon_{cr}\right) \\ & +2a\left[1+\epsilon_{cr}(1-\xi^2)\right] \\ & -\frac{\xi a^2}{\sqrt{3}}\left\{\xi^2 - 2 + \left[\frac{15}{2}k\pi(1-\xi^2)\right.\right. \\ & \left.\left. +\frac{176}{3} - 12\sqrt{3} + \left(\frac{179}{3} - 12\sqrt{3}\right)\xi^2\right]\epsilon_{cr}\right\} \\ D_{OL}\theta_{2,cr}(\xi) = & \pm\frac{3\sqrt{3}}{2}\sqrt{1-\xi^2}\left[1+\epsilon_{cr}\right] \\ & \pm 2a\epsilon_{cr}\xi\sqrt{1-\xi^2} \\ & \pm\frac{\sqrt{1-\xi^2}}{\sqrt{3}}a^2\left\{\xi^2 + \left[\frac{15}{2}k\pi(1-\xi^2)\right.\right. \\ & \left.\left. +12\sqrt{3} - 54 + \left(\frac{179}{3} - 12\sqrt{3}\right)\xi^2\right]\epsilon_{cr}\right\} \end{array} . \tag{7.57}$$

Here, again, we have $k\pi$ terms which become large for higher order critical curves.

Finally, let us calculate the caustics at the second order in a. Plugging Eq. (7.54) with (7.56) into the lens equations, we find

$$\mu_s = \pm(-1)^k r_c (1-\xi^2)^{3/2} \tag{7.58}$$

$$\begin{aligned} \gamma = & -(k-1)\pi - 4a\left[\frac{k\pi}{3\sqrt{3}} + \log(2\sqrt{3}-3)\right] \\ & + r_c \xi^3, \end{aligned} \tag{7.59}$$

where we define

$$r_c = \frac{2}{9}a^2(5k\pi + 8\sqrt{3} - 36). \tag{7.60}$$

The analytical expressions of the Kerr black hole caustics, given by Eqs. (7.58)-(7.59) to the second order in the black hole spin a, represent a major achievement of this paper. Before discussing their shape and all the physical implications, it is a good idea to test our formulae by comparing them to the results obtained by alternative methods. In Ref. [28], the intersections of the caustics with the equatorial plane were found using the SDL approximation only, without any limitation for the black hole spin. The first test is to analytically expand the formulae of Ref. [28] to the second order in a, without using any numerical integrations. Indeed, we get the same expressions as in Eq. (7.59), evaluated for $\xi = \pm 1$. Furthermore, we can draw in the same plot the intersections of the caustics with the equatorial plane as calculated in this paper along with those calculated in Ref. [28]. Rather than making two separate plots for prograde and retrograde photons, we can make a

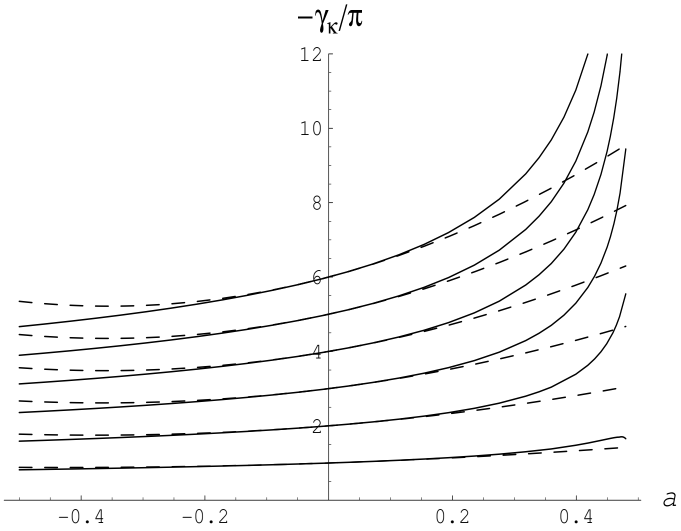

Figure 7.4: Comparison between the intersections of the caustics with the equatorial plane as calculated in Ref. [28] without the perturbative approximation for the black hole spin (solid lines) and the ones calculated in the present paper (dashed lines). The plot refers to the caustics of order $2 \leq k \leq 7$.

unique plot, letting a vary in the range $[-0.5, 0.5]$ and keeping the values of Eq. (7.59) for $\xi = 1$. So, the left side of the plot ($a < 0$) represents the intersections for retrograde photons and the right side ($a > 0$) represents the intersections of prograde photons. We see in Fig. 7.4 that the second order approximations (dashed lines) follow the exact expressions of Ref. [28] very accurately. We can estimate that for lower order caustics the perturbative approximation works up to $a \simeq 0.3$, while for the last caustic in the plot ($k = 7$) we have to stop at $a \simeq 0.1$. In any case, the validity range is impressively large, reaching values of the black hole spin comparable to the extremal case. This encourages us to make extensive and confident use of the second order approximation for a full description of Kerr lensing phenomenology.

Now, let us discuss the shape and the extension of Kerr lensing caustics. Looking at Eq. (7.58), it is interesting to note that the upper half of the critical curve is mapped in the lower half of the caustic for odd k, while it is mapped in the upper half if k is even. As already found numerically in Ref. [115], the caustics have the characteristic astroid shape shown in Fig. 7.5, common to all tangential caustics after the breaking of the axial symmetry. The four cusps are in $\xi = \pm 1$ and $\xi = 0$ choosing different signs for μ_s.

The caustics have the same extension in γ and μ. We recall that γ is just the azimuthal angle of the Boyer-Lindquist coordinates taken from the reference axis starting from the black hole and going in the direction opposite to the observer, while μ is the cosine of the polar angle ϑ. As said before, we can trust our results as long as the perturbative terms remain small. In this regime, $\mu \simeq \frac{\pi}{2} - \vartheta$. Then, we deduce that the caustics have the same extension in the azimuthal and in the polar direction.

The extension is parameterized by the quantity r_c, which is the semi-axis of the caustic. We see that it grows with the black hole spin a and with the caustic order k. Thus, for higher caustic orders, the perturbative approximation fails for smaller and smaller values of a, while it remains good for lower order caustics. This was already noted while commenting Fig. 7.4.

The drift from the optical axis of the caustic is given by the first order term in Eq. (7.59). Indicating it by $\Delta\gamma$, in Tab. 1 we report the obtained values for the first 6 relativistic caustics, starting from $k = 2$, for values of the black hole spin going up to $a = 0.2$. We see that the drift may

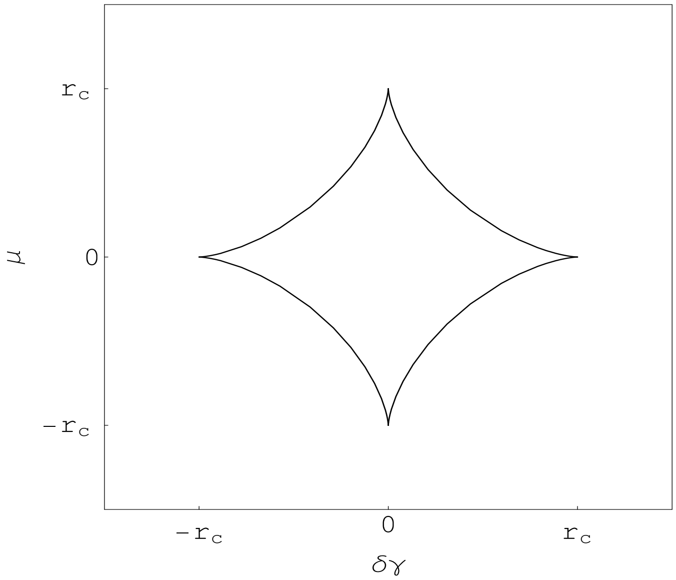

Figure 7.5: The typical caustic in Kerr gravitational lensing has the astroid shape and the same angular extension r_c (given by Eq. (7.60)) along the azimuthal and the polar direction.

	a=0.01	a=0.05	a=0.1	a=0.2
$\Delta\gamma_2$	0.018	0.088	0.18	0.35
$\Delta\gamma_3$	0.042	0.21	0.42	0.84
$\Delta\gamma_4$	0.066	0.33	0.66	1.3
$\Delta\gamma_5$	0.09	0.45	0.9	1.8
$\Delta\gamma_6$	0.11	0.57	1.14	2.3
$\Delta\gamma_7$	0.14	0.69	1.39	2.8

Table 7.1: Drift (in radians) of the caustics of order k with $2 \leq k \leq 7$, for different values of a.

	a=0.01	a=0.05	a=0.1	a=0.2
$r_{c,2}$	0.00021	0.0052	0.021	0.082
$r_{c,3}$	0.00056	0.014	0.056	0.22
$r_{c,4}$	0.0009	0.023	0.09	0.36
$r_{c,5}$	0.0013	0.031	0.13	0.5
$r_{c,6}$	0.0016	0.04	0.16	0.64
$r_{c,7}$	0.002	0.05	0.2	0.78

Table 7.2: Radius (in radians) of the caustics of order k with $2 \leq k \leq 7$, for different values of a.

become very large, amounting to several radians already for the 5th order caustic, while still in a regime where the perturbative solution is valid. For higher order caustics, the number of loops may be significantly different from the planar orbit result $(k-1)/2$. Another important consideration is that we do not need perfect alignment between source, lens and observer to have gravitational lensing. To enhance the images associated with a critical curve of order k, the source must align with the corresponding order k caustic, which may be well off the optical axis. Moreover, the relativistic images are not enhanced all at at the same time, since caustics of different order move far away each other.

In Table 2 we report the radii of the first 6 relativistic caustics for different values of a. The extension of the caustics is of second order in a and thus remains much smaller than the drift, reaching some tenth of radians in the perturbative regime. Outside of this regime, it is difficult to know what would happen to higher order caustics. Would their vertical extension saturate before reaching the poles or would they wrap around the pole? Would they meet each other and make transitions to more complicated structures? The answers to these questions need further research, both analytically and numerically. We just want to remark that the finite extension of relativistic caustics is of striking importance for phenomenology, as will be clear in the next sections.

7.5 Gravitational lensing near caustics

The description of the caustics is the fundamental step for a full description of gravitational lensing. In this section we will give a complete analytic resolution of the Kerr lens equation for sources close to relativistic caustics.

The starting point is the second order lens equations, built adding (7.52) to (7.46) and (7.53) to (7.47). Let us consider a source whose distance from the k-th order caustic is of order a^2 (thus being comparable to the caustic size). Then its position can be expressed in the following way

$$\mu_s = a^2 \delta\mu_s \tag{7.61}$$

$$\gamma = \gamma_{cau}^{(1)} + a^2 \delta\gamma, \tag{7.62}$$

where $\gamma_{cau}^{(1)}$ is the caustic position at the first order in a, expressed by Eq. (7.51). Correspondingly, the images associated to the critical curve of order k will be enhanced. They will be described by

$$\psi = k\pi + a^2 \delta\psi. \tag{7.63}$$

Substituting Eqs. (7.61)-(7.63) in the lens equations, the zero and first order terms cancel out and we are only left with the second order terms

$$\begin{aligned} \delta\mu_s = \; & S\frac{(-1)^k}{9}\sqrt{1-\xi^2}\,[9\,\delta\psi \\ & +(1-\xi^2)(5k\pi + 8\sqrt{3} - 20)\Big] \end{aligned} \tag{7.64}$$

$$\begin{aligned}\delta\gamma = & -\frac{\xi}{9}\left[9\,\delta\psi - 32\right. \\ & \left. +(3-\xi^2)(5k\pi + 8\sqrt{3} - 20)\right].\end{aligned} \tag{7.65}$$

This is the Kerr lens equation close to the caustic of order k. S is just a sign which takes into account the fact that the (ψ, ξ) parametrization only covers half of the observer sky. So, $S = +1$ for the upper half of the observer sky and $S = -1$ for the lower half. We can easily check that the Jacobian (7.55) is just a^2 times the Jacobian of this lens equation

$$\frac{D}{a^2} = \frac{\partial(\delta\mu_s)}{\partial\xi}\frac{\partial(\delta\gamma)}{\partial(\delta\psi)} - \frac{\partial(\delta\mu_s)}{\partial(\delta\psi)}\frac{\partial(\delta\gamma)}{\partial\xi}. \tag{7.66}$$

The surprisingly simple form of the lens equation encourages its analytical resolution. The $\delta\gamma$ equation can be easily solved for $\delta\psi$:

$$\delta\psi = -\frac{\delta\gamma}{\xi} + \frac{1}{9}\left[32 - (3-\xi^2)(5k\pi + 8\sqrt{3} - 20)\right]. \tag{7.67}$$

Plugging this expression into the $\delta\mu_s$ equation, we can write it in the form

$$\delta\mu_s\xi = -S(-1)^k\sqrt{1-\xi^2}(\delta\gamma + x_c\xi), \tag{7.68}$$

where $x_c = r_c/a^2$ and r_c is the semi-axis of the caustic as defined by Eq. (7.60). Squaring both sides we get a fourth order equation for ξ

$$x_c^2\xi^4 + 2x_c\delta\gamma\xi^3 + (\delta\gamma^2 + \delta\mu_s^2 - x_c^2)\xi^2 - 2x_c\delta\gamma\xi - \delta\gamma^2 = 0. \tag{7.69}$$

The real solutions of this equation are images for a source in $(\gamma_{cau}^{(1)} + a^2\delta\gamma, a^2\delta\mu_s)$. It is easy to check that we have two images if the source is outside the caustic and four images if it is inside.

Once we have found the solutions of the squared equation, we have to go back to the original equation (7.68). Each root of Eq. (7.69) satisfies Eq. (7.68) only with one choice of S. This determines the half-sky where the image appears. It is the upper half if $S = 1$ and the lower half if $S = -1$. Then, we can easily calculate the value of $\delta\psi$ for each image through (7.67) and then go back to ϵ by Eqs. (7.32) and (7.23). Finally we can write the images as

$$\begin{aligned}D_{OL}\theta_1 = & -\frac{3\sqrt{3}}{2}\xi(1+\epsilon_{cr}) + 2a[1 + \epsilon_{cr}(1-\xi^2)] \\ & +\frac{a^2\xi}{6\sqrt{3}}[12 - 6\xi^2 + \epsilon_{cr}(76 - 82\xi^2 + 27\delta\psi)]\end{aligned} \tag{7.70}$$

$$\begin{aligned}D_{OL}\theta_2 = & \, S\frac{3\sqrt{3}}{2}\sqrt{1-\xi^2}\left[(1+\epsilon_{cr}) + \frac{4}{3\sqrt{3}}a\xi\epsilon_{cr}\right. \\ & \left. +\frac{a^2}{27}(6\xi^2 - \epsilon_{cr}(48 - 82\xi^2 + 27\delta\psi))\right],\end{aligned} \tag{7.71}$$

with ξ and $\delta\psi$ solving Eqs. (7.64)-(7.65).

In the particular case $\delta\mu_s = 0$ (source on the equatorial plane), the solutions are $\xi = \pm 1$ and $\xi = \delta\gamma/x_c$ (double root). The first two solutions are two images staying on the equatorial plane, which are physical for any value of $\delta\gamma$. The other two are acceptable only if $|\delta\gamma| \leq x_c$ because ξ is defined in the range $[-1, 1]$. This is in agreement with the fact that x_c represents the caustic semi-axis. These two images form symmetrically w.r.t. the equatorial plane, grazing the critical curve from the outside. When these additional images are present, the former two are inside the critical curve, while when they are absent the remaining images are one inside and the other outside of the critical curve so that global parity is conserved in caustic crossing.

On the other hand, if $\delta\gamma = 0$, we have the solutions $\xi = 0$ (double root) and $\xi = \pm\sqrt{1 - (\delta\mu_s/x_c)^2}$. The first two form very close to the polar direction on opposite sides of the critical curve, while the last two are real only for $|\delta\mu_s| < x_c$. They form symmetrically w.r.t. the polar direction and graze the critical curve from the inside. As before, things work in such a way that global parity is conserved.

Now let us make an example with a physical source and a physical black hole. Sgr A* has a mass of 3.61×10^5 solar masses. Let us suppose that its spin is $a = 0.02$ (Liu & Melia estimate $a = 0.044$ [91], but different methods point to different values). Then we are able to calculate the caustic positions and shapes. As a source, consider a star with a radius $R_S = 3R_\odot$ at $200AU$ from Sgr A*. This is the order of magnitude of the periapse distance of the observed stars orbiting Sgr A*, like S2 or S14 [56]. In Fig. 7.6 we show what we would see if this star approaches the first retro-lensing caustic. The position of this caustic is in $\gamma = 177.98°$, so slightly displaced from the optical axis. This means that the source should be almost in front of the observer, very close to the optical axis. On the left panels of Fig. 7.6 we show several positions of the source relative to the caustic, as seen by the black hole. Notice that with these values of a, source radius and distance the size of the source is comparable to that of the caustic. On the right panels, we show the corresponding images and the shadow in dashed style. We see that when the source is far from the caustic (top panels) there are two small images. The bigger one is below the black hole if the source is above the equatorial plane (we recall that this is normal in a retro-lensing situation). When the source approaches the caustic (second row panels), the two images do not lie on opposite sides w.r.t the black hole. This distortion is a consequence of the axial symmetry breaking. When the source enters the caustic, two more images form (third and fourth row panels). If the source orbits with a velocity of the order of the circular orbit speed $\sqrt{GM/D_{LS}}$, the whole caustic crossing takes 3.4 hours, much longer than the typical times of the primary caustic crossing, which takes just few seconds [115]. Furthermore, since the higher order caustics are much more extended, the probability of caustic crossing is much higher.

In Fig. 7.7 we have shown the case where the same source approaches the first relativistic standard lensing caustic ($k = 3$), which now is displaced to $\gamma = 4.8°$ on the right of the black hole. As this caustic is larger, the source now looks smaller compared to the caustic, as we see in left panels. When the source is far from the caustic (top panels), there are two images, the bigger one being on the same side of the source (standard lensing situation). As the sources approaches, the images and the black hole are no longer on the same line (second row panels), then formation of two new images takes place (third and fourth row panels). In this case, the caustic crossing takes 9.2 hours, for a source velocity equal to the circular orbit velocity.

Fig. 7.8 zooms on two images generated by different sources in the caustics $k = 2$ and $k = 3$. The first source generates the outer tangential arc while the second source generates the inner tangential arc. This is because the more loops the photons perform, the closer they get to the black hole. Then higher order images appear closer and closer to the shadow. What astonishes of this picture is the tremendously small thickness of the arcs. These may be greatly elongated and even form full rings if the source is larger than the caustic, but their radial size is really very small. In Figs. 7.6-7.7, we had to exaggerate the thickness in order to show them in a more evident way. The next section will be devoted to the calculation of the length and the thickness of the arcs, i.e. the magnification of the images.

7.5.1 Magnification

In standard weak field gravitational lensing the magnification is the ratio between the angular area of an image and the angular area of the source if no lensing occurred. This does not necessarily make sense when high deflection takes place, since the side of the source seen by the black hole is generally different from the side seen by the observer. Then, if the source does not emit isotropically, a magnification calculated in the standard way would not give the correct ratio between the brightness of the image and that of the source. For example, in the retrolensing situation, the source is in front of the black hole. So the photons going towards the black hole leave the source from the side opposite

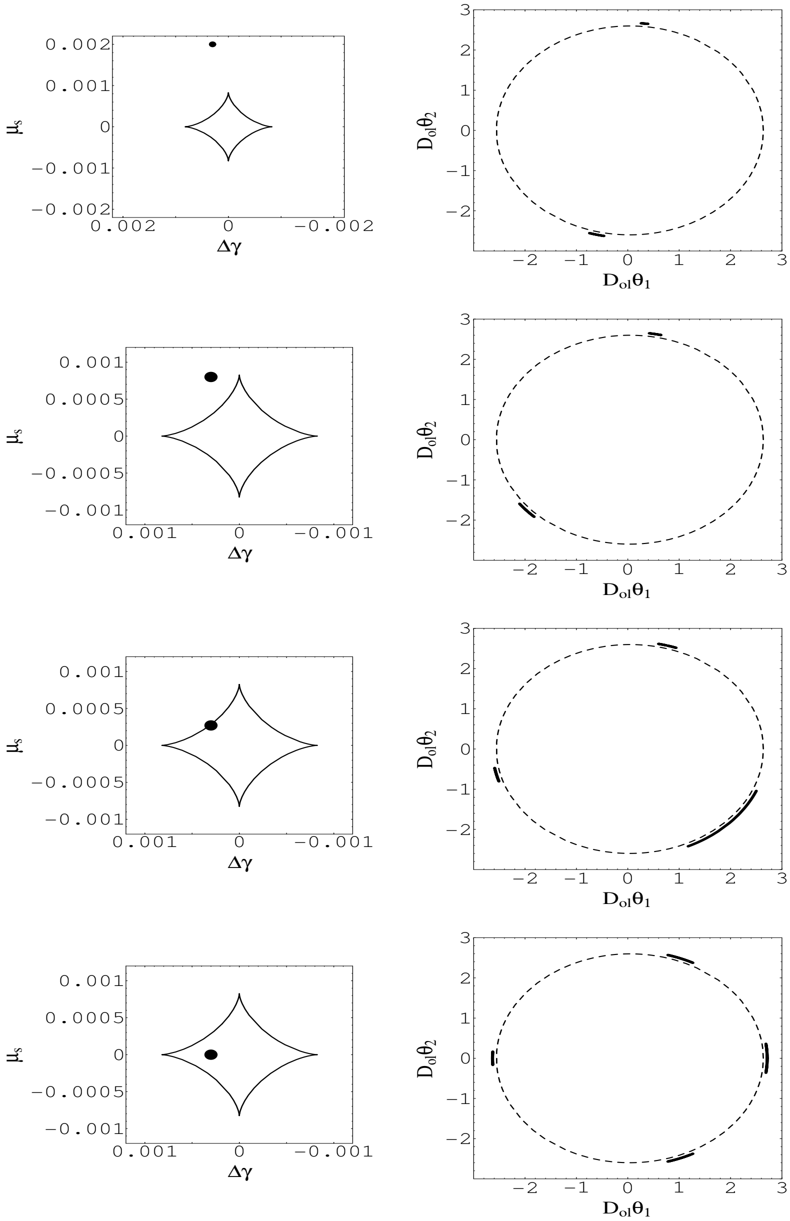

Figure 7.6: Formation of the images for a source approaching the first restrolensing caustic ($k = 2$). On the left we show several positions for a source and on the right we have the corresponding images around the shadow (in dashed style). The thickness of the images has been exaggerated to make them more evident.

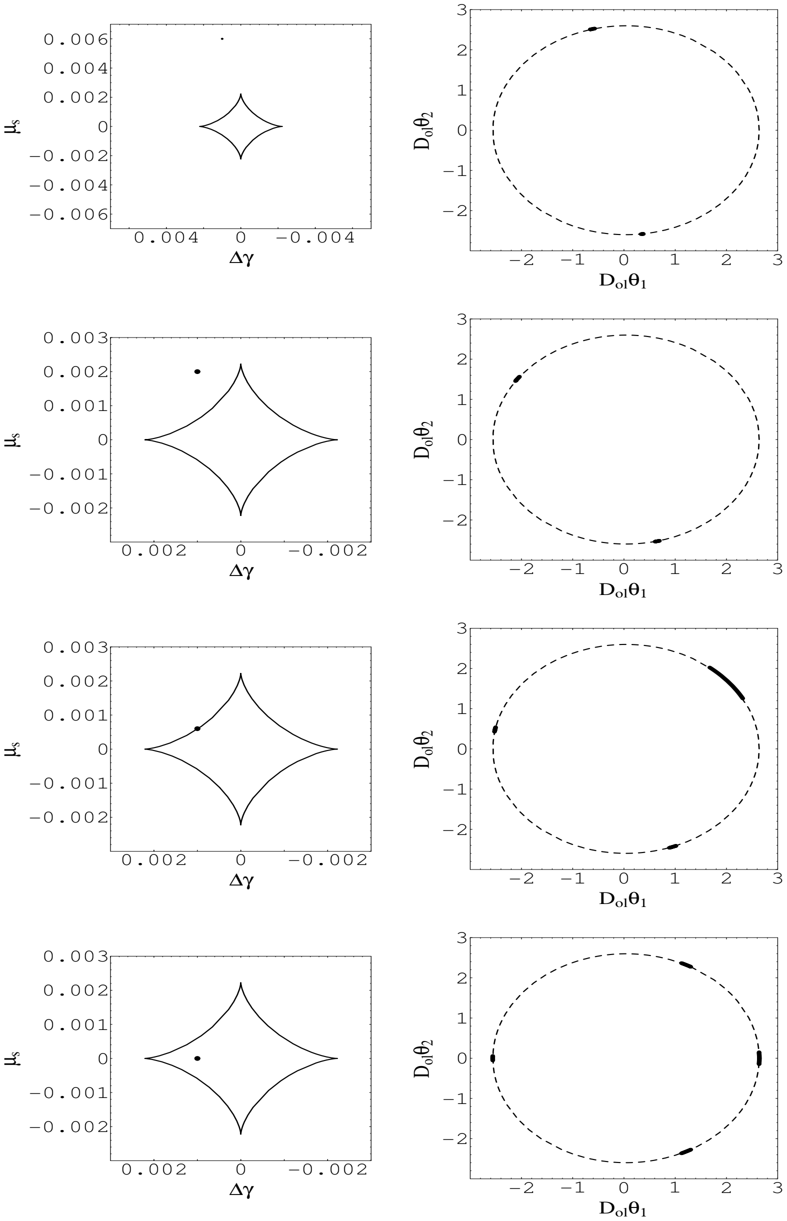

Figure 7.7: Formation of the images for a source approaching the first relativistic standard lensing caustic ($k = 3$). On the left we show several positions for a source and on the right we have the corresponding images around the shadow (in dashed style). The thickness of the images has been exaggerated to make them more evident.

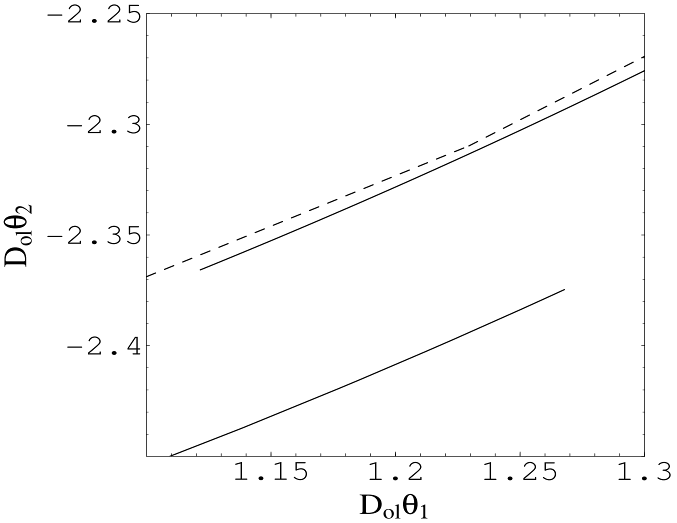

Figure 7.8: A zoom very close to the shadow border (in dashed style), showing at the same time the images of two sources, one being in the $k = 2$ caustic (outer tangential arc) and the other being in the $k = 3$ caustic (inner tangential arc).

to the one seen by the observer. For simplicity, in this section we shall assume that the source emits isotropically. The formulae can be easily corrected in the case this does not happen. The isotropic emission hypothesis ensures that the source as seen by the observer is simply D_{LS}^2/D_{OS}^2 smaller than as seen by an observer in the black hole position in the absence of the lens.

The angular area of the image in the observer sky is simply $d\theta_1 d\theta_2$. The angular area of the source in the black hole Boyer-Lindquist coordinates is $|\sin\vartheta_s d\gamma d\vartheta_s| = d\gamma d\mu_s$, when the source is very far from the black hole. Then, the magnification matrix is just the Jacobian matrix of the lens map in the form

$$\left\{ \begin{array}{l} \gamma = \gamma(\theta_1, \theta_2) \\ \mu_s = \mu_s(\theta_1, \theta_2) \end{array} \right. . \tag{7.72}$$

Yet, we have Eqs. (7.64)-(7.65) in the form

$$\left\{ \begin{array}{l} \delta\gamma = \delta\gamma(\delta\psi, \xi) \\ \delta\mu_s = \delta\mu_s(\delta\psi, \xi) \end{array} \right. \tag{7.73}$$

and Eqs. (7.70)-(7.71) in the form

$$\left\{ \begin{array}{l} \theta_1 = \theta_1(\delta\psi, \xi) \\ \theta_2 = \theta_2(\delta\psi, \xi) \end{array} \right. \tag{7.74}$$

Then we can find the Jacobian matrix of Eq. (7.72) as

$$\frac{\partial(\gamma, \mu_s)}{\partial(\theta_1, \theta_2)} = a^2 \frac{\partial(\delta\gamma, \delta\mu_s)}{\partial(\delta\psi, \xi)} \left[\frac{\partial(\theta_1, \theta_2)}{\partial(\delta\psi, \xi)}\right]^{-1}, \tag{7.75}$$

where we have used the matrix notation

$$\frac{\partial(y_1, y_2)}{\partial(x_1, x_2)} = \left(\begin{array}{cc} \frac{\partial y_1}{\partial x_1} & \frac{\partial y_1}{\partial x_2} \\ \frac{\partial y_2}{\partial x_1} & \frac{\partial y_2}{\partial x_2} \end{array} \right) \tag{7.76}$$

and we have noted that $d\gamma = a^2 d(\delta\gamma)$ and $d\mu_s = a^2 d(\delta\mu_s)$.

Then writing the explicit expression of the elements of J is straightforward, once we correctly take care of all the signs. We will not write them here, but we shall give the two eigenvalues of the Jacobian matrix

$$\lambda_r = \frac{2D_{OL}}{3\sqrt{3}\epsilon_{cr}} \tag{7.77}$$

$$\lambda_t = \frac{2D_{OL}}{3\sqrt{3}(1+\epsilon_{cr})}D_0 \tag{7.78}$$

with D_0 being proportional to the Jacobian studied in the former section (7.55)

$$D_0 = \pm\sqrt{1-\xi^2}D = \frac{(-1)^k a^2}{9}\left[9\,\delta\psi - (92-24\sqrt{3}-15k\pi)(1-\xi^2)\right]. \tag{7.79}$$

Since ϵ_{cr} is fixed by the caustic order k, λ_r is always positive, while λ_t vanishes whenever D_0 does. This condition is fulfilled when Eq. (7.56) holds, i.e. on critical images. It is possible to show that the two eigenvectors associated to λ_r and λ_t respectively become radial and tangential in the limit $a \to 0$. So, when the source is close to a caustic, all images are elongated in a direction nearly tangential to the critical curve, as already noticed in the previous subsection. We shall call λ_r and λ_t radial and tangential eigenvalues respectively, though they are such only in the limit $a \to 0$, actually.

Finally, we can write the radial and tangential magnification of the images w.r.t. the source as seen by the observer. These are

$$\mu_r = \frac{D_{OS}}{D_{LS}}\frac{1}{\lambda_r} = \frac{D_{OS}}{D_{LS}}\frac{3\sqrt{3}\epsilon_{cr}}{2D_{OL}} \tag{7.80}$$

$$\mu_t = \frac{D_{OS}}{D_{LS}}\frac{1}{|\lambda_t|} = \frac{D_{OS}}{D_{LS}}\frac{3\sqrt{3}(1+\epsilon_{cr})}{2D_{OL}|D_0|}. \tag{7.81}$$

Of course, the total magnification is $\mu = \mu_r\mu_t$. A good check is to reduce this formula in the Schwarzschild limit to compare with Refs. [104, 26, 27, 29], and in the equatorial limit, to compare with Ref. [28]. The first limit is obtained sending a to zero keeping the source position $(a^2\delta\gamma, a^2\delta\mu_s)$ fixed. This is equivalent to put x_c to zero in Eqs. (7.69), (7.67). Then the images are in

$$\xi = \pm\delta\gamma/\sqrt{\delta\gamma^2+\delta\mu_s^2} \tag{7.82}$$

$$\delta\psi = -\frac{16\delta\mu_s^2}{9(\delta\gamma^2+\delta\mu_s^2)} \mp \sqrt{\delta\gamma^2+\delta\mu_s^2}. \tag{7.83}$$

Substituting in Eq. (7.81), we find

$$\mu_{Sch} = \frac{D_{OS}^2}{D_{LS}^2 D_{OL}^2}\frac{27\epsilon_{cr}(1+\epsilon_{cr})}{4a^2\sqrt{\delta\gamma^2+\delta\mu_s^2}}. \tag{7.84}$$

Identifying $a^2\sqrt{\delta\gamma^2+\delta\mu_s^2}$ with the misalignment of the source with the point-like caustic position, we exactly find the magnification of Refs. [104, 29].

The equatorial limit is recovered when $\delta\mu_s = 0$. Then we have two equatorial images plus two non-equatorial images if the source is inside the caustic. The two equatorial images are described by

$$\xi = \pm 1 \tag{7.85}$$

$$\delta\psi = -r_c \mp \delta\gamma. \tag{7.86}$$

Inserting these values in Eq. (7.81), we find

$$\mu_{eq} = \frac{D_{OS}^2}{D_{LS}^2 D_{OL}^2}\frac{27\epsilon_{cr}(1+\epsilon_{cr})}{4a^2|\delta\gamma \pm r_c|}, \tag{7.87}$$

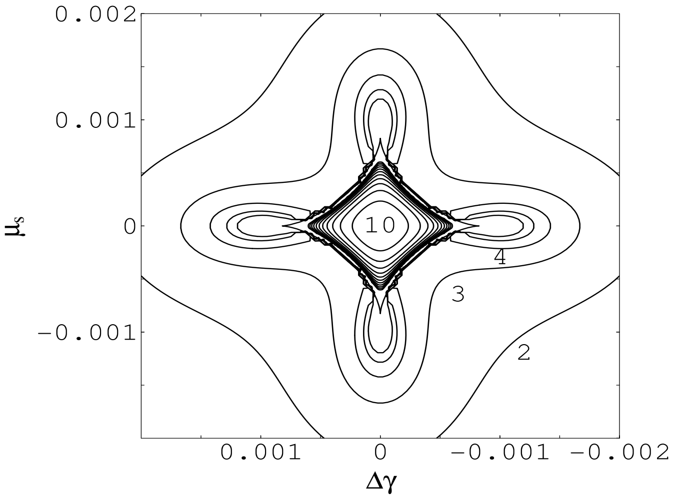

Figure 7.9: Tangential magnification map centered on the $k = 2$ caustic (the first retro-lensing caustic) for $a = 0.02$ and $D_{LS} = 100AU$.

which is the leading term close to the equatorial cusps as found in Ref. [28].

The magnification of relativistic images is usually very low. This is expected by the fact that a very small perturbation in the photon trajectory may completely change its final direction. Referring to a source at 100AU from Sgr A*, by Eq. (7.80) we find a radial magnification

$$\mu_r^{(2)} = 5.3 \times 10^{-5} \left(\frac{100AU}{D_{LS}} \right) \tag{7.88}$$

$$\mu_r^{(3)} = 2.3 \times 10^{-6} \left(\frac{100AU}{D_{LS}} \right) \tag{7.89}$$

for the relativistic images of order 2 and 3 respectively. These very low values, which are independent (at lowest order) of the distance of the source from the caustic, justify the very thin arcs of Fig. 7.8.

The tangential magnification diverges when the source crosses a caustic. However, at most the images may merge to form a full Einstein ring, which gives the maximal tangential magnification. Dividing the angular area of a circular corona of radius $3\sqrt{3}(1+\epsilon_{cr})/(2D_{OL})$ and thickness $\mu_r(2R_S)/D_{OS}$ by the angular area of the source $\pi(R_S/D_{OS})^2$, we obtain the maximal total magnification

$$\begin{aligned} \mu_{max}^{(2)} = & \frac{1}{R_S} \frac{D_{OS}^2}{D_{LS}} \frac{27\epsilon_{cr}(1+\epsilon_{cr})}{D_{OL}^2} = \\ & 8.7 \times 10^{-3} \left(\frac{R_S}{R_\odot} \right)^{-1} \left(\frac{D_{LS}}{100AU} \right)^{-1}. \end{aligned} \tag{7.90}$$

$$\begin{aligned} \mu_{max}^{(3)} = & \frac{1}{R_S} \frac{D_{OS}^2}{D_{LS}} \frac{27\epsilon_{cr}(1+\epsilon_{cr})}{D_{OL}^2} = \\ & 3.8 \times 10^{-4} \left(\frac{R_S}{R_\odot} \right)^{-1} \left(\frac{D_{LS}}{100AU} \right)^{-1}. \end{aligned} \tag{7.91}$$

In Fig. 7.9 we show a map of the tangential magnification centered on the first retro-lensing caustic (the caustic order is $k = 2$) for $a = 0.02$. To get the total magnification map, it is necessary to multiply the values on this map by the radial magnification (7.88), which is practically constant in a the neighborhood of the caustic. It is interesting to note that the tangential magnification is greater than one in a large region surrounding the caustic. This means that the cross section for the generation of large relativistic tangential arcs is quite high. This is a very important characteristic of relativistic images that we are going to exploit in the next section when discussing their observability.

For a source at the center of the caustic, we have an Einstein cross where all images have the same magnification. Then the total magnification takes a very simple expression

$$\mu_c = \frac{D_{OS}^2}{D_{LS}^2 D_{OL}^2} \frac{27\epsilon_{cr}(1+\epsilon_{cr})}{r_c} \tag{7.92}$$

where r_c is the semi-axis of the caustic as defined by Eq. (7.60).

7.6 Perspectives for observations

The relativistic images appear just outside the shadow of the black hole. In order to distinguish them, we need a resolution of the order of μas. The present world record has been achieved with Very Long Baseline Interferometry (VLBI) in the mm band and amounts to 18 μas [88]. However, in this band, there are no good compact candidate sources around Sgr A* for gravitational lensing. More interesting are the infrared and especially the X-ray band.

7.6.1 Infrared band

In the infrared K-band, centered at $\lambda = 2.2$ μm, the exinction by interstellar dust allows good observations of the stellar environment around Sgr A* [56]. Many stars have been detected and followed during their orbital motion around Sgr A*, providing the best dynamical constraints on its mass distribution. Surprisingly, these stars are of early spectral types, leaving open the question on the presence of such young stars in the galactic center. In the K-band, these stars have magnitudes between $m_K = 13$ and $m_K = 16$.

As regards the angular resolution in the K-band, the VLT units can be combined to perform interferometry observations with an equivalent baseline of 200 m and a maximal angular resolution of 2.2 mas (http://www.eso.org/projects/vlti). Some space missions performing nulling interferometry (TPF, http://www.terrestrial-planet-finder.com; DARWIN, http://ast.star.rl.ac.uk/darwin) should be launched in the near future. According to the mission designs, some spacecraft should fly in formation at distances of the order of tens of meters. A futuristic development of such idea might lead to much higher resolutions. The baseline needed for 1μas resolution is of the order of hundreds of kilometers. High precision formation flying may be achieved by laser ranging and microthrusters in the wake of what is being studied for LISA (http://lisa.nasa.gov), where the distance between the spacecraft is 5 million km.

Some of the stars around Sgr A* may cross some caustics and generate bright relativistic images. However, they would be embedded in the flux coming from Sgr A* environment. In the quiescent state, Sgr A* flux in the K-band should have $m_K \geq 18.8$ [65]. The infrared emission of Sgr A* is believed to originate in the inner 10 Schwarzschild radii of the black hole [147], with the Schwarzschild radius being

$$R_{Sch} = \frac{2GM}{c^2} = 1.1{\times}10^{10} \text{ m}. \tag{7.93}$$

Then it is necessary to establish whether relativistic images can overcome the background flux. As conservation of surface brightness holds in gravitational lensing, the relativistic images must have the same surface brightness of the original source as seen by the observer,

$$I_S = \frac{L_S}{4\pi D_{OS}^2 \Omega_S}, \tag{7.94}$$

where L_S the intrinsic luminosity of the source, $D_{OS} \simeq 8$ kpc is the distance to the source and Ω_S is the angular area in the sky subtended by the source, which is $\Omega_S \simeq \pi (R_S)^2/D_{OS}^2$. For a source of 10 solar radii with $m_K = 15$, the surface brightness of the relativistic images is four order of magnitudes larger than that of Sgr A*.

However, relativistic images have a tiny angular area and their contribution to the number of photons collected by a pixel in a CCD detector may be very small. To get an idea of this fact, let us consider a CCD detector where every pixel collects energy flux from an angular area of size ω_p^2. If a relativistic image, in the form of a tangential arc of angular thickness $\omega_{arc} = \mu_r (2R_S)/D_{OS}$, lies on the pixel area, the flux received is $S \propto I_S(\omega_p \times \omega_{arc})$. On the other hand, the noise coming from the environment of Sgr A* to the single pixel is $N \propto I_{Sgr}\omega_p^2$. Then, the signal-to-noise ratio for a single pixel is

$$\begin{aligned} \frac{S}{N} &= \frac{I_S}{I_{Sgr}} \frac{\omega_p}{\omega_{arc}} && (7.95) \\ &\simeq 2.2 \left(\frac{\omega_p}{1\mu as}\right)^{-1} \left(\frac{R_S}{10R_\odot}\right)^{-1} \left(\frac{D_{LS}}{100AU}\right)^{-1}. && (7.96) \end{aligned}$$

i.e. a pixel with a tangential arc receives only twice more K-band photons than other pixels. The S/N could be improved by taking a smaller pixel size or stars with lower radii and higher brightness, but we cannot go very far. Taking into account absorption by the matter surrounding the black hole that would surely take place and fluctuations in the surface brightness of Sgr A*, we doubt that relativistic images of stellar sources can be actually detected in the K-band by present or near future technology.

7.6.2 X-ray band

In the X-rays, Chandra is leading very important observations discovering the physics of high energy electromagnetic sources in the central region of the Galaxy [15] with a resolution of the order of 0.5 arcseconds. The space mission project MAXIM (http://maxim.gsfc.nasa.gov) will represent a major leap toward high resolution, reaching the striking resolution of 0.1 μas. With such observational facility, a complete and detailed imaging of the black hole will be possible.

It is very interesting to consider that Sgr A* luminosity in the 2-10 keV band is 2×10^{33} ergs s^{-1}, which is much lower than expected if the black hole were accreting at the Eddington rate, i.e $L = 3\times10^{44}$ ergs s^{-1} [15]. There are several models for Sgr A* accretion. Models based on Bondi accretion (spherically symmetric inflow) predict the X-ray emission to be created in a region of the order of $10^2 R_{Sch}$ [96]. Models based on advection dominated flow [80] predict the emission to be dominated by cooler gas at larger radii, of the order of $10^4 R_{Sch}$.

Indeed, many X-ray sources have been detected in the neighbourhood of Sgr A*, with a luminosity comparable or even slightly higher than the supermassive black hole [102]. These sources are probably Low Mass X-ray Binaries (LMXB) which seem very numerous in the galactic center. The situation seems really appealing, since we have a population of bright compact sources, with possibly poor contamination from the intrinsic luminosity of Sgr A*. It is believed that the most of the X-ray emission from a LMXB comes from a region of tens of kilometers. Then we can assume $R_S \simeq 10^2$ km, with an X-ray flux of $L_S \simeq L_{Sgr} = 2\times10^{33}$ ergs s^{-1}. If we consider an emitting region of $10^2 R_{Sch}$ for Sgr A*, there are 14 orders of magnitude between the surface brightness of an LMXB and the surface brightness of the X-ray emission of the supermassive black hole environment. Then, the signal-to-noise ratio for a single pixel imaging a tangential arc, Eq. (7.95), is

$$\frac{S}{N} = 0.9\times10^6 \left(\frac{\omega_p}{1\mu as}\right)^{-1} \left(\frac{R_S}{100km}\right)^{-1} \left(\frac{D_{LS}}{100AU}\right)^{-1} \tag{7.97}$$

i.e. the signal in a pixel touched by a tangential arc is nearly 6 order of magnitudes higher than the noise from Sgr A* environment for a detector with the accuracy of 1 μas. The contamination from Sgr A* environment seems to be completely under control. Relativistic gravitational self-lensing of Sgr A* would just produce relativistic Einstein rings with the same surface brightness of Sgr A*. The only serious danger for photons coming from outside Sgr A* and deflected by the central black hole is absorption by the matter surrounding it. However, even if some absorption certainly occurs, it seems difficult to fill a gap of so many orders of magnitudes between the surface brightness of the relativistic images and that of Sgr A* without affecting the luminosity of Sgr A* as well.

Of course, the idea firstly proposed by Rauch & Blandford that some X-ray flares may be explained by lensing of nearby sources is fully plausible in this scenario [115].

7.7 Conclusions

In this paper we have made an analytical treatment of gravitational lensing by Kerr black holes in the strong deflection limit. In order to achieve our objective we have made three approximations.

The first one is the strong deflection limit approximation for all radial integrals. This is just an expansion of the elliptic integrals that result from integrations over the full radial motion of a photon. Restricting to photons suffering a very large deflection, for all the radial integrals we have only kept the leading term diverging as $\log \epsilon$ and the constant term (ϵ being the separation between the image and the shadow border as seen by the observer). As shown in several articles, this limit gives a very good approximation starting from photons deflected by an angle of order π [46, 104, 26, 33].

The second approximation has been to consider only small values of the black hole spin a. This has allowed us to take the Schwarzschild gravitational lensing as a starting point for the derivation of the corrections due to the presence of an intrinsic angular momentum of the black hole. As far as we could compare our results with available exact ones, we have verified a considerably wide applicability range of our approximation. For the first relativistic images, we can safely apply our treatment up to $a = 0.1$ ($a = 0.5$ being the extremal Kerr black hole in our units).

The third restriction has been to consider only equatorial observers. This considerably simplifies all calculations without affecting the complete investigation of the most significant physical situation, namely the black hole in Sgr A*. In fact, it is natural to assume that the equatorial plane of this supermassive black hole coincides with the galactic plane. In any case, a full investigation stepping beyond this restriction is in progress.

The first achievement of this paper has been the analytical description of the Kerr caustics. At the first order in a we find that they are just shifted along the equatorial plane still remaining point-like, while at second order they are resolved into typical diamond-shaped figures. We are thus able to calculate the position and the extension of the caustics for any order of relativistic images (as long as we remain in the perturbative regime). As stated in Sect. IV, the strong deflection limit treatment does not cover the primary caustic ($k = 1$ in our formulae), since this caustic is formed in the weak field regime for $D_{LS} \gg 1$ [115, 126]. With no regard to the lensing regime, the effect of the angular momentum of the deflector is similar, with caustics getting a diamond-shaped structure and drifting from the optical axis. Whereas magnification effects due to the primary caustic are very large, its size is very small, so that the formation of multiple images (which is the most evident manifestation of the presence of a non-negligible spin) is very difficult to achieve. The significant extension of relativistic caustics strongly enhances the cross-section for multiple images and puts them in a much better position for testing the Kerr nature of the black hole. It has to be remarked that our perturbative investigation still leaves open the possibility that metamorphosis may occur at large values of a. Though this has been numerically excluded for the primary caustic [115], it is possible that higher order caustics develop more complicated structures in a strongly non-pertubative regime.

The second achievement has been the analytical inversion of the lens mapping near the caustics, which has allowed us to draw fascinating pictures of the relativistic images generated by a hypothetical source close to a relativistic caustic.

However, the most important result has been the possibility of doing concrete analytical estimates of the size and luminosity of the relativistic images. The LMXBs surrounding Sgr A* provide an ideal population of sources, which may eventually bump into a relativistic caustic and generate appreciable relativistic images. This is because they are compact sources with very high surface brightness in the X-rays, compared to that of Sgr A*. This seems not to be the case for stellar sources in the infrared K-band, which have a too small surface brightness. Using our formulae for the magnification of relativistic images, we are entitled to claim that future space missions performing X-ray interferometry with resolutions of the order of 1 μas will see these relativistic images with high probability.

Chapter 8

Kerr black hole lensing for generic observers in the strong deflection limit [1]

We generalize our previous work on gravitational lensing by a Kerr black hole in the strong deflection limit, removing the restriction to observers on the equatorial plane. Starting from the Schwarzschild solution and adding corrections up to the second order in the black hole spin, we perform a complete analytical study of the lens equation for relativistic images created by photons passing very close to a Kerr black hole. We find out that, to the lowest order, all observables (including shape and shift of the black hole shadow, caustic drift and size, images position and magnification) depend on the projection of the spin on a plane orthogonal to the line of sight. In order to break the degeneracy between the black hole spin and its inclination relative to the observer, it is necessary to push the expansion to higher orders. In terms of future VLBI observations, this implies that very accurate measures are needed to determine these two parameters separately.

As predicted by General Relativity, photons passing near a black hole suffer deviations from their original trajectory. If the minimum distance between photon and black hole is much larger than the gravitational radius, a weak field approximation of the metric tensor is sufficient to describe the light deflection. Two images of the original source are then detected by the observer. On the other hand, photons passing very close to the black hole may suffer very large deviations without falling into the black hole. These photons may perform one or more loops around the black hole before reemerging in the observer direction, thus generating two infinite sets of relativistic images very close to the black hole shadow. It can be easily intuited that these relativistic images represent a unique probe to gain information on the very strong gravitational fields surrounding the black holes. Through their study it would be possible to learn the properties of black holes and get new insight on General Relativity in a strong field regime. The features of relativistic images will thus represent a possible challenge arena for alternative theories of gravitation.

Even though a general relativity approach to this subject typically results in involved equations and heavy numerical integrations, a surprisingly simple formula for the deflection angle induced by a Schwarzschild black hole in the Strong Deflection Limit (SDL) was proposed by Darwin [46] and revived in Refs. [92, 104, 26]. The logarithmic divergence of the deflection angle in the impact parameter was showed to be universal and valid for all spherically symmetric black holes [27], as every class of such black holes leads to the same expansion for the deflection angle, with coefficients depending on the specific form of the black hole metric. The SDL method was then applied to several classes of black holes, ranging from Reissner-Nordström to black holes in string theory, from braneworld black holes to wormholes [54]. By the SDL method it is thus possible to quantify the

---

[1] Published in [32]

observables related to relativistic images for any class of spherically symmetric black holes, allowing an easy comparison among different theories. For alternative methods, see Refs. [62, 143].

For spinning black holes, things do not work so easily. Starting from the geodesics equations in Kerr spacetime, that Carter [41] reduced to first order equations depending on four constants of motion, many numerical approaches have been developed to study and visualize such geodesics. Numerical efforts have also been profused in the context of gravitational lensing to investigate the apparent shape of the accretion disk of the black hole [92, 59, 144], the light curve of a star orbiting around it [45] and the structure of the caustics [115], which turned out to be extended and to have a 4-cusped astroid structure. Some interesting general results have recently been derived through Morse theory [76]. The extension of the SDL methodology to Kerr black holes was firstly performed in Ref. [28] and the SDL formula was recovered for photons lying near to the equatorial plane. Anyway the expansion coefficients had to be calculated numerically as functions of the lens spin.

A first step towards a complete analytical treatment of this subject was made in Ref. [31] (hereafter Paper I and entirely reported in chapter 7) where the lens equation was analytically solved in the limit of small values of the angular momentum of the black hole (denoted by a) and for observers lying on its equatorial plane. This last assumption, besides ensuring simpler equations, was justified by the fact that the most important black hole candidate (Sgr A*, firstly suggested in Ref. [143]) is hosted in the center of our Galaxy and presumably has a spin-axis perpendicular to the Galactic plane, where the solar system lies. The expansions for small values of the angular momentum allowed to use the Schwarzschild SDL formula as a starting point for the description of the deflection of light rays looping around a Kerr black hole.

This analytical approach provided very simple equations (which could even be inverted for sources near to a caustic) and a full description of the extended structure of the caustics, which were confirmed to have a 4-cusped structure, symmetric w.r.t. the equatorial plane and shifted from the optical axis. Only the first order caustic cannot be recovered in the SDL approach as it is formed in the weak deflection regime [115, 126]. It was also shown that the extension of relativistic caustics enhances the cross section for the creation of additional images, whose magnification is sensible in a relatively large region around the caustic. Direct observations of these relativistic images, which should be possible with the resolutions achieved by future projects, could test the Kerr nature of black hole lenses (see e.g. Refs. [33, 31] for updated discussions on observational perspectives). It is interesting to compare the lensing effect of a Kerr black hole to that of a Schwarzschild black hole embedded in an external gravitational field. Also in the latter case astroid caustics arise, though with different sizes and positions [34].

In this Paper we further investigate Kerr black hole lensing, getting rid of the *equatorial observer* hypothesis. In spite of the presence of a new parameter (the inclination of the spin axis relative to the line of sight, that we shall indicate by ϑ_o), the surprisingly simple structure of all analytical results is preserved. Our philosophy will be to try to confine all technicalities to appendix B or refer the reader to Paper I for more detailed derivations. This paper will thus keep its main focus on the implications of all results on observable quantities. What emerges from our study is that all observables (to the lowest order) just depend on $a \sin \vartheta_o$, that is the projection of the spin on a plane orthogonal to the line of sight. The consequences of this fact will be discussed in the conclusions in Section 7.

Our paper is structured as follows: in Section 2 we recall the main properties of Kerr geodesics. In Section 3, we trace the borders of the shadow of the Kerr black hole for all values of the observer declination. In Section 4 we apply the SDL to null Kerr geodesics illustrating the main strategy and referring to appendix B for the details. In Section 5 we derive the critical curves and caustics structure and in Section 6 we analyze the lens mapping in the neighbourhood of a caustic, finding the position and the magnification of the images, concluding with a discussion on the detectability of relativistic images.

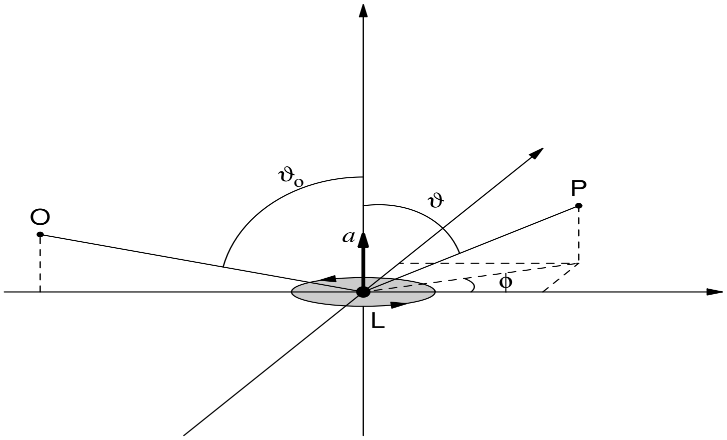

Figure 8.1: Boyer-Lindquist coordinates in a Kerr metric, also referred as spin-oriented coordinates in the text. L is the black hole with spin a. O is the observer and P is a generic point. The gray disk visualizes the equatorial plane of the black hole.

8.1 Kerr geodesics

In this section, we shall review the basics of Kerr geodesics and introduce the notations to be used throughout the paper. For more details on the physical meaning of all quantities, the reader may refer to Paper I or directly to Ref. [43].

The main subject of our paper is the Kerr black hole, whose metric in Boyer-Lindquist coordinates [24], $x^\mu \equiv (t, x, \vartheta, \phi)$ reads

$$\begin{aligned} ds^2 = & \frac{\Delta - a^2 \sin^2\vartheta}{\rho^2} dt^2 - \frac{\rho^2}{\Delta} dx^2 - \rho^2 d\vartheta^2 \\ & - \frac{\left(x^2+a^2\right)^2 - a^2 \Delta \sin^2\vartheta}{\rho^2} \sin^2\vartheta d\phi^2 \\ & + \frac{2ax \sin^2\vartheta}{\rho^2} dt d\phi \qquad (8.1) \\ \Delta = & x^2 - x + a^2, \qquad (8.2) \\ \rho^2 = & x^2 + a^2 \cos^2\vartheta. \qquad (8.3) \end{aligned}$$

Distances are measured in units of the Schwarzschild radius ($2MG/c^2 = 1$), ϑ and ϕ are the colatitude and azimuth respectively, x is the radial coordinate and a is the specific angular momentum of the black hole, running from 0 (Schwarzschild black hole) to 1/2 (extremal Kerr black hole) in our units.

We consider a static observer at Boyer-Lindquist coordinates $(D_{OL}, \vartheta_o, \phi_o)$. The distance between observer and black hole is thus D_{OL}, while the colatitude ϑ_o of the observer coincides with the inclination of the spin on the line of sight $\overline{OL}$. Exploiting the freedom to choose the zero of the azimuth, we set $\phi_o = \pi$. We will very often use the notation $\mu \equiv \cos\vartheta$. Thus we also define $\mu_o \equiv \cos\vartheta_o$. Fig. 8.1 illustrates Boyer-Lindquist coordinates for a generic point P and for the observer O in particular.

Lightlike geodesics can be expressed in the following form in terms of the first integrals of motion J and Q found by Carter [41]

$$\pm \int \frac{dx}{\sqrt{R}} = \pm \int \frac{d\vartheta}{\sqrt{\Theta}} \qquad (8.4)$$

$$
\begin{aligned}
\phi_f - \phi_i = \quad & a \int \frac{x^2 + a^2 - aJ}{\Delta\sqrt{R}} dx - a \int \frac{dx}{\sqrt{R}} \\
& + J \int \frac{\csc^2 \vartheta}{\sqrt{\Theta}} d\vartheta, \qquad (8.5)
\end{aligned}
$$

where

$$
\begin{aligned}
\Theta = \quad & Q + a^2 \cos^2 \vartheta - J^2 \cot^2 \vartheta \qquad (8.6) \\
R = \quad & x^4 + (a^2 - J^2 - Q)x^2 + (Q + (J - a)^2)x \\
& - a^2 Q, \qquad (8.7)
\end{aligned}
$$

and ϕ_i is the initial value of the azimuthal coordinate of the photon.

The roots of R represent inversion points in the radial motion. In gravitational lensing we consider photons coming from infinity, grazing the black hole and going back to infinity. For such trajectories there is only one inversion point x_0, representing the closest approach distance. The minimum allowed value of x_0 can be found solving the equations $R(x) = 0$ and $R'(x) = 0$ simultaneously. However, in Kerr black hole, we do not have a unique minimum closest approach x_m, but rather a continuous family of values which depend on the approach trajectory followed by the photon. In particular, it is possible to establish a relation among the minimum closest approach x_m and the corresponding values of the constants of motion J and Q, that we shall indicate by J_m and Q_m (see e.g. Ref. [43])

$$
J_m = \frac{x_m^2(2x_m - 3) + a^2(1 + 2x_m)}{a(1 - 2x_m)} \qquad (8.8)
$$

$$
Q_m = \frac{x_m^3 \left[2a^2 - x_m(x_m - 3/2)^2\right]}{a^2(x_m - 1/2)^2}. \qquad (8.9)
$$

x_m also represents the radius of the unstable circular photon orbit. This radius is fixed to 3/2 when $a = 0$ (Schwarzschild black hole). In the case of Kerr black holes, x_m may vary between two limiting values x_{m+}, x_{m-}, depending on the incoming direction of the photon. The two limiting values can be analytically obtained solving the equation $Q_m = 0$ (in fact, it is possible to show that gravitational lensing trajectories cannot be realized for $Q < 0$ [43]). To the third order in a, they read [31]

$$
x_{m\pm} = \frac{3}{2} \mp \frac{2}{\sqrt{3}} a - \frac{4}{9} a^2 \mp \frac{20}{27\sqrt{3}} a^3 + O(a^4). \qquad (8.10)
$$

For example, photons whose orbit lies on the equatorial plane may turn either in the same sense of the black hole (prograde photons) or in the opposite sense (retrograde photons). Prograde photons are allowed to get closer to the black hole, with a minimum closest approach given by x_{m+}, while retrograde photons must stay farther than x_{m-}, in order to be deflected without falling into the black hole. Photons whose orbit does not lie on the equatorial plane are characterized by intermediate values of x_m, with $Q_m > 0$. Thus x_m can be used to parametrize the family of unstable photon orbits allowed in Kerr metric or, equivalently, the incoming direction of the photon. The corresponding values of the constants of motion are uniquely determined by Eqs. (8.8) and (8.9).

Although exact expressions for x_{m+} and x_{m-} are available, it is convenient to start with a perturbative expansion *ab initio* in order to be prepared to face more complicated quantities in the following [31]. Throughout our treatment, only for x_m we need to push the expansion to the third order, in order to obtain some quantities to the second order in a.

8.2 The shadow of a Kerr black hole

The constants of motion J and Q have an immediate link to the position in the sky where the observer detects the photon. In fact, we can define angular coordinates (θ_1, θ_2) on the observer sky

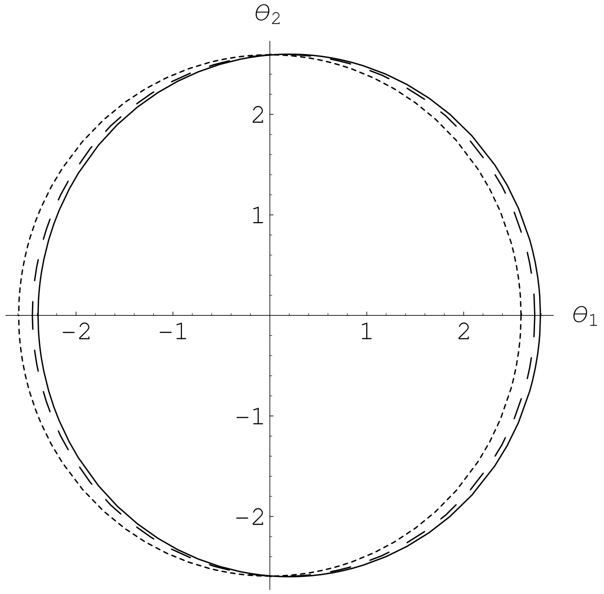

Figure 8.2: The shadow of the black hole in the observer sky for $a = 0.1$ and different values of the observer position ϑ_o. The solid line is for $\vartheta_o = \pi/2$ (equatorial observer), the dashed line is for $\vartheta_o = \pi/4$ and the dotted line is for $\vartheta_o = 0$ (polar observer).

centered on the black hole position. We choose the orientation of these coordinates in such a way that the spin axis of the black hole is projected on the θ_2-axis (see Fig.7.2).

As shown in Ref. [43], photons detected by the observer at angular coordinates (θ_1, θ_2) are characterized by constants of motion given by

$$J = -\theta_1 D_{OL} \sqrt{1-\mu_o^2}, \tag{8.11}$$

$$Q = \theta_2^2 D_{OL}^2 + \mu_o^2(\theta_1^2 D_{OL}^2 - a^2). \tag{8.12}$$

These relations can be easily recovered taking the limit for large distances in the equations of motion of the photon. They show that J can be identified with the component of the orbital angular momentum of the photon along the spin axis, whereas $Q + J^2 + \mu_o^2 a^2$ is the squared total angular momentum of the photon.

Note that, with our choice of (θ_1, θ_2), in the limit of equatorial observer $\mu_o = 0$, prograde photons ($J > 0$, $Q = 0$) are detected by the observer on the left side of the black hole, while retrograde photons ($J < 0$, $Q = 0$) are detected on the right side. Conversely, in the limit of polar observers ($\mu_o \to \pm 1$), the projected angular momentum J vanishes, while $Q \to (\theta_1^2 + \theta_2^2) D_{OL}^2 - a^2$.

Inverting Eqs. (8.11) and (8.12), we find the position (θ_1, θ_2) in the sky where the photon is detected with given constants of motion J and Q, apart from an ambiguity in the sign of θ_2

$$\theta_1 = -\frac{J}{D_{OL}\sqrt{1-\mu_o^2}}, \tag{8.13}$$

$$\theta_2 = \pm D_{OL}^{-1} \sqrt{Q + \mu_o^2 \left(a^2 - \frac{J^2}{1-\mu_o^2} \right)}. \tag{8.14}$$

These relations can be used to convert the locus (J_m, Q_m), parametrized by x_m according to Eqs. (8.8) and (8.9) in the (J, Q)-space, into a new one $(\theta_{1,m}, \theta_{2,m})$ in the observer sky. However, not all values of x_m in the range $[x_{m+}, x_{m-}]$ are acceptable. This can be easily understood, as photons lying on the equatorial plane can never reach non-equatorial observers. The reality condition for $\theta_{2,m}$ restricts x_m to the range $[x_{p+}, x_{p-}]$, where x_{p+} and x_{p-} are the roots of the equation $\theta_{2,m} = 0$. To third order in a, these quantities read

$$\begin{aligned} x_{p\pm} = & \frac{3}{2} \mp \frac{2}{\sqrt{3}} a \sqrt{1-\mu_o^2} - \frac{4}{9} a^2 (1+\mu_o^2) \\ & \mp \frac{4}{27\sqrt{3}} a^3 (5+6\mu_o^2) \sqrt{1-\mu_o^2} + O(a^4). \end{aligned} \tag{8.15}$$

Comparing with Eq. (8.10), we see that $x_{p\pm} \to x_{m\pm}$ in the limit $\mu_o \to 0$. On the other hand, when $\mu_o \to \pm 1$, the allowed range for x_m shrinks to a single value $x_p \to \frac{3}{2} - \frac{8}{9}a^2$. This witnesses that when the observer is on the polar axis the axial symmetry of the lensing configuration is restored and all unstable photon orbits have the same radius again.

When a vanishes, x_{p+} and x_{p-} both coincide with the Schwarzschild photon sphere radius, 3/2, while, when a is not zero, they are distinct and every value of x_m in the interval $[x_{p+}, x_{p-}]$ uniquely fixes the amplitude of the oscillation of the photon orbit on the equatorial plane, as we shall see later. On the basis of this consideration, in Paper I (with $\mu_o = 0$) we introduced a parametrization of x_m in the range $[x_{m+}, x_{m-}]$, replacing a with $a\xi$ in Eq. (8.10), with the parameter ξ varying in the range $[-1, 1]$.

In order to take into account the changes from Eq. (8.10) to (8.15), we have to update such parametrization, since it is not directly applicable to the case $\mu_o \neq 0$. Our new parametrization for x_m is

$$\begin{aligned} x_m = & \frac{3}{2} - \frac{2}{\sqrt{3}} a\xi \sqrt{1-\mu_o^2} - \frac{4}{9} a^2 (1+\mu_o^2) \\ & - \frac{4}{27\sqrt{3}} a^3 \xi (5+6\mu_o^2) \sqrt{1-\mu_o^2} + O(a^4). \end{aligned} \tag{8.16}$$

As ξ varies in the interval $[-1, 1]$ we get all possible values of x_m in the interval $[x_{p+}, x_{p-}]$. It will become clear later that ξ is strictly related to the position angle of the generic point in the observer sky.

With this parametrization, we can rewrite Eqs.(8.8)-(8.9) to the second order in a as

$$\begin{aligned} J_m(\xi) = & \frac{3\sqrt{3}}{2} \xi \sqrt{1-\mu_o^2} - a(1-\mu_o^2)(1+\xi^2) \\ & - a^2 \frac{\xi\sqrt{1-\mu_o^2}}{3\sqrt{3}} [5 - 2\xi^2 - 2\mu_o^2(1-\xi^2)], \end{aligned} \tag{8.17}$$

$$\begin{aligned} Q_m(\xi) = & \frac{27}{4} \left[1 - (1-\mu_o^2)\xi^2\right] \\ & - 3\sqrt{3} a\xi \sqrt{1-\mu_o^2} [1 + \mu_o^2 - (1-\mu_o^2)\xi^2] \\ & - a^2 [(1+\mu_o^2)^2 - 4(1-\mu_o^2)\xi^2 \\ & + 3(1-\mu_o^2)^2 \xi^4]. \end{aligned} \tag{8.18}$$

Notice that the presence of a in the denominators of Eqs.(8.8)-(8.9) allows ξ to be present already in the zero-order terms in Eqs.(8.17)-(8.18), permitting the use of the ξ-parametrization in Schwarzschild spacetime as well. However, since this parametrization has been introduced in a slightly different way w.r.t. Paper I, the expressions derived here cannot be directly compared to those of Paper I, except for those quantities that are independent of ξ. For example, eliminating ξ from Eqs. (8.17) and (8.18), one can derive an expression for the locus (J_m, Q_m) in the form $Q_m(J_m)$. Doing the same with the expressions of Paper I, one would indeed find the same function $Q_m(J_m)$ in the limit $\mu_o \to 0$.

Inserting Eqs. (8.17) and (8.18) in Eqs. (8.13)-(8.14) we get

$$\begin{aligned} D_{OL}\theta_{1,m} &= -\frac{3\sqrt{3}}{2}\xi + a\sqrt{1-\mu_o^2}(1+\xi^2) \\ &+a^2\frac{\xi}{3\sqrt{3}}[5-2\mu_o^2-2\xi^2(1-\mu_o^2)], \end{aligned} \tag{8.19}$$

$$\begin{aligned} D_{OL}\theta_{2,m} &= \pm\frac{3\sqrt{3}}{2}\sqrt{1-\xi^2} \mp a\xi\sqrt{1-\xi^2}\sqrt{1-\mu_o^2} \\ &\mp a^2\frac{\sqrt{1-\xi^2}}{3\sqrt{3}}[1+2\mu_o^2-2\xi^2(1-\mu_o^2)]. \end{aligned} \tag{8.20}$$

This locus is formed by the points in the observer sky where photons with minimum closest approach would show up. No gravitational lensing images are possible inside this locus, which is thus also known as the shadow of the black hole. In Fig. 8.2 we show it for different values of μ_o. Note that, to zero order, $\theta_{1,m} \propto -\xi$ and $\theta_{2,m} \propto \sqrt{1-\xi^2}$, justifying the identification of ξ with the cosine of the position angle in the (θ_1, θ_2) plane as taken from the opposite of the θ_1-axis. This fact facilitates the physical interpretation of the parameter ξ.

The shadow of the black hole is the first observable in extreme gravitational lensing by supermassive black holes. It thus deserves some further analysis in order to understand the effect of the spin and the observer position.

First we note that $\theta_{1,m}$ and $\theta_{2,m}$, to second order in a, satisfy the ellipse equation

$$\frac{(\theta_{1,m}-\theta_0)^2}{A_1^2} + \frac{\theta_{2,m}^2}{A_2^2} = 1 \tag{8.21}$$

with the origin shifted rightward by

$$\theta_0 = \frac{2a\sqrt{1-\mu_o^2}}{D_{OL}}, \tag{8.22}$$

and semiaxes given by

$$A_1 = D_{OL}^{-1}\left(\frac{3\sqrt{3}}{2} - \frac{a^2}{\sqrt{3}}\right) \tag{8.23}$$

$$A_2 = D_{OL}^{-1}\left(\frac{3\sqrt{3}}{2} - \frac{a^2}{\sqrt{3}}\mu_o^2\right). \tag{8.24}$$

By these analytical expressions for the shadow, we can make several considerations. The presence of a non-vanishing spin causes a slight distortion and a displacement of the shadow from the black hole position. When the observer lies on the spin axis ($\mu_o = \pm 1$), the axial symmetry is restored and the shadow returns to be centered on the black hole and circular. However, even in this limiting case, the radius of the shadow is no longer $3\sqrt{3}/2$ as in Schwarzschild, but it is slightly smaller, being $3\sqrt{3}/2 - a^2/\sqrt{3}$.

It has been proposed that the observation of the shape of the shadow of a black hole by VLBI may help to determine the parameters of a Kerr black hole, such as its mass, its angular momentum and the inclination of the spin [59, 148]. However, both in the shift θ_0 and in the ellipticity

$$e \equiv \frac{A_2 - A_1}{A_2} = \frac{2}{9}a^2(1-\mu_o^2) \tag{8.25}$$

the black hole spin and the observer declination appear in the same combination $a\sqrt{1-\mu_o^2} = a\sin\vartheta_o$, which represents the projection of the spin on a plane orthogonal to the line of sight. Thus it is impossible to determine both the absolute value of the spin and its inclination from the shape of the shadow. The only possibility is that we already know the distance D_{OL} and the mass of the black hole to such accuracy that we are able to extract a from a measure of the minor semi-axis A_1 solely. However, since the spin contribution to the major semi-axis is only of second order in a, we need a very high accuracy in the shadow observation in order to appreciate such a small contribution. For example, if $a = 0.1$, the spin contribution to A_1 is of order 0.2%. As already pointed in Ref. [148] by numerical examples, the disentanglement of a and ϑ_o is only possible for values of the black hole spin very close to the extremal case. By our perturbative formulae, we have justified this claim analytically. Of course, for high values of a, when higher orders contribute to determine the shape of the shadow, the degeneracy between a and ϑ_o can be broken, in agreement with what stated in Ref. [148].

It has been pointed out in Paper I that as long as we deal with Kerr black holes with spin smaller than $a = 0.2$, the perturbative approximation works surprisingly well. Then, the degeneracy between a and ϑ_o in the shadow of the black hole poses a serious difficulty to the determination of the parameters of the black hole by the simple observation of the shadow. As we shall see in the next sections, this degeneracy plagues all gravitational lensing observables in different degrees.

8.3 Kerr lensing in the Strong Deflection Limit

As in Paper I, we introduce the following parametrization of the observer sky

$$\left\{ \begin{array}{l} \theta_1(\epsilon,\xi) = \theta_{1,m}(\xi)(1+\epsilon) \\ \theta_2(\epsilon,\xi) = \theta_{2,m}(\xi)(1+\epsilon) \end{array} \right. . \tag{8.26}$$

Varying ξ in the range $[-1,1]$ and ϵ in the range $[-1,\infty]$, we can obviously cover the whole upper half of the observer sky, since ξ establishes the position angle of the light ray w.r.t. the $(-\theta_1)-$axis (through Eqs. (8.19) and (8.20)) whereas ϵ fixes the angular distance from the shadow of the black hole. In fact, in the following, ϵ will be generically referred to as the separation from the shadow of the black hole.

We are interested into light rays experiencing very large deflections by a Kerr black hole. These light rays reach the observer from directions (θ_1, θ_2) very close to the shadow. In the parametrization (8.26), they are thus described by light rays with very small positive ϵ, while keeping ξ in the whole range $[-1,1]$. The SDL amounts to performing the integrals in the geodesics equations (8.4)-(8.5), to the lowest orders in the separation from the shadow ϵ.

The values of the constants of motion J and Q, corresponding to such strongly deflected photons, can be found using Eqs. (8.11)-(8.12):

$$J(\xi,\epsilon) = \quad J_m(\xi)(1+\epsilon) \tag{8.27}$$

$$Q(\xi,\epsilon) = \quad Q_m(\xi)(1+2\epsilon) + 2a^2\epsilon\mu_o^2. \tag{8.28}$$

Substituting these expressions in Eq. (8.7) and solving the equation $R = 0$ for x_0, we get the closest approach distance as

$$x_0(\xi,\delta) = x_m(\xi)(1+\delta) \tag{8.29}$$

$$\delta = \sqrt{\frac{2\epsilon}{3}}\left[1 - \frac{2}{3\sqrt{3}}a\hat{\xi} + \frac{2}{27}a^2(10-\mu_o^2-14\hat{\xi}^2)\right] \tag{8.30}$$

where we have introduced the compact notation

$$\hat{\xi} = \xi\sqrt{1-\mu_o^2}. \tag{8.31}$$

As ϵ represents the separation of the image in the observer sky from the shadow of the black hole, δ represents the relative difference between the closest approach x_0 and the minimum closest approach $x_m(\xi)$ fixed by the position angle through ξ. It will be synthetically called approach parameter. As δ decreases, we expect the deflection to increase more and more. In the limit $\delta \to 0$, the photon is injected into the unstable orbit with radius $x_m(\xi)$. Conversely, photons with a large approach parameter are weakly deflected. Of course, the relation between ϵ and δ ensures that the SDL can be equivalently stated in terms of either of the two parameters.

Let us introduce our gravitational lensing configuration. As said before, the observer is at radial coordinate D_{OL}, at polar angle ϑ_o and azimuthal angle $\phi_o = \pi$. We will call optical axis the line connecting the lens and the observer. The source is assumed to be static at Boyer-Lindquist coordinates $(D_{LS}, \vartheta_s, \phi_s)$.

Our lens equations are provided by Eqs. (8.4)-(8.5), where we identify the final value of the azimuthal coordinate with the observer's one ($\phi_f = \phi_o = \pi$), and the initial value with the source's one $\phi_i = \phi_s$. In these equations there are two radial integrals and two angular integrals. The radial integrals are solved using the SDL technique and expanding all coefficients to second order in a, as in Paper I. The results of this procedure are reported in Appendix B. Similarly, the angular integrals are solved to second order in a in Appendix B.

Once all integrals are calculated, we have to solve Eqs. (8.4)-(8.5) in terms of the source coordinates (ϕ_s, μ_s), so that they are in the lens map form

$$\left\{ \begin{array}{l} \mu_s = \mu_s(\delta, \xi) \\ \phi_s = \phi_s(\delta, \xi) \end{array} \right. . \tag{8.32}$$

Note that the lens equation will be written in terms of the approach parameter δ and the position angle through ξ. Through Eqs. (8.30) and (8.26) we can then go back to the coordinates in the observer sky (θ_1, θ_2).

In the following sections, we will calculate the critical curves and the caustics of the Kerr gravitational lens order by order. The procedure is indeed identical to that described in Paper I, safe for the complication introduced by the additional parameter μ_o. However, once we manage to recast all equations in the best forms, the results remain very simple, so that a thorough discussion of the effects of spin and observer colatitude is possible.

8.4 Derivation of the relativistic caustics

8.4.1 Zero-order caustics

The first task is to recover the results for a Schwarzschild black hole, imposing the limit $a \to 0$.

Using the results of AppendixB to the zero-order, Eqs. (8.4) and (8.5) read respectively

$$\begin{aligned} \psi &= m\pi \mp \arcsin \frac{\mu_s}{\sqrt{1-\hat{\xi}^2}} \\ &\pm (-1)^m \arcsin \frac{\mu_o}{\sqrt{1-\hat{\xi}^2}}, \end{aligned} \tag{8.33}$$

$$\begin{aligned} \phi_s &= \pi - Sign[\xi] m\pi \pm \arctan \frac{\mu_s \hat{\xi}}{\sqrt{1-\mu_s^2-\hat{\xi}^2}} \\ &\mp (-1)^m \arctan \frac{\mu_o \hat{\xi}}{\sqrt{1-\mu_o^2-\hat{\xi}^2}}, \end{aligned} \tag{8.34}$$

where the new variable

$$\psi = -2\log\delta + 2\log[12(2-\sqrt{3})], \tag{8.35}$$

allows us to put the equations in a very compact form. ψ actually coincides with the deflection induced by a Schwarzschild black hole with the same mass of our Kerr black hole. On the ground of this connection, we shall often refer to ψ as "scalar deflection" in the following.

The double signs coming from the angular integrals must be treated as follows: if the photon moves out of the source increasing its initial value of μ, then we must choose the upper signs, otherwise we will select the lower signs. These double signs are the relics of those present in Eqs. (8.4) and (7.5). For more details about their origin, the reader is referred to the Appendix B. m represents the number of inversions in the polar motion of the photon.

Introducing the quantity

$$\psi_o = \mp(-1)^m \arcsin \frac{\mu_o}{\sqrt{1-\hat{\xi}^2}}, \tag{8.36}$$

we can easily solve Eqs. (8.33)-(8.34) w.r.t. ϕ_s and μ_s to get the zero-order lens equation

$$\begin{aligned} \mu_s &= \mp(-1)^m \sqrt{1-\hat{\xi}^2} \sin(\psi+\psi_o), && (8.37) \\ \phi_s &= \pi(1-m) + \arctan\left[\hat{\xi}\tan\psi_o\right] \\ &\quad - \arctan\left[\hat{\xi}\tan(\psi+\psi_o)\right]. && (8.38) \end{aligned}$$

Since the azimuth ϕ is a coordinate with period 2π, we have eliminated the $Sign[\xi]$ in front of $m\pi$ in Eq. (8.38). In the derivation of Eq. (8.38) from Eqs. (8.34) and (8.37), we have used the relations

$$\frac{\mu_s}{\sqrt{1-\mu_s^2-\hat{\xi}^2}} = \mp\tan(\psi+\psi_o) \tag{8.39}$$

$$\frac{\mu_o}{\sqrt{1-\mu_o^2-\hat{\xi}^2}} = \mp(-1)^m \tan\psi_o \tag{8.40}$$

and exploited the fact that the number of inversions in the polar motion is just the integer part of $(\psi+\psi_o+\pi/2)/\pi$.

Let us understand the meaning of the zero-order lens equations. Eq. (8.37) states that the photon performs symmetric oscillations on the equatorial plane (recall that $\mu \equiv \cos\vartheta$) with amplitude $\sqrt{1-\hat{\xi}^2}$, which depends on the observer declination and the trajectory chosen by the photon (polar $\xi=0$, equatorial $\xi=\pm1$ or whatever). The number of oscillations depends on the scalar deflection ψ, which diverges when the approach parameter $\delta\to0$. ψ_o is the initial condition of the oscillation, which depends on the observer declination. The double signs take into account the fact that the oscillations occur in opposite ways depending on the starting sign of $\dot{\mu}$.

Eq. (8.37) is the azimuthal motion of the photon. It can be better understood when we choose equatorial photons with $\hat{\xi}=1$. Then it just reduces to $\phi=\pi-\psi$, which states that the azimuthal shift is the scalar deflection minus π, as expected in this simple case. Different values of ξ need to be analyzed by some spherical trigonometry, in order to understand the trigonometric functions in Eq. (8.37).

After the zero order lens equation is constructed, we can study the structure of critical curves and caustics. The Jacobian of the lens map, D, can be easily calculated from (8.37) and (8.38). We find

$$\frac{\partial\mu_s}{\partial\xi} = \pm(-1)^m \frac{\hat{\xi}\sqrt{1-{\mu_o}^2}}{\sqrt{1-\hat{\xi}^2}} \sec\psi_o \sin\psi \tag{8.41}$$

$$\frac{\partial\mu_s}{\partial\psi} = \mp(-1)^m \sqrt{1-\hat{\xi}^2}\cos(\psi+\psi_o) \tag{8.42}$$

$$\frac{\partial\phi_s}{\partial\xi} = -\frac{\cos(\psi+\psi_o)\sec\psi_o\sin\psi}{\sqrt{1-\mu_o^2}} \tag{8.43}$$

$$\frac{\partial \phi_s}{\partial \psi} = -\frac{\hat{\xi}\sec^2(\psi+\psi_o)}{1+\hat{\xi}^2\tan^2(\psi+\psi_o)} \tag{8.44}$$

and using Eqs. (8.31) and (8.36), we finally have

$$D = \frac{\partial \mu_s}{\partial \xi}\frac{\partial \phi_s}{\partial \psi} - \frac{\partial \mu_s}{\partial \psi}\frac{\partial \phi_s}{\partial \xi} = \mp(-1)^m \frac{\sin\psi}{\sqrt{1-\xi^2}}. \tag{8.45}$$

Since all transformations from (ψ, ξ) to (θ_1, θ_2) are non-singular (except for the points $\xi = \pm 1$), the solutions of the equation $D = 0$ determine the critical curves. To zero order we have

$$\psi_k = k\pi. \tag{8.46}$$

As expected, the critical curves correspond to values of the scalar deflection that are multiples of π. Having introduced the most generic coordinate system for the black hole has not prevented us from recovering the Schwarzschild result. Through Eqs. (8.35), (8.30) and (8.26) we reconstruct the critical curves in the observer coordinates

$$\begin{array}{l} D_{OL}\theta_{1,k}(\xi) = -\frac{3\sqrt{3}\xi}{2}\left[1+\epsilon_k\right] \\ \\ D_{OL}\theta_{2,k}(\xi) = \pm\frac{3\sqrt{3}}{2}\sqrt{1-\xi^2}\left[1+\epsilon_k\right] \end{array}, \tag{8.47}$$

where

$$\epsilon_k = 216(2-\sqrt{3})^2 e^{-k\pi} \tag{8.48}$$

is the separation of the critical curve from the shadow.

We will refer to the integer number k as the critical curve (or caustic) order. Eqs. (8.47) describe a series of concentric rings, parametrized by ξ, slightly larger than the shadow of the black hole and whose radius $\frac{3\sqrt{3}}{2}(1+\epsilon_k)$ exponentially decreases to the shadow radius with increasing critical curve order.

The equations of the caustics are easily found introducing Eq. (8.46) into (8.37)-(8.38) and exploiting the fact that the number of inversions m coincides with k if $\psi = k\pi$. We have

$$\mu_s = (-1)^k \mu_o, \quad \phi_s = (1-k)\pi. \tag{8.49}$$

As already known, the Schwarzschild caustics are point-like and lie on the optical axis. They are in front of the black hole ($\mu_s = \mu_o$, with ϕ_s being an odd multiple of π) for even values of k (retrolensing caustics), and behind it ($\mu_s = -\mu_o$, with ϕ_s being an even multiple of π) for odd k (standard lensing).

The SDL description is limited to large deflections ($\psi \geq \pi$), thus working better and better for higher order caustics [27, 33]. It cannot be applied to the first order one ($k = 1$) whose full description can be derived in the weak deflection limit for sources sufficiently far from the lens. In what follows, we focus on caustics of order $k \geq 2$ and investigate how their structure is affected by the concomitant action of the lens spin and the observer declination.

8.4.2 First-order caustics

We now introduce first order corrections to the zero-order solutions found in the previous section. Starting from the results of Appendix B, we solve the lens equations perturbatively adding the first order terms to Eqs. (8.37)-(8.38), obtaining

$$\begin{aligned}\mu_s = \; & \mp(-1)^m \sqrt{1-\hat{\xi}^2}\sin(\psi+\psi_o) \\ & \mp(-1)^m \frac{2a\hat{\xi}}{3\sqrt{3}}\sqrt{1-\hat{\xi}^2}\cos\psi_o \sin\psi, \end{aligned} \tag{8.50}$$

$$\begin{aligned}\phi_s = \; & (1-m)\pi + \arctan\left[\hat{\xi}\tan\psi_o\right] \\ & -\arctan\left[\hat{\xi}\tan(\psi+\psi_o)\right] \\ & -\frac{4a}{3\sqrt{3}}\Big[\psi + 3\sqrt{3}\log(2\sqrt{3}-3) \\ & -\frac{1-\hat{\xi}^2}{2}\frac{\cos(\psi+\psi_o)\sin\psi\cos\psi_o}{1-(1-\hat{\xi}^2)\sin^2(\psi+\psi_o)}\Big]. \end{aligned} \tag{8.51}$$

The Jacobian of the lens equation to first order is

$$D = \mp(-1)^m \frac{\sin\psi}{\sqrt{1-\xi^2}}\left(1+\frac{2a\xi\sqrt{1-\mu_o^2}}{\sqrt{3}}\right), \tag{8.52}$$

which is always solved by Eq. (8.46), thus implying that the scalar deflection ψ and consequently the approach parameter δ are not affected by lens spinning to the first order. Anyway, due to the spin dependence in Eq. (8.30), first order corrections modify the separation of the critical curves from the shadow. They read

$$\begin{aligned} D_{OL}\theta_{1,k} = \; & -\frac{3\sqrt{3}\xi}{2}(1+\epsilon_k) + \\ & a\left[1+\xi^2+\epsilon_k(1-\xi^2)\right]\sqrt{1-{\mu_o}^2}, \\ D_{OL}\theta_{2,k} = \; & \pm\frac{3\sqrt{3}(1+\epsilon_k)\sqrt{1-\xi^2}}{2} \mp \\ & a\xi\sqrt{1-\xi^2}(1-\epsilon_k)\sqrt{1-{\mu_o}^2}, \end{aligned} \tag{8.53}$$

where ϵ_k is still the zero-order separation defined in Eq. (8.48).

Coming to the caustics, from Eqs. (8.50)-(8.51) and (8.46) we get

$$\mu_s = (-1)^k \mu_o, \tag{8.54}$$

$$\phi_s = \pi(1-k) - \Delta\phi_k \tag{8.55}$$

$$\Delta\phi_k = 4a\left[\frac{k\pi}{3\sqrt{3}} - \log(2\sqrt{3}-3)\right]. \tag{8.56}$$

So, caustics are still point-like but the alignment with the optical axis is now missing because of first order corrections, as already pointed out in Paper I. The azimuthal shift is proportional to the caustic order, it does not depend on the observer declination and is negative, thus implying a clockwise drift, if we look at the black hole from the north pole. This means that, as k is still the number of inversion points, prograde (retrograde) light rays, emitted by a source on a caustic point, perform more (less) than $(k-1)/2$ loops. Moreover, as the caustics drift from the optical axis and from each other, perfect alignment of observer, lens and source is not required for the enhancement of the images which are enhanced one at a time, as sources cannot cross more than one caustic point at the same time. For numerical values of the shift see Paper I, Table 1.

8.4.3 Second-Order Caustics

In this section we investigate the effects of second order corrections in the black hole spin on the critical curves and caustics. Following the same steps as in the previous subsection, we can add the second order terms $a^2\delta\mu_s^{(2)}$ to Eqs. (8.50) and $a^2\delta\phi_s^{(2)}$ to (8.51). Since they have quite long expressions, we report them in Appendix B and proceed with the analysis of the second order lens equation. In fact, although the general second order lens equation is quite involved, it is easy to solve the Jacobian determinant equation $D = 0$ in terms of the second order perturbation of ψ, starting from the zero order solution (8.46). We get

$$\psi_k = k\pi + a^2\delta\psi, \tag{8.57}$$

where

$$\delta\psi = -\frac{1}{18}\left[9x_c(3 - 2\mu_o^2 - 3\hat{\xi}^2) + 32(1 - \hat{\xi}^2)\right] \tag{8.58}$$

and

$$x_c = \frac{2}{9}(5k\pi + 8\sqrt{3} - 36). \tag{8.59}$$

Using Eqs. (8.35) and (8.30) we can calculate the second order corrections to the approach parameter δ and the shadow separation ϵ. After that, by Eqs. (8.26), we can derive the second order corrections to the critical curves given in Eq. (8.53)

$$\begin{aligned} D_{OL}\theta_{1,k}^{(2)} &= a^2\tfrac{\xi}{3\sqrt{3}}\Big[5 - 2\mu_o^2 - 2\hat{\xi}^2 \\ &\quad +\epsilon_k\left(29 - 8\mu_o^2 - 32\hat{\xi}^2\right)\Big], \\ D_{OL}\theta_{2,k}^{(2)} &= \mp a^2\tfrac{\sqrt{1-\xi^2}}{3\sqrt{3}}\Big[1 + 2\mu_o^2 - 2\hat{\xi}^2 \\ &\quad +\epsilon_k\left(21 - 32\hat{\xi}^2\right)\Big], \end{aligned} \tag{8.60}$$

where the zero-order separation ϵ_k is always given by Eq. (8.48).

Plugging Eq. (8.57) into the lens map, we get the caustics parametric equations up to the second order in a:

$$\mu_s = (-1)^k\mu_o \pm a^2 x_c(1 - {\mu_o}^2)^{3/2}(1 - \xi^2)^{3/2}, \tag{8.61}$$

$$\phi_s = (1 - k)\pi - \Delta\phi_k - a^2 x_c\xi^3\sqrt{1 - {\mu_o}^2}. \tag{8.62}$$

As explained in Section 8.4.1, the double sign in Eq. (8.61) allows for the possibilities that the photon starts its journey by increasing μ or by decreasing μ, respectively. it is necessary to take both possibilities into account in order to cover the whole caustic. In agreement with Paper I and other works where the same results are found numerically (e.g.[115]), we get extended caustics whose shape is a 4-cusped astroid, with cusps in $\xi = \pm 1$ and $\xi = 0$ (for different signs of initial $\dot{\mu}$). The extension of the caustics along μ and along ϕ is different. However, choosing appropriate coordinates centered on the caustic, it is possible to show that the extension in the sky as seen by the black hole is the same along both axes (see next subsection).

8.4.4 Observables related to critical curves and caustics

After second order corrections to critical curves and caustics have been derived, we can discuss their dependence on a and ϑ_o.

First we note that the critical curves obtained adding Eq. (8.60) to (8.53) satisfy the ellipse equation

$$\frac{(\theta_{1,k} - \theta_0)^2}{A_{1,k}^2} + \frac{\theta_{2,k}^2}{A_{1,k}^2} = 1 \tag{8.63}$$

with the same origin shift as the shadow (Eq. (8.22)) and semiaxes given by

$$\begin{aligned} A_{1,k} &= D_{OL}^{-1}\left\{\frac{3\sqrt{3}}{2}(1+\epsilon_k)\right. \\ &\left.-a^2\frac{4-\epsilon_k(4-9x_c\mu_o^2)}{4\sqrt{3}}\right\} \end{aligned} \tag{8.64}$$

$$\begin{aligned} A_{2,k} &= D_{OL}^{-1}\left\{\frac{3\sqrt{3}}{2}-\left[16\epsilon_k^2-4(3+\epsilon_k^2)\mu_o^2\right.\right. \\ &\left.\left.+27x_c\epsilon_k(1+\epsilon_k)(3-2\mu_o^2)\right]\frac{a^2}{12\sqrt{3}(1+\epsilon_k)}\right\}. \end{aligned} \tag{8.65}$$

The critical curves tend to coincide with the shadow in the limit $k \to \infty$, which corresponds to photons winding an infinite number of times, thus tending to the unstable photon orbit. The ellipticity of the critical curves is

$$e = a^2(1-\mu_o^2)\frac{4(3+\epsilon_k^2)+81x_c\epsilon_k(1+\epsilon_k)}{54(1+\epsilon_k)^2}, \tag{8.66}$$

which is slightly higher than that of the shadow for the lower order critical curves, but tends to that of the shadow as $k \to \infty$. In particular, we see that shift and ellipticity of the critical curves still depend on the combination $a \sin\vartheta_o$, as for the shadow. So, even the observation of several critical curves cannot help to determine a and ϑ_o separately.

Let us come to the caustics. Here the situation is more subtle and needs to be investigated with grain of salt.

Suppose we have no independent knowledge of the direction of the black hole spin or, at least, the direction of the spin is not known to a great accuracy. Then, the observer will construct his coordinates allowing for a non-vanishing position angle ν for the spin axis. The uncertainty in ν will be determinant in the following discussion. Let us thus introduce $(x, \hat{\vartheta}, \hat{\phi})$ as observer-oriented coordinates, still centered at the black hole, but with the polar axis perpendicular to the optical axis and the azimuth $\hat{\phi}$ taken from the direction opposite to the observer. In general, if the observer ignores the spin axis, the spin axis of the black hole would have a position angle ν from the polar axis as fixed by the observer. The coordinate transformation from (μ, ϕ) to $(\hat{\vartheta}, \hat{\phi})$ is

$$\begin{aligned} \hat{\vartheta} &= \arccos\left[\mu\sqrt{1-\mu_o^2}\cos\nu+\mu_o\sqrt{1-\mu^2}\cos\phi\cos\nu\right. \\ &\left.+\sqrt{1-\mu^2}\sin\phi\sin\nu\right] \end{aligned} \tag{8.67}$$

$$\begin{aligned} \hat{\phi} &= \arctan\left[\left(\sqrt{1-\mu^2}\sin\phi\cos\nu\right.\right. \\ &\left.-\mu_o\sqrt{1-\mu^2}\cos\phi\sin\nu-\mu\sqrt{1-\mu_o^2}\sin\nu\right) \\ &\left.\cdot\left(\sqrt{1-\mu^2}\sqrt{1-\mu_o^2}\cos\phi-\mu\mu_o\right)^{-1}\right]. \end{aligned} \tag{8.68}$$

Fig. 8.3 illustrates the geometrical meaning of these coordinates.

Transforming the caustics (8.61)-(8.62) from the spin-oriented coordinates (μ, ϕ) to the observer-oriented coordinates $(\hat{\vartheta}, \hat{\phi})$, and expanding to second order in a, we get

$$\begin{aligned} \hat{\vartheta}_s &= \frac{\pi}{2}-(-1)^k\Delta\phi_k\sqrt{1-\mu_o^2}\sin\nu \\ &-(-1)^k\frac{1}{2}\Delta\phi_k^2\mu_o\sqrt{1-\mu_o^2}\cos\nu \\ &-R_k\left[(-1)^k\xi^3\sin\nu\pm(1-\xi)^{3/2}\cos\nu\right] \end{aligned} \tag{8.69}$$

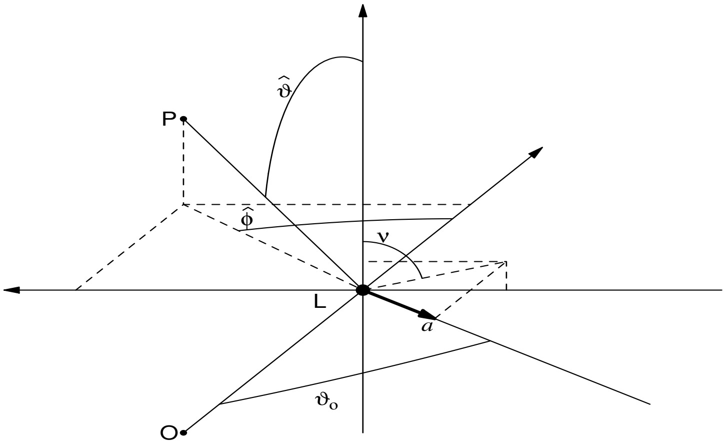

Figure 8.3: Observer-oriented coordinates $(\hat{\vartheta}, \hat{\phi})$ introduced in the text. L is the black hole with spin a. O is the observer and P is a generic point. ϑ_o is the inclination of the spin on the line of sight, ν is the position angle of the spin.

$$\begin{aligned}\hat{\phi}_s \quad &= (1-k)\pi - \Delta\phi_k \sqrt{1-\mu_o^2} \cos\nu \\ &+\frac{1}{2}\Delta\phi_k^2 \mu_o \sqrt{1-\mu_o^2} \sin\nu \\ &-R_k \left[\xi^3 \cos\nu \pm (-1)^k (1-\xi)^{3/2} \sin\nu\right], \end{aligned} \tag{8.70}$$

where

$$R_k \equiv a^2 x_c (1-\mu_o^2) = \frac{2}{9} a^2 (1-\mu_o^2)(5k\pi + 8\sqrt{3} - 36) \tag{8.71}$$

is the semi-amplitude of the caustic. In fact, we can appreciate that, in observer-oriented coordinates, the extension of the caustic is the same in both polar and azimuthal directions, as anticipated before for any coordinate system centered on the caustic. So, the extension is quadratic in the spin and is maximal for equatorial observers, while the astroid shrinks to a single point when the observer lies on the spin axis. The caustic extension also increases linearly with the caustic order k.

Then, we note that the angular shift of the center of the caustic from the optical axis is

$$\begin{aligned}\Delta_k \quad &\equiv \arccos[\sin\hat{\vartheta} \cos\hat{\phi}] = \Delta\phi_k \sqrt{1-\mu_o^2} \\ &= 4a\sqrt{1-\mu_o^2} \left[\frac{k\pi}{3\sqrt{3}} - \log(2\sqrt{3}-3)\right]. \end{aligned} \tag{8.72}$$

It is linear in the black hole spin and the caustic order. Similarly to the semi-amplitude, also the shift is maximal for equatorial observers and vanishes for polar observers, when the axial symmetry is restored.

The shift and the semi-amplitude of the caustics are very easy quantities to determine in case of observation of the relativistic images generated by a source crossing a relativistic caustic. In fact, if the observer is able to identify the source and follow its direct image throughout the duration of the caustic crossing event, then he would immediately determine the position of the caustic and estimate its extension. Unfortunately, even in these two quantities, the black hole spin and the observer declination always appear in the combination $a\sqrt{1-\mu_o^2} = a \sin\vartheta_o$, making the breaking of the degeneracy between these two parameters impossible. On the other hand, it is easy to determine the order k of the caustic involved in the lensing event, since the ratio

$$\frac{\Delta_k^2}{R_k} = \frac{8\left[k\pi + 3\sqrt{3}\log(2\sqrt{3}-3)\right]^2}{3\left(5k\pi + 8\sqrt{3} - 36\right)} \tag{8.73}$$

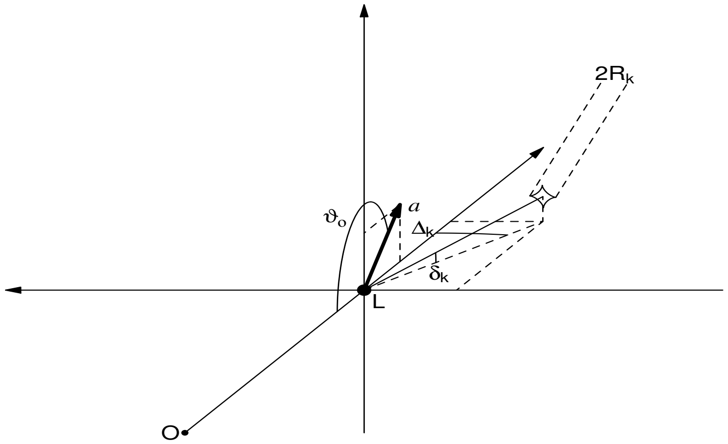

Figure 8.4: A typical caustic in Kerr lensing. The extension is the same in both directions. Having chosen coordinates such that the position angle of the spin vanishes, the caustic has an azimuthal shift Δ_k and a vertical shift δ_k w.r.t. the line of sight.

only depends on k and increases monotonically in k, without degeneracy between any two values.

One possibility for the separate determination of a and μ_o arises in case the spin position angle ν is known to a very good accuracy from independent measures. Then we can move to a more convenient coordinate frame where $\nu = 0$. If this is possible, looking at Eqs. (8.69) and (8.70) we see that the shift in the azimuthal direction is linear in a, while a residual quadratic shift is present in the polar direction, which amounts to

$$\begin{aligned} \delta_k &\equiv \frac{1}{2}\Delta\phi_k^2\mu_o\sqrt{1-\mu_o^2} \\ &= 8a^2\mu_o\sqrt{1-\mu_o^2}\left[\frac{k\pi}{3\sqrt{3}} - \log(2\sqrt{3}-3)\right]^2 . \end{aligned} \tag{8.74}$$

Then, if one is able to measure this residual shift, one can extract the observer colatitude ϑ_o as

$$\cot\vartheta_o = \frac{2\delta_k}{\Delta_k^2}. \tag{8.75}$$

Once the observer position relative to the spin axis is known, we can use either Δ_k or R_k to extract the black hole spin a. However, as for the case of the direct determination of a from the measure of the minor semi-axis of the shadow, this is a higher order measure, which requires very accurate independent information.

Fig. 8.4 shows a caustic and illustrates the meaning of the semi-amplitude R_k, the horizontal shift Δ_k and the vertical shift δ_k. The picture is done for a standard lensing caustic (k odd) with $\vartheta_o > \pi/2$, so that the caustic is displaced upward (see Eq. (8.69)).

As usual we can trust our results as long as the perturbative terms remain small. In extremal or close-to-extremal Kerr black holes, higher orders in a would play a major role in the critical curves and caustics profile. In that case, the degeneracy between a and ϑ_o can be probably broken also through the determination of the extension and position of the caustics or through the analysis of the critical curves. However, in the literature there is no investigation of Kerr black holes with high spin that is deep enough to allow a comparison with our perturbative results for low spins.

8.5 Gravitational lensing near caustics

8.5.1 Position of the relativistic images

Although in our picture the images cannot be found analytically for arbitrary source positions using the lens mapping that we have derived, they can be actually found for sources in the neighbourhood of a caustic. This is indeed the most interesting case, as the relativistic images are highly magnified and become observable only if this event occurs. Assuming that the distance between the source and a caustic of order k is of the order of a^2 (thus comparable with the caustic semiaxis), we can write the source position as

$$\mu_s = (-1)^k \mu_o + a^2 \delta\mu_s, \tag{8.76}$$

$$\phi = (1-k)\pi - \Delta\phi_k + a^2 \delta\phi_s, \tag{8.77}$$

In this assumption, the images will be very close to the critical curve of order k. Then the scalar deflection will be

$$\psi = k\pi + a^2 \delta\psi. \tag{8.78}$$

Plugging the last equation into the lens map written up to corrections of second order in a and inverting with respect to $\delta\mu_s$ and $\delta\phi_s$, we get

$$\begin{aligned}\delta\mu_s = \; & \mp\frac{1}{9}\sqrt{1-\mu_o^2}\sqrt{1-\xi^2}\,[9\delta\psi \\ & +(5k\pi+8\sqrt{3}-20)(1-(1-{\mu_o}^2)\xi^2)\Big],\end{aligned} \tag{8.79}$$

$$\begin{aligned}\delta\phi_s = \; & \frac{\xi}{9\sqrt{1-{\mu_o}^2}}\Big[92-24\sqrt{3}-15k\pi-9\delta\psi \\ & +2{\mu_o}^2(5k\pi+8\sqrt{3}-36) \\ & +(5k\pi+8\sqrt{3}-20)(1-{\mu_o}^2)\xi^2\Big].\end{aligned} \tag{8.80}$$

Solving (8.80) with respect to $\delta\psi$ and plugging its expression into (8.79), we find

$$\delta\mu_s\xi = -S(-1)^k(1-{\mu_o}^2)(\delta\phi_s + x_c\sqrt{1-{\mu_o}^2}\xi)\sqrt{1-\xi^2}, \tag{8.81}$$

where x_c is given by Eq. (8.59) and $S = \mp(-1)^k$. This equation can be more conveniently written in terms of observer-oriented coordinates $(\hat{\vartheta}_s, \hat{\phi}_s)$. Supposing that the position angle of the spin has been well established by observations of the shadow or by the shift of the caustic itself, we put $\nu = 0$ for simplicity and write

$$\hat{\vartheta}_s = \frac{\pi}{2} - (-1)^k\delta_k + \delta\hat{\vartheta}_s \tag{8.82}$$

$$\hat{\phi}_s = (1-k)\pi - \Delta\phi_k + \delta\hat{\phi}_s, \tag{8.83}$$

with

$$\delta\hat{\vartheta}_s = -a^2\frac{\delta\mu_s}{\sqrt{1-\mu_o^2}} \tag{8.84}$$

$$\delta\hat{\phi}_s = a^2\delta\phi_s\sqrt{1-\mu_o^2}. \tag{8.85}$$

Then, we can write Eq. (8.81) directly in terms of these coordinates as

$$\delta\hat{\vartheta}_s\xi = S(-1)^k(\delta\hat{\phi}_s + R_k\xi)\sqrt{1-\xi^2}, \tag{8.86}$$

where R_k is the semi-amplitude of the caustic given by Eq. (8.71). The solutions of these equation for arbitrary source positions $(\delta\hat{\vartheta}_s, \delta\hat{\phi}_s)$ determine the relativistic images generated by the Kerr black hole. As the roots of Eq. (8.86) are found squaring both its sides, the solutions of the squared equation satisfy the original one only for one choice of S. S is directly related to the half-sky where the image appears. In fact, we recall that the parameterization (8.26) has an ambiguity in the sign of θ_2. This ambiguity can be solved observing that the photon reaches the observer from the upper side of the black hole if S is positive and from the lower side if S is negative. This fact can be easily established remembering that in all our equations the upper signs hold when the photon leaves the source by increasing its μ coordinate. Then, if its polar motion undergoes one inversion ($k = 1$), the photon reaches the observer from above and we coherently have $S = 1$. On the other hand, if the lower signs hold, the photon begins its motion decreasing its μ coordinate. With one inversion, it reaches the observer from below and coherently we have $S = -1$. The same reasoning can be repeated with an arbitrary number k of inversions in the polar motion.

It can be easily verified that Eq. (8.86) has four real solutions if the source is inside the caustic and only two real solutions if the source is outside. Once the coordinate ξ (which, we recall, represents the cosine of the position angle) of the image is known, Eq. (8.80) can be used to determines the value of $\delta\psi$ (perturbation of the scalar deflection). However, it is important to stress that Eq. (8.86) determines ξ to zero order only. Therefore, though the positions of the images in the observer sky are generically given by

$$\begin{aligned} D_{OL}\theta_1 = & -\frac{3\sqrt{3}}{2}\xi(1+\epsilon_k) \\ & +a\sqrt{1-{\mu_o}^2}\left[1+\xi^2+\epsilon_k(1-\xi^2)\right]+ \\ & \frac{a^2\xi}{6\sqrt{3}}\left\{10-4\xi^2(1-\mu_o^2)-4\mu_o^2+\epsilon_k\left[27\delta\psi\right.\right. \\ & \left.\left.+58-64\xi^2(1-\mu_o^2)-16\mu_o^2\right]\right\}, \end{aligned} \tag{8.87}$$

$$\begin{aligned} D_{OL}\theta_2 = & S\frac{3\sqrt{3}}{2}\sqrt{1-\xi^2}(1+\epsilon_k) \\ & -aS\xi\sqrt{1-\xi^2}\sqrt{1-\mu_o^2}(1-\epsilon_k) \\ & -S\frac{a^2}{6\sqrt{3}}\sqrt{1-\xi^2}\left\{2-4\xi^2(1-\mu_o^2)+4\mu_o^2\right. \\ & \left.+\epsilon_k\left[27\delta\psi+42-64(1-\mu_o^2)\xi^2\right]\right\}, \end{aligned} \tag{8.88}$$

to the second order in a, only a zero order expression of ξ is actually available. So, the position of the images is accurate only to zero order in a and is given by

$$D_{OL}\theta_1 = -\frac{3\sqrt{3}}{2}\xi(1+\epsilon_k) \tag{8.89}$$

$$D_{OL}\theta_2 = S\frac{3\sqrt{3}}{2}\sqrt{1-\xi^2}(1+\epsilon_k). \tag{8.90}$$

To zero order, we see that the images of order k lie along the critical curve of order k (we remind that ϵ_k is just the separation of the critical curve of order k from the shadow (8.48)), with position angle determined by the solutions of Eq. (8.86). If a more accurate theoretical prediction of the images position (including first order corrections) is needed, it is necessary to push the lens equation to the third order. Indeed this would be a worthy (though heavy) task since the equation for the images (8.86) depends on a only through R_k. As noticed before, this quantity only depends on the projection of the spin on the line of sight. So, once more, the observables (in this case the positions of the images) only depend on $a\sin\vartheta_o$ to the lowest order. However, contrarily to the former observables, the positions of the images could be detected to an accuracy sufficiently high to be sensitive at least to first order corrections in a. So, it would be indeed desirable to check whether the positions of the images may help to break the degeneracy between the absolute value of the spin and its inclination on the optical axis.

8.5.2 Magnification

The magnification is defined as the ratio of the angular area of the image and the corresponding angular area of the source. The angular area of the image is simply $|d\theta_1 d\theta_2|$, while the angular area of the source is $|\sin\vartheta_s d\phi_s d\vartheta_s|$ or $|\sin\hat{\vartheta}_s d\hat{\phi}_s d\hat{\vartheta}_s|$ if one uses observer-oriented coordinates. Then the magnification can be calculated as $|\sin\hat{\vartheta}_s|^{-1}$ times the inverse of the Jacobian determinant of the lens application in the form

$$\left\{ \begin{array}{l} \hat{\phi}_s = \hat{\phi}_s(\theta_1,\theta_2) \\ \hat{\vartheta}_s = \hat{\vartheta}_s(\theta_1,\theta_2) \end{array} \right. . \tag{8.91}$$

Following the same approach of Paper I, we can find the expression of the magnification for sources in the neighbourhood of caustics exploiting the available relations (8.85)-(8.84) and (8.79)-(8.80) to get

$$\left\{ \begin{array}{l} \delta\hat{\phi}_s = \delta\hat{\phi}_s(\delta\psi,\xi) \\ \delta\hat{\vartheta}_s = \delta\hat{\vartheta}_s(\delta\psi,\xi) \end{array} \right. \tag{8.92}$$

and (8.87)-(8.88)

$$\left\{ \begin{array}{lcl} \theta_1 & = & \theta_1(\delta\psi,\xi) \\ \theta_2 & = & \theta_2(\delta\psi,\xi) \end{array} \right. . \tag{8.93}$$

Then the perturbation of the scalar deflection $\delta\psi$ and the cosine of the position angle ξ play the role of intermediate variables between the source coordinates $(\hat{\vartheta}_s, \hat{\phi}_s)$ and the image coordinates in the observer sky (θ_1, θ_2).

Since $\sin\hat{\vartheta}_s d\hat{\phi}_s = d(\delta\hat{\phi}_s)$ and $d\hat{\vartheta}_s = d(\delta\hat{\vartheta}_s)$ to the lowest order, the Jacobian of the map (8.91) reduces to

$$\frac{\partial(\hat{\phi}_s,\hat{\vartheta}_s)}{\partial(\theta_1,\theta_2)} = \frac{\partial(\delta\hat{\phi}_s,\delta\hat{\vartheta}_s)}{\partial(\delta\psi,\xi)} \left[\frac{\partial(\theta_1,\theta_2)}{\partial(\delta\psi,\xi)}\right]^{-1}, \tag{8.94}$$

where we have used the matrix notation

$$\frac{\partial(y_1,y_2)}{\partial(x_1,x_2)} = \left(\begin{array}{cc} \frac{\partial y_1}{\partial x_1} & \frac{\partial y_1}{\partial x_2} \\ \frac{\partial y_2}{\partial x_1} & \frac{\partial y_2}{\partial x_2} \end{array} \right). \tag{8.95}$$

As the derivatives and the Jacobian matrix have very involved expressions, we do not go too much into detail and only report here the two eigenvalues of the Jacobian matrix

$$\lambda_r = \frac{2D_{OL}}{3\sqrt{3}\epsilon_k}, \tag{8.96}$$

$$\lambda_t = \frac{2D_{OL}D_O}{27\sqrt{3}(1+\epsilon_k)}, \tag{8.97}$$

where

$$\begin{aligned} D_O = \; & (-1)^k \frac{a^2}{2} \left\{ 9x_c \left[3 - 2\mu_o^2 - 3\hat{\xi}^2\right] \right. \\ & \left. +32(1-\hat{\xi}^2) + 18\delta\psi \right\}. \end{aligned} \tag{8.98}$$

In a first approximation λ_r only depends on the caustic order k and is always positive. On the other hand λ_t vanishes at caustic crossing (see. Eq.(8.58)). Following Paper I, we will call λ_r and λ_t, respectively, radial and tangential eigenvalues, although they are such only in the limit $a \to 0$. Taking into account that the flux received by the observer is D_{LS}^2/D_{OS}^2 times the flux received by the black hole, the radial and tangential magnifications are

$$\mu_r = \frac{D_{OS}}{D_{LS}} \frac{1}{\lambda_r}, \tag{8.99}$$

$$\mu_t = \frac{D_{OS}}{D_{LS}} \frac{1}{|\lambda_t|} \tag{8.100}$$

while the total magnification is given by $\mu = \mu_r \mu_t$.

An interesting thing to note is that the radial magnification is completely independent of a and μ_o. It is just the same as in the Schwarzchild black hole case. On the other hand, the tangential magnification is sensitive to the caustic structure, which can be seen more clearly if we plug the solution of the lens equation (8.80) for $\delta\psi$ into Eq. (8.98). In fact, we have

$$\mu_t = (-1)^k \frac{D_{OS}}{D_{LS}} \frac{3\sqrt{3}(1+\epsilon_k)\xi}{2D_{OL}\left(R_k \xi^3 + \delta\hat{\phi}_s\right)}, \tag{8.101}$$

where the $(-1)^k$ accounts for the parity of the image and ξ must be determined solving Eq. (8.86). The whole dependence of the magnification on the black hole spin and the observer declination is through the caustic semi-amplitude R_k, where they appear in the usual combination $a \sin\vartheta_o$.

8.5.3 Relativistic images around Sgr A*

In this subsection we want to complement the discussion about the detectability of relativistic images done in Paper I by some additional considerations. Indeed there are many aspects that may prevent the positive detection of relativistic images around Sgr A*. The photons with the right incident direction for performing a complete loop around a black hole and then reach the observer are very few from the beginning. Moreover, during their journey, photons may be scattered or absorbed by the accreting matter surrounding the supermassive black hole. Finally, the photons surviving up to the observer must be recognized and distinguished from the noise coming from the environment.

Scattering and absorption from accreting matter, are strongly model-dependent and cannot be easily quantified without non-trivial assumptions on the infalling plasma physics. We are not going to face this important problem here, since it demands an extensive investigation beyond the purpose of this work.

On the other hand, our gravitational lensing analysis allows us to give sharp answers on the brightness and spatial properties of the images. In Paper I, we have suggested that the observed Low-Mass X-ray Binaries (LMXB) orbiting around Sgr A* provide an ideal population of sources for the gravitational lensing in the SDL [102]. Of course we need to resolve the shadow of Sgr A* in order to identify relativistic images around it. This requires a resolution of the order of the μas, which is just one step beyond the limit reached in the radio band. In the X-ray band, projects of space interferometry which could reach resolutions even better than μas are under study (MAXIM, http://maxim.gsfc.nasa.gov). When such projects will become reality, a complete imaging of Sgr A* will be possible and the relativistic images could be distinguished.

Apart from spatial resolution, which can be attained by realistic future projects, in order to detect a signal in the X-ray band from a relativistic image, we need a sufficient number of photons. With an intrinsic luminosity $L_S \sim 2 \times 10^{33}$ ergs s^{-1} in the band $2-10$ keV, emitted by a surface with radius $R_S = 100$km, LMXBs are as powerful sources as Sgr A* itself but enjoy a much higher surface brightness [102]. If one of these sources crosses a relativistic caustic of order k, the angular area of the resulting relativistic image is the original source area $\pi R_S^2/D_{OS}^2$ multiplied by the magnification factor μ. As long as the source is inside the caustic, the magnification stays higher than a minimum value corresponding to a source located at the center of the caustic. The central magnification has been calculated in Paper I and amounts to

$$\mu_c = \frac{D_{OS}^2}{D_{LS}^2 D_{OL}^2} \frac{27\epsilon_k(1+\epsilon_k)}{4R_k}, \tag{8.102}$$

for each of the four relativistic images present when the source is inside the caustic.

For a detector with collecting area A_D, the observed flux, taking into account an absorption factor $\varepsilon = 0.158$, deduced from Ref. [15], is thus

$$F_k = \varepsilon \frac{L_S}{4\pi R_S^2} \left(\mu_c \frac{\pi R_S^2}{D_{OS}^2} \right) A_D. \tag{8.103}$$

With $D_{OL} = 8$kpc, $M_{BH} = 4.3 \times 10^6 M_\odot$ [17] and $D_{OS} \simeq D_{OL}$ (since $D_{LS} \ll D_{OL}$), we have

$$F_2 = 2.3 \times 10^{-11} \mathrm{ergs\ s}^{-1} \left(\frac{\mathrm{D_{LS}}}{\mathrm{100AU}} \right)^{-2} \left(\frac{\mathrm{a}}{0.02} \right)^{-2} \left(\frac{\mathrm{A_D}}{\mathrm{100m^2}} \right), \tag{8.104}$$

for a source crossing the caustic of order $k = 2$ and a black hole spin $a = 0.02$ [91]. This flux is independent of the source radius, as long as the source is much smaller than the caustic extension, as in our case. We have considered a collecting area $A_D = 100m^2$ which might be realistically obtained by future space detectors. The count rate for photons in the considered band (with average energy 6 keV) is thus of the order of 2.4×10^{-3} s^{-1}, which is comparable to the counts usually reported as positive detections by the Chandra satellite for faint sources [15, 102]. Of course, such a high value for the count rate can only be achieved with a collecting area as large as that we have considered here, which is roughly 100 times larger than that of Chandra.

Sgr A* itself emits in the X-rays and provides a background noise to the signal of a relativistic image. The image of an LMXB is entirely contained within a single pixel of a hypothetic detector where every pixel covers 1μas$\times 1\mu$as of sky. We can estimate the noise due to Sgr A* considering that its intrinsic luminosity is of the same order as L_S[15, 102], but its emitting region has a radius R_{Sgr} of the order of 100 Schwarzschild radii. Then, every pixel is affected by a noise from Sgr A* of the order of

$$F_{Sgr} = \varepsilon \frac{L_S}{4\pi R_{Sgr}^2} \omega_p^2 A_D, \tag{8.105}$$

where ω_p is the size of the pixel. We thus have

$$F_{Sgr} = 3.7 \times 10^{-14} \mathrm{ergs\ s}^{-1} \left(\frac{\omega_\mathrm{p}}{1\mu\mathrm{as}} \right)^2 \left(\frac{\mathrm{A_D}}{\mathrm{100m^2}} \right), \tag{8.106}$$

which is roughly 600 times smaller than F_2. This proves that the background from Sgr A* is indeed negligible for relativistic images of order 2 if one has sufficient resolving power. It is also important to stress that these estimates has been calculated considering the minimum magnification μ_c for a source inside a caustic. When the source is close to a fold or a cusp, the brightness of the relativistic image can be sensibly higher.

We conclude this discussion mentioning that the brightness of relativistic images of order 3 is $0.016F_2$, which allows a marginal detection w.r.t. the noise by Sgr A*, while relativistic images of higher order are too faint to be detected, at least for the configuration examined here.

8.6 Conclusions

This paper completes the cycle of papers devoted to the study of gravitational lensing by Kerr black holes in the Strong Deflection Limit. After the first pioneering work of Ref. [28], where equatorial lensing was reduced to the same problem already solved for spherically symmetric black holes [27], in Ref. [31] we managed to make a complete analytical treatment of Kerr lensing for equatorial observers, introducing a perturbative expansion in the spin a. In this work we have extended that idea to Kerr lensing with a generic observer. Though the strategy is essentially unchanged, the introduction of a new parameter (the inclination of the spin or equivalently the observer colatitude ϑ_o) has increased the difficulty of the derivation. Nevertheless, our investigation has reached its objective: a basically simple and accurate description of Kerr lensing phenomenology with arbitrary observer position.

An essential summary of the main results obtained includes: the shape of the shadow of the black hole (8.21); the shape of all critical curves (8.63); the shape and position of the caustics (Eqs. (8.69) and (8.70)); the position of the images (Eqs. (8.89)-(8.90) with Eq. (8.86)) and their magnification (Eqs. (8.99) with (8.96) and (8.101)) for sources close to a caustic.

To the second order in a, the shadow of the black hole and the critical curves are ellipses slightly displaced from the black hole position. The ellipticity is slightly higher in critical curves than in the shadow. The caustics are displaced from the optical axis and show the characteristic 4-cusped astroid shape with the same extension in both directions. The caustic shrinks back to a single point when the observer lies on the spin axis, restoring the axial symmetry. There are two additional images when the source is inside a caustic.

The fundamental fact that emerges is that all observables to the lowest order are functions of $a \sin \vartheta_o$, which represents the projection of the black hole spin on a plane orthogonal to the line of sight. These observables include: the shift and the ellipticities of the shadow and of critical curves; the shift and the extension of the caustics; the position and the magnification of the images.

The degeneracy between the absolute value of the spin and its inclination on the line of sight can only be broken by next-to-leading order terms in all observables. This has been explicitly shown considering the shadow and critical curves semi-axes and the caustic vertical shift. These are second order contributions to zero-order quantities, thus requiring extremely accurate measures, which may be very challenging. For example, if the black hole spin is $a = 0.1$, in order to break the degeneracy we need a relative accuracy of order $a^2 = 0.01$ in the measures.

The most promising way to break the degeneracy is through higher order corrections to the positions of the images. In fact, our second order treatment is only sufficient to determine the position angle of the images to zero order in a. Indeed the first order corrections are likely to be at reach of future VLBI observations, but unfortunately they require at least a third order treatment of Kerr lensing in order to be determined analytically. This could represent the main target for future theoretical developments of our methodology.

Of course, if the black hole spin is close to the extremal value $a = 0.5$, the degeneracy breaking terms arising from higher orders in a grow to the same size as the lowest order contributions and the problem would not be the degeneracy between a and ϑ_o but the correct theoretical interpretation of the observations in a non-perturbative frame, in order to perform a safe parameters extraction.

Chapter 9

Appendix A

A.1 Resolution of radial integrals

In this appendix we recall the SDL technique used in Ref. [27] to solve radial integrals, applying it to the integrals that appear in the geodesics equations. We rewrite them here for an easier reading

$$I_1 = 2\int_{x_0}^{\infty} \frac{dx}{\sqrt{R}} \tag{A-1}$$

$$I_2 = 2\int_{x_0}^{\infty} \frac{x^2 + a^2 - aJ}{\Delta\sqrt{R}} dx. \tag{A-2}$$

First we change the integration variable from x to z by the transformation

$$x = \frac{x_0}{1-z}. \tag{A-3}$$

As a consequence, the integration domain $[x_0, \infty]$ becomes $[0, 1]$.

Then, each of the integrals I_1, I_2 can be written in the form

$$I_i = \int_0^1 R_i(z) f(z) dz \tag{A-4}$$

$$f(z) = \frac{1}{\sqrt{R(z)}}, \tag{A-5}$$

where the two functions $R_i(z)$ can be easily read by Eqs. (7.24)-(7.25) taking into account the Jacobian of the transformation (A-3):

$$R_1(z) = \frac{2x_0}{(1-z)^2} \tag{A-6}$$

$$R_2(z) = \frac{2x_0}{(1-z)^2} \frac{x_0^2 + (1-z)^2(a^2 - aJ)}{x_0^2 - x_0(1-z) + a^2(1-z)^2}. \tag{A-7}$$

Now we consider the expansion of $R(z)$ in a neighborhood of $z = 0$. Since $z = 0$ means $x = x_0$ and x_0 is a root of $R(x)$, we deduce that $R(z = 0) = 0$. Then the expansion of $R(z)$ reads

$$R(z) = \alpha z + \beta z^2 + o(z^2), \tag{A-8}$$

where the coefficients of the expansion are

$$\begin{aligned}\alpha = \;& x_0\left[(a-J)^2+Q+2(a^2-J^2-Q)x_0\right.\\ &\left.+4x_0^3\right] \qquad \text{(A-9)}\\ \beta = \;& x_0\left[(a-J)^2+Q+3(a^2-J^2-Q)x_0\right.\\ &\left.+10x_0^3\right] \qquad \text{(A-10)}\end{aligned}$$

We use this expansion to define

$$f_0(z)=\frac{1}{\sqrt{\alpha z+\beta z^2}}. \qquad \text{(A-11)}$$

The radial integrals can be split in two pieces

$$I_i = I_{i,D}+I_{i,R} \qquad \text{(A-12)}$$

$$I_{i,D} = \int_0^1 R_i(0)f_0(z)dz \qquad \text{(A-13)}$$

$$I_{i,R} = \int_0^1 \left[R_i(z)f(z)-R_i(0)f_0(z)\right]dz. \qquad \text{(A-14)}$$

The first integral gives the result

$$I_{i,D}=\frac{2R_i(0)}{\sqrt{\beta}}\log\frac{\sqrt{\beta}+\sqrt{\alpha+\beta}}{\sqrt{\alpha}}. \qquad \text{(A-15)}$$

α, β and $R_i(0)$ are known functions of x_0, J, Q and a. Now we can use the SDL parameterizations (7.20), (7.21), (7.22) for all these quantities, so that they become functions of ξ, δ (or equivalently ϵ) and a. Then, in the spirit of SDL approximation, we keep the leading order in δ, which goes as $\log\delta$, and the next-to-leading order which is constant in δ. Finally, we expand the obtained expression to second order in a.

As regards the integrals $I_{i,R}$, the integrand function is regular in the whole integration domain. Sending δ to zero, the integrand does not diverge. So, this integral contributes to the SDL expansion with another constant in δ plus higher order terms that we can neglect. It is convenient to make the second order expansion in a before the integration, in order to have a sum of easily integrable functions. We can then add the result of the integral $I_{i,R}$ to the integral $I_{i,D}$, to reconstruct the full SDL formulae for radial integrals:

$$\begin{aligned}I_1 =\;& -a_1\log\delta+b_1 \qquad \text{(A-16)}\\ I_2 =\;& -a_2\log\delta+b_2 \qquad \text{(A-17)}\end{aligned}$$

The coefficients expanded to second order in a read

$$\begin{aligned}a_1 =\;& \frac{4}{3\sqrt{3}}+\frac{16}{27}a\xi+\frac{8}{27\sqrt{3}}(1+3\xi^2)a^2 \qquad \text{(A-18)}\\ b_1 =\;& a_1\log\left[6\left(\sqrt{3}-1\right)^2\right]\\ &-\frac{8}{27\sqrt{3}}a^2\left(5-2\sqrt{3}\right)(1-\xi^2) \qquad \text{(A-19)}\end{aligned}$$

$$a_2 = \frac{4}{\sqrt{3}}+\frac{8}{3}a\xi+\frac{8\sqrt{3}}{27}(1+7\xi^2)a^2 \qquad \text{(A-20)}$$

$$\begin{aligned} b_2 = \quad & [a_2 + 4(1+2a^2)] \log \left[6(\sqrt{3}-1)^2\right] \\ & -2(1+2a^2)\log 48 - \frac{8}{3\sqrt{3}} a\xi(3\sqrt{3}-2) \\ & +\frac{8}{27}a^2[19\sqrt{3} - 12 + \xi^2(14-25\sqrt{3})]. \end{aligned} \tag{A-21}$$

The separation of I_i into $I_{i,D}$ and $I_{i,R}$ is necessary to isolate the term generating the $\log\delta$ into an easier integral.

A.2 Resolution of angular integrals

This appendix is devoted to the resolution of the angular integrals

$$J_1 = \pm \int \frac{1}{\sqrt{\Theta}} d\vartheta \tag{A-22}$$

$$J_2 = \pm \int \frac{csc^2\vartheta}{\sqrt{\Theta}} d\vartheta. \tag{A-23}$$

Introducing the variable $\mu = \cos\vartheta$, the two integrals become

$$J_1 = \pm \int \frac{1}{\sqrt{\Theta_\mu}} d\mu \tag{A-24}$$

$$J_2 = \pm \int \frac{1}{\sqrt{(1-\mu^2)\Theta_\mu}} d\mu, \tag{A-25}$$

where

$$\Theta_\mu = \quad a^2(\mu_-^2 + \mu^2)(\mu_+^2 - \mu^2) \tag{A-26}$$

$$\mu_\pm^2 = \quad \frac{\sqrt{b_{JQ}^2 + 4a^2 Q_m} \pm b_{JQ}}{2a^2} \tag{A-27}$$

$$b_{JQ} = \quad a^2 - J_m^2 - Q_m, \tag{A-28}$$

and we have already replaced J and Q with J_m and Q_m, coherently with the fact that we only retain terms which are logarithmically diverging or constant in δ (or equivalently ϵ).

Θ_μ has two zeros in $\mu = \pm\mu_+$. Then the photon performs symmetric oscillations of amplitude μ_+ w.r.t. the equatorial plane. It is useful to write the explicit expressions of μ_+ and μ_- in terms of a and ξ, using Eqs. (7.12)-(7.13) and expanding to second order in a. We find

$$\mu_+ = \quad \sqrt{1-\xi^2}\left(1 + \frac{4a\xi}{3\sqrt{3}} - \frac{8a^2\xi^2}{27}\right) \tag{A-29}$$

$$\begin{aligned} \mu_- = \quad & \frac{3\sqrt{3}}{2a} - 2\xi + \frac{a(4-8\xi^2)}{3\sqrt{3}} \\ & + \frac{4a^2\xi(12-17\xi^2)}{27}. \end{aligned} \tag{A-30}$$

The oscillation amplitude is $\sqrt{1-\xi^2}$ plus corrections due to the black hole spin. This is coherent with the fact that for a photon reaching the observer from the equatorial plane ($\xi = \pm 1$) the amplitude of the oscillation goes to zero. On the other hand, a photon moving on a polar orbit ($\xi = 0$) performs oscillations of maximal amplitude, touching the poles of the black hole. Now, to perform the angular integrals, it is wise to expand the integrands to second order in a and then integrate. Then, the primitive functions read

$$\begin{aligned}
F_{J_1}(\mu) \quad &= \frac{2}{3\sqrt{3}} \arcsin \frac{\mu}{\sqrt{1-\xi^2}} \\
&+ \frac{8}{27} a\xi \left[\arcsin \frac{\mu}{\sqrt{1-\xi^2}} - \frac{\mu}{\sqrt{1-\mu^2-\xi^2}} \right] \\
&+ \frac{2a^2}{81\sqrt{3}} \Bigg[(33\xi^2 - 9) \arcsin \frac{\mu}{\sqrt{1-\xi^2}} \\
&+ \frac{\mu(\mu^4 + 2\mu^2(\xi^2-1) + 1 + 6\xi^2 - 7\xi^4)}{(1-\mu^2-\xi^2)^{3/2}} \Bigg]
\end{aligned} \tag{A-31}$$

$$\begin{aligned}
F_{J_2}(\mu) \quad &= \frac{2}{3\sqrt{3}\xi} \arctan \frac{\mu\xi}{\sqrt{1-\mu^2-\xi^2}} \\
&+ \frac{8}{27\xi^2} a \left[\arctan \frac{\mu\xi}{\sqrt{1-\mu^2-\xi^2}} - \frac{\mu\xi}{\sqrt{1-\mu^2-\xi^2}} \right] \\
&+ \frac{4a^2}{81\sqrt{3}} \Bigg[\frac{12 - 21\xi^2 + 20\xi^4}{\xi^3} \arctan \frac{\mu\xi}{\sqrt{1-\mu^2-\xi^2}} \\
&+ \frac{4\mu(1-\xi^2)(3\mu^2 - 3 + 4\xi^2)}{\xi^2(1-\mu^2-\xi^2)^{3/2}} \\
&+ \arctan \frac{\mu}{\sqrt{1-\mu^2-\xi^2}} \Bigg]
\end{aligned} \tag{A-32}$$

The integration limits are the values of μ at the observer and source position. The observer is at $\mu_o = 0$, since it lies on the equatorial plane, while the source is in $\mu_s = \cos\vartheta_s$. Notice that the choice of an equatorial observer leads to a considerable simplification, since $F_{J_1}(0) = F_{J_2}(0) = 0$. Moreover, we have to consider that during the photon motion, μ may perform several oscillations between $-\mu_+$ and μ_+, depending on how many loops the photon makes around the black hole before escaping. So, we have to add an arbitrary integer number m of integrals covering the whole domain $[-\mu_+, \mu_+]$. The final results read

$$\begin{aligned}
J_1 = \quad & \pm F_{J_1}(\mu_s) \\
& + \frac{2m\pi}{3\sqrt{3}} \left[1 + \frac{4a\xi}{3\sqrt{3}} + \frac{a^2(11\xi^2 - 3)}{9} \right]
\end{aligned} \tag{A-33}$$

$$\begin{aligned}
J_2 = \quad & \pm F_{J_2}(\mu_s) + \frac{2m\pi}{3\sqrt{3}\xi} \Bigg[1 + \frac{4a}{3\sqrt{3}\xi} \\
& + \frac{2a^2(12 - 21\xi^2 + \xi^3 + 20\xi^4)}{27\xi^2} \Bigg],
\end{aligned} \tag{A-34}$$

where the minus signs hold if the photon initially increases its latitude and the plus signs hold if the latitude decreases initially.

Chapter 10

Appendix B

B.1 Resolution of radial integrals

This appendix reports the calculation of the radial integrals appearing in the geodesics equations (8.4) and (8.5). The double signs remind us that the integration along the whole trajectory of the photon must be performed in such a way that all pieces bounded by two consecutive inversion points must sum up with the same sign [43]. Gravitational lensing trajectories have only one inversion point in x_0, the closest approach distance. Thus we just have to sum the contributions due to two branches (approach and departure). These two branches of the photon trajectory are actually related by the time-reversal symmetry, so that the results of the whole radial integrals are just twice the contributions covering the departure branch. Summing up, the radial integrals reduce to

$$I_1 = 2\int\limits_{x_0}^{\infty} \frac{dx}{\sqrt{R}} \tag{B-1}$$

$$I_2 = 2\int\limits_{x_0}^{\infty} \frac{x^2+a^2-aJ}{\Delta\sqrt{R}} dx., \tag{B-2}$$

where we have neglected the corrections due to the finiteness of D_{OL} and D_{LS}, thus extending the integration domain to $+\infty$. The resolution by the SDL technique can be read from the appendix A of Paper I, since the only change comes when we replace J and Q by their new expressions containing μ_o. Thus we can directly jump to the results, which read

$$I_1 = \quad -a_1 \log\delta + b_1 \tag{B-3}$$

$$I_2 = \quad -a_2 \log\delta + b_2. \tag{B-4}$$

The coefficients expanded to second order in a are

$$a_1 = \frac{4}{3\sqrt{3}} + \frac{16}{27}a\hat{\xi} + \frac{8}{81\sqrt{3}}a^2(7+4\mu_o^2+5\hat{\xi}^2) \tag{B-5}$$

$$b_1 = a_1\log[12(2-\sqrt{3})] - \frac{8}{81}(5\sqrt{3}-6)a^2(1-\hat{\xi}^2) \tag{B-6}$$

$$\begin{aligned} a_2 &= \frac{4}{\sqrt{3}} + \frac{8}{3}a\hat{\xi} + \frac{8}{9\sqrt{3}}(3+2\mu_o^2+5\hat{\xi}^2) \qquad \text{(B-7)} \\ b_2 &= a_2\frac{1}{2\sqrt{3}}\left\{(2\sqrt{3}+6)\log[12(2-\sqrt{3})] - 3\log(48)\right\} \end{aligned}$$

$$
\begin{aligned}
&-\frac{4}{9}a\hat{\xi}[18-4\sqrt{3}+3\sqrt{3}\log(3)+6\sqrt{3}\log(2-\sqrt{3})] \\
&+\frac{4}{27}a^2\Big\{26\sqrt{3}-16-2\sqrt{3}\log(3)+8\mu_o^2-12\sqrt{3}\mu_o^2 \\
&+(3-\mu_o^2)[12\log(2-\sqrt{3})+6\log(3)]-\hat{\xi}^2[38\sqrt{3}-20 \\
&+5(1+2\sqrt{3})\log(3)+30\log(2-\sqrt{3})]\Big\}
\end{aligned}
\tag{B-8}
$$

with $\hat{\xi}=\xi\sqrt{1-\mu_o^2}$.

B.2 Resolution of angular integrals

This appendix is devoted to the resolution of the angular integrals

$$J_1 = \pm\int \frac{1}{\sqrt{\Theta}}d\vartheta \tag{B-9}$$

$$J_2 = \pm\int \frac{csc^2\vartheta}{\sqrt{\Theta}}d\vartheta. \tag{B-10}$$

Introducing the variable $\mu=\cos\vartheta$, the two integrals become

$$J_1 = \pm\int \frac{1}{\sqrt{\Theta_\mu}}d\mu \tag{B-11}$$

$$J_2 = \pm\int \frac{1}{(1-\mu^2)\sqrt{\Theta_\mu}}d\mu, \tag{B-12}$$

where

$$\Theta_\mu = a^2(\mu_-^2+\mu^2)(\mu_+^2-\mu^2) \tag{B-13}$$

$$\mu_\pm^2 = \frac{\sqrt{b_{JQ}^2+4a^2Q_m}\pm b_{JQ}}{2a^2} \tag{B-14}$$

$$b_{JQ} = a^2-J_m^2-Q_m, \tag{B-15}$$

and we have already replaced J and Q with J_m and Q_m, coherently with the fact that we only retain terms that are logarithmically diverging or constant in the approach parameter δ (or equivalently in the separation from the shadow ϵ).

Θ_μ has two zeros in $\mu=\pm\mu_+$. Then the photon performs symmetric oscillations of amplitude μ_+ w.r.t. the equatorial plane. It is useful to write the explicit expressions of μ_+ and μ_- in terms of the spin a and ξ (cosine of the position angle in the observer sky). Using Eqs. (8.17)-(8.18) in Eq. (B-14) and expanding to the second order in a, we find

$$\mu_+ = \sqrt{1-\hat{\xi}^2}\left[1+aA_+ +\frac{1}{2}a^2A_+^2\right] \tag{B-16}$$

$$
\begin{aligned}
\mu_- = &\frac{3\sqrt{3}}{2a}-2\hat{\xi}-4a\frac{(\mu_o^2+\hat{\xi}^2)}{3\sqrt{3}} \\
&+\frac{4}{27}a^2\hat{\xi}(3-10\mu_o^2-8\hat{\xi}^2)
\end{aligned}
\tag{B-17}
$$

where

$$A_+ = \frac{2\hat{\xi}(1-\mu_o^2)(1-\xi^2)}{3\sqrt{3}(1-\hat{\xi}^2)} \tag{B-18}$$

In a first approximation, the oscillation amplitude μ_+ is $\sqrt{1-\hat{\xi}^2}$, plus corrections due to the black hole spin. Note that the minimal amplitude of the oscillations is obtained for $\xi=\pm1$, which gives

$\mu_+ = |\mu_o|$. Purely equatorial trajectories with $\mu_+ = 0$ are involved in gravitational lensing only if the observer itself lies on the equatorial plane. On the other hand, polar photons ($\xi = 0$) perform oscillations with maximal amplitude $\mu_+ = 1$, touching the poles of the black hole.

Now it is convenient to introduce a new integration variable $z = \mu/\mu_+$, which allows to eliminate the dependence on a in the integration extrema. The integrals become

$$J_1 = \pm \int \frac{1}{\sqrt{\Theta_z}} dz \tag{B-19}$$

$$J_2 = \pm \int \frac{1}{(1-\mu_+^2 z^2)\sqrt{\Theta_z}} dz, \tag{B-20}$$

with

$$\Theta_z = a^2(\mu_-^2 + \mu_+^2 z^2)(1-z^2). \tag{B-21}$$

In order to perform the angular integrals, it is wise to expand the integrands to second order in a and then integrate. The primitive functions read

$$\begin{aligned} F_{J_1}(z) &= \frac{2}{3\sqrt{3}} \arcsin(z) \left[1 + \frac{4}{3\sqrt{3}} a\hat{\xi} \right. \\ &\left. -\frac{1}{27} a^2 (1 - 8\mu_o^2 - 25\hat{\xi}^2)\right] \\ &+\frac{2}{81\sqrt{3}} a^2 (1-\hat{\xi}^2) z\sqrt{1-z^2} \end{aligned} \tag{B-22}$$

$$\begin{aligned} F_{J_2}(z) &= \frac{2}{3\sqrt{3}\hat{\xi}} \arctan\left[\frac{z\hat{\xi}}{\sqrt{1-z^2}}\right] \Big\{1 \\ &+\frac{2}{3\sqrt{3}\hat{\xi}} a(1-\mu_o^2+\hat{\xi}^2) + \frac{2}{27\hat{\xi}^2} a^2 \Big[3(1+\mu_o^4-\hat{\xi}^2) \\ &+11\hat{\xi}^4 - 6\mu_o^2(1-\hat{\xi}^2)\Big]\Big\} + \frac{4}{81\sqrt{3}} a^2 \arcsin(z) \\ &-\frac{4}{27\hat{\xi}} \frac{z\sqrt{1-z^2}(1-\mu_o^2-\hat{\xi}^2)}{1-(1-\hat{\xi}^2)z^2} \Big\{a \\ &+\frac{a^2}{3\sqrt{3}\hat{\xi}\left[1-(1-\hat{\xi}^2)z^2\right]} \Big[3(1-\mu_o^2)+\hat{\xi}^2 \\ &-z^2\left(3-4\hat{\xi}^2+\hat{\xi}^4-\mu_o^2(3-5\hat{\xi}^2)\right)\Big]\Big\} \end{aligned} \tag{B-23}$$

Similarly to radial integrals, the angular integrals appear with double signs reminding that they must be performed piece by piece between any two consecutive inversion points and all contributions must be summed with the same sign [43]. The integration covers the whole trajectory of the photon, which may perform several oscillations around the equatorial plane. The integration must start from the source position $z_s \equiv \mu_s/\mu_+$ and must end at the observer position $z_o \equiv \mu_o/\mu_+$. Let us indicate by m the number of inversion points in the polar motion touched by the photon. Still we must consider two possibilities depending on the direction taken by the photon starting from z_s. In fact, we may have a trajectory in which z is initially either growing or decreasing. In the first case, the first pieces of the angular integrals cover the domain $[z_s, 1]$. After that, we have $m-1$ integrals covering the whole domain $[-1, 1]$. All these integrals must be taken with the same sign so that they always sum up. Finally, if m is even, the photon reaches z_o with growing z and the last piece covers the domain $[-1, z_o]$, otherwise z is finally decreasing and the domain is $[z_o, 1]$. The total angular integrals are thus given by the sum of all these contributions covering the domains just described. Exploiting the primitive functions (B-22) and (B-23), we can express each integral as (in the following, i takes the values 1 or 2)

$$\begin{aligned} J_i \quad &= F_{J_i}(1) - F_{J_i}(z_s) + (m-1)\left[F_{J_i}(1) - F_{J_i}(-1)\right] \\ &+ F_{J_i}(z_o) - F_{J_i}(-1) \end{aligned} \tag{B-24}$$

for m even and

$$\begin{aligned} J_i \quad &= F_{J_i}(1) - F_{J_i}(z_s) + (m-1)\left[F_{J_i}(1) - F_{J_i}(-1)\right] \\ &+ F_{J_i}(1) - F_{J_i}(z_o) \end{aligned} \tag{B-25}$$

for m odd.

Noting that both primitives are odd functions of z, we have $F_{J_i}(-1) = -F_{J_i}(1)$ and we can express the angular integrals in the compact form

$$J_i = \mp\left[F_{J_i}(z_s) - (-1)^m F_{J_i}(z_o)\right] + 2mF_{J_i}(1). \tag{B-26}$$

The $(-1)^m$ ensures that the sign of the z_o-term is the same as the z_s-term if the number of inversions is odd and is opposite if m is even. We have also introduced a double sign to take into account the possibility that z is initially decreasing from the starting value z_s.

For future reference, we also write the explicit values of $F_{J_i}(1)$

$$\begin{aligned} F_{J_1}(1) \quad &= \frac{\pi}{3\sqrt{3}}\left[1 + \frac{4a\hat{\xi}}{3\sqrt{3}} \right. \\ &\left. - \frac{a^2(1 - 8\mu_o^2 - 25\hat{\xi}^2)}{27}\right] \end{aligned} \tag{B-27}$$

$$\begin{aligned} F_{J_2}(1) \quad &= \frac{\pi}{3\sqrt{3}\hat{\xi}}\left\{1 + \frac{2a}{3\sqrt{3}\hat{\xi}}(1 - \mu_o^2 + \hat{\xi}^2) \right. \\ &+ \frac{2a^2}{27\hat{\xi}^2}\left[3(1 + \mu_o^4 - \hat{\xi}^2) + \hat{\xi}^3 + 11\hat{\xi}^4 \right. \\ &\left.\left. - 6\mu_o^2(1 - \hat{\xi}^2)\right]\right\}. \end{aligned} \tag{B-28}$$

B.3 Second order contributions to the lens equation

In this appendix we report the expressions for $\delta\mu_s^{(2)}$ and $\delta\phi_s^{(2)}$, which must be added to Eqs. (8.50) and (8.51) to obtain the second order lens equation. They read

$$\begin{aligned} \delta\mu_s^{(2)} \quad &= \mp(-1)^m \frac{\sqrt{1 - \hat{\xi}^2}}{54}\left\{6(\hat{\xi}^2 - 1)\cos\psi_1 \right. \\ &+ \left[(1 + 3\hat{\xi}^2)\cos\psi_o \right. \\ &\left.\left. + (1 - \hat{\xi}^2)\cos(2\psi_1 + \psi_o)\right]\sin\psi\right\} \end{aligned} \tag{B-29}$$

$$\begin{aligned} \delta\phi_s^{(2)} \quad &= \frac{1 - \hat{\xi}^2}{27\hat{\xi}^2}\cos^2\psi_o\left[1 - 21\hat{\xi}^2 + (1 - \hat{\xi}^2)\cos 2\psi_o\right] \cdot \\ &\cdot \left[\arctan(\hat{\xi}\tan\psi_o) - \arctan(\hat{\xi}\tan\psi_1)\right] \\ &- \frac{2 + (1 - \hat{\xi}^2)\cos 2\psi_1}{9(\cos^2\psi_1 + \hat{\xi}^2\sin^2\psi_1)}\hat{\xi}\psi_n \\ &+ \frac{1}{864\hat{\xi}(\cos^2\psi_1 + \hat{\xi}^2\sin^2\psi_1)^2}\sum_{i=0}^{3} p_i\hat{\xi}^{2i}, \end{aligned} \tag{B-30}$$

where $\psi_1 = \psi + \psi_o$, $\psi_n = 5\psi + 8\sqrt{3} - 20$ and

$$\begin{aligned}
p_0 &= 64\cos^3\psi_1\cos^3\psi_o\sin\psi && \text{(B-31)}\\
p_1 &= 384\cos\psi_1 + 2(7 + 4\cos 2\psi_o + \cos 4\psi_o)\sin 2\psi_1\\
&\quad -(11 + 20\cos 2\psi_o + 5\cos 4\psi_o)\sin 4\psi_1\\
&\quad +4\left[384 + (14\sin 2\psi_o + 5\sin 4\psi_o)\cos^2\psi_1\right]\cos 2\psi_1\\
&\quad +96(12 - \cos^2\psi_1\cos^3\psi_o\sin\psi_o) && \text{(B-32)}\\
p_2 &= 768(1 - \cos 4\psi_1) - 8(9 + \cos 2\psi_o)\cos^2\psi_o\sin 2\psi_1\\
&\quad +(13 + 28\cos 2\psi_o + 7\cos 4\psi_o)\sin 4\psi_1\\
&\quad +8(9 - 11\cos 2\psi_1)\cos^2\psi_1\sin 2\psi_o\\
&\quad +4(9 + 7\cos 2\psi_1)\sin^2\psi_1\sin 4\psi_o && \text{(B-33)}\\
p_3 &= 384(3 + \cos 4\psi_1) - (5 + 3\cos 4\psi_o)\sin 4\psi_1\\
&\quad +2(9 - \cos 4\psi_o + 24\cos 2\psi_o\sin^2\psi_1)\\
&\quad -20(\sin^2 2\psi_1\sin 2\psi_o + \sin^2\psi_1\sin 4\psi_o)\\
&\quad -12(128 + \sin^2\psi_1\sin 4\psi_o)\cos 2\psi_1. && \text{(B-34)}
\end{aligned}$$

Bibliography

[1] C. Afonso, J. N. Albert, J. Andersen, et al. A&A, 400, 951 (2003).

[2] C. Alcock *et al.*, ApJ **461**, 84 (1996).

[3] C. Alcock *et al.*, ApJ **486**, 697 (1997).

[4] C. Alcock *et al.*, ApJ **541**, 270 (2000).

[5] C. Alcock *et al.*, ApJ **542**, 281 (2000).

[6] C. Alcock *et al.*, ApJ **552**, 582 (2001).

[7] C. Alcock *et al.*, Nature **414**, 617 (2001).

[8] C. Alcock *et al.*, ApJ Supplement Series **136**, 439 (2001).

[9] D. R. Alves, ApJ, **601**, L151 (2004).

[10] Amore, P., & Arceo, S., Phys. Rev. D **73**, 083004 (2006).

[11] R. Ansari, M. Aurière, P. Baillon, *et al.*, A&A **324**, 843 (1997).

[12] H. Asada & M. Kasai, Progress of Theoretical Physics **104**, 95 (2000).

[13] H. Asada, M. Kasai & T. Yamamoto, Phys. Rev. D **67**, 043006 (2003).

[14] R.D. Atkinson, Astron. Jour. **70**, 517 (1965).

[15] F.K. Baganoff *et al.*, ApJ **591**, 891 (2003).

[16] A. C. Becker, A. Rest, C. Stubbs, et al., astro-ph/0409167.

[17] A.M. Beloborodov *et al.*, astro-ph/0601273, F. Eisenhauer, R. Genzel, T. Alexander et al., ApJ **628**, 246(2005).

[18] A. Bhadra, Phys. Rev. D **67**, 103009 (2003); E. F. Eiroa, Phys. Rev. D **71**, 083010 (2005); R. Whisker, Phys. Rev. D **71**, 064004 (2005); A. S. Majumdar and N. Mukherjee, Int. Jour.Mod. Phys. D **14**, 1095 (2005); J. M. Tejeiro and E. A. Larranaga, gr-qc/0505054.

[19] D. P. Bennett, ApJ **633**, 906 (2005).

[20] D. P. Bennett, A. C. Becker, & A. Tomaney, ApJ **631**, 301 (2005).

[21] J. Binney & S. Tremaine, *Galactic Dynamics*, Princeton Univ. Press, 1987.

[22] R. D. Blum, ApJ **444**, 89 (1995).

[23] J. Bodenner & C. M. Will, Am. J. Phys. **71**, 770 (2003).

[24] R.H. Boyer and R.W. Lindquist, Jour. of Math. Phys. **8**, 265 (1967).

[25] I. A. Bond *et al.*, MNRAS **327**, 868 (2001).

[26] V. Bozza, S. Capozziello, G. Iovane, and G. Scarpetta, Gen. Relativ. Gravit. **33**, 1535 (2001).

[27] V. Bozza, Phys. Rev. D **66**, 103001 (2002).

[28] V. Bozza, Phys. Rev. D **67**, 103006 (2003).

[29] V. Bozza and L. Mancini, ApJ **611**, 1045 (2004).

[30] V. Bozza and L. Mancini, Gen. Rel. and Grav. **36**, 435 (2004).

[31] V. Bozza, F. De Luca, G. Scarpetta, and M.Sereno, Phys. Rev. D **72**, 083003 (2005).

[32] V. Bozza, F. De Luca and G. Scarpetta, Phys. Rev. D. **74**, 063001 (2006).

[33] V. Bozza and L. Mancini, ApJ **627**, 790 (2005).

[34] V. Bozza and M. Sereno, Phys. Rev. D **73**, 103004 (2006).

[35] I. Bray, Phys. Rev. D **34**, 367 (1986).

[36] A. Cabrera-Lavers *et al.*, astro-ph/0702109.

[37] M. López-Corredoria *et al.*, AJ **133**, L154 (2007).

[38] S. Calchi Novati *et al.*, A&A **443**, 911 (2005).

[39] S. Calchi Novati, F. De Luca, Ph. Jetzer, G. Scarpetta, A&A **459**, 407 (2006).

[40] S. Calchi Novati *et al.*, A&A **443**, 911 (2005).

[41] B. Carter, Phys. Rev. **174**, 1559 (1968).

[42] G. Chabrier, ApJ **554**, 1274-1281 (2001).

[43] S. Chandrasekhar, *Mathematical Theory of Black Holes*, Clarendon Press, Oxford (1983).

[44] A. A. Cole, E. Tolstoy, J. S. Gallagher, & T. A. Smecker-Hane, AJ, 129, 1465 (2005).

[45] C.T. Cunningham and J.M. Bardeen, ApJ **183**, 237 (1973).

[46] C. Darwin, Proc. of the Royal Soc. of London **249**, 180 (1959).

[47] J. T. A. De Jong, L. M. Widrow, P. Cseresnjes, *et al.* A&A **446**, 855 (2006).

[48] X.Delfosse et *al.*, A&A **364**, 217 (2000).

[49] A. De Rújula, Ph. Jetzer and E. Massó, MNRAS **250**, 348 (1991).

[50] A. De Rújula, Ph. Jetzer and E. Massó, On the nature of the dark halo of our Galaxy, *Astron. Astrophys.* **254**, 99 (1992).

[51] E. Dweck *et al.*, ApJ **445**, 716 (1995).

[52] I.G. Dymnikova, in *IAU Symp. 114: Relativity in Celestial Mechanics and Astrometry. High Precision Dynamical Theories and Observational Verifications*, edited by J. Kovalevsky and V. A. Brumberg (1986).

[53] E. F. Eiroa and D. F. Torres, Phys. Rev. D **69**, 063004 (2004).

[54] E.F. Eiroa, G.E. Romero, and D.F. Torres, Phys. Rev. D **66**, 024010 (2002); A. Bhadra, Phys. Rev. D **67**, 103009 (2003); E. F. Eiroa, Phys. Rev. D **71**, 083010 (2005); R. Whisker, Phys. Rev. D **71**, 064004 (2005); A. S. Majumdar and N. Mukherjee, Int. J. Mod. Phys. D **14**, 1095 (2005); J. M. Tejeiro and E. A. Larranaga, gr-qc/0505054; E.F. Eiroa, gr-qc/0511065; K. K. Nandi, Y.-Z. Zhang, and A. V. Zakharov, gr-qc/0602062; K. Sarkar and A. Bhadra, gr-qc/0602087.

[55] A. Einstein, Erklärung der Perihelbewegung des Merkur aus der allgemeinen Relativitaetstheorie. *Sitzungberichte der Preussichen Akademie der Wissenschaften*, erster Halbband:831,1915.

[56] F. Eisenhauer, R. Genzel, T. Alexander et al., astro-ph/0502129.

[57] P. Englmaier and O. Gerhard, MNRAS **304**, 512 (1999).

[58] R. Epstein & I. I. Shapiro, Phys. Rev. D **22**, 2947 (1980).

[59] H. Falcke, F. Melia, and E. Agol, ApJ **528**, L13 (1999).

[60] E. B. Formalont and R. A. Sramek. Measurements of the solar gravitational deflectioon of radio waves in agreement with general relativity. *Phys. Rev. Letters*, **36**:1475,1976.

[61] K. C. Freeman, ARA&A **25**, 603 (1987).

[62] S. Frittelli and E.T. Newman, Phys. Rev. D **59**, 124001 (1999); S. Frittelli, T.P. Kling, and E.T. Newman, Phys. Rev. D **61**, 064021 (2000); M.P. Dabrowski and F.E. Schunck, ApJ **535**, 316 (2000); K.S. Virbhadra and G.F.R. Ellis, Phys. Rev. D **65**, 103004 (2002); V. Perlick, Phys. Rev. D **69**, 064017 (2004); V. Perlick, Living Rev. Rel. **7**, 9 (2004); P. Amore and S.A. Diaz, gr-qc/0602106.

[63] C. Gallart, P. B. Stetson, E. Hardy, F. Pont, & R. Zinn, ApJ, 614, L109 (2004).

[64] O. E. Gerhard, MNRAS, 265, 213 (1993).

[65] A.M. Ghez *et al.*, ApJ **601**, L159 (2004); R. Genzel *et al.*, Nature **425**, 934 (2003).

[66] J. F. Glicenstein, Astron. Astroph. **343**, 1025 (1999).

[67] H.Goenner, *Einfuehrung in die Kosmologie*, Spektrum Akademischer Verlag, Heidelberg, 1994.

[68] A. Gould, ApJ, **404**, 451 (1993).

[69] A. M. Green & K. Jedamzik, A&A, **395**, 31 (2002).

[70] K. Griest *et al.*, ApJ **372**, 79 (1991).

[71] G. Gyuk, N. Dalal, & K. Griest, ApJ, **535**, 90 (2000).

[72] C. Hagmann *et al.*, Phys. Rev. Lett. **51**, 1415 (1983).

[73] C. Hamadache *et al.*, A&A **454**,185-199 (2006).

[74] C. Han and A. Gould, ApJ **447**, 53 (1995).

[75] C. Han and A. Gould, ApJ **592**, 172 (2003).

[76] W. Hasse and V. Perlick, gr-qc/0511135.

[77] Q. Hu et al., astro-ph/0701197.

[78] J. Ibañez, Astron. Astroph. **124**, 175 (1983).

[79] J. Ibáñez & J. Martín, Phys. Rev. D **26**, 384 (1982).

[80] S. Ichimaru, ApJ **214**, 840 (1977); M.J. Rees, M. C. Begelman, R.D. Blandford, and E.S. Phinney, Nature **295**, 17 (1982); R. Narayan, I. Yi, and R. Mahadevan, Nature **374**, 623 (1995); M.A. Abramovicz, X. Chen, S. Kato, J.-P. Lasota, and O. Regev, ApJ **438**, L37 (1995); R. Mahadevan, Nature **394**, 651 (1998).

[81] P. Jetzer, L. Mancini, & G. Scarpetta, A&A, **393**, 129, paper I (2002).

[82] C. Keeton & A. O. Petters, Phys. Rev. D **72**, 104006 (2005).

[83] M. Kiraga and B. Paczyński, ApJ **430**, 101 (1994).

[84] S. Kopeikin, J. Math. Phys. **38**, 2587 (1997).

[85] S. Kopeikin & G. Schäfer, Phys. Rev. D **60**, 124002 (1999).

[86] S. Kopeikin & B. Mashhoon, Phys. Rev. D **65**, 064025 (2002).

[87] J. Kratochvil *et al.*, JCAP 07, 001 (2004).

[88] T.P. Krichbaum *et al.*, Proc. 6th European VLBI Network Symposium, Bonn, Germany, astro-ph/0207022.

[89] T. Lasserre, C. Afonso, J. N. Albert, et al., A&A **355**, L39 (2000).

[90] J. R. Lewis and K. C. Freeman, AJ **97**, 139 (1989).

[91] S. Liu and F. Melia, ApJ **573**, L23 (2002).

[92] J.P. Luminet, A&A **75**, 228 (1979).

[93] L. Mancini *et al.*, A&A **427**, 61-77 paper II (2004).

[94] S. Mao and B. Paczyński, ApJ **374**, L37-L40 (1991).

[95] J. P. Mbelek, A&A **424**, 761 (2004).

[96] F. Melia, ApJ **387**, L25 (1992); **426**, 577 (1994).

[97] F. Melia and H. Falcke, Annual Review of Astronomy and Astrophysics **39**, 309 (2001)

[98] D. Méra, G. Chabrier & I. Baraffe, ApJ **459**:L87-L90 (1996).

[99] G. E. Miller & J. M. Scalo, ApJS, 41, 513.

[100] D. Minniti, J. Borissova, M. Rejkuba, et al. Science, **301**, 1508 (2003).

[101] J. J. Mohr *et al.*, ApJ **517**, 627 (1999).

[102] M.P. Muno *et al.*, ApJ **622**, L113 (2005).

[103] R.J. Nemiroff, Amer. Jour. Phys. **61**, 619 (1993).

[104] H.C. Ohanian, Amer. Jour. Phys. **55**, 428 (1987).

[105] S. J. Peale, ApJ **509**, 177 (1998).

[106] B. Paczyński, ApJ **304**, 1 (1986).

[107] B. Paczyński, ApJ **371**, 63 (1991).

[108] R. Peccei & H. Quinn, Phys. Rev. Lett. **38**, 1440 (1977).

[109] V. Perlick, Phys. Rev. D **69**, 064017 (2004).

[110] A.O. Petters, MNRAS **338**, 457 (2003).

[111] S. Picaud & A. C. Robin, A&A **428**, 891 (2004).

[112] S. Pineault & R. C. Roeder, ApJ **212**, 541 (1977).

[113] P. Popowski *et al.*, ApJ **631**, 879-905 (2005).

[114] J.R. Primack, D. Seckel and B. Sadoulet, Ann. Rev. Nucl. Part. Sci., **38**,751,1988.

[115] K.P. Rauch and R.D. Blandford, ApJ, **421**, 46 (1994).

[116] M.J. Reid, ARA& A **31**, 345 (1993).

[117] C. Reylé and A. C. Robin, A&A **373**,886-894 (2001).

[118] C. Renault *et al.*, A&A **324**, L69-L72 (1997).

[119] Riffeser, A., Fliri, J., Seitz, S., & Bender, R., ApJS,**163**, 225 (2006).

[120] E. Roulet and S. Mollerach, Phys. Rep. **279**, 67-118 (1997).

[121] B. Sadoulet, Rev. Mod. Phys. **71**, 197 (1999).

[122] B. P. Schmidt, Bull. Astr. Soc. India **32**, 269-281 (2004).

[123] P. Schneider, J. Ehlers and E. E. Falco, Gravitational Lenses (Springer-Verlag: Berlin), 1992.

[124] P. Schneider and A. Weiss, A&A **164**, 237 (1986).

[125] M. Sereno, Phys. Letters A **305**, 7 (2002).

[126] M. Sereno, MNRAS **344**, 492 (2003).

[127] M. Sereno, Phys. Rev. D **67**, 064007 (2003).

[128] M. Sereno, V. F. Cardone, Astron. Astroph. **396**, 393 (2002).

[129] S. Capozziello, V. F. Cardone, V. Re & M. Sereno, MNRAS **343**, 360 (2003).

[130] M. Sereno, MNRAS **357**, 1205 (2005).

[131] M. Sereno & F. De Luca, Phys. Rev. D **74**, 123009 (2006).

[132] J. Soldner, Über die Ablenkung eines Lichtstrahls von seiner geradlinigen Bewegung durch die Attraktion eines Weltkörpers, an welchem er nahe vorbeigeht. *Berliner Astronomiches Jahrbuch* 1804, pag. 161,1804.

[133] D. N. Spergel *et al.*, ApJ **148**, 175-194 (2003).

[134] K. Z. Stanek *et al.*, ApJ **477**, 163 (1997).

[135] T. Sumi *et al.*, ApJ **636**,240 (2006).

[136] C. L. Thomas *et al.*, ApJ **631**, 906-934 (2005).

[137] P. Tisserand, & A. Milsztajn, astro-ph/0501584.

[138] P. Tisserand *et al.*, astro-ph/0607207.

[139] R. P. Van der Marel & M. Franx, ApJ, **407**, 525 (1993).

[140] R. P. Van der Marel *et al.*, AJ **124**, 2639-2663 (2002).

[141] R. P. Van der Marel, astro-ph/0404192.

[142] S.E. Vazquez and E.P. Esteban, Nuovo Cim. **119B**, 489 (2004).

[143] K.S. Virbhadra and G.F.R. Ellis, Phys. Rev. D **62**, 084003 (2000).

[144] S.U. Viergutz, A&A **272**,355 (1993); A. de Vries, Class. Quant. Grav. **17**, 123 (2000); R. Takahashi, ApJ **611**, 996 (2004); K. Beckwith and C. Done, MNRAS **359**, 1217 (2005).

[145] M. D. Weinberg, ApJ **532**, 922 (2000).

[146] S. Weinberg, *Gravitation and Cosmology : principles and applications of the general theory of relativity*, John Wiely & Sons,NY,1972.

[147] F. Yuan, E. Quataert, and R. Narayan, ApJ **606**, 894 (2004).

[148] A.F. Zakharov, A.A. Nucita, F. De Paolis, and G. Ingrosso, astro-ph/0411511.

[149] Z. Zheng *et al.*, ApJ **555**, 393 (2001).

[150] M. Zoccali *et al.*, ApJ **530**, 418-428 (2000).

List of Figures

Acknowledgements

The reserach activity that I pursued during the last threee years as a PhD student resulted in this Thesis. I am grateful to my tutors Prof. G. Scarpetta and Prof. Ph. Jetzer for the frequent and useful discussions and constant support.

Special thanks go to V. Bozza, S. Calchi Novati and M. Sereno for allowing me to collaborate with them on interesting and stimulating topics and to Tobias Goerdt who helped me with the German version of the introduction to this thesis.

CURRICULUM VITAE

Personal data

Name, first name: De Luca, Fabiana
Place and date of birth: Benevento, Italy, 16/6/1980
Nationality: Italian
Marital status: Not married
Corresponding address: University of Zurich
Institute for Theoretical Physics
Winterthurerstrasse 190
CH-8057 Zurich
Switzerland
Phone number: (+41) 1 6355806
Email: fadeluca@physik.unizh.ch

Education

10/2003-5/2007: PhD in Physics, Dr. sc. nat., University of Zurich, Switzerland
PhD thesis: *Gravitational lensing as a tool to detect dark matter and to test gravity theories*
Thesis supervisors: Prof. Philippe Jetzer
Prof. Gaetano Scarpetta

10/1998-07/2003: Laurea in Fisica, Universita' degli Studi di Salerno
Master subjects: Theoretical physics, Astrophysics
Diploma thesis: *Schwarzschild black holes entropy*
Thesis supervisor: Prof. Gaetano Scarpetta

09/1993-07/1998: Maturita' Linguistica, Magistrale G. Guacci, Benevento, Italy

Publications

V. Bozza, F. De Luca, G. Scarpetta, M. Sereno, *Analytic Kerr black hole lensing for equatorial observers in the strong deflection limit*, Phys. Rev. D **72**, 083003 (2005).

V. Bozza, F. De Luca, G. Scarpetta, *Kerr black hole lensing for a generic observer in the strong deflection limit*, Phys. Rev. D. **74**, 063001 (2006).

S. Calchi Novati, F. De Luca, Ph. Jetzer and G. Scarpetta, *Microlensing towards LMC: a study of the LMC halo contribution*, A&A **459**, 407 (2006).

M. Sereno & F. De Luca, *Analytic Kerr black hole lensing in the weak deflection limit* Phys. Rev. D **74**, 123009 (2006).

S. Calchi Novati, F. De Luca, Ph. Jetzer, L. Mancini and G. Scarpetta, *Microlensing constraints on the Galactic Bulge IMF*, submitted to A&A.

Schools and Conferences

Bertinoro (FC, Italy), Scuola Nazionale di Astrofisica, 16-21 May 2004

Novigrad (Croatia), Summer School Novicosmo 2005, 5-17 September 2005

Turin (Italy), Meeting NA12, 27-28 October 2005

Naples, 1st Workshop of Astronomy and Astrophysics for Students, 19-20 April 2006

Berlin, 11th Marcel Grossman Meeting, 23-29 July 2006

Naples, NA12 Meeting, 26-27 October 2006